Neutrino Oscillation Analysis at the T2K experiment including studies of new uncertainties on interactions involving additional final state hadrons

Edward Thomas Atkin
Imperial College London

A thesis submitted to Imperial College London
for the degree of Doctor of Philosophy in Physics

Abstract

The Tokai to Kamioka (T2K) experiment is a long-baseline neutrino experiment based in Japan. The experiment aims to make precise measurements of neutrino oscillation parameters, in particular, the δ_{CP}, Δm^2_{32}, θ_{23}, θ_{13} parameters and the ordering of the neutrino mass states. To make these measurements the T2K experiments utilises the Japan Proton Accelerator Research Complex (J-PARC) which produces an intense neutrino beam. This neutrino beam is aimed across Japan towards the Super-Kamiokande (SK) detector on West coast of Japan, 295 km away from J-PARC. Properties of the unoscillated neutrino beam are constrained by a series of near detectors at the J-PARC site: ND280 and INGRID. The measurements of the unoscillated and oscillated neutrino beam allow the T2K experiment to measure neutrino oscillation parameters. The general approach of the T2K oscillation analysis strategy will be described as well as the Markov Chain Monte Carlo methods and Bayesian techniques used by the MaCh3 analysis framework which was used for the analysis.

An important part of measuring neutrino oscillation parameters accurately is assigning appropriate systematic uncertainties. One of the largest sources of systematic uncertainty for the T2K experiment comes from the simulation of neutrino interactions. A more sophisticated treatment of systematic uncertainties related to Charged Current (CC) interactions producing multiple pions (CC Multi-π) and CC Deep Inelastic Scattering interactions (CC DIS) has been developed as part of the improvements to the T2K oscillation analysis. A better description of the uncertainties associated with these interactions is desired for including higher energy data samples into the T2K oscillation analysis.

The latest results on neutrino oscillation parameters from the T2K experiment are shown. This analysis uses the full run 1–10 dataset as well as significantly improved systematic uncertainties. The highlights of these results are that CP conserving values of the δ_{CP} parameter are ruled out at over 90% significance, the upper octant of $\sin^2\theta_{23}$ is preferred as is the normal ordering of the neutrino mass states.

To make more precise statements about neutrino oscillation parameters in the future

the T2K experiment will need to reduce the statistical uncertainty on them. One way to do this is by adding more data samples at SK into the analysis. The sensitivity of the T2K experiment with the addition of a sample targeting ν_μCC1π interactions will be presented. This sample has the potential to improve the sensitivity of the analysis, especially to the Δm^2_{32} and θ_{23} oscillation parameters. This new sample is also expected to contain significantly more CC Multi-π and CC DIS interactions than other samples used in the analysis. The importance of the improved systematics that were developed for CC Multi-π and CC DIS interactions to this new sample will also be shown.

Declaration

The analyses described in this thesis are my own work as part of the T2K collaboration. The work by others and the inputs provided to the analysis are properly cited and referenced.

Chapters 1, 2 and 3 are summaries of the field of Neutrino Physics and the T2K experiment and constitute the work of many people. The work of theorists and experimentalists to the field is appropriately cited throughout. Chapter 4 and 5 then describe the statistical techniques and analysis strategy used by the analyses presented in this thesis. Most of these techniques are common within Physics and data science whereas others have been developed by members of the collaboration specifically for the T2K analysis. The citations for these techniques are given where appropriate. Internal T2K sources that are cited, such as T2K Technical Notes, can be made available upon request of the collaboration.

Chapter 6 describes the development of new uncertainties that are then used in the analysis in chapter 7. The development and implementation of these new uncertainties is all my own and described in the text. This work built on previous studies by another T2K collaborator. The inputs for the rewighting to the AGKY model shown in chapter 6 are the only non-publically available item used and were made and provided by Christopher Bronner. Chapter 7 then shows the latest oscillation analysis results from the T2K experiment which were presented publically at the Neutrino 2020 conference [1]. This analysis used data and inputs made by the T2K collaboration and was the result of my own work along with other analysers.

Chapter 8 then extends the analysis in chapter 7 with the inclusion of new inputs. These inputs were made with the help of other T2K collaborators and built on the work done by Dr. Tomoyo Yoshida. The studies presented in chapter 8 are all my own work and were produced purely for the purpose of this thesis.

Copyright Declaration

Acknowledgements

Firstly, I would like to thank my supervisor Professor Morgan Wascko and assistant-supervisor Dr. Patrick Dunne for always providing the support and expertise needed for me to write this thesis. I hope to have many more engaging discussions about physics or otherwise with you both for many years to come. This is also true of the entire long baseline group at Imperial College London, in particular; Professor Yoshi Uchida, Dr. Mark Scott, Dr. Per Jonsson and Dr. Abbey Waldron. I have been very fortunate to feel that I could turn to any member of the long baseline group for help or advice throughout the Ph.D.. I also want to thank my fellow students in the neutrino group who have made day-to-day life at Imperial both informative and entertaining. Special thanks to Dr. Artur Sztuc, Dr. Toby Nonnenmacher, Dr. Wilf Shorrock and Charlie Naseby. Whether it's been discussions about Physics, lengthy group meetings, trips to the Queen's Arms or Karaoke in Japan, life as part of the Imperial group has been jolly.

Being part of the T2K collaboration has been an incredibly rewarding part of the past years. Fellow collaborators have always provided support whenever needed and have given fruitful feedback to work I have presented. I would like to thank all members of the oscillation analysis and NIWG groups at T2K who I have worked with a lot during the course of the Ph.D.. In particular, Dr. Asher Kaboth, Dr. Will Parker, Dr. Clarence Wret, Dr. Luke Pickering, Dr. Kevin Wood, Dr. Balint Radics and Dr. Christophe Bronner. Your technical help, expertise and company have been key to work in this thesis and my education during the Ph.D.

My family and friends have been another pillar of support through the course of the Ph.D.. My parents, siblings and Libby Atkin as well as the entire Nastas family have all been an invaluable source of support and entertainment throughout.

Finally, I would like to thank Maria Nastas. I never expect you to put yourself through the torment of reading this thesis, but I hope you know that I could not have done this without your continual love and support.

Contents

1 Introduction **36**

2 Theory of neutrinos and neutrino oscillations **40**

2.1 Standard Model 40

2.1.1 The discovery of the neutrino and Weak interactions 42

2.2 Neutrino oscillation theory 45

2.2.1 Three-flavour neutrino oscillations 45

2.2.2 Anti-neutrino oscillations 51

2.2.3 Majorana Neutrinos 51

2.2.4 Neutrino oscillations in matter 52

2.2.5 Charge-parity violation 54

2.2.6 Phenomenology of neutrino oscillations 57

2.3 Experimental overview 61

2.3.1 Solar neutrino experiments 61

2.3.2 Reactor neutrino experiments 65

2.3.3 Atmospheric neutrino experiments 67

2.3.4 Long-baseline neutrino experiments 69

2.4 Neutrino Interactions 71

2.4.1 Interaction types 72

2.4.2 Nuclear Effects 74

2.4.3 Final State Interactions 75

3 The Tokai-to-Kamiokande experiment 77

3.1 Making the neutrino beam 78

3.1.1 Making the proton beam 79

3.1.2 The T2K beamline 79

3.1.3 Magnetic Horns 80

3.1.4 Beam Dump and Muon monitor 81

3.1.5 Off-Axis Technique 82

3.2 The Near Detector suite 85

3.2.1 Interactive Neutrino Grid 85

3.2.2 The Near Detector at 280m 87

3.3 The Super-Kamiokande Detector 89

4 Analysis Technique 92

4.1 Neutrino oscillation analysis 92

4.1.1 Event reconstruction at ND280 94

4.1.2 ND280 data 96

4.1.3 Event reconstruction at SK 99
4.1.4 SK data 102
4.1.5 Statistical treatment of ND280 and SK data 103
4.2 Nuisance parameters 104
4.2.1 Neutrino Flux 105
4.2.2 Neutrino interaction model 108
4.2.3 Detector systematics 116
4.2.4 Neutrino oscillation parameters 120
4.3 T2K Likelihood function 122
4.4 Fake Data Studies 124

5 Markov Chain Monte Carlo 126

5.1 Markov Chain Monte Carlo 126
5.1.1 Metropolis-Hastings algorithm 129
5.2 Chain diagnostics 131
5.2.1 Burn-in 131
5.2.2 Auto-correlations 132
5.3 Making measurements of parameters 134
5.3.1 Marginalisation of nuisance parameters 135
5.3.2 Best-fit values and credible intervals 135
5.3.3 Reweighting of priors 137
5.4 Computational improvements 138

5.5 Validation of fitter 140
5.5.1 Cross-checks with other analysis frameworks 140
5.5.2 Likelihood Scans 141
5.5.3 Asimov fits 141

6 Neutrino Interaction Uncertainties for the T2K Oscillation analyses 145

6.1 Deep Inelastic scattering 146
6.2 Deep Inelastic scattering at T2K 149
6.2.1 CC Multi-π and CC DIS at ND280 150
6.2.2 CC Multi-π and CC DIS at SK 150
6.3 Improved nuisance parameters for CC Multi-π and CC DIS interactions . 151
6.3.1 Previous uncertainty 152
6.3.2 New nuisance parameters for the oscillation analysis 153
6.3.3 Impact on MC predictions 161
6.4 Behaviour of parameters in a fit to data 164
6.5 Summary 165

7 Neutrino Oscillation analysis using runs 1–10 **167**

7.1 Data and MC predictions at ND280 168
7.2 Data and MC predictions at SK 171
7.3 Fits to T2K data only (without reactor constraint) 173
7.3.1 Oscillation parameter constraints 173

7.4 Fit to T2K Data with reactor constraint 176

7.4.1 Oscillation parameter constraints 177

7.5 Comparison of results with Data 180

7.6 Studies on the prior constraint used on δ_{CP} 184

7.7 Summary of results 186

7.7.1 Discussion of δ_{CP} 189

8 Oscillation Analysis including the ν_μ CC$1\pi^+$ data sample at Super-Kamiokande 193

8.1 ν_μCC1π event selection 194

8.2 MC predictions at SK for the FHC ν_μCC1π sample 198

8.3 Improved sensitivity to oscillation parameters 203

8.4 Effect of mismodeling CC Multi-π and CC DIS interactions 209

8.5 Summary 221

9 Conclusion and outlook 223

A Neutrino Interaction Uncertainties 237

A.1 BY inputs 237

A.2 Bodek-Yang reweighting validations 240

A.2.1 H2O 240

A.2.2 CH 240

B Analysis Technique 257

B.1 ND280 sample binning 257

B.2 SK sample binning 258

C Oscillation Analysis Results **260**

C.1 Pre-fit ND280 predictions 260

C.2 SK Event rate predictions 269

C.2.1 SK Event rate predictions with nuisance parameters at post-ND280 fit values 269

C.2.2 SK event rates, nuisance parameter at pre-ND280 fit values 279

C.3 Comparison to data without reactor constraints 289

D Oscillation Analysis including the ν_μCC1π sample at SK **291**

D.1 Fake data at ND280 291

List of Figures

2.1 The particles which make up the standard model of particle physics [7]. . 41

2.2 A Feynman diagram of a Fermi interaction. The interaction is considered point-like where the coupling of the interaction is given by the Fermi constant G_F. 43

2.3 Feynman diagrams of a CC (left) and an NC (right) neutrino interaction on a nucleon. 45

2.4 A visualisation of the neutrino flavour eigenstates oscillating from flavour α to flavour β after propagating a distance L. The upper diagram shows neutrino oscillations with flavour eigenstates and the lower diagram shows them with mass eigenstates. "Prop(ν_i)" is shorthand for the propagation of the neutrino mass eigenstate through a vacuum. "Amp" denotes amplitude. Figure taken from [20]. 47

2.5 Feynman diagrams of the CC and NC coherent forward scattering which is responsible for matter effects. The CC channel can only occur on electron neutrinos. Figure from [8]. 53

2.6 Electron-neutrino appearance probability as a function of neutrino energy for different values of δ_{CP} and the different mass hierarchies. It can be seen that changing the mass hierarchy has a very similar impact to change the values of δ_{CP}. This effect is caused by matter effects. Figure from [24]. . 54

2.7 A schematic of the effect of C, P and CP operators on the transitions of a neutrino of flavour α and left or right-handed chiral states to a neutrino of flavour β. If CP is violated the process on the left will not be observed to be equal to the that on the right. Although ν_α^{RH} and $\bar{\nu}_\alpha^{LH}$ states are not allowed in the standard model they are included to make it clear how the C and P operators behave. 56

2.8 Diagrams of the two possible orderings the neutrino masses could take. The case where Δm^2_{32} is positive is referred to as the Normal Ordering and when Δm^2_{32} is negative this is referred to as the Inverted Ordering. 59

2.9 Neutrino fluxes as a function of neutrino energy for different processes in the Sun as predicted by the standard solar model. Notice that for all processes the neutrino energy is still below 20 MeV. Figure taken from [40]. 62

2.10 Results from the SNO collaboration which solved the solar neutrino problem and showed that neutrinos from the sun oscillate. The results show that the measured neutrino fluxes from elastic scattering (ES), CC and NC channels are consistent with the Standard Solar Model (SSM). Figure taken from [3]. 64

2.11 A comparison of the ratio of the expected unoscillated $\bar{\nu}_e$ events and the observed number of events and the distance to the reactor for several experiments. The thin-dashed line shows the ratio of expected and observed events assuming $\sin^2 2\theta_{12} = 0.833$ and $\Delta m^2_{21} = 5.5 \times 10^{-5}\text{eV}^2$. Figure from [45]. 66

2.12 A plot showing the electron antineutrino survival probability for the Double-Chooz experiment. The impact individual impact of θ_{13} (orange) and θ_{12} (blue) can be seen as well as their combined impact. It can be seen that θ_{13} is associated with the higher frequency oscillations while θ_{12} with the longer oscillations. Figure taken from [46]. 67

2.13 A diagram showing the production of atmospheric neutrinos and other processes in the atmosphere. Figure taken from [50]. 69

2.14 Comparison of constraints on the θ_{23} and Δm^2_{32} oscillation parameters for the NH only for different long-baseline and atmospheric neutrino experiments. The results from NOvA, SK, IceCube can be found at [53], [54] and [38] respectively. The T2K results are those presented in chapter 7 of this thesis. Figure taken from [55]. Generally, different long-baseline experiments agree broadly on the favoured parameter values. 71

2.15 Neutrino interaction cross sections predicted by the NEUT generator [56] for the different interaction modes described. CCQE and 2p-2h occur at typically lower energies, while CCRES and CC DIS (and CC Multi-π which will be introduced later) occur a typically higher energies. The T2K flux shape is superimposed on the plot as well to compare the energy regime that T2K operates at. 72

2.16 CCQE Feynman diagram. 75

2.17 CCRES Feynman diagram. 75

2.18 CC DIS Feynman diagram. 76

3.1 A schematic of the T2K experiment showing the J-PARC facility and Near Detectors on the east-coast of Japan as well as the far detector Super-Kamiokande on the west-coast of Japan. 78

3.2 A diagram of the T2K beamline (also known as the secondary beamline) and its different components (left) and a cross section of the target station, decay volume and beam dump (right). Figures taken from [62] 79

3.3 ν_μ flux prediction at SK (left) showing the parent mesons in neutrino mode. The majority of ν_μs come from pions. On the right the $\bar{\nu_\mu}$ flux in neutrino mode can be seen to be orders of around 100 times lower than the ν_μ flux showing that the use of magnetic horns has significantly reduced this wrong-sign background in neutrino mode. 81

3.4 Neutrinos which are produced at a larger angle relative to the pion direction, $\theta_{\nu\pi}$, have lower energies compared to those produced in the direction of the pion. The result of this effect is a lowering and sharpening of the neutrino beam energy. 83

3.5 Placing the detectors at an off-axis (OA) angle of 2.5° sharpens the neutrino flux at SK, $\Phi_{\nu_\mu}^{295km}$ at $\sim$ 0.6 GeV which coincides with the lowest probability of muon-neutrino survival as shown in the top panel [64]. . . 83

3.6 A diagram of the T2K secondary beamline showing the positions of the various monitors used to measure the proton beam. 84

3.7 Exploded view of the ND280 detector showing the sub-detectors. The beam direction goes from the left to the right of the image. Figure from [60]. 85

3.8 INGRID detector where the cross shape can clearly be seen. The beam centre is in the middle of the cross shape. Figure taken from [65]. 85

3.9 A diagram of one of the 14 modules that make up the INGRID detector. On the left the layers of scintillator (blue) and iron planes can be seen and on the right the fully assembled module surrounded by veto planes (black) can be seen. Figure taken from [62]. 86

3.10 An example of a neutrino interaction in an INGRID module. The neutrino enters from the left and interacts in the detector. The red circles indicate the position of the reconstructed hit and the size of the circle the size of the reconstructed signal. The green layers are scintillator, grey iron layers and the blue the veto planes surrounding the module. Figure taken from [62]. 86

3.11 The SK detector with the Inner and Outer detectors clearly visible. The detector has an overburden of $\sim$ 1000 m and is accessed by a tunnel. Figure from [68]. 90

3.12 Two example event displays of the SK detector. Left is a muon-like ring and on the right is an example of an electron-like ring. The colour represents the arrival time of light at a PMT with violet corresponding to earlier times and red to later times. The size of the squares represents the number of photo-electrons detected [64]. 91

4.1 The mean reconstructed lepton momentum against true lepton momentum for events recosntructed as CC0π (left) and CC1π (right) events in FGD1. The error bars are the mean of a gaussian fitted to the reconstructed momentum distribution for each true momentum bin. In both samples, the momentum resolution for muons with true momentum less than 2 GeV is typically below 100 MeV with this steadily increasing with higher true momentum. 96

4.2 The energy loss against momentum for different particle types. The lines indicate MC expectations for different positively charged particle types and the points data points taken from the first T2K physics run. Figure taken from [62]. 97

4.3 Fractional residual of reconstructed and true neutrino energy for the FHC 1Rμ and FHC 1ReCC1π samples at SK. 101

4.4 A comparison of the thin target configuration (left) and replica target configuration (right) used at the NA61 experiment. Figure taken from [78] 106

4.5 The fractional uncertainty on the neutrino beam prediction for the different neutrino flavours in both neutrino and anti-neutrino mode. The fractional uncertainty is also broken down by the source of uncertainty. 107

4.6 The flux covariance matrix used in the neutrino oscillation analysis. The labels show the parameters which are associated with the different detectors, horn operating modes and neutrino flavours. In general the flux covariance which are positively correlated with other flux parameters. . . 109

4.7 Examples of cross-section parameters splines which are used to apply systematic uncertainties in the oscillation analysis. The red markers indicate the spline knots where the exact reweighting of a parameter has been calculated at whereas the black line is the result of a cubic spline fit being used with these knots. The x-axis on these plots is the relative shift from nominal where the nominal is 0. The spline knots used are chosen to cover parameter values of at least 3σ away from a parameters prior central value. 111

4.8 The covariance matrix used for the prior uncertainties for nuisance parameters related to neutrino interactions. The covariance is given as a fraction of the nominal value for parameters where the nominal value is not equal to zero for example for the non-resonant I-$\frac{1}{2}$ background parameter $\sqrt{V_{ij}}$ is given by the prior uncertainty 0.4 divided by the nominal value 1.3 which is $\frac{0.4}{1.3} \approx 0.31$. For parameters where the nominal value is 0 then $\sqrt{V_{ij}}$ is simply the prior uncertainty such as for the E_b parameters.One can see that in the covariance matrix used for the pre-fit is mainly diagonal. . . . 118

5.1 An example of random sampling being used to estimate π by estimating the area of a circle. The red points all fall into the area of the circle and hence the integral and the blue points are those that do not fall within the circle. Figure taken from [100] 127

5.2 A schematic showing the key steps of the Metropolis-Hastings algorithm. This processes is repeated until the number of desired steps have been taken. 131

5.3 The negative LLH of several chains against the number of steps taken. It can clearly be seen that the chains all converge to similar values of the likelihood after $\sim 100 \times 10^3$ steps. The negative LLH often gives very high values initially as initial parameter values can be very unlikely. 132

5.4 Auto-correlation vs. lag for two different nuisance parameters. The auto-correlation decreases as lag increases and is below 0.2 for a lag of 30,000 which what the step size tuning procedure aims for. 133

5.5 An example of 1D and 2D marginalised posterior distributions which also highlight the slight different in parameter value with the highest value in the posterior distribution. 136

5.6 An example of 1D CI on δ_{CP} marginalised over both mass hierarchies. . . 137

5.7 A comparison of the step time per MCMC step before and after improvements to the code were made. The step time is reduced by $\sim 40\%$. 140

5.8 2D likelihoods scan for Δm^2_{32} vs. $\sin^2\theta_{23}$ (top) and θ_{13} vs. δ_{CP} (bottom). The best-fit values found in the likelihood scans are extremely close to the input oscillation parameter values indicating that the likelihood calculation is working correctly. The contours indicate values of constant likelihood. 142

5.9 2D constraints on oscillation parameters from an Asimov A fit. Good agreement is found between the input oscillation parameter values and the best fit values retrieved from the fit. The top plots show constraints marginalised over the normal mass hierarchy, middle over inverted mass hierarchy and bottom over both mass hierarchies. 144

6.1 CCRES, CC Multi-π and CC DIS components for the FGD1 CC1π (top) and CC Other (bottom) FHC samples. The z-axis is the fraction of events of a given interaction that make up the nominal MC prediction in each bin. 151

6.2 Comparisons of the cross sections in MC events using PDFs with BY corrections and without (No BY). A significant difference can be seen in the low Q^2 region for both CC Multi-π and CC DIS interactions. 154

6.3 Example of inputs used for reweighting the MC prediction in the fit. The area of large difference comes in regions of low Q^2. This can be seen as the largest weights in the inputs can be seen in these regions. 156

6.4 Comparisons of MC events reweighted from using BY corrections to without BY corrections using the inputs given in fig. 6.3 for ν_μ CC Multi-π (top) and CC DIS (bottom) interactions on water. Comparisons are given in the two variables the inputs were made in i.e. Q^2 (left) and E_ν in the nucleon frame (right). The lower panels in all the plots show the difference between reweighted MC and that generated without BY corrections. Generally the reweight MC matches well with MC events that were generated without BY corrections however some differences arise a low Q^2 and low E_ν in the nucleon frame. However, these differences are small and in a region where the cross sections are very small originally. To aid in the comparisons the integral of each distribution is given in the legend for the MC events made with BY corrections, the reweighted ones and those generated without BY corrections to the PDFs. 158

6.5 Examples of splines used for the BY uncertainty for CC DIS (left) and CC Multi-π (right) interactions. These splines exhibit typical behaviour in returning weights larger than one for positive variations relative to nominal and negative for variations less than zero. The red stars indicate the spline knot positions. 159

6.6 Examples of inputs used for reweighting MC predictions based on uncertainties on the CC Multi-π multiplicity model. The weights are taken from the ratio of predictions using the AGKY multiplicity model to the nominal NEUT prediction. The x-axis is true neutrino energy. 160

6.7 Examples of the splines response to the AGKY reweighting at different parameter values. 160

6.8 The impact of the new uncertainties on CC DIS and CC Multi-π interactions on the FGD1 CC-1π FHC sample at ND280. The impact is shown as a ratio to the nominal MC prediction and for variation of $+1\sigma$ and -1σ. 162

6.9 The impact of the new uncertainties on CC DIS and CC Multi-π interactions on the FGD1 CC-Other FHC sample at ND280. The impact is shown as a ratio to the nominal MC prediction and for variation of $+1\sigma$ and -1σ. 163

6.10 Variations of the three new systematic parameters for CC DIS and CC Multi-π interactions and how they affect the FHC 1Rμ MC prediction at SK. It can be seen that the parameters which affect CC Multi-π interactions have the largest impact since there are more CC Multi-π interactions predicted for this sample than CC DIS interactions. 164

6.11 Parameter value comparisons pre-fit (i.e. at prior central values) (red), post a fit to ND280 data only (blue) and then post a joint-fit of ND280 and SK data (black). The joint-fit has very similar post-fit parameter values compared to the ND280 only data fit as the ND280 data provides a much larger constrain on parameters. 165

7.1 The beam power, running period and POT accumulated for each run of the J-PARC beamline. Runs 1–10 can be seen to span 10 years of data taking. Figure from [116]. 168

7.2 Pre-fit p_μ projections of data and nominal MC broken down by interaction mode for FHC selections. The FGD1 samples can be seen on the left and FGD2 on the right. Figures taken taken [117]. 170

7.3 The MC prediction for each data sample at SK with the data overlaid. Top left is the FHC 1Rμ sample, top right FHC 1Re sample, middle left RHC 1Rμ, middle right the RHC 1Re sample and bottom the FHC 1ReCC1π sample. 172

7.4 Data-fit results without reactor constraint: 2D credible intervals for Δm^2_{32} vs. $\sin^2\theta_{23}$ (left) and δ_{CP} vs. $\sin^2\theta_{13}$ (right) marginalised over NH (top), IH (middle) and both mass orderings (bottom). 174

7.5 Data-fit results without reactor constraint: 1D credible intervals on δ_{CP} (left) and $\sin^2\theta_{13}$ (right) marginalised over NH (top), IH (middle) and both mass orderings (bottom). 175

7.6 Data-fit results without reactor constraint: 1D credible intervals on Δm^2_{32} (left) and $\sin^2\theta_{23}$ (right) marginalised over NH (top), IH (middle) and both mass orderings (bottom). 176

7.7 Data-fit results with reactor constraint: 2D credible intervals for Δm^2_{32} vs. $\sin^2\theta_{23}$ (left) and δ_{CP} vs. $\sin^2\theta_{13}$ (right). Credible intervals are shown marginalised over the NH (top). marginalised over the IH (middle) and marginalised over both hierarchies (bottom). 178

7.8 Data-fit results with reactor constraint: 1D credible intervals on δ_{CP} and $\sin^2\theta_{13}$. The $\sin^2\theta_{13}$ credible intervals are very similar to the Gaussian prior from the reactor experiments. 179

7.9 Data-fit results with reactor constraint: 1D credible intervals on Δm^2_{32} (left) and $\sin^2\theta_{23}$ (right) marginalised over NH (top), IH (middle) and both mass orderings (bottom). 180

7.10 Post-fit distribution (blue) and one sigma error band (red) with run 1–10 data (black) for each SK selection overlaid. Posterior predictive distributions are made using a Markov chain from a joint SK and ND280 fit. The post-fit distribution and errors are made by taking the mean and RMS from a posterior predictive distribution in each bin. 182

7.11 Post-fit distribution (blue) and one sigma error band (red) with run 1–10 data (black). Posterior predictive distributions are made using a Markov chain from a joint SK and ND fit. The post-fit distribution and errors are made by taking the mean and RMS from a posterior predictive distribution in each bin. The data error bars in this figure are Poisson errors rather than $\sqrt{N}$ as in fig. 7.10. 183

7.12 1D $\sin\delta_{\mathrm{CP}}$ credible intervals with a prior flat in $\sin\delta_{\mathrm{CP}}$ (rather than flat in δ_{CP}) for the normal hierarchy, inverted hierarchy and both hierarchies (bottom). It can be seen that in $\sin\delta_{\mathrm{CP}}$ that values close to 1 are excluded at 99% and values around -1 are preferred which is consistent with previous results shown. It can also be seen that $\sin\delta_{\mathrm{CP}} = 0$ is still disfavoured at 90% even under this change in prior. 185

7.13 A comparison of 2D constraints on oscillation parameters with and without the reactor constrained prior being used. 188

7.14 A "bayesian triangle" plot showing the 68% (dashed) and 90% (solid) credible intervals for the data fit using the reactor constraint. This shows all four oscillation parameters that the T2K experiment is sensitive in 2D and also 1D. 190

7.15 Oscillated predictions for the 1Re sample at SK for FHC mode (left) and RHC mode (right). The predictions use the best-fit oscillation parameters with reactor constraint. The predicted spectra for different values of δ_{CP} (0, $-\pi/2$ and $+\pi/2$) are also shown which highlights that the T2K results prefer a value of $-\pi/2$. This can naively be seen by eye from the better agreement between the data points and the $\delta_{\mathrm{CP}} = -\pi/2$ prediction for FHC and RHC mode. 191

7.16 Radial plots showing the 1D constraints on δ_{CP} using the reactor constraint. For the NH (top left), IH (top right) and marginalised across both mass hierarchies (bottom). In all cases the best-fit value prefers a value close to $-\pi/2$. It can also be seen that the CP-conserving values of 0 and π are disfavoured at $\sim 2\sigma$ for all cases. Another interesting note is that large regions of δ_{CP} are disfavoured at more than 3σ. 192

8.1 A cartoon of a ν_μCC1π signal event where a CCRES interaction producing a muon and pion above Cherenkov threshold. The light blue rings are Cherenkov rings. Figure taken from [118]. 195

8.2 The ν_μ differential cross section as a function of neutrino energy on H_2O for different neutrino interactions. The T2K neutrino flux is also shown to compare the energy range that the T2K experiment operates at. At the T2K flux peak energy of ~ 0.6 GeV CCQE can be seen to have the highest interaction probability. Then above this energy the CCQE differential cross section decreases and the differential cross sections of other interaction modes increase. In particular CCRES and CC Multi-π become significant at $\sim$ 1GeV. 197

8.3 Predictions of the ν_μCC1π sample at SK in true neutrino energy (left) and reconstructed neutrino energy (right). The top plots are the predictions without oscillations and the lower plots are using the Asimov A neutrino oscillation parameters. The plots are broken down by each interaction mode. 201

8.4 A comparison of the neutrino interaction modes and visible final state topologies for oscillated events in the ν_μCC1π sample at SK using the Asimov A oscillation parameters. The number of events in each bin corresponds to a percentage of all the events in the sample. The overlap between CCRES interactions and visible $1\mu + 1\pi$ can be seen to be by far the largest component of the sample as expected. No secondary particles are considered in these topology definitions. 202

8.5 Predicted spectra for the ν_μCC1π sample at SK using different neutrino oscillation parameters. To compare the oscillated spectra these predictions are also given as a ratio to the prediction using the Asimov A neutrino oscillation parameter values. For the different predictions if a neutrino oscillation parameter has been changed from the Asimov A set then the value is given and any predictions labelled "IH" are for the inverted hierarchy and have the sign of Δm^2_{32} set to be negative. 204

8.6 A comparison of the CIs from an Asimov fit using five SK samples and also including the ν_μCC1π sample. The CIs show a small increase in the sensitivity to Δm^2_{32} and a minor broadening of the uncertainty on θ_{23}. These are all shown not using the reactor constraint on θ_{13}. 207

8.7 1D CIs for an Asimov fit using five SK samples and one also using the ν_μCC1π sample at SK. It is now clearer in 1D that the Δm^2_{32} uncertainty decreases slightly but the θ_{23} constraint is very similar in both except for a small shift in the CIs. 208

8.8 The fake data (left) and nominal MC (middle) at ND280 used in the FDS as well as the ratio of the fake data to the nominal MC (right) for the FGD1 CC1π and CC-Other samples in FHC. The fake data varies from the nominal MC most in the CC1π and CC-Other samples since these samples contain the most CC Multi-π and CC DIS interactions. The fake data, nominal MC and their ratios for all samples at ND280 are shown in appendix D.1. 210

8.9 The fake data (left) and nominal MC (middle) at ND280 and the ratio of the fake data to the nominal MC (right) for the FGD1 CC0π, CC1π and CC-Other samples in RHC. The largest differences are in the CC1π and CC-Other samples since these samples contain more CC Multi-π and CC DIS interactions. The fake data, nominal MC and their ratios for all samples at ND280 are shown in appendix D.1. 211

8.10 The fake data (left) and nominal MC (middle) at SK used in the FDS as well as the ratio of the fake data to the nominal MC (right) for each sample at SK. The fake data varies from the nominal MC most in the two samples which target interactions with a pion. 212

8.11 The fake data and nominal MC (left) at SK used in the FDS as well as the ratio of the fake data to the nominal MC (right) for each sample at SK. The fake data varies from the nominal MC most in the two samples which target interactions with a pion which is expected as CC Multi-π and CC DIS interactions are a larger background in these sample. In particular, there is a large difference in the ν_μCC1π fake data compared to the nominal MC prediction. 213

8.12 A comparison of the results on oscillation parameters from a FDS and an Asimov fit. The change in the credible intervals indicates the bias introduced by the change to CC Multi-π and CC DIS interactions in the fake data. 215

8.13 Comparison of the parameter values for the FDS and an Asimov fit where parameter values are set to their prior central values. The nuisance parameters related to CCRES interactions as well as the CC Multi-π, CC DIS and CC Misc. normalisation parameters can be seen to have moved from their inputted prior central values which indicates a bias in these parameters. 216

8.14 A comparison of the parameter values for the FDS and an Asimov fit where parameter values are set to their prior central values. Here the parameters relating to the neutrino flux in FHC mode at ND280 are shown. Each parameter related to a different normalisation parameter covering a range of true neutrino energy given by the x-axis. 217

8.15 Comparison of the parameter values for the FDS and an Asimov fit where parameter values are set to their prior central values. Here the parameters relating to the neutrino flux in RHC mode at ND280 are shown. Each parameter related to a different normalisation parameter covering a range of true neutrino energy given by the x-axis. 218

8.16 Comparison of the parameter values for the FDS and an Asimov fit where parameter values are set to their prior central values. Here the parameters relating to the neutrino flux in FHC mode at SK are shown. Each parameter related to a different normalisation parameter covering a range of true neutrino energy given by the x-axis. 219

8.17 Comparison of the parameter values for the FDS and an Asimov fit where parameter values are set to their prior central values. Here the parameters relating to the neutrino flux in RHC mode at SK are shown. Each parameter related to a different normalisation parameter covering a range of true neutrino energy given by the x-axis. 220

A.1 All the inputs for different nuclei and neutrino flavours for applying an uncertainty based on the BY corrections for CC DIS interactions. The general feature across all inputs are the large weights at low Q^2 values. The inputs extend to much larger values of both Q^2 and E_ν in the nucleon frame but are zoomed in on here to show the key features. 238

A.2 All the inputs for different nuclei and neutrino flavours for applying an uncertainty based on the BY corrections for CC Multi-π interactions. The general feature across all inputs are the large weights at low Q^2 values. The inputs extend to much larger values of both Q^2 and E_ν in the nucleon frame but are zoomed in on here to show the key features. 239

A.3 Comparisons of MC events reweighted from using BY corrections to without BY corrections using the inputs given in fig. 6.3 for CC Multi-π interactions on water for ν_μ, ν_e, $\bar{\nu}_\mu$ and $\bar{\nu}_e$. Comparisons are given in Q^2. The lower panels in all the plots show the difference between reweighted MC and that generated without BY corrections. 241

A.4 Comparisons of MC events reweighted from using BY corrections to without BY corrections using the inputs given in fig. 6.3 for CC DIS interactions on water for ν_μ, ν_e, $\bar{\nu}_\mu$ and $\bar{\nu}_e$. Comparisons are given in Q^2. The lower panels in all the plots show the difference between reweighted MC and that generated without BY corrections. 242

A.5 Comparisons of MC events reweighted from using BY corrections to without BY corrections using the inputs given in fig. 6.3 for CC Multi-π interactions on water for ν_μ, ν_e, $\bar{\nu}_\mu$ and $\bar{\nu}_e$. Comparisons are given in E_ν. The lower panels in all the plots show the difference between reweighted MC and that generated without BY corrections. 243

A.6 Comparisons of MC events reweighted from using BY corrections to without BY corrections using the inputs given in fig. 6.3 for CC DIS interactions on water for ν_μ, ν_e, $\bar{\nu}_\mu$ and $\bar{\nu}_e$. Comparisons are given in E_ν. The lower panels in all the plots show the difference between reweighted MC and that generated without BY corrections. 244

A.7 Comparisons of MC events reweighted from using BY corrections to without BY corrections using the inputs given in fig. 6.3 for CC Multi-π interactions on water for ν_μ, ν_e, $\bar{\nu}_\mu$ and $\bar{\nu}_e$. Comparisons are given in Bjorken-x. The lower panels in all the plots show the difference between reweighted MC and that generated without BY corrections. 245

A.8 Comparisons of MC events reweighted from using BY corrections to without BY corrections using the inputs given in fig. 6.3 for CC DIS interactions on water for ν_μ, ν_e, $\bar{\nu}_\mu$ and $\bar{\nu}_e$. Comparisons are given in Bjorken-x. The lower panels in all the plots show the difference between reweighted MC and that generated without BY corrections. 246

A.9 Comparisons of MC events reweighted from using BY corrections to without BY corrections using the inputs given in fig. 6.3 for CC Multi-π interactions on water for ν_μ, ν_e, $\bar{\nu}_\mu$ and $\bar{\nu}_e$. Comparisons are given in Bjorken-y. The lower panels in all the plots show the difference between reweighted MC and that generated without BY corrections. 247

A.10 Comparisons of MC events reweighted from using BY corrections to without BY corrections using the inputs given in fig. 6.3 for CC DIS interactions on water for ν_μ, ν_e, $\bar{\nu}_\mu$ and $\bar{\nu}_e$. Comparisons are given in Bjorken-y. The lower panels in all the plots show the difference between reweighted MC and that generated without BY corrections. 248

A.11 Comparisons of MC events reweighted from using BY corrections to without BY corrections using the inputs given in fig. 6.3 for CC Multi-π interactions on CH for ν_μ, ν_e, $\bar{\nu}_\mu$ and $\bar{\nu}_e$. Comparisons are given in Q^2. The lower panels in all the plots show the difference between reweighted MC and that generated without BY corrections. 249

A.12 Comparisons of MC events reweighted from using BY corrections to without BY corrections using the inputs given in fig. 6.3 for CC DIS interactions on CH for ν_μ, ν_e, $\bar{\nu}_\mu$ and $\bar{\nu}_e$. Comparisons are given in Q^2. The lower panels in all the plots show the difference between reweighted MC and that generated without BY corrections. 250

A.13 Comparisons of MC events reweighted from using BY corrections to without BY corrections using the inputs given in fig. 6.3 for CC Multi-π interactions on CH for ν_μ, ν_e, $\bar{\nu}_\mu$ and $\bar{\nu}_e$. Comparisons are given in E_ν. The lower panels in all the plots show the difference between reweighted MC and that generated without BY corrections. 251

A.14 Comparisons of MC events reweighted from using BY corrections to without BY corrections using the inputs given in fig. 6.3 for CC DIS interactions on CH for ν_μ, ν_e, $\bar{\nu}_\mu$ and $\bar{\nu}_e$. Comparisons are given in E_ν. The lower panels in all the plots show the difference between reweighted MC and that generated without BY corrections. 252

A.15 Comparisons of MC events reweighted from using BY corrections to without BY corrections using the inputs given in fig. 6.3 for CC Multi-π interactions on CH for ν_μ, ν_e, $\bar{\nu}_\mu$ and $\bar{\nu}_e$. Comparisons are given in Bjorken-x. The lower panels in all the plots show the difference between reweighted MC and that generated without BY corrections. 253

A.16 Comparisons of MC events reweighted from using BY corrections to without BY corrections using the inputs given in fig. 6.3 for CC DIS interactions on CH for ν_μ, ν_e, $\bar{\nu}_\mu$ and $\bar{\nu}_e$. Comparisons are given in Bjorken-x. The lower panels in all the plots show the difference between reweighted MC and that generated without BY corrections. 254

A.17 Comparisons of MC events reweighted from using BY corrections to without BY corrections using the inputs given in fig. 6.3 for CC Multi-π interactions on CH for ν_μ, ν_e, $\bar{\nu}_\mu$ and $\bar{\nu}_e$. Comparisons are given in Bjorken-y. The lower panels in all the plots show the difference between reweighted MC and that generated without BY corrections. 255

A.18 Comparisons of MC events reweighted from using BY corrections to without BY corrections using the inputs given in fig. 6.3 for CC DIS interactions on CH for ν_μ, ν_e, $\bar{\nu}_\mu$ and $\bar{\nu}_e$. Comparisons are given in Bjorken-y. The lower panels in all the plots show the difference between reweighted MC and that generated without BY corrections. 256

C.1 p_μ projections of data and nominal MC broken down by interaction mode for RHC $\bar{\nu}_\mu$ selections. 261

C.2 p_μ projections of data and nominal MC broken down by interaction mode for RHC ν_μ selections. 262

C.3 $\cos\theta_\mu$ projections of data and nominal MC broken down by interaction mode for FHC selections. 263

C.4 $\cos\theta_\mu$ projections of data and nominal MC broken down by interaction mode for RHC $\bar{\nu}_\mu$ selections. 264

C.5 $\cos\theta_\mu$ projections of data and nominal MC broken down by interaction mode for RHC ν_μ selections. 265

C.6 p_μ-cos θ_μ distributions for the nominal MC for the samples in FHC mode with the binning used in the fit to data. 266

C.7 p_μ-cos θ_μ distributions for the nominal MC for the samples in RHC mode with the binning used in the fit to data. 267

C.8 p_μ-cos θ_μ distributions for the nominal MC for the wrong-sign samples in RHC mode with the binning used in the fit to data. 268

C.9 Mean predictions for each SK sample from the run 1–10 data fit without reactor constraints. Data points are shown in orange. The result of 2500 randomly sampling all parameter values from the posterior is shown in the 2D histogram. The mean predictions are calculated by taking the mean of this distribution in each energy bin. A Markov chain from jointly fitting ND280 and SK data was used and all parameters are sampled. 289

C.10 Post-fit distribution (blue) and one sigma error band (red) with run 1–10 data (black) for each SK selection overlaid. Posterior predictive distributions are made using a Markov chain from a joint SK and ND fit where all parameters are sampled. The post-fit distribution is calculated by taking the mean from the posterior predictive distribution in each bin. Similarly the one sigma error band is calculated by taking the RMS of the posterior predictive distribution in each bin. 290

D.1 The fake data (left) and nominal MC (middle) at ND280 used in the FDS as well as the ratio of the fake data to the nominal MC (right). The fake data varies from the nominal MC most in the CC1π and CC-Other samples since these samples contain the most CC Multi-π and CC DIS interactions. 292

D.2 The fake data (left) and nominal MC (middle) at ND280 used in the FDS as well as the ratio of the fake data to the nominal MC (right). The fake data varies from the nominal MC most in the CC1π and CC-Other samples since these samples contain the most CC Multi-π and CC DIS interactions. 293

D.3 The fake data (left) and nominal MC (middle) at ND280 used in the FDS as well as the ratio of the fake data to the nominal MC (right). The fake data varies from the nominal MC most in the CC1π and CC-Other samples since these samples contain the most CC Multi-π and CC DIS interactions. 294

List of Tables

2.1 The best-fit oscillation parameters from a combined analysis of experimental results taken from [26]. Values for $\sin^2\theta_{23}$ and Δm^2_{32} are given for the normal mass ordering. 61

3.1 The decays of the primary mesons produced at the target which produce a neutrino beam in neutrino mode. The two most probable decays and their decay fraction are shown for each meson. The two-body decay of π^+s to a μ and ν_μ has the largest decay fraction and is responsible for most of the neutrinos produced. 80

4.1 A summary of the cross-section parameters used in this analysis. Coulomb corrections are omitted in this table as they take no input from the cross-section model and are applied in the calculation of reconstructed energy. It should also be noted that although a parameters range may not be explicitly restricted, the priors constrain the parameters to a finite range and if a non-physical weight is calculated it is set to 0. 117

4.2 The central values and uncertainties for $\sin^2\theta_{12}$, $\sin^2\theta_{13}$ (when results are quoted as using the 'reactor constraint") and Δm^2_{12}. 122

5.1 Oscillation parameter values used for Asimov A fits. 143

7.1 The total number of data events for each SK selection for runs 1-10. . . . 171

7.2 The 1D best-fit parameter values and $1\,\sigma$ credible interval from this analysis. For the best-fit value of Δm^2_{32} for both orderings the 1σ range within the mass ordering where the best-fit is in is quoted. 187

7.3 Posterior probabilities from T2K data fits for normal and inverted hierarchies, as well as upper and lower octants. The probabilities are calculated by calculating the fraction of Markov chain steps in each region of parameter-space. 189

8.1 Unoscillated event rate predictions for the ν_μCC1π sample at SK. The large contributions from CCRES and CC Multi-π interactions show the importance of these modes in accurately predicting these samples at SK. 199

8.2 Oscillated event rate predictions for the ν_μCC1π sample at SK using the Asimov A oscillation parameters. The large contributions from CCRES and CC Multi-π interactions after oscillations have been applied show the importance of these modes in accurately predicting these samples at SK. 200

C.1 Post-ND280 fit event rate prediction for FHC $1R_\mu$ sample: 19.664×10^{20} POT, unoscillated 269

C.2 Post-ND280 fit event rate prediction for FHC $1R_e$ sample: 19.664×10^{20} POT, unoscillated 270

C.3 Post-ND280 fit event rate prediction for RHC $1R_\mu$ sample: 16.34556×10^{20} POT, unoscillated 271

C.4 Post-ND280 fit event rate prediction for RHC $1R_e$ sample: 16.34556×10^{20} POT, unoscillated 272

C.5 Post-ND280 fit event rate prediction for FHC CC-$1\pi^+$ sample: 19.664×10^{20} POT, unoscillated 273

C.6 Post-ND280 fit event rate prediction for FHC $1R_\mu$ sample: 19.664×10^{20} POT, oscillated 274

C.7 Post-ND280 fit event rate prediction for FHC $1R_e$ sample: 19.664×10^{20} POT, oscillated 275

C.8 Post-ND280 fit event rate prediction for RHC $1R_\mu$ sample: 16.34556×10^{20} POT, oscillated 276

C.9 Post-ND280 fit event rate prediction for RHC $1R_e$ sample: 16.34556×10^{20} POT, oscillated 277

C.10 Post-ND280 fit event rate prediction for FHC CC-$1\pi^+$ sample: 19.664×10^{20} POT, oscillated 278

C.11 Pre-ND280 fit event rate prediction for FHC $1R_\mu$ sample: 19.664×10^{20} POT, unoscillated 279

C.12 Pre-ND280 fit event rate prediction for RHC $1R_\mu$ sample: 16.34556×10^{20} POT, unoscillated 280

C.13 Pre-ND280 fit event rate prediction for FHC $1R_e$ sample: 19.664×10^{20} POT, unoscillated 281

C.14 Pre-ND280 fit event rate prediction for RHC $1R_e$ sample: 16.34556×10^{20} POT, unoscillated 282

C.15 Pre-ND280 fit event rate prediction for FHC CC-$1\pi^+$ sample: 19.664×10^{20} POT, unoscillated 283

C.16 Pre-ND280 fit event rate prediction for FHC $1R_\mu$ sample: 19.664×10^{20} POT, oscillated 284

C.17 Pre-ND280 fit event rate prediction for RHC $1R_\mu$ sample: 16.34556×10^{20} POT, oscillated 285

C.18 Pre-ND280 fit event rate prediction for FHC $1R_e$ sample: 19.664×10^{20} POT, oscillated 286

C.19 Pre-ND280 fit event rate prediction for RHC $1R_e$ sample: 16.34556×10^{20} POT, oscillated 287

C.20 Pre-ND280 fit event rate prediction for FHC CC-1π^+ sample: 19.664×10^{20} POT, oscillated 288

Chapter 1

Introduction

Neutrinos are one the of most abundant particles in the universe, yet they barely interact with the matter which makes it up. Despite this, these ghostly particles could hold one of the pieces of the puzzle as to why our universe is matter, rather than antimatter, dominated. The phenomenon of neutrino oscillations provides a process by which neutrinos (matter) can behave distinctly from antineutrinos (antimatter). These oscillations may allow further mechanisms via which the evolution of the universe has led to an abundance of matter. Therefore, the study of neutrino oscillations is of great importance in the understanding of why our universe exists as it does. This thesis describes my research as part of the Tokai-to-Kamiokande (T2K) collaboration which studies neutrino oscillations at the T2K experiment [2]. The analysis presented in this thesis gives world-leading measurements of neutrino oscillations and in particular, the charge-parity violating phase, δ_{CP}.

Neutrino oscillations were only experimentally confirmed in 1998 [3] [4]. Since then there have been huge advancements in this field. Many experiments have measured different aspects of the behaviour of neutrino oscillations through neutrinos produced in the Sun, nuclear reactors, the atmosphere or man-made neutrino beams. In 2015 this effort was recognised through the Nobel Prize in physics being awarded to Arthur McDonald and Takaaki Kajita for their experimental work in the discovery of neutrino oscillations. There are many neutrino oscillation experiments which continue to make evermore precise measurements of neutrino oscillations. The T2K experiment is one of

these experiments and is making some of the most precise measurements in the field by looking at neutrino oscillations from a man-made neutrino beam source in Japan.

Although many advances in the field of neutrino oscillations have been made, many open questions remain. One of these is the magnitude of charge-parity (CP) violation in neutrino oscillations. Matter and antimatter are related through a CP transformation. Therefore, if matter and antimatter behave differently, CP symmetry is violated. In order to measure this, it is essential that neutrino oscillations and the parameters which govern them are known precisely. Another unknown is the ordering of the neutrino masses. Currently, there are three known neutrino mass states, but we do not know which of these is the heaviest. The precise measurement of neutrino oscillations will enable the ordering of the neutrino masses to be determined. Whether the ordering of the neutrino masses reflects the ordering elsewhere in the standard model (where the third-generation is the heaviest) is an important question to answer in our understanding of the standard model.

This thesis presents an analysis using Markov Chain Monte Carlo to measure neutrino oscillation parameters with a larger dataset and improved treatments of systematic parameters; particularly those related to neutrino interactions. Building on this further, the improvement in the sensitivity of the T2K experiment to neutrino oscillation parameters by adding a new data samples is shown as well as studies showing the importance of the improved systematic parameters to this data sample.

The 8 chapters of this thesis describe: the theoretical motivation for measuring neutrino oscillation and the status of research in the field, the T2K experiment, the analysis techniques used, neutrino interaction uncertainties and improvements made to their treatment, a neutrino oscillation analysis with increased data samples and improved treatment of systematic uncertainties, sensitivity improvements to this analysis by including additional data samples into the analysis and finally a discussion of the results and projections.

Chapter 2 describes the theoretical motivation for experimental measurements of neutrino oscillations. A brief overview of weak interactions, mass generation and CP violation in the standard model is given. The requirement of CP violation for a matter-

antimatter asymmetry to have arisen in the universe is described using the Sakahrov conditions. A derivation of three-flavour neutrino oscillations is given which is the basis of the parameterisation used in the analysis presented in chapter 7. This chapter also contains an overview of other experimental results which have significantly contributed to current understanding of neutrino oscillations.

In chapter 3 the J-PARC beam facility and the T2K experiment is described with emphasis placed on the parts of the experiment which are most related to neutrino oscillation analyses. This includes descriptions of the beamline and beamline monitors, the near detectors and the far detector (Super-Kamiokande).

An overview of the analysis and statistical techniques used in T2K neutrino oscillation analyses and the analysis in chapter 7 is given in chapter 4. How an oscillation analysis is conducted at T2K, the statistical likelihood function used and the inputs to an analysis are described. Furthermore, Bayesian inference and Markov Chain Monte Carlo (MCMC) methods are introduced as this was the analysis technique used to extract the neutrino oscillation results in the analysis in chapter 7 and chapter 8.

Chapter 6 will give a greater description of neutrino interactions and the treatment of systematic parameter uncertainties which arise from them. Improvements to the modelling of systematic parameters related to Deep Inelastic Scattering (DIS) used in the analysis described in chapter 7 are discussed here. Studies related to uncertainties coming from the modelling of resonant pion production are also given in this chapter. These uncertainties are highly relevant to future analysis and the sensitivities presented in chapter 8.

A neutrino oscillation analysis at T2K using the improved systematic treatment I developed is presented in chapter 7 . Firstly, the pre-fit Monte Carlo (MC) predictions are shown, then fits to simulated data are used to validate the analysis framework and then best-fit oscillation and systematic parameters from a fit to data are shown. The best-fit neutrino oscillation parameter results and systematic parameter values will be presented using T2K-only data as well as using T2K data and a constraint on the θ_{13} mixing angle from reactor neutrino experiments which increases the sensitivity of T2Ks measurement.

Chapter 8 then focuses on improving the analysis shown in chapter 7 by including new data samples at Super-Kamiokande (SK). These new data samples target different event topologies in SK compared to the current data samples used in the T2K oscillation analysis. The inclusion of these data samples increases the number of data events used in the analysis. The neutrino interactions in these new samples also, typically, originate from higher energy neutrinos than other data samples included in the analysis. This results in a measurement of neutrino oscillation parameters using a larger phase-space than previous analyses. Both the additional data and larger phase-space of the new data samples are expected to increase the sensitivity of the analysis and thus improve the measurement of neutrino oscillation parameters.

Finally, a discussion of the results shown in this thesis is given in chapter 9. The implications of this analysis and the future prospects of neutrino oscillation measurements are discussed.

Chapter 2

Theory of neutrinos and neutrino oscillations

2.1 Standard Model

The standard model of particle physics has been one of the key breakthroughs of the last hundred years. It unites the electromagnetic, weak and strong forces as well as explaining the masses of particles, through the Higgs mechanism, in one description. The standard model has developed through both theoretical and experimental breakthroughs, with the discovery of the Higgs boson in 2012 [5] [6] perhaps being the culmination of this. The particles which make up the standard model are: force carrying gauge bosons such as the $W^{\pm}$ and Z^0 bosons, leptons which are spin-1/2 particles and quarks which are spin-1/2 particles with an associated colour charge. Two classes of leptons exist; charged and neutral. The neutral leptons of the standard model are neutrinos which are the focus of this thesis. Three generations of quarks and leptons exist. For each generation of quark there are two flavours associated with it; up and down for the first generation, charm and strange for the second generation and top and bottom for the third generation. For each generation of lepton there exists a charged lepton and a neutral lepton associated with the same lepton flavour. The particles that make up the standard model are shown in fig. 2.1.

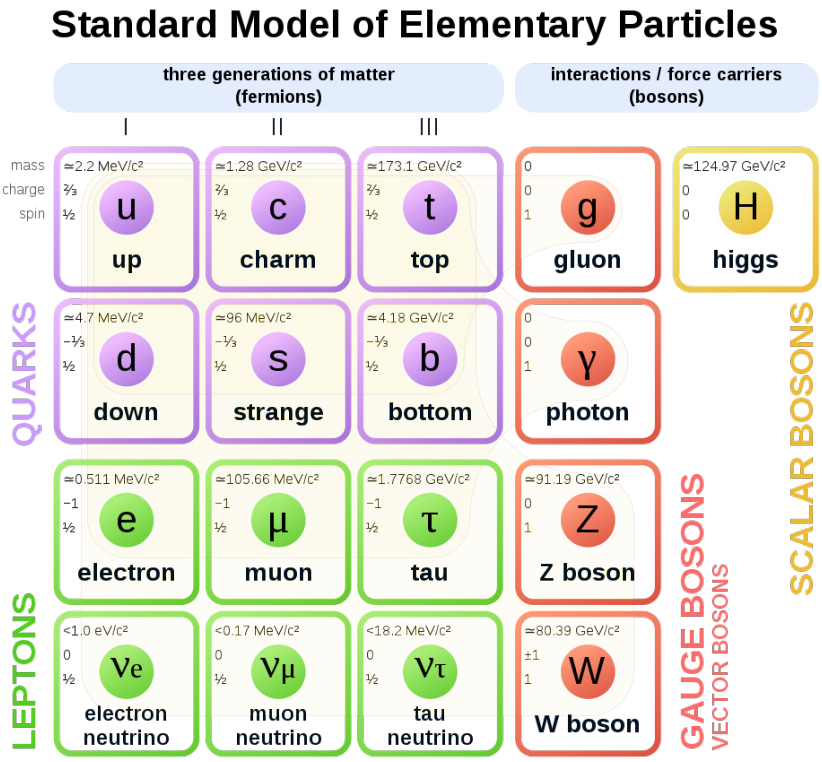

Figure 2.1: The particles which make up the standard model of particle physics [7].

In this thesis, I will focus on the key parts of the standard model which have particular relevance to neutrinos and neutrino oscillations. The particles of primary interest for this thesis are leptons and in particular neutrinos and their weak interactions. The weak interactions of leptons and the discovery of the neutrino are discussed in section 2.1.1 while neutrino oscillations are discussed in section 2.2.

Although the Standard Model and many of its parameters have been tested to high precision at the Large Hadron Collider (LHC) it is known that it does not fully explain all the phenomena that are observed in nature. Neutrinos are one of these curious areas where the standard model cannot explain their observed properties. As will be discussed later, neutrinos have been observed to have mass whereas they are massless in the standard model. In the standard model particles acquire their mass by interacting with the Higgs field. However, the neutrino masses cannot be accounted for in this same way without extending the standard model in some manner [8].

Another phenomenon the standard model does not explain is the asymmetry of matter and antimatter observed in the universe [9]. To explain this asymmetry additional

theories built around mechanisms via which matter can behave distinctly from antimatter are required. A discussion of matter-antimatter asymmetry and its relevance to neutrinos is given in section 2.2.5

The fact that the standard model cannot describe all the phenomena observed in nature is the driving force behind much of particle physics. This thesis studies neutrinos and the phenomenon of neutrino oscillations, which are not described by the standard model, and could help answer some of the key open questions in particle physics.

2.1.1 The discovery of the neutrino and Weak interactions

Neutrinos were first theorised by Wolfgang Pauli to explain the continuous energy spectrum of electrons from beta decay. In order to explain this (without breaking energy conservation), Pauli proposed that the continuous energy spectrum was due to a third weakly interacting, possibly massless, neutral particle being produced in the decay [10]. Enrico Fermi then continued this work and developed a theory of beta decays and weak interactions known as Fermi theory where particles interact through point-like interactions given by

$$\frac{G_F}{\sqrt{2}} g_{\mu\nu} \left[\bar{\psi}_3 \gamma^\mu \psi_1\right] \left[\bar{\psi}_4 \gamma^\mu \psi_2\right], \tag{2.1}$$

where G_F is the Fermi constant, $g_{\mu\nu}$ is the diagonal metric tensor, ψ_i are fermion fields corresponding to those in fig. 2.2 and γ^μ are gamma matrices which can be found in most particle physics textbooks such as [8] and [11]. This formalism provides a fairly reliable low energy approximation of weak interactions in the standard model but is missing some crucial properties of weak interactions.

In 1957 Wu *et. al* discovered a crucial property of Weak interactions by looking at decays of Co^{60} in a strong magnetic field [12]. They discovered that the Weak force violates parity, meaning that weak interactions cannot take the form as given in eq. (2.1). Parity (P) is a symmetry whereby changing coordinates from $\vec{x}$ to $-\vec{x}$, where $\vec{x}$ represent spatial co-ordinates, does not change the laws of physics. Parity is conserved in electromagnetic and strong interactions and was assumed to also hold for weak interactions. However, Wu *et al.* explicitly found that parity was not conserved for weak interactions. This then led Feynman and Gell-Mann [13] to propose a form of the weak interaction

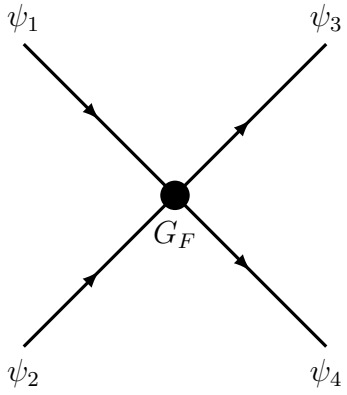

Figure 2.2: A Feynman diagram of a Fermi interaction. The interaction is considered point-like where the coupling of the interaction is given by the Fermi constant G_F.

which maximally violates parity. The parity violating form of the weak interaction is given by

$$\frac{G_F}{\sqrt{2}} g_{\mu\nu} \left[\bar{\psi}_3 \gamma^\mu \left(1-\gamma^5\right) \psi_1\right] \left[\bar{\psi}_4 \gamma^\mu \left(1-\gamma^5\right) \psi_2\right], \tag{2.2}$$

and is known as the "V-A" form of the weak interaction. The V-A name comes from the fact that the $\bar{\psi}\gamma^\mu\psi$ term is the vector form of an interaction and the $\bar{\psi}\gamma^\mu\gamma^5\psi$ term takes an axial form. The V-A structure of the weak interaction predicts several phenomena which have been validated by experimental observations. The V-A structure results in only certain spin projections of spinors playing a role in weak interactions. These projections are known as chiral states and are eigenstates of the γ^5 operator. In fact any Dirac spinor can be decomposed into two chiral projection, left-handed and right-handed [11]

$$\psi = \psi_L + \psi_R, \tag{2.3}$$

where ψ_L and ψ_R are these left-handed and right-handed projections respectively and are defined as

$$\frac{(1-\gamma^5)}{2}\psi \equiv \psi_L, \qquad \frac{(1+\gamma^5)}{2}\psi \equiv \psi_R. \tag{2.4}$$

Similarly for antiparticles these chiral projections are

$$\frac{(1-\gamma^5)}{2}\bar{\psi} \equiv \bar{\psi}_R, \qquad \frac{(1+\gamma^5)}{2}\bar{\psi} \equiv \bar{\psi}_L. \tag{2.5}$$

The form of weak interactions in eq. (2.2) will be useful when discussing neutrino-nucleon interactions in section 2.4 as well as CP violation in section 2.2.5.

The other part of the puzzle which Fermi theory was lacking was the number and concept of flavour. The realisation that there were three distinct types of neutrino, each

associated with a charged lepton was key to developing the concept of flavour and its conservation in weak interactions. The neutrinos produced in beta decay were know to be associated with the electron produced in the decay; these became known as electron neutrinos. In 1962 at Brookhaven National Laboratory an experiment provided evidence of neutrinos that were associated with muons [14]. The experiment produced neutrinos from pion decay (where a muon and what we now call a muon neutrino are produced) and placed a spark chamber behind 42 ft of iron. The shielding reduced the muon background in the detector and allowed the tracks of the charged leptons produced by the neutrinos as they traverse the spark chamber to be measured. Six tracks were observed all of which were identified as muons whereas electron neutrino would have been expected to produce electron-like tracks. This observation disproved the hypothesis that muon neutrinos and electron neutrinos were the same particle. The discovery of the third neutrino flavour would not be directly observed for nearly 40 years since the muon neutrino was observed. The tau neutrino was observed at the DONUT experiment [15] in 2001 by identifying tau lepton tracks from a highly energetic ($\sim$ 100 GeV) neutrino beam. There is the possibility of more neutrino flavours existing however, the number of neutrino flavours has been tested through precise measurements of the invisible Z-boson decay width [16]. This measurement confirmed the three flavour model of neutrinos. These experimental observations of three distinct neutrino flavours have been key in the formulation of weak interactions in the standard model.

In the standard model, particles interact through the exchange of gauge bosons. In the case of Weak interactions these are $W^{\pm}$ and Z^0 bosons. The charged bosons $W^{\pm}$ are responsible for charged-current (CC) interactions and the neutral boson Z^0 is then responsible for neutral-current (NC) interactions. Feynman diagrams of CC and NC neutrino interactions can be seen in fig. 2.3 A derivation of electroweak interactions in the standard model can be found in particle physics textbooks such as [11], [8] and [17].

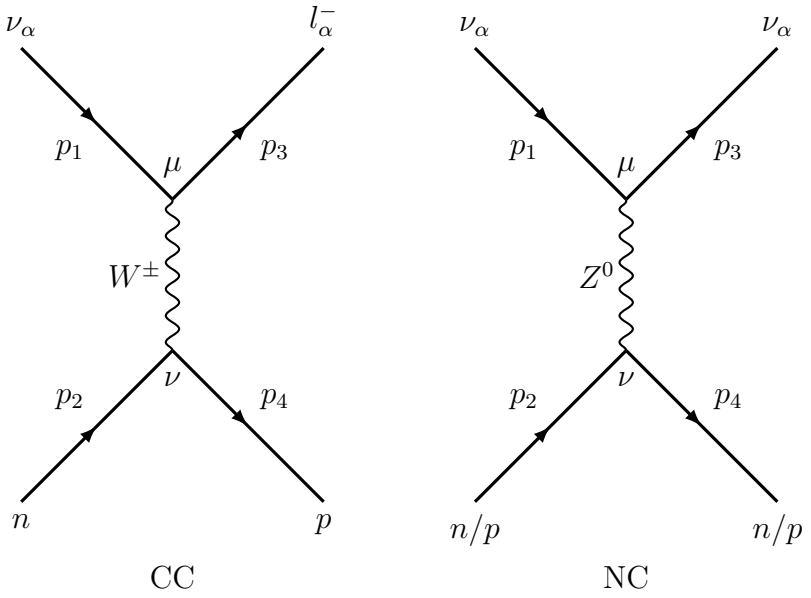

Figure 2.3: Feynman diagrams of a CC (left) and an NC (right) neutrino interaction on a nucleon.

2.2 Neutrino oscillation theory

Neutrinos interact through the Weak force. As described in section 2.1 this results in neutrinos having some unique characteristics in the standard model. In particular, the production of neutrinos in a CC interaction where a neutrino has an associated flavour combined with the assumption that neutrinos have a small ($\mathcal{O}$(eV)) but non-zero mass gives rise to the mixing of neutrino flavours. This chapter will describe how this mixing occurs for the three-flavour neutrino case of the standard model and describe some of the key phenomenology which results from this mixing. A description of some neutrino experiments that have helped to examine the nature of neutrino oscillations will be described to help paint a picture of the current understanding of the field.

2.2.1 Three-flavour neutrino oscillations

When neutrinos interact via weak interactions, such as those given in fig. 2.3, they interact through their weak eigenstates. However, when propagating through space neutrinos propagate through their mass eigenstates. Therefore, when a neutrino propagates all three neutrino mass eigenstates will play a role. The fact that neutrinos propagate and inter-

act through different eigenstates is the key to the phenomenon of neutrino oscillations. The mixing between flavour and mass eigenstates is described by the Pontecorvo-Maki-Nakagawa-Sakata (PMNS) matrix [18] [19]. This is a 3×3 unitary matrix and can be written as

$$U = \begin{pmatrix} U_{e1} & U_{e2} & U_{e3} \\ U_{\mu 1} & U_{\mu 2} & U_{\mu 3} \\ U_{\tau 1} & U_{\tau 2} & U_{\tau 3} \end{pmatrix}, \tag{2.6}$$

where e, μ and τ are the three flavours of neutrino and 1, 2 and 3 correspond to the three neutrino mass eigenstates. The linear sum along a column can now be seen to give the combination of flavour eigenstates which makes up a neutrino mass eigenstate and similarly, the sum across a row can be seen to give the combination of mass eigenstates for a particular neutrino flavour state . Therefore, in any weak interaction with a neutrino of flavour α this weak eigenstate can be replaced with a linear combination of mass eigenstates

$$|\nu_\alpha\rangle = \sum_{i=1,2,3} U^*_{\alpha i} |\nu_i\rangle , \tag{2.7}$$

where $|\nu_\alpha\rangle$ is a weak eigenstate, $\alpha = e, \mu, \tau$ is the flavour of the neutrino, $|\nu_i\rangle$ is a mass eigenstate, $i = 1, 2, 3$ and $U^*_{\alpha i}$ is an element of the PMNS matrix .

One of the key features of the PMNS matrix is its unitarity. This unitarity requires that the three neutrino flavour eigenstates are orthogonal to each other or that a neutrino flavour α is always guaranteed to be associated with a lepton of flavour α in an interaction mediated by a $W^\pm$ boson i.e. flavour is conserved. This can be written:

$$\langle \nu_\alpha | \nu_\beta \rangle = \left(\sum U^*_{\alpha i} |\nu_i\rangle \right)^\dagger \left(\sum U^*_{\beta j} |\nu_j\rangle \right) \tag{2.8}$$

$$\delta_{\alpha\beta} = \sum_i \sum_j U^*_{\beta j} U_{\alpha i} \langle \nu_i | \nu_j \rangle \tag{2.9}$$

$$\delta_{\alpha\beta} = \sum_i U^*_{\beta i} U_{\alpha i}, \tag{2.10}$$

where the orthogonality of each flavour and mass eigenstate has been used. The unitarity of the PMNS matrix also means that a neutrino mass eigenstate can be written as

$$|\nu_i\rangle = \sum_\alpha U_{\alpha i} |\nu_\alpha\rangle . \tag{2.11}$$

The above equations can then be used to consider the probability of a neutrino of flavour α being detected as flavour β after a distance, L; which is exactly what neutrino

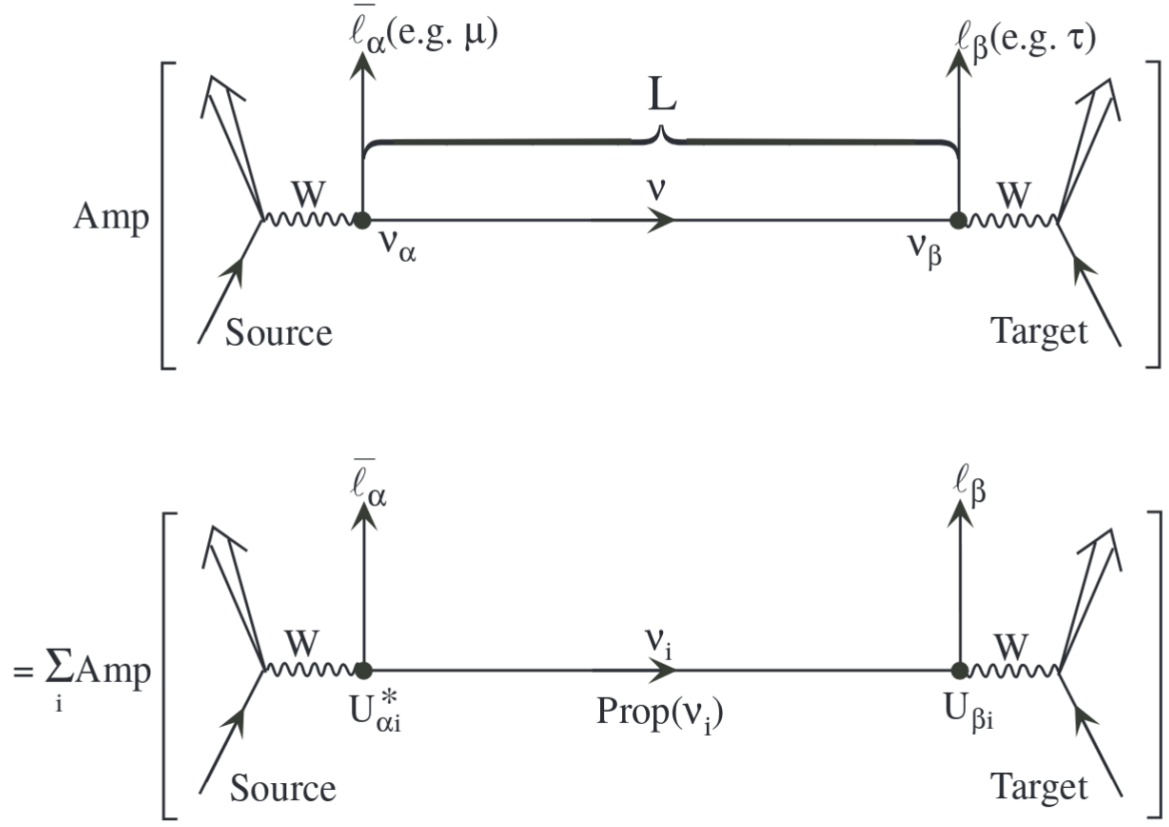

Figure 2.4: A visualisation of the neutrino flavour eigenstates oscillating from flavour α to flavour β after propagating a distance L. The upper diagram shows neutrino oscillations with flavour eigenstates and the lower diagram shows them with mass eigenstates. "Prop(ν_i)" is shorthand for the propagation of the neutrino mass eigenstate through a vacuum. "Amp" denotes amplitude. Figure taken from [20].

oscillation experiments wish to measure. This question is best visualised with the aid of fig. 2.4. The initial neutrino mass eigenstate i is an eigenstate of the Hamiltonian, $\mathcal{H}$ such that it can be written generically as

$$\mathcal{H} \left|\nu_i\right\rangle = E_i \left|\nu_i\right\rangle , \tag{2.12}$$

where E_i is the mass of the neutrino mass eigenstate. The evolution of the neutrino state in time t is then given by the Schrödinger equation:

$$i\frac{d}{dt}\left|\nu_i(t)\right\rangle = \mathcal{H}\left|\nu_i\right\rangle . \tag{2.13}$$

This means that a neutrino mass eigenstate can be written as a plane wave

$$\left|\nu_i(t)\right\rangle = e^{-ip\cdot x}\left|\nu_i\right\rangle , \tag{2.14}$$

$$= e^{-i(E_i t - p_i L)}\left|\nu_i\right\rangle , \tag{2.15}$$

where t is time, p and x are the momentum and position four-vectors, L is the distance travelled by the neutrino and p_i is the momentum of a mass eigenstate. It is also worth noting that in the above equations and for the rest of this thesis, natural units are used such that $\hbar = c = 1$. Then using eq. (2.7) a neutrino of flavour α can be written as

$$|\nu_\alpha(t)\rangle = \sum_i U^*_{\alpha i} \, |\nu_i\rangle \, e^{-i(E_i t - p_i L)}. \tag{2.16}$$

and now, using eq. (2.11) the evolution of a neutrino flavour state can be written as

$$|\nu_\alpha(t)\rangle = \sum_i U^*_{\alpha i} \left(\sum_\beta U_{\beta i} \, |\nu_\beta\rangle \right) e^{-i(E_i t - p_i L)}. \tag{2.17}$$

From equation eq. (2.17), the amplitude of flavour β in the time-evolved flavour eigenstate at time t can be easily found to be

$$\langle \nu_\beta | \nu_\alpha(t)\rangle = \sum_i U^*_{\alpha i} \, (U_{\beta i}) \, e^{-i(E_i t - p_i L)}. \tag{2.18}$$

The probability of a neutrino of flavour α oscillating to flavour β after a time, t, can now be calculated to be

$$P\left(\nu_\alpha \to \nu_\beta\right) = |\, \langle \nu_\beta | \nu_\alpha(t)\rangle \,|^2 \tag{2.19}$$

$$= \sum_i \sum_j U^*_{\alpha i} U_{\beta i} U_{\alpha j} U^*_{\beta j} e^{-i((E_i - E_j)t - (p_i - p_j)L)}. \tag{2.20}$$

However, due to the fact that the energy of a neutrino for any mass state will be identical (in other words $E_i = E_j$), this can be simplified to

$$P\left(\nu_\alpha \to \nu_\beta\right) = \sum_i \sum_j U^*_{\alpha i} U_{\beta i} U_{\alpha j} U^*_{\beta j} e^{i(p_i - p_j)L}. \tag{2.21}$$

This can then be further simplified by assuming that the neutrino mass is small compared to the neutrino energy, which is a very good approximation as neutrinos are ultra-relativistic. By doing this, a binomial expansion yields

$$p_i = \sqrt{E^2 - m_i^2} \tag{2.22}$$

$$\simeq E - \frac{m_i^2}{2E}, \tag{2.23}$$

where E is the neutrino energy. Inserting this into eq. (2.20) then gives

$$P\left(\nu_\alpha \to \nu_\beta\right) = \sum_i \sum_j U^*_{\alpha i} U_{\beta i} U_{\alpha j} U^*_{\beta j} e^{-i\frac{\Delta m^2_{ij}}{2E} t}, \tag{2.24}$$

where Δm^2_{ij} is the mass-squared difference and is defined as

$$\Delta m^2_{ij} \equiv m^2_i - m^2_j. \tag{2.25}$$

Finally, in neutrino oscillation experiments the time that a neutrino takes to propagate from where it is produced in flavour α and detected in flavour β and cannot be accurately measured. Neutrino oscillation experiments instead measure neutrino oscillations along the known distance between the neutrino beam source and the detector. Since neutrinos are ultra-relativistic particles, to a very good approximation it is possible to say $t = L$ leading to

$$P\left(\nu_\alpha \to \nu_\beta\right) = \sum_i \sum_j U^*_{\alpha i} U_{\beta i} U_{\alpha j} U^*_{\beta j} e^{-i\frac{\Delta m^2_{ji}}{2E}L}. \tag{2.26}$$

This form now gives the probability of a neutrino of flavour α oscillating to flavour β after travelling a distance L and answers the question posed earlier. However, eq. (2.26) is often re-written by taking advantage of the unitarity of U. The unitarity of U means that when $L = 0$

$$P\left(\nu_\alpha \to \nu_\beta, L = 0\right) = \sum_{i,j} U^*_{\alpha i} U_{\beta i} U_{\alpha j} U^*_{\beta j} \tag{2.27}$$

$$= \sum_i U^*_{\alpha i} U_{\beta i} \sum_j U_{\alpha j} U^*_{\beta j} \tag{2.28}$$

$$= \delta_{\alpha\beta} \tag{2.29}$$

which then implies

$$\delta_{\alpha\beta} = \sum_i |U^*_{\alpha i}|^2 |U_{\beta i}|^2 + 2\Re \sum_{i>j} U^*_{\alpha i} U_{\beta i} U_{\alpha j} U^*_{\beta j} \tag{2.30}$$

$$\sum_i |U^*_{\alpha i}|^2 |U_{\beta i}|^2 = \delta_{\alpha\beta} - 2\Re \sum_{i>j} U^*_{\alpha i} U_{\beta i} U_{\alpha j} U^*_{\beta j}. \tag{2.31}$$

By splitting eq. (2.26) into its real and imaginary terms, the relation in eq. (2.31)

can be used to give a more convenient trigonometric description.

$$P(\nu_\alpha \to \nu_\beta) = \sum_i |U_{\alpha i}|^2 |U_{\beta i}|^2 + 2\Re \sum_{i>j} U^*_{\alpha i} U_{\beta i} U_{\alpha j} U^*_{\beta j} e^{-i\frac{\Delta m^2_{ij}}{2E}L} \tag{2.32}$$

$$+ 2\Im \sum_{i>j} U^*_{\alpha i} U_{\beta i} U_{\alpha j} U^*_{\beta j} e^{-i\frac{\Delta m^2_{ij}}{2E}L} \tag{2.33}$$

$$= \sum_i |U_{\alpha i}|^2 |U_{\beta i}|^2 + 2\Re \sum_{i>j} U^*_{\alpha i} U_{\beta i} U_{\alpha j} U^*_{\beta j} \cos\left(\frac{\Delta m^2_{ij}}{2E}L\right) \tag{2.34}$$

$$+ 2\Im \sum_{i>j} U^*_{\alpha i} U_{\beta i} U_{\alpha j} U^*_{\beta j} \sin\left(\frac{\Delta m^2_{ij}}{2E}L\right) \tag{2.35}$$

$$= \delta_{\alpha\beta} - 2\Re \sum_{i>j} U^*_{\alpha i} U_{\beta i} U_{\alpha j} U^*_{\beta j} \left[1 - \cos\left(\frac{\Delta m^2_{ij}}{2E}L\right)\right] \tag{2.36}$$

$$+ 2\Im \sum_{i>j} U^*_{\alpha i} U_{\beta i} U_{\alpha j} U^*_{\beta j} \sin\left(\frac{\Delta m^2_{ij}}{2E}L\right). \tag{2.37}$$

Then using double-angle trigonometric relations the oscillation probability can be written

$$P(\nu_\alpha \to \nu_\beta) = \delta_{\alpha\beta} - 4\Re \sum_{i>j} U^*_{\alpha i} U_{\beta i} U_{\alpha j} U^*_{\beta j} \sin^2\left(\frac{\Delta m^2_{ij}}{4E}L\right) \tag{2.38}$$

$$+ 2\Im \sum_{i>j} U^*_{\alpha i} U_{\beta i} U_{\alpha j} U^*_{\beta j} \sin\left(\frac{\Delta m^2_{ij}}{2E}L\right). \tag{2.39}$$

Since the PMNS matrix, U, is a unitary 3×3 matrix, it can be parameterised in terms of three mixing angles θ_{12}, θ_{13}, θ_{23} and a complex phase δ [11]. When using this the PMNS matrix then has the form

$$\begin{pmatrix} U_{e1} & U_{e2} & U_{e3} \\ U_{\mu 1} & U_{\mu 2} & U_{\mu 3} \\ U_{\tau 1} & U_{\tau 2} & U_{\tau 3} \end{pmatrix} = \begin{pmatrix} c_{12}c_{13} & s_{12}c_{13} & s_{13}e^{-i\delta_{CP}} \\ -s_{12}c_{23} - c_{12}s_{23}s_{13}e^{i\delta_{CP}} & c_{12}c_{23} - s_{12}s_{23}s_{13}e^{i\delta_{CP}} & s_{23}c_{13} \\ s_{12}s_{23} - c_{12}s_{23}s_{13}e^{i\delta_{CP}} & -c_{12}s_{23} - s_{12}s_{23}s_{13}e^{i\delta_{CP}} & c_{23}c_{13} \end{pmatrix}, \tag{2.40}$$

where c_{ij} and s_{ij} are $\cos\theta_{ij}$ and $\sin\theta_{ij}$ respectively. Often, this form of the PMNS matrix is decomposed into three matrices which separates mixing angles conveniently.

$$U = \underbrace{\begin{pmatrix} 1 & 0 & 0 \\ 0 & c_{23} & s_{23} \\ 0 & -s_{23} & c_{23} \end{pmatrix}}_{atmospheric} \underbrace{\begin{pmatrix} c_{13} & 0 & s_{13}e^{-i\delta} \\ 0 & 1 & 0 \\ -s_{13}e^{i\delta} & 0 & c_{13} \end{pmatrix}}_{cross-mixing} \underbrace{\begin{pmatrix} c_{12} & s_{12} & 0 \\ -s_{12} & c_{12} & 0 \\ 0 & 0 & 1 \end{pmatrix}}_{solar} \tag{2.41}$$

In eq. (2.41) the first matrix labelled "atmospheric" contains the θ_{23} mixing angle and is primarily responsible for the oscillation of ν_μs and ν_τs. The second matrix depends on the mixing angle θ_{13} and the complex phase δ. The matrix labelled "solar" then contains the mixing angle θ_{12} which dominates the mixing found in solar ν_e and ν_μ.

2.2.2 Anti-neutrino oscillations

So far when discussing neutrino oscillations, only neutrinos have been discussed. To calculate the oscillation probability for antineutrinos eq. (2.39) needs to be modified slightly. Anti-neutrinos can be produced in the same process as neutrinos but are associated with a charged anti-lepton at an interaction vertex rather than a lepton. Therefore, the equivalent of eq. (2.11) for antineutrinos is

$$|\bar{\nu}_\alpha\rangle = \sum_{i=1,2,3} U_{\alpha i} \, |\bar{\nu}_i\rangle \, , \tag{2.42}$$

where the only difference is the lack of the conjugate on the element of the PMNS element, $U_{\alpha i}$. The kinematics of antineutrinos are the same as for neutrinos so the derivation outlined applies to both. Again, the only difference is the complex conjugate of the PMNS elements. The oscillation probability for antineutrinos is then given by:

$$P\left(\bar{\nu_\alpha} \to \bar{\nu_\beta}\right) = \delta_{\alpha\beta} - 4\Re \sum_{i>j} U^*_{\alpha i} U_{\beta i} U_{\alpha j} U^*_{\beta j} \sin^2\left(\frac{\Delta m^2_{ij}}{4E} L\right) \tag{2.43}$$

$$- 2\Im \sum_{i>j} U^*_{\alpha i} U_{\beta i} U_{\alpha j} U^*_{\beta j} \sin\left(\frac{\Delta m^2_{ij}}{2E} L\right), \tag{2.44}$$

where the important change to note is the change in sign of the imaginary term. The fact that the imaginary term changes sign for neutrino and anti-neutrino oscillations can give rise to a CP-violation in the neutrino sector.

2.2.3 Majorana Neutrinos

It is important to note that in this discussion of neutrino oscillation, neutrinos have always assumed to be Dirac-like in nature meaning that neutrinos are distinct from antineutrinos. However, neutrinos could instead be Majorana in nature, whereby left-handed and right-handed chiral states are related through a charge conjugation. The interpretation of a Majorana neutrino is that neutrinos and antineutrinos are the same particle. The PMNS matrix would then include additional phases to take this behaviour into account but these do not actually change the neutrino oscillaiton probablity as given in eq. (2.39) or eq. (2.44). Therefore, neutrino oscillation experiments are not sensitive to Majorana phases and they are ignored in the analysis in this thesis and generally in oscillation experiments.

Whether neutrinos are Majorana or Dirac in nature is still an open question in particle physics. Neutrinos being Majorana in nature would have serious implications for neutrino mass generation mechanisms, CP-violation and hence also baryogenesis. Throughout the rest of this thesis neutrinos are assumed to be Dirac particles but a thorough description of Majorana neutrinos can be found in [8].

2.2.4 Neutrino oscillations in matter

In the derivation described in section 2.2.1 it was assumed that the neutrino eigenstates were propagating through a vacuum. In most cases the neutrinos that are detected at experiments propagate through matter, whether it be the Earth or the sun. The presence of matter affects how neutrinos oscillate as the neutrinos will experience a weak potential from the particles in that material such that the Hamiltonian becomes

$$\mathcal{H} = \mathcal{H}_{vac} + \mathcal{H}_{matter}, \tag{2.45}$$

where $\mathcal{H}_{vac}$ is the Hamiltonian for oscillations in matter and $\mathcal{H}_{matter}$ is the weak potential that neutrinos experience from the presence of matter. The addition of this term to the Hamiltonian means that the mass eigenstates described in section 2.2.1 are modified.

For the density of matter in the Earth and the sun, coherent scattering of neutrinos on the particles is the largest contribution to $\mathcal{H}_{matter}$. In a coherent scatter, the medium will be left unchanged which means that neutrino eigenstates which have coherently scattered can interfere with other scattered or unscattered neutrino eigenstates. This effect then changes the oscillation probabilities from those that are expected in a vacuum.

The coherent scattering mentioned above has different contributions for electron, muon and tau neutrinos. The matter in the Earth is made up of electrons, protons and neutrons. This means that electron neutrinos have a contribution from both CC and NC interactions with the electrons in the Earth whereas muons and taus only have NC contributions. Since the NC contributions affect all flavours in the same manner they do not modify neutrino oscillation probabilities but lead to an overall change in the phase which is not observable. Therefore, the CC component for electron neutrinos is the important potential to consider when calculating neutrino oscillation probabilities.

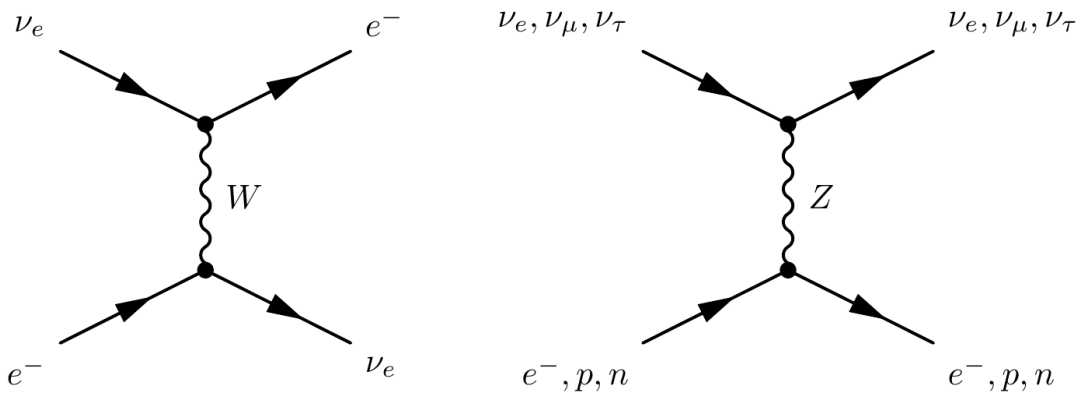

Figure 2.5: Feynman diagrams of the CC and NC coherent forward scattering which is responsible for matter effects. The CC channel can only occur on electron neutrinos. Figure from [8].

Feynman diagrams for coherent forward scattering can be seen in fig. 2.5. The derivation of the weak potential is not given here but can be found in many textbooks such as [8]. The perturbing potential $\mathcal{H}_{matter}$ from the CC coherent scattering of electron neutrinos is given by

$$\mathcal{H}_{matter} = \pm\sqrt{2}G_F n_e, \tag{2.46}$$

where G_F is the Fermi constant and n_e is the density of electrons and the $\pm$ sign corresponds to neutrinos (+) and antineutrinos (−).

It is worth noting for solar neutrino experiments (see section 2.3.1), where the density of matter changes rapidly when neutrinos propagate from the sun into the vacuum of space, matter effects give rise to resonances. The effect of these resonances in the sun is called the Mikheyev-Smirnov-Wolfenstein (MSW) effect [21]. For long-baseline experiments (see section 2.3.4) neutrinos propagate through the Earth's crust, where the density of matter is constant to a very good approximation. Therefore the MSW effect is not present for an experiment looking at terrestrial neutrino sources. Instead matter effects can play a role in the measurement of neutrino oscillation parameters as they affect neutrinos and antineutrinos, as well as different neutrino flavours, differently. As mentioned in eq. (2.46), $\mathcal{H}_{matter}$ changes sign for neutrinos and antineutrinos which means that matter effects impact neutrino and anti-neutrino oscillations differently. This has implications for long-baseline experiments measuring CP violation in neutrino oscillations as the presence of matter mimics CP violation. Figure 2.6 shows the electron neutrino

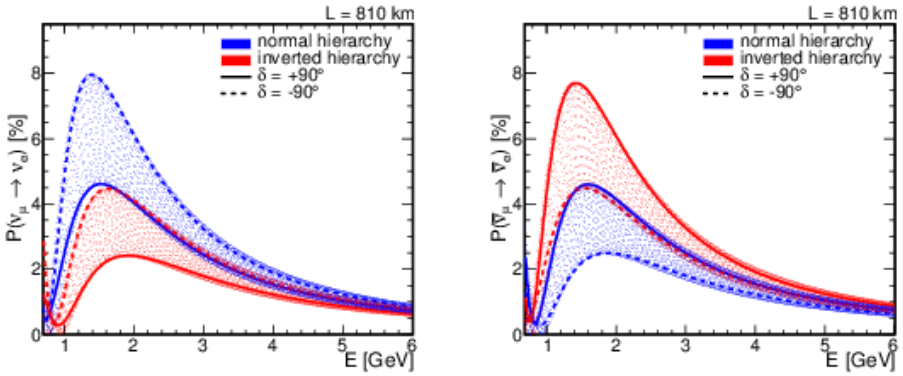

Figure 2.6: Electron-neutrino appearance probability as a function of neutrino energy for different values of δ_{CP} and the different mass hierarchies. It can be seen that changing the mass hierarchy has a very similar impact to change the values of δ_{CP}. This effect is caused by matter effects. Figure from [24].

appearance probability for different values of δ_{CP} and for the different mass hierarchies and shows this impact. In the analysis presented in this thesis a constant matter density of 2.6 gcm^{-3} [22] is assumed and matter effects are fully taken into account using the Prob3++ [23] software package when calculating oscillation probabilities.

2.2.5 Charge-parity violation

Parity violation has been discussed with regard to weak interactions in section 2.1. Since parity violation projects out only left-handed neutrino and right-handed neutrino states this also implies that another symmetry known as Charge conjugation is broken. Another important symmetry in particle physics is Charge conjugation (C) which transforms a particle to an anti-particle and *vice versa*. If only left-handed particles can interaction via weak interactions then transforming this into an anti-particle will result in a left-handed anti-particle which cannot occur due to the V-A structure of weak interactions. However, the combined effect of both C and P results in an allowed weak interaction. The effect of C, P and CP operators can be seen in fig. 2.7. Charge-parity (CP) violation has a special place in particle physics and may help to explain the matter-antimatter asymmetry that is observed in the universe. The fact that matter and antimatter are found in such unequal supply in the universe requires there to have been some cause during the evolution of the universe to create this asymmetry. Three conditions, known as Sakharov conditions [25]

(named after the person who first formulated them), must be satisfied in order to achieve a matter-antimatter asymmetry. These are:

1. Non-conservation of baryon number
2. Violation of C and CP symmetry
3. Deviation from thermal equilibrium in the universe.

CP (and C) violation is one of these conditions which is why CP violation has such a central role in explaining the matter-antimatter asymmetry in the universe.

The weak force is the only part of the standard model where CP violation has been observed. Specifically CP violation has only currently been observed in the flavour-mixing of quarks [26]. However, the magnitude of CP violation from quarks alone is not sufficient to explain the CP violation required to explain the matter-antimatter asymmetry in the universe [9]. CP violation gives a mechanism by which matter and antimatter can behave distinctly. For neutrino oscillations CP violation would manifest itself in neutrinos behaving distinctly from antineutrinos. If neutrinos were observed to behave differently to antineutrinos then this would indicate CP violation. When measuring CP violation in lepton flavour mixing there is a convenient variable that is used called the Jarlskog invariant, J_{CP} [27]. This variable is useful when measuring CP violation as it does not depend on the choice of basis used to describe the flavour mixing in weak interactions. For the PMNS matrix the Jarlskog invariant takes the form

$$J_{CP} = \frac{1}{8}\cos\theta_{13}\sin(2\theta_{13})\sin(2\theta_{12})\sin(2\theta_{23})\sin\delta_{CP}, \tag{2.47}$$

where θ_{ij} and δ_{CP} are the mixing angles and complex-phase of the PMNS matrix that have already been introduced. This parameter will be particularly useful when considering the phenomenology of neutrino oscillations in section 2.2.6.

One of the reasons that the study of neutrinos and neutrino oscillations is important is that there is the potential for large amounts of CP-violation to be observed. In the quark sector, the mixing of flavour states has been measured very precisely and gives a Jarlskog invariant of $J_{CP,quark} = 3 \times 10^{-5}$ [26]. In contrast, the mixing of flavour states in the neutrino sector through neutrino oscillations is $J_{CP,\nu} = 0.03 \times \sin\delta_{CP}$ [26],

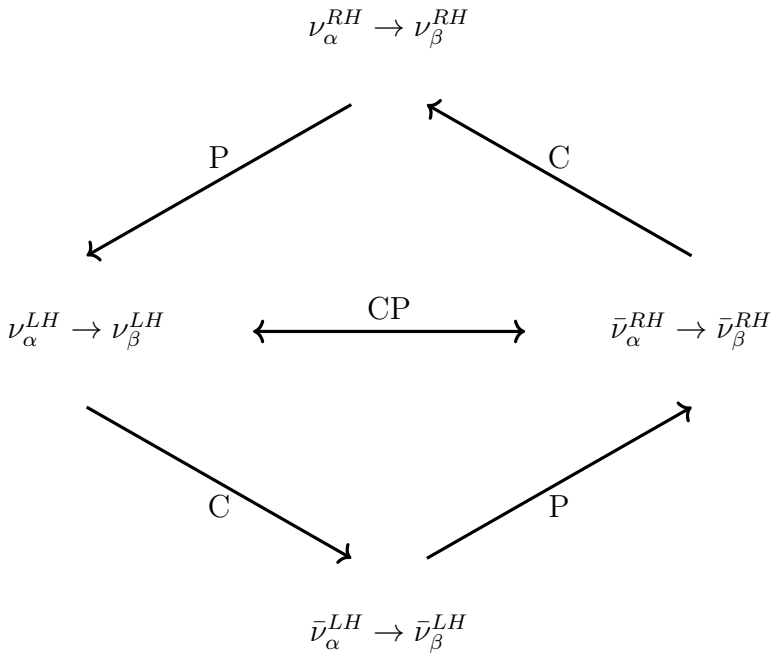

Figure 2.7: A schematic of the effect of C, P and CP operators on the transitions of a neutrino of flavour α and left or right-handed chiral states to a neutrino of flavour β. If CP is violated the process on the left will not be observed to be equal to the that on the right. Although ν_α^{RH} and $\bar{\nu}_\alpha^{LH}$ states are not allowed in the standard model they are included to make it clear how the C and P operators behave.

which is potentially three orders of magnitude greater than that in the quark sector. The measurement of neutrino oscillation parameters, in particular δ_{CP}, is therefore important in establishing the magnitude of CP-violation in the neutrino sector, which in turn could help explain how the matter-antimatter asymmetry in the universe came about.

2.2.6 Phenomenology of neutrino oscillations

Equation (2.39) and eq. (2.44) contain lots of phenomenological features which neutrino experiments are trying to explore and measure. Before moving on to discussing neutrino experiments it is useful to highlight some of the key features of three-flavour neutrino oscillations. For this thesis, it is most useful to consider the approximate oscillation probabilities for $\nu_\mu(\bar{\nu}_\mu) \to \nu_\mu(\bar{\nu}_\mu)$ and $\nu_\mu(\bar{\nu}_\mu) \to \nu_e(\bar{\nu}_e)$ flavour transitions. These oscillations channels are used by T2K experiment and other long-baseline neutrino experiments to measure neutrino oscillation parameters.

The $\nu_\mu(\bar{\nu}_\mu) \to \nu_\mu(\bar{\nu}_\mu)$ channel looks for muon neutrino disappearance and, neglecting higher order terms and matter effects, is given by

$$\begin{aligned} 1 - P(\nu_\mu \to \nu_\mu) \approx & 4\cos^2\theta_{13}\sin^2\theta_{23} \\ & \times (1 - \cos^2\theta_{13}\sin^2\theta_{23})\sin^2\left(\Delta m^2_{32}\frac{1.27L}{E}\right), \end{aligned} \tag{2.48}$$

where the factor of 1.27 is now included to express the neutrino energy in units of GeV, baseline in terms of km and the neutrino mass splitting in eV^2.

The $\nu_\mu(\bar{\nu}_\mu) \to \nu_e(\bar{\nu}_e)$ channel searches for electron-neutrino appearance and, again neglecting matter effects and higher order terms, is given by

$$\begin{aligned} P(\nu_\mu(\bar{\nu_\mu}) \to \nu_e(\bar{\nu_e})) \approx & \sin^2\theta_{23}\sin^2 2\theta_{13}\sin^2\left(1.27\frac{\Delta m^2_{32}L}{E}\right) \\ & - (+)\frac{1.27\Delta m^2_{21}L}{E}8J_{CP}\sin^2\left(1.27\frac{\Delta m^2_{32}L}{E}\right), \end{aligned} \tag{2.49}$$

where J_{CP} is the Jarlskog invariant described in section 2.2.5 and the + and − signs correspond to the neutrino and anti-neutrino oscillation probabilities respectively. This form is particularly useful when considering CP violation in the neutrino sector.

From eq. (2.48) and eq. (2.49) it is now easier to discuss the key features of neutrino oscillations, again, with particular emphasis to the T2K experiment and long-baseline

experiments in general (long-baseline experiments will be discussed in more detail in chapter 3 and section 2.3.4 respectively).

1. If $\Delta m^2_{ij} = 0$ neutrinos cannot oscillate to other flavour eigenstates. This is one of the reasons why the discovery of neutrino oscillations was so important. The observation of neutrino oscillations shows that neutrinos do have a mass. This has significant implications for the standard model and possible mass generation mechanisms for neutrinos.

2. Neutrino oscillations in a vacuum depend on the mass-squared splitting and not the absolute neutrino masses. This means that experiments measuring the neutrino oscillation parameters cannot measure the absolute mass of neutrinos. Furthermore, this means that an ambiguity exists in the sign of the mass splitting. As mentioned in the discussion of matter effects, solar neutrino experiments have determined the sign of Δm^2_{21} but the sign of Δm^2_{32} is still unknown. This gives two possible orderings the "normal" ordering, where $\Delta m^2_{32} > 0$ and so $m_3 > m_1$; and the "inverted" ordering, where $\Delta m^2_{32} < 0$ and so $m_3 < m_1$. A diagram of the two mass orderings can be seen in fig. 2.8. Sometimes the mass ordering is also called the mass hierarchy and then normal and inverted hierarchy (NH and IH) for the specific ordering of mass states. These two terms will be used interchangeably throughout this thesis.

3. CP violation can occur in neutrino oscillations due to the different signs in eq. (2.49) for neutrinos and antineutrinos. Measuring CP violation and the CP-violating phase δ_{CP} can be done by measuring neutrino oscillations using both neutrinos and antineutrinos. Furthermore, eq. (2.48) and eq. (2.49) make it clear that it is electron-neutrino appearance which gives long-baseline neutrino experiments sensitivity to J_{CP}. It should also be clear from these equations that both muon neutrino disappearance and electron neutrino appearance have common parameters which they depend on. Therefore these oscillation channels are complimentary to each other and measuring both channels aids in constraining oscillation parameters.

4. For electron neutrino appearance if the angle $\theta_{13} \approx 0$ then the magnitude of CP violation and the possibility of measuring it in the neutrino sector becomes much

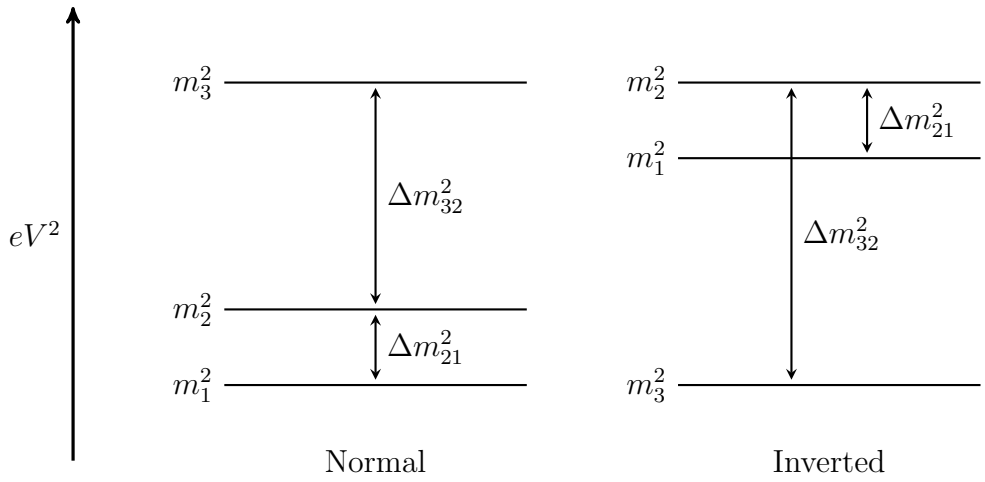

Figure 2.8: Diagrams of the two possible orderings the neutrino masses could take. The case where Δm^2_{32} is positive is referred to as the Normal Ordering and when Δm^2_{32} is negative this is referred to as the Inverted Ordering.

smaller. Although this comment is true for any of the mixing angles (as if $\theta_{ij} = 0$ then $J_{CP} = 0$) it is worth stressing since historically θ_{13} was the last mixing parameter to be measured. Further to this it can be seen that θ_{13} and its uncertainty is the leading contribution to measuring J_{CP}.

5. For muon neutrino disappearance, there is a dependence on $\sin^2\theta_{23}(1 - \sin^2\theta_{23})$. Due to the symmetry of the $\sin^2\theta_{23}$ function, this leads to a degeneracy in values of $\sin^2\theta_{23}$. For example, values of $\sin^2\theta_{23} = 0.4$ and $\sin^2\theta_{23} = 0.6$ will give identical oscillation probabilities using eq. (2.48). It is only through higher order terms (and analysing electron neutrino appearance channels jointly with muon neutrino disappearance channels) that this degeneracy is broken. This degeneracy in values $\sin^2\theta_{23}$ means that the octant of $\sin^2\theta_{23}$ (that is whether $\sin^2\theta_{23} < 0.5$ or $\sin^2\theta_{23} > 0.5$) is currently not known with great certainty.

6. Degeneracies between oscillation parameters are frequent. It is difficult to measure features of the PMNS matrix due to many degeneracies existing between different oscillation parameters (eight in total [28]). For current-generation experiments this is not a major problem due to precision of the measurements being made but will be important for future-generation experiments.

From these features it then feels natural to ask what we should be measuring and to

highlight what current generation experiments are measuring.

- $\boldsymbol{\delta_{CP}}$ — the magnitude of CP violation in the neutrino sector and in particular the magnitude of δ_{CP} is important in understanding the matter-antimatter asymmetry in the universe as discussed in section 2.2.5. In the first instance, verifying whether δ_{CP} is neither 0 nor π (CP-conserving values) would mean that $J_{CP} \neq 0$. Current-generation neutrino experiments, such as T2K, are aiming to measure if CP is conserved in the neutrino sector. However, these experiments will not have sufficient statistics to exclude CP conservation at the 5σ significance level. Future-generation experiments such as DUNE [29] and Hyper-K [30] are aiming to discover CP violation and then also to measure the angle of δ_{CP} precisely. The magnitude of CP violation in the neutrino sector also has implications for some theories of leptogenesis [31] [32].

- **Mass Ordering** — whether the ordering of the neutrino masses is normal ordered (NO) or inverted ordered (IO). Measuring whether the ordering of the mass states in neutrinos reflects the ordering in the rest of the standard model is important in understanding the lepton-flavour mixing and mass generation mechanisms [33]. Again, it will be down to future-generation experiments such as DUNE, Hyper-K and JUNO [34] to discover the mass ordering but current-generation experiments are able to make statements about the mass ordering as well.

- $\boldsymbol{\theta_{23}}$ — the magnitude of θ_{23} along with its octant give important information about the structure of the PMNS matrix. In turn this informs which models or symmetries could exist at higher energy scales to result in the PMNS matrix that is observed [35].

- $\boldsymbol{\theta_{13}}$ — as mentioned already, θ_{13} has an important role in constraining the measurement of δ_{CP} and J_{CP}. Presently reactor neutrino experiments (which will be discussed in section 2.3.2) give the best constraints on θ_{13}. In the future, the measurement of θ_{13} will be improved by both future reactor and long-baseline neutrino experiments such as JUNO, DUNE and Hyper-K.

Table 2.1: The best-fit oscillation parameters from a combined analysis of experimental results taken from [26]. Values for $\sin^2\theta_{23}$ and Δm^2_{32} are given for the normal mass ordering.

Oscillation parameter	Best-fit value
$\sin^2\theta_{12}$	0.307 ± 0.013
$\sin^2\theta_{13}$	$(2.18 \pm 0.07) \times 10^{-2}$
$\sin^2\theta_{23}$	0.545 ± 0.021
Δm^2_{23}	$(2.453 \pm 0.034) \times 10^{-3}$
Δm^2_{12}	$(7.53 \pm 0.18) \times 10^{-5}$ eV^2
δ_{CP}	$(1.36 \pm 0.17)\pi$ rad

2.3 Experimental overview

Neutrino oscillation parameters have been measured and are being measured by a variety of different experiments. Over the past decades these experiments have discovered neutrino oscillations and have led to the clearer understanding of the PMNS matrix that exists today. The global-average parameter values for the parameters of the PMNS matrix are given in table 2.1. The different mixing angles and mass splitting of neutrino oscillations affect neutrinos on different energy and distance scales, so to measure all these parameters neutrino experiments come in a variety of different forms. In this chapter, neutrino experiments are categorised by the source of the neutrinos that they use to measure oscillation parameters; solar, reactor, atmospheric and accelerator.

2.3.1 Solar neutrino experiments

The Sun produces a copious number of neutrinos. For each 1 cm^2 of matter on Earth there are $\sim 10^{10}$ solar neutrinos passing through it every second [36]. The Sun produces neutrinos through various phases of solar nuclear processes. The dominant process which

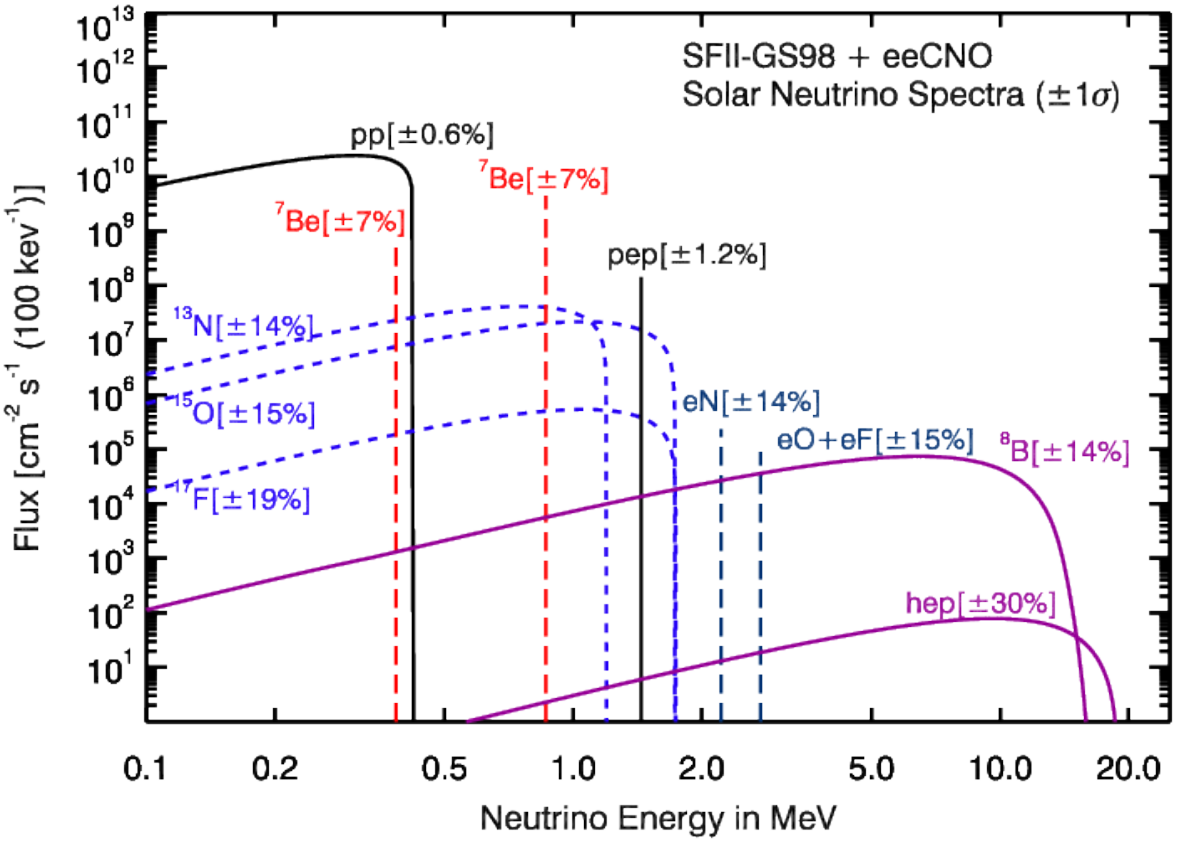

Figure 2.9: Neutrino fluxes as a function of neutrino energy for different processes in the Sun as predicted by the standard solar model. Notice that for all processes the neutrino energy is still below 20 MeV. Figure taken from [40].

results in neutrino production is the process

$$\mathrm{p} + \mathrm{p} \rightarrow \mathrm{np} + e^{+} + \nu_e, \tag{2.50}$$

$$\mathrm{np} + \mathrm{p} \rightarrow \mathrm{He}_2^3 + \gamma, \tag{2.51}$$

$$\mathrm{He}_2^3 + \mathrm{He}_2^3 \rightarrow \mathrm{He}_2^4 + \mathrm{p} + \mathrm{p}. \tag{2.52}$$

This process is referred to as the "pp chain" and due to the small mass difference between deuteron, np, and the two protons (and small binding energy of deuteron) this means that the neutrinos produced by this process are very low energy (~ 0.5 MeV). There are other process that produce neutrinos in the sun each producing a different energy spectrum of neutrinos. Figure 2.9 shows the neutrino energy spectra from different processes in the sun. Several neutrino experiments such as BOREXINO [37], the Sudbury Neutrino Experiment (SNO) [3], IceCube [38] and SK [39] are able to measure neutrinos coming from these different processes.

Solar neutrinos also played a lead role in the story of the discovery of neutrino oscillations. As early as the 1960s it was thought that neutrinos could be used to measure the total solar output and the different processes which produce neutrinos. The Homestake experiment aimed to measure the rate of solar neutrinos through the use of 615 tonnes of C_2Cl_4 [41]. When a solar neutrino interacts with this mass, the Cl would decay into an Ar^{37}_{18} through the inverse beta decay process

$$\nu_e + Cl^{37}_{17} \rightarrow Ar^{37}_{18} + e^-. \tag{2.53}$$

By counting the number of Ar^{37} atoms the rate of solar neutrino interactions could be established. The experiment expected to measure $\sim$ 1.7 interactions per day. However, the observed interaction rate was much lower at 0.48 ± 0.4 interactions per day. This severe deficit could not be explained by well-understood solar models and became known as the solar neutrino problem. Ray Davis received the Nobel prize for his development of the Homsestake experiment and the discovery of the solar neutrino problem. The problem found by the Homestake experiment was confirmed by several other experiments, however, it would not be solved until the late 1990s.

To try to solve the solar neutrino problem, many large experiments were built. Solar neutrinos are produced as electron neutrinos so it seemed natural to look for the lack of solar neutrinos not in channels just sensitive to electron neutrinos but to all flavours of neutrinos. The Sudbery Neutrino Observatory (SNO) was one of the experiments which aimed to measure all three flavours of neutrino to establish if the neutrinos produced at the sun could indeed have changed flavour. SNO detected B^8 solar neutrinos through three different reactions:

$$\nu_e + d \rightarrow e^- + p + p(CC), \tag{2.54}$$

$$\nu_\alpha + d \rightarrow \nu_\alpha + p + n(NC), \tag{2.55}$$

$$\nu_\alpha + e^- \rightarrow \nu_\alpha + e^-(ES). \tag{2.56}$$

where d is deuterium (which is contained in the heavy water SNO used in their fiducial volume), ν_α is any flavour neutrino ($\alpha = e, \mu, \tau$). The first process is a CC interaction which will only be sensitive to electron neutrinos. The second process is an NC interaction and will be sensitive to all flavours of neutrino. Then the third process looks for elastic scattering (ES) of a neutrino on an electron which is also sensitive to all neutrino flavours

but with reduced sensitivity to muon and tau neutrinos as these can only be observed via NC interactions. By examining these three processes the SNO experiment was able to look at the solar flux in all three channels. The results of this are shown in fig. 2.10 and the excess in the NC flux strongly suggests that electron neutrinos produced in the sun are undergoing flavour oscillations. These results, as well as findings from atmospheric neutrinos by the Super-Kamiokande experiment in Japan [4], experimentally verified that neutrinos oscillate between flavour states. In addition, these experimental results clearly showed that neutrinos are massive particles. Arthur McDonald and Takaaki Kajita won the Nobel Prize in physics in 2015 for their roles in the discovery of neutrino oscillations at SNO and Super-Kamiokande.

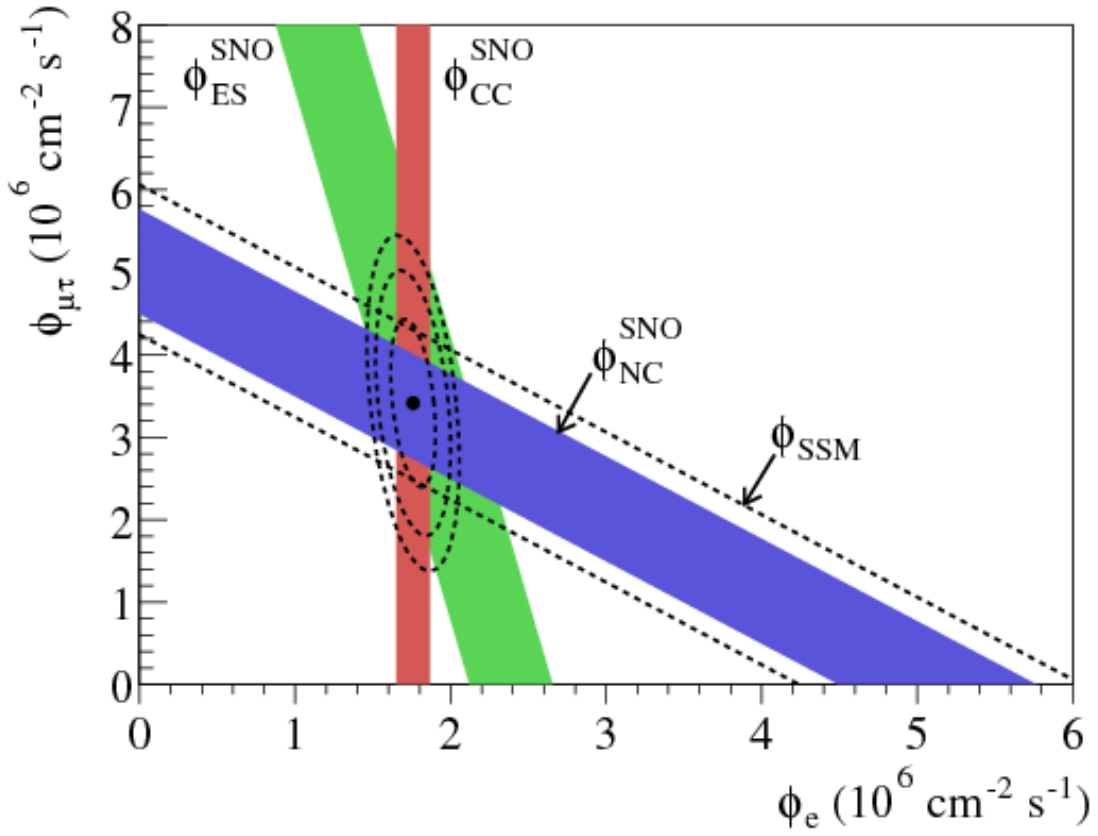

Figure 2.10: Results from the SNO collaboration which solved the solar neutrino problem and showed that neutrinos from the sun oscillate. The results show that the measured neutrino fluxes from elastic scattering (ES), CC and NC channels are consistent with the Standard Solar Model (SSM). Figure taken from [3].

2.3.2 Reactor neutrino experiments

Reactor neutrino experiments such as Daya Bay [42], Double-Chooze [43] and RENO [44] measure neutrino oscillations using the neutrinos produced by nuclear fission reactors. Often, the experiment is situated just a few tens to hundreds of metres away from the reactor core. The energy of the neutrinos produced from the reactor and this short-baseline allow reactor neutrino experiments to be uniquely sensitive to some neutrino oscillation parameters. Nuclear fission reactors produce an incredibly large number of neutrinos. They do this through β decay:

$$X_{\mathrm{N}}^{\mathrm{n}} \rightarrow X_{\mathrm{N}}^{\mathrm{'\,n\text{-}1}} + e^{-} + \bar{\nu_e}, \tag{2.57}$$

where X is the decaying nucleus, $X^{'}$ is the nucleus after decaying, n is the proton number of the element and N is the mass number of the element. From this processes it is apparent that the neutrinos which reactor neutrinos measure are antineutrinos. Due to the high rate of beta decay in nuclear reactors the neutrino flux produced is very large compared to natural sources. Modern reactors (assuming 3 GW of thermal power) produce neutrinos at a rate of $\sim 6 \times 10^{20}$ s^{-1} [8]. The close proximity of the reactor neutrino experiments to the reactor core means that, despite the flux being isotropic, a large neutrino flux still traverses reactor neutrino experiments.

The β decay process in eq. (2.57) is also informative about how reactor neutrino experiments measure neutrino oscillations. The typical energy of a β decay is 0–5 MeV meaning that the electron antineutrinos produced by reactors are low in energy. From eq. (2.44) this implies that the oscillation length of these neutrinos is small. Indeed, this is why reactor neutrino experiments are placed at such short distances from nuclear reactors. Further to this, because of their low energy, if these electron antineutrinos were to oscillate to a muon or tau antineutrino a charged lepton could not be produced because the production threshold of these leptons is much higher than the energy of the neutrino. Due to this, reactor neutrino experiments cannot measure electron antineutrinos oscillating to the muon or tau channels directly but instead look for electron neutrino disappearance. Reactor neutrino experiments are therefore sensitive to the neutrino oscillation parameters which affect electron neutrino disappearance which are: θ_{13}, θ_{12} and Δm^2_{21}. Experiments have different sensitivities to these parameters depending

on the distance between the reactor(s) and the experiment. Figure 2.11 shows the different baselines which reactor neutrino experiments use as well as how the solar mixing parameters impact the observed number of neutrino events. Figure 2.12 then shows the oscillations arising from θ_{13} which short baseline reactor experiments are most sensitive to.

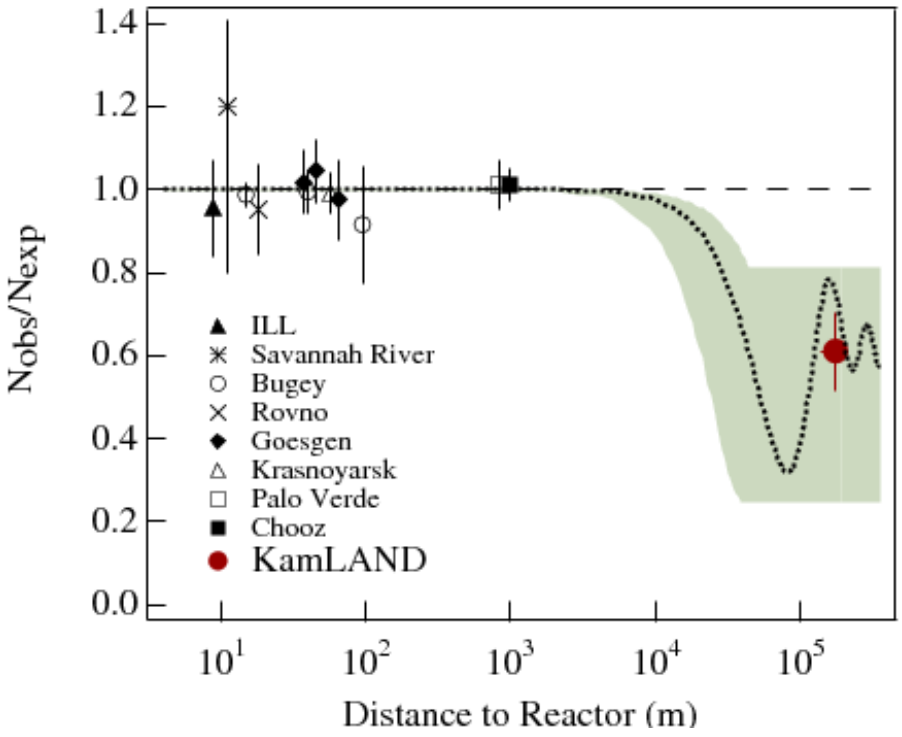

Figure 2.11: A comparison of the ratio of the expected unoscillated $\bar{\nu}_e$ events and the observed number of events and the distance to the reactor for several experiments. The thin-dashed line shows the ratio of expected and observed events assuming $\sin^2 2\theta_{12} = 0.833$ and $\Delta m^2_{21} = 5.5 \times 10^{-5}\text{eV}^2$. Figure from [45].

Reactor neutrino experiments usually measure neutrino events by looking for inverse beta decay interactions in which a positron and a neutron are produced. Different experiments measure this in different ways but typically this is done by detecting the visible energy produced by the positron. Perhaps the key part of measuring the electron antineutrino event rate is reducing the background coming from other sources. This is done in a variety of ways but the recapture of the neutron by a nucleus gives a prompt signal which can be used to significantly reduce background events [47].

Reactor neutrinos currently give the best sensitivity to the θ_{13} mixing angle. How-

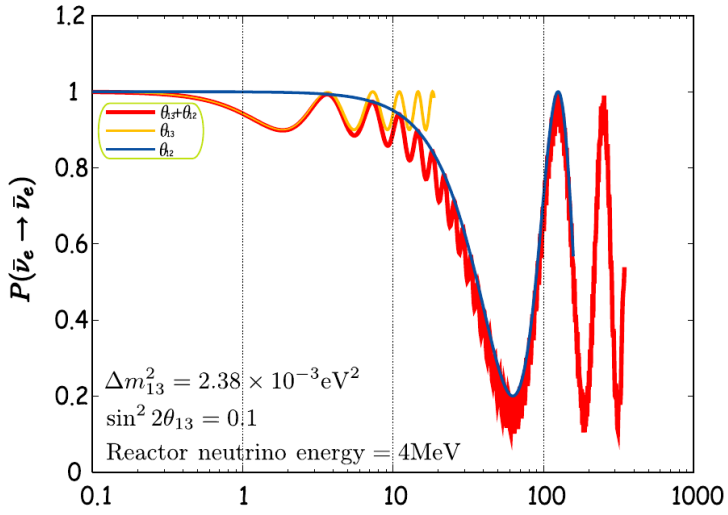

Figure 2.12: A plot showing the electron antineutrino survival probability for the Double-Chooz experiment. The impact individual impact of θ_{13} (orange) and θ_{12} (blue) can be seen as well as their combined impact. It can be seen that θ_{13} is associated with the higher frequency oscillations while θ_{12} with the longer oscillations. Figure taken from [46].

ever, long-baseline neutrino experiments (which will be discussed in section 2.3.4) are also sensitive to this mixing angle. At long-baseline experiments θ_{13} is in a large part responsible for electron neutrino appearance. The other oscillation parameter which is responsible for electron neutrino appearance is δ_{CP}. If the θ_{13} parameter is known more precisely by reactor neutrino experiments, long-baseline experiments can use these measurements to make more precise statements about the δ_{CP} oscillation parameter. In the analysis presented in chapter 7, results using T2K data only and also using the PDG world-average constraint on θ_{13} are shown. The measurements made by using the θ_{13} constraint give more precise measurements than using T2K data only. How the θ_{13} constraint is used in the T2K oscillation analysis is described in chapter 4.

2.3.3 Atmospheric neutrino experiments

Similarly to solar neutrino experiments, experiments have been measuring neutrinos produced from the atmosphere for several decades and were also instrumental in solving the solar neutrino problem through the discovery of neutrino oscillations. Atmospheric

neutrino experiments are able to make some of the most precise measurements of neutrino oscillation parameters. The detectors used in these experiments are often large and this combined with the high rate of atmospheric neutrinos [48] means that these experiments benefit from having high statistics of data. Some current examples of experiments measuring atmospheric neutrinos are IceCube [49] and SK [4].

Neutrinos are produced in the atmosphere via the decay of mesons produced from interactions of cosmic rays in the atmosphere. Cosmic rays rays are primarily made up of protons and when these interact with nuclei in the atmosphere many secondary particles can be produced. These secondary particles can then go on to decay themselves. It is these secondary and tertiary particles which are most often detected by atmospheric neutrino experiments. The processes which are most responsible for muon neutrino production are:

$$\pi^+ \to \mu^+ + \nu_\mu, \tag{2.58}$$

$$(\mu^+ \hookrightarrow e^+ + \nu_e + \bar{\nu}_\mu), \tag{2.59}$$

$$\pi^- \to \mu^- + \bar{\nu}_\mu, \tag{2.60}$$

$$(\mu^- \to e^- + \bar{\nu}_e + \nu_\mu), \tag{2.61}$$

where process in brackets are subsequent decays of particles [26]. At higher energies, kaon production can also lead to electron neutrino and anti-neutrino production instead of the pion decay paths given above.

The processes of neutrino production in the atmosphere occur uniformly throughout the Earth's atmosphere. This means atmospheric neutrinos entering a detector can come from any direction as neutrinos produced in the atmosphere can travel through the Earth virtually unimpeded. Neutrinos entering from different zenith angles will have traversed a different distance through the Earth from where they were produced in the atmosphere. This means atmospheric neutrino experiments do not measure neutrino oscillations with a fixed baseline but over many. The baseline a neutrino has travelled depends on the angle the neutrino enters the detector at. It is by measuring the zenith angle (which implicitly gives the baseline), flavour and the energy of neutrinos detected that atmospheric neutrino experiments measure neutrino oscillation parameters. Furthermore, as different zenith angles correspond to neutrinos having passed through different lengths of the Earth,

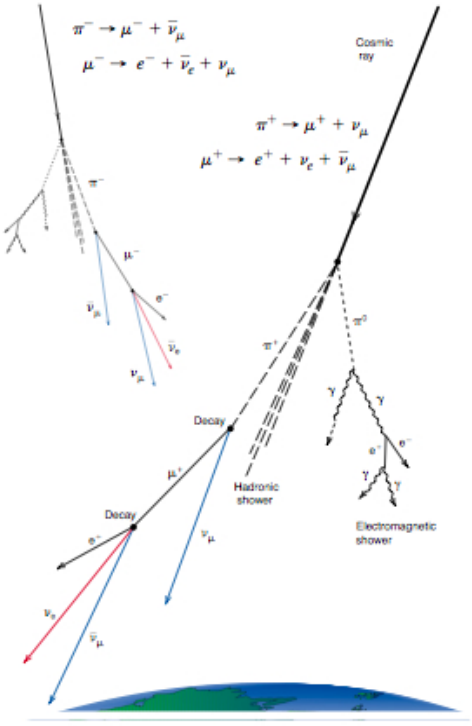

Figure 2.13: A diagram showing the production of atmospheric neutrinos and other processes in the atmosphere. Figure taken from [50].

matter effects play an important role in atmospheric neutrinos. Depending on the true mass ordering or value of Δm^2_{32} in nature, atmospheric neutrinos will evolve differently in the presence of matter effects. This means atmospheric neutrino experiments give some of the best measurements of Δm^2_{32} and the mass ordering. The most recent constraints on oscillation parameters from Super-Kamiokande are given in fig. 2.14.

2.3.4 Long-baseline neutrino experiments

This thesis focuses on oscillation analyses at the T2K experiment. The T2K experiment is a long-baseline neutrino experiment which uses a man-made neutrino beam and measures neutrino oscillations across a baseline of 295 km. Unlike other neutrino experiments, the neutrino beam is explicitly made for the experiment. This means that long-baseline experiments can be designed or tuned in specific ways to be most sensitive to neutrino oscillation parameters. Similarly, because the neutrino beam is man-made the energy and number of neutrinos produced can be constrained by monitoring the neutrino beam.

Often, long-baseline neutrino experiments measure neutrino interactions using two detectors. One detector close to the source of the neutrino beam (called a near detector) which measures unoscillated neutrinos and one detector placed far away from the neutrino source (unsurprisingly called a far detector) which measures neutrinos after oscillations. There are several long-baseline experiments including past experiments, such as MINOS [51], current experiments, such T2K and NOvA [52], and future experiments, such as Hyper-K [30] and DUNE [29].

Long-baseline experiments measure neutrino oscillation parameters using neutrinos produced from a man-made beam. A beam of neutrinos can be produced by colliding a proton beam with a nuclear target. A multitude of hadrons are produced from this collision which then decay to produce neutrinos. A more detailed description of how a neutrino beam is produced, specifically for the T2K experiment, is given in chapter 3.

The neutrino beams that long-baseline experiments use are mainly composed of muon neutrinos. Due to this, long-baseline experiments search for muon neutrino disappearance and electron neutrino appearance. This makes long-baseline experiments most sensitive to neutrino oscillation parameters which affect these disappearance and appearance probabilities such as the θ_{23}, Δm^2_{32}, θ_{13} and δ_{CP} parameters. Figure 2.14 shows oscillation parameter constraints for θ_{23} and Δm^2_{32} for various different long-baseline and atmospheric experiments. Long-baseline experiments are also sensitive to the mass ordering through matter effects with experiments with longer baselines being more sensitive to the mass ordering. In addition, long-baseline experiments have the unique ability to change from using a neutrino beam to using an anti-neutrino beam. As discussed in section 2.2 a difference in neutrino oscillation probability can arise between neutrinos and antineutrinos. This means that long-baseline neutrino oscillation experiments are sensitive to the oscillation parameters which can lead to neutrinos and antineutrinos oscillating with different probabilities. In particular, long-baseline neutrino experiments are sensitive to the δ_{CP} parameter and are in a unique position to measure the magnitude of CP violation in the neutrino sector.

This thesis focuses on improving the constraints on oscillation parameters that the T2K oscillation analysis makes through improved treatment of systematic uncertainties and with increased data statistics and additional data samples. The results presented in

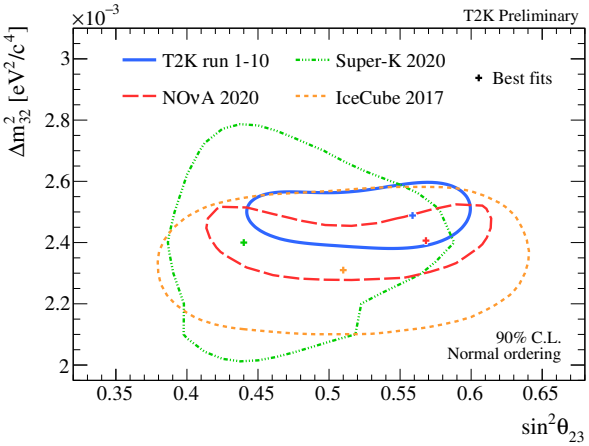

Figure 2.14: Comparison of constraints on the θ_{23} and Δm^2_{32} oscillation parameters for the NH only for different long-baseline and atmospheric neutrino experiments. The results from NOvA, SK, IceCube can be found at [53], [54] and [38] respectively. The T2K results are those presented in chapter 7 of this thesis. Figure taken from [55]. Generally, different long-baseline experiments agree broadly on the favoured parameter values.

chapter 7 show the latest results from the T2K experiment which contain world-leading measurements on oscillation parameters. Further to this, I have worked towards the next iteration of the T2K oscillation analysis which will include additional data samples being used. This work is presented in chapter 8 and should provide improved constraints on oscillation parameters.

2.4 Neutrino Interactions

Neutrino experiments do not measure neutrinos directly. Instead they measure the particles produced when neutrinos interact. This section aims to briefly describe neutrino interactions and in particular how the different process result in different types, number and momenta of particles. The description given below is very skewed towards neutrino interactions that are most relavent for the T2K experiment i.e. neutrinos an energy from a few hundered MeV to a few GeV. How the uncertainties associated with the prediction of these interactions are handled in the analysis will be discussed in chapter 4.

2.4.1 Interaction types

As has already been described in section 2.1.1, neutrinos interact via the weak force. Only neutrinos interacting through CC channels are of use to measure neutrino oscillation parameters as the lepton produced is the same flavour as the neutrino. This allows the flavour content of the oscillated neutrinos to be measured and from this neutrino oscillation parameters. Neutrinos interacting via NC channels do not directly produce a lepton, instead they produce a background of interactions which are indistinguishable from CC interactions (by producing neutral pions which then decay to photons which can be mis-identified as electrons for example). This section focuses on the description of CC interactions but uncertainties on different NC channels will be highlighted in chapter 4.

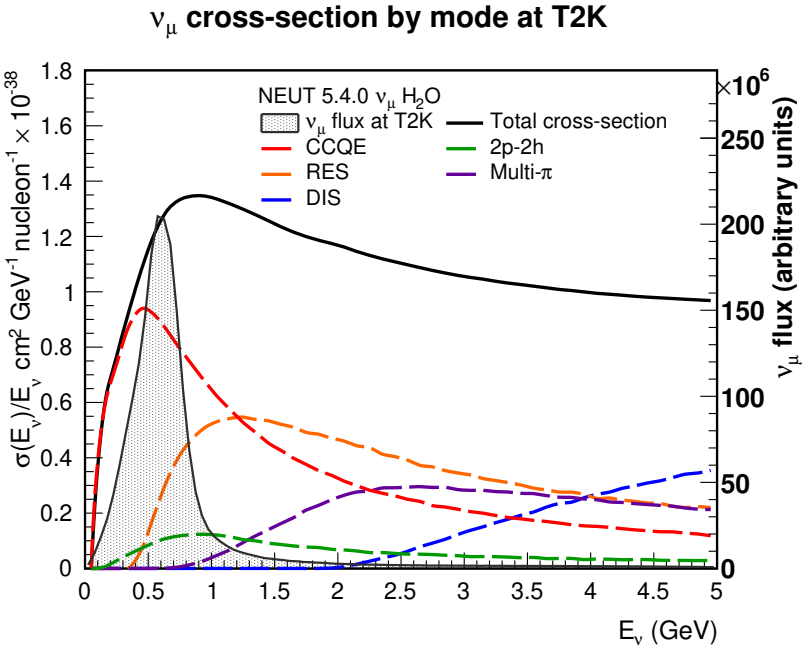

Figure 2.15: Neutrino interaction cross sections predicted by the NEUT generator [56] for the different interaction modes described. CCQE and 2p-2h occur at typically lower energies, while CCRES and CC DIS (and CC Multi-π which will be introduced later) occur a typically higher energies. The T2K flux shape is superimposed on the plot as well to compare the energy regime that T2K operates at.

CC neutrino interactions can be categorised into four main energy regions; those dominated by quasi-elastic interactions (CCQE), by multi-nucleon knockout (2p-2h), by

resonant pion production (CCRES) and then by Deep Inelastic Scattering (CC DIS). Figure 2.15 shows these different neutrino interaction regions as a function of neutrino energy. Below is a very brief description of these interactions and some of the challenges involved in modelling them in simulations. For a fuller description of neutrino interactions, see [57], [58] and [8] for example.

- **CCQE** - interactions involve the interaction of neutrinos on single nucleons which produce a charged lepton and an outgoing nucleon. Uncertainties on these interactions mainly come from the form factors used to describe the momentum-transfer of the neutrino to the nucleon. A Feynman diagram of a CCQE interaction is shown in fig. 2.16.

- **2p-2h** - similar to CCQE interactions but now neutrinos interact with a correlated pair of nucleons and also include contributions two-nucleon currents from meson exchange. The modelling of the correlations between nucleons are theoretically challenging and different models predict different interaction probabilities and kinematics. These interactions are quite probable a T2K energies so lots of work has been done in previous analyses to develop appropriate uncertainties for these.

- **CCRES** - interactions where the nucleon gets excited into a Δ-resonance which then decays to produce a pion. These interactions get contributions from many different nucleon resonances as well as non-resonant backgrounds. Including all these contributions is challenging to model and hence these interactions can have large uncertainties. A Feynman diagram of a CCRES interaction is shown in fig. 2.17.

- **CC DIS** - interactions involve the interaction of a neutrino with a constituent quark of a nucleon. These interactions can then produce a multitude of hadrons through the fragmentation of the nucleon. At higher energies these interactions are well understood but the transition region between CCRES and CC DIS is particularly challenging to model. A Feynman diagram of a CC DIS interaction is shown in fig. 2.18.

Typically, CCQE and 2p-2h interactions are more probable at lower energies (0–1 GeV), CCRES interactions at medium energies (1–3 GeV) and CC DIS interactions at

higher energies (above 3 GeV). Since the T2K neutrino beam has a peaked energy distribution around 0.6 GeV, CCQE interactions are the most frequent to occur in both the ND280 and SK detectors. However, CCRES and CC DIS interactions still play an important role at T2K energies both in improving the modelling of backgrounds to neutrino oscillations and improving measurements of neutrino oscillation parameters themselves. In fact, the inclusion of these higher energy interactions into the T2K neutrino oscillation analysis are the focus of this thesis. The construction of models to describe these neutrino interactions is a difficult task. Theorists build models from first principles but with relatively scarce neutrino interaction data to compare to, which (if any) model best describes different neutrino interactions is rarely clear. This often results in large uncertainties on neutrino cross sections relating to the choice of model used in MC or the value of parameters used in a model. To make matters worse, the detector medium of long baseline experiments are fairly large nuclei such as Oxygen and Carbon. This means that the dynamics of the nucleons (with which neutrinos interact) within the nucleus can impact interactions through a variety of nuclear effects. In addition, any particle produced in a neutrino interaction then has to propagate through the nuclear medium.

2.4.2 Nuclear Effects

For a description of neutrino interactions to be complete, the nucleus within which an interaction occurs must also be understood. There are a variety of nuclear models which describe the momentum distribution of the nucleons that make up the nucleus. These different models ultimately play an important role in the kinematics of the outgoing particles from neutrino interactions. Such nuclear models include more simple examples such as a Relativistic Fermi Gas, where the momenta of nuclei are described by a step function up to a momentum known as the Fermi momentum, to more sophisticated models such as a Spectral Function, where the nucleons are describes by nuclear shells. These nuclear effects can be very important to account for when simulating neutrino interactions. For a fuller description of nuclear effects and their implications for neutrino oscillation experiments see [59].

2.4.3 Final State Interactions

The interactions of particles as they propagate through the nuclear medium are commonly referred to as Final State Interactions (FSI). One of the main features of FSI is that it can result in the particles observed in the detector having unobserved parent particles or having scattered as they exit the nucleus. This means particles can have different momenta or a different charge to what they initially had or can result in a particle being absorbed and hence never detected. This results in an ambiguity in the observed particles seen in the detector and the type of interaction that created the particle. For example a CCRES interaction which creates a pion could appear in the detector without any observed pions if the pion is absorbed through FSI. Similarly, a CCQE interaction could be reconstructed with a pion if a pion is produced through FSI. The impact of the nucleus through nuclear dynamics and FSI is very important in the study of neutrino interactions.

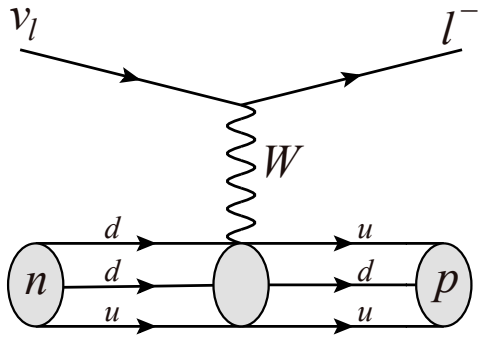

Figure 2.16: CCQE Feynman diagram.

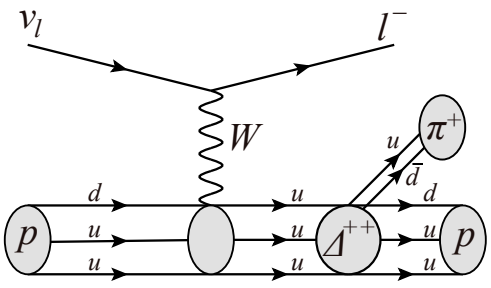

Figure 2.17: CCRES Feynman diagram.

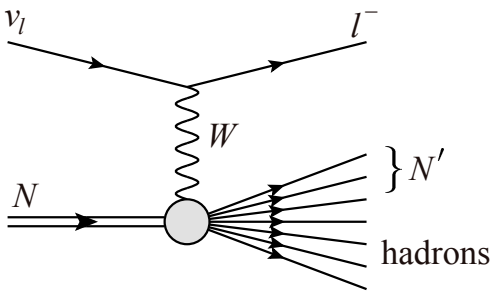

Figure 2.18: CC DIS Feynman diagram.

Chapter 3

The Tokai-to-Kamiokande experiment

The subject of this thesis is the study of neutrino oscillations at the Tokai-to-Kamiokande (T2K) experiment. The T2K experiment is a long baseline neutrino experiment based in Japan. Being a long-baseline neutrino experiment, T2K has three main parts; the beam facility, the near detectors and the far detector. The beam facility is where the neutrino beam is produced and aimed towards the near and far detectors. The near detectors are then used to measure properties of neutrino interactions and the neutrino beam before any neutrinos have oscillated. Then the far detector measures the neutrinos and neutrino beam after the neutrinos have travelled hundreds of kilometres and have had the chance to oscillate. Using the data collected in these detectors, analyses are then performed to measure the parameters of the PMNS parameterisation of neutrino oscillations. This chapter describes the detectors and basic design of the T2K experiment with emphasis placed on the parts which are most crucial to the neutrino oscillation analysis. First, how the neutrino beam is produced will be described, then the suite of near detectors and finally the far detector Super-Kamiokande.

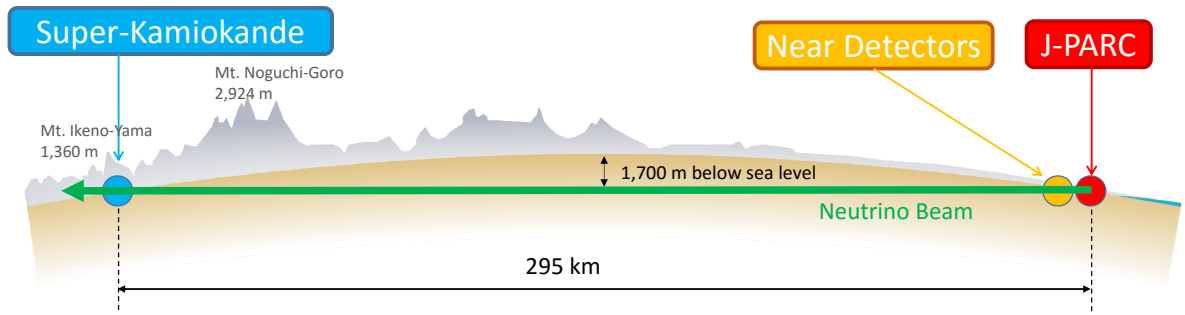

Figure 3.1: A schematic of the T2K experiment showing the J-PARC facility and Near Detectors on the east-coast of Japan as well as the far detector Super-Kamiokande on the west-coast of Japan.

3.1 Making the neutrino beam

The near detectors are situated on the east cost of Japan at the J-PARC facility. This facility also provides the neutrino beam that is used to measure neutrino oscillation parameters. The production and understanding of this neutrino beam is therefore, the core part of the whole T2K experiment. To make the neutrino beam, the J-PARC facility first accelerates protons to produce a high energy proton beam. These protons are subsequently passed into the T2K beamline where these protons are used to produce the neutrino beam by colliding the proton beam onto a target and then focusing the mesons which are produced using magnetic horns.

3.1.1 Making the proton beam

The J-PARC beamline consists of three main parts; the linear accelerator (LINAC), the rapid-cycling synchrotron (RCS) and then the main ring (MR). First, the LINAC is used to accelerate negative Hydrogen ions to $\sim$ 400 MeV [60]. These ions then pass through a carbon foil where their electrons are stripped, making them protons. The protons are accelerated further to 3 GeV in the RCS before being injected into the Main Ring (MR) where they finally reach kinetic energies of 30 GeV.

3.1.2 The T2K beamline

After the proton spills have been accelerated in the main ring they then are extracted into the T2K beamline. In each cycle eight proton bunches are extracted from the MR and the power of this beam is measured by a set of current transformers. The power of the extracted proton beam has increased over time and reached over 500 kW in the latest data taking period [61]. The T2K beamline is where the proton beam is pointed towards the near detectors and SK and then actually turned into a neutrino beam. This is done by colliding the proton beam onto a target and then focusing the mesons that are produced from this into a beam. These mesons then subsequently decay into neutrinos. An overview of the T2K beamline can be seen in fig. 3.2.

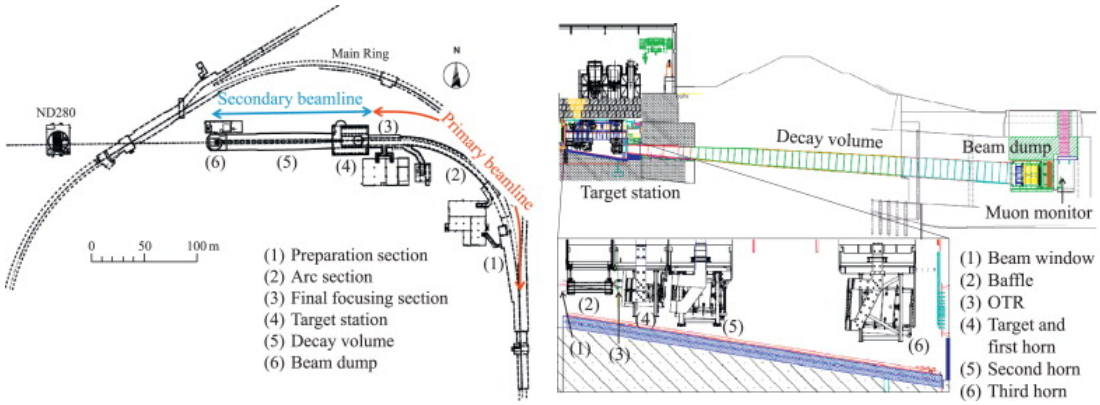

Figure 3.2: A diagram of the T2K beamline (also known as the secondary beamline) and its different components (left) and a cross section of the target station, decay volume and beam dump (right). Figures taken from [62]

.

π^+	K^+	K^0_L
$\hookrightarrow \mu^+ + \nu_\mu$ (99.99%)	$\hookrightarrow \mu^+ + \nu_\mu$(68.56%)	$\hookrightarrow \pi^- + e^+ + \nu_e$ (40.55%)
$\hookrightarrow e^+ + \nu_e$ (00.01%)	$\hookrightarrow \pi^0 + e^+ + \nu_e$ (5.07%)	$\hookrightarrow \pi^- + \mu^+ + \nu_\mu$ (27.04%)

Table 3.1: The decays of the primary mesons produced at the target which produce a neutrino beam in neutrino mode. The two most probable decays and their decay fraction are shown for each meson. The two-body decay of π^+s to a μ and ν_μ has the largest decay fraction and is responsible for most of the neutrinos produced.

Target

After the protons have entered the T2K beamline, they are then collided with a target. The target is 91.4 cm (1.9 interaction lengths) long and 2.6 cm wide and made of graphite. In the collision with the target, the protons in the beam interact with the nucleons in the target and produce a multitude of hadrons. Primarily, charged pions, $\pi^\pm$ are produced but K mesons ($K^\pm$, K^0 and $\bar{K}^0$) also make up a significant fraction of the mesons produced. It is these mesons which then go on to decay to produce the neutrino beam. The target is designed to deliberately be long and thin to decrease scattering of these mesons after they have been produced. The decay of the three mesons mentioned and their decay-fractions are shown in table 3.1. The decays of these mesons results in a neutrino beam which is predominantly composed of muon neutrinos.

3.1.3 Magnetic Horns

The neutrino beam is a result of the decay of mesons produced in collisions between the initial proton beam and the graphite target. However, several different species of meson will be produced and each of these with various momenta and directions. The T2K experiment aims to measure neutrino oscillations parameters by studying the oscillation of muon neutrinos and antineutrinos. Therefore, ideally the neutrino beam would be comprised of entirely muon neutrinos or antineutrinos. To try to achieve this, the T2K experiment uses three magnetic horns which focus and deflect mesons. This allows for a more intense neutrino beam to be made but also allows the momenta and charge of

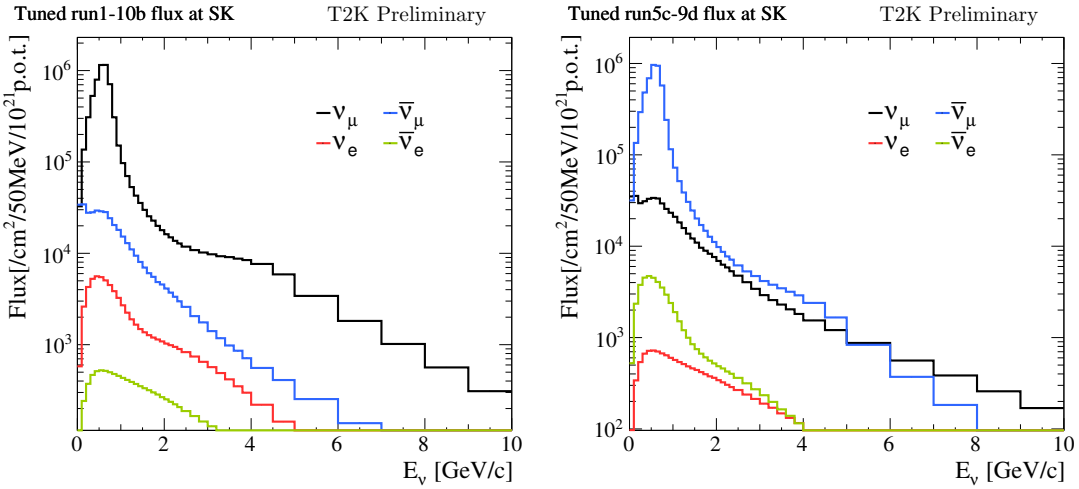

Figure 3.3: ν_μ flux prediction at SK (left) showing the parent mesons in neutrino mode. The majority of ν_μs come from pions. On the right the $\bar{\nu_\mu}$ flux in neutrino mode can be seen to be orders of around 100 times lower than the ν_μ flux showing that the use of magnetic horns has significantly reduced this wrong-sign background in neutrino mode.

the mesons, which go on to produce the neutrino beam, to be selected.. The horns are operated with a +250 kA current when operating in neutrino mode as this mainly selects π^+ mesons which then produce muon neutrinos. Similarly, the horns can be operated with a -250 kA current to run in antineutrino mode to select mainly π^- mesons. Neutrino mode is often referred to as Forward Horn Current (FHC) and antineutrino mode Reverse Horn Current (RHC). In both FHC and RHC there will be a "wrong-sign" component coming from antineutrinos in FHC and neutrinos in RHC mode due to the sign selection of the horns not being 100% efficient. After passing through the magnetic horns, the mesons then enter a ∼96 m long decay volume where they decay to produce the neutrino beam. The predicted neutrino beam at SK can be seen in fig. 3.3 where the different flavour components of the beam can be seen.

3.1.4 Beam Dump and Muon monitor

A beam dump made of 75 tons of graphite is located at the end of the decay volume. This prevents any remaining mesons from continuing downstream beyond this point. Only muons with an energy above ∼5 GeV (and neutrinos) can propagate through the beam dump. These muons are measured by the muon monitor to give information about

the neutrino beam for each proton bunch in a spill. There are two sets of muon monitors, one is a set of ionisation chambers and the other silicon photodiodes. The profile of the muons can be reconstructed in 2D and is used to constrain the neutrino flux direction and intensity.

3.1.5 Off-Axis Technique

The T2K experiment uses an off-axis neutrino beam, meaning that most of the near detectors and the SK detector are 2.5° away from the axis of the beam. To demonstrate why the experiment is setup this way, the dependence of neutrino energy on the off-axis angle can be demonstrated by looking at the kinematics of two-body decays. The neutrino beam is produced by the decay of mesons, primarily through the two-body decay of a pion to a muon neutrino and a muon. Using the approach in [63] the neutrino energy from this two-body decay can be calculated using:

$$E_\nu = \frac{m_\pi^2 - m_\mu^2}{2(E_\pi - p_\pi \cos\theta_{\nu\pi})}, \tag{3.1}$$

where m_π and m_μ are the pion and muon masses respectively, E_ν is the neutrino energy, E_π is the pion energy, p_π is the pion momentum and $\theta_{\nu\pi}$ is the angle relative to the pion direction which the neutrino is produced at. From eq. (3.1) it can be seen that the neutrino energy is dependent on $\theta_{\nu\pi}$ meaning off-axis angle can be used to change the energy distribution of a neutrino beam. The effect of changing $\theta_{\nu\pi}$ is shown in fig. 3.4.

The advantage of having the detectors off-axis is that it results in a neutrino flux which is peaked at ∼0.6 GeV, the energy at which muon-neutrino disappearance is maximal for the T2K baseline. The sharper flux shape also helps to reduce backgrounds from mis-reconstructed events at higher neutrino energies. The flux shape for different off-axis angles and oscillation probabilities are shown in fig. 3.5.

Beamline monitors

To understand the neutrino beam well, a series of detectors are situated in the T2K beamline to monitor the proton beam and resultant neutrino beam. These monitors give valuable information in the simulation of the neutrino beam and its associated uncertainties.

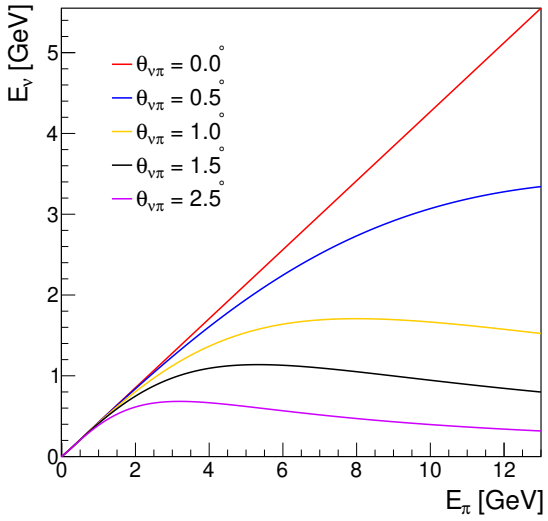

Figure 3.4: Neutrinos which are produced at a larger angle relative to the pion direction, $\theta_{\nu\pi}$, have lower energies compared to those produced in the direction of the pion. The result of this effect is a lowering and sharpening of the neutrino beam energy.

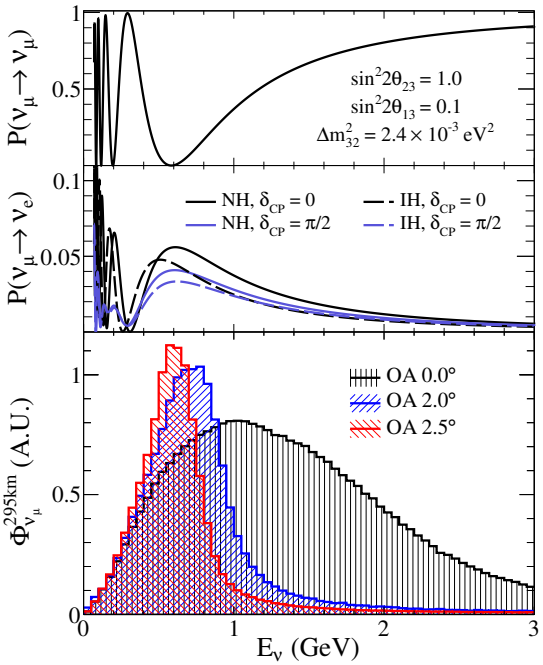

Figure 3.5: Placing the detectors at an off-axis (OA) angle of 2.5° sharpens the neutrino flux at SK, $\Phi^{295km}_{\nu_\mu}$ at $\sim$ 0.6 GeV which coincides with the lowest probability of muon-neutrino survival as shown in the top panel [64].

A diagram showing the positions of the various monitors in the T2K beamline is shown in fig. 3.6. These monitors measure the proton beam intensity, position and energy loss [62]. The beam intensity is measured through Current Transformers (CTs). The beam position is measured using ElectroStatic Monitors (ESMs) which measure the induced current on electrodes to then calculate the beam position. The beam profile is measured in two main ways; firstly with Segmented Secondary Emission Monitors (SSEMs) which consist of thin titanium strips placed horizontally and vertically, the protons in the beam collide with these strips to produce secondary electrons. These secondary electrons are then used to measure the beam profile. The other way to measure the beam profile is using the Optical Transition Radiation (OTR) monitor. The OTR measures optical transition radiation from the proton beam passing through a thin titanium foil which is placed perpendicular to the beam. The light produced when the beam interacts with the foil is imaged by a camera. Finally, the neutrino beam itself is monitored using a muon monitor which is situated behind the beam dump (see fig. 3.2). The muon monitor measures the muons produced in the decays of the mesons which also produce the neutrinos for the beam. All of the information from these monitors is used in the simulation of the neutrino beam which is then used for physics analyses. The uncertainties associated with the neutrino beam are described in chapter 4. More detailed descriptions of these monitors can be found in [62].

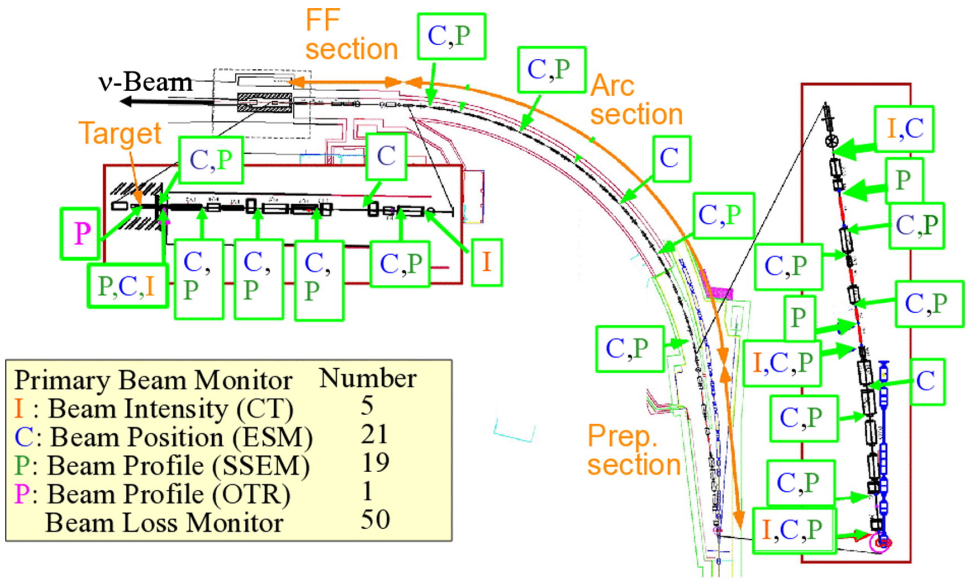

Figure 3.6: A diagram of the T2K secondary beamline showing the positions of the various monitors used to measure the proton beam.

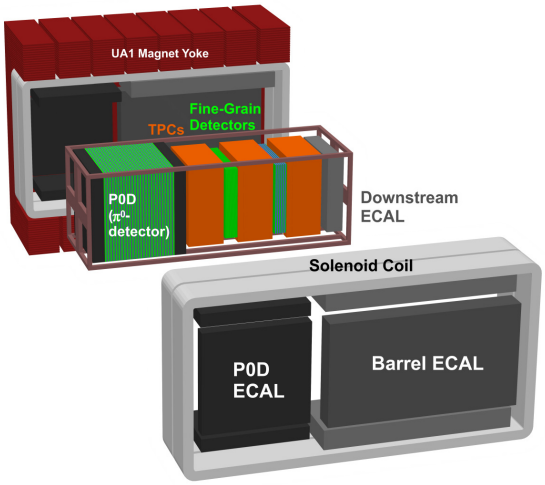

Figure 3.7: Exploded view of the ND280 detector showing the sub-detectors. The beam direction goes from the left to the right of the image. Figure from [60].

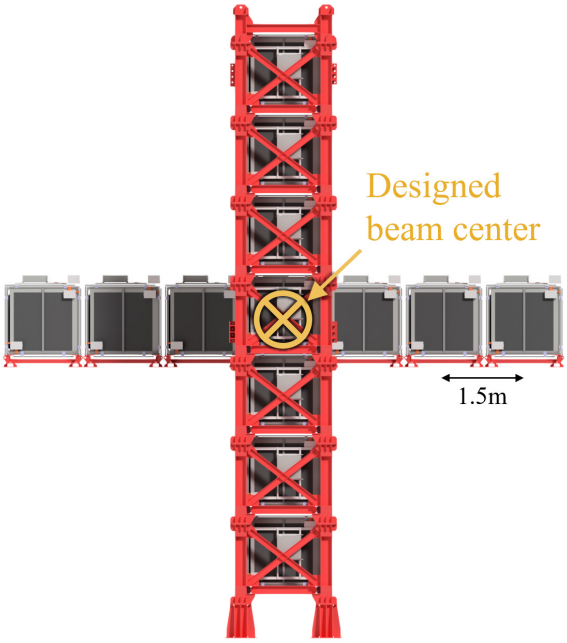

Figure 3.8: INGRID detector where the cross shape can clearly be seen. The beam centre is in the middle of the cross shape. Figure taken from [65].

3.2 The Near Detector suite

The J-PARC facility also hosts a suite of near detectors. These near detectors measure neutrino interactions at a short baseline (i.e. before oscillations). By measuring these interactions before oscillations, constraints on neutrino beam and neutrino interaction models can be made. When measuring the oscillated neutrinos at SK, the uncertainty on oscillation parameters is significantly reduced because of these constraints from the near detectors. The near detectors are also used for neutrino cross-section measurements which are a very active part of the T2K experiment but are not discussed here.

3.2.1 Interactive Neutrino Grid

To accurately measure oscillation parameters at the far detector the systematic uncertainty on the neutrino flux from the beam must be at the $\sim 3\%$ level [66]. The Interactive Neutrino GRID (INGRID) precisely measures the neutrino beam profile and has mea-

sured the neutrino beam directionality to within 0.25 mrad [66]. INGRID is situated below ND280 at the same distance from the target as ND280 but is on the beam axis. INGRID is made up of 14 identical modules in a cross shaped geometry which can be seen in fig. 3.8.

Each of the modules are made up of alternating layers of plastic scintillator and iron which allow the rate of neutrino interactions in each module to be determined. This then allows the neutrino beam position to be monitored extremely precisely. All modules are surrounded by veto planes to reject cosmic rays which may enter a module. A diagram of an INGRID module and an example neutrino event in a module are shown in fig. 3.9.

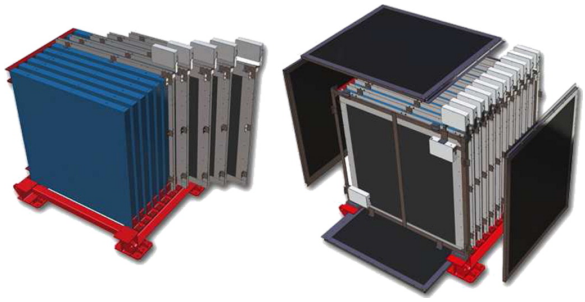

Figure 3.9: A diagram of one of the 14 modules that make up the INGRID detector. On the left the layers of scintillator (blue) and iron planes can be seen and on the right the fully assembled module surrounded by veto planes (black) can be seen. Figure taken from [62].

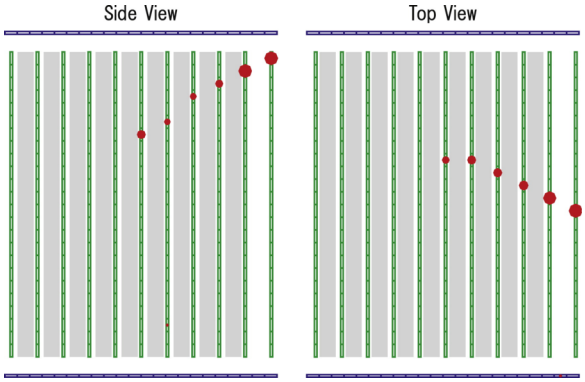

Figure 3.10: An example of a neutrino interaction in an INGRID module. The neutrino enters from the left and interacts in the detector. The red circles indicate the position of the reconstructed hit and the size of the circle the size of the reconstructed signal. The green layers are scintillator, grey iron layers and the blue the veto planes surrounding the module. Figure taken from [62].

3.2.2 The Near Detector at 280m

The Near Detector at 280 m (ND280) is designed to accurately reconstruct neutrino interactions to constrain neutrino beam and neutrino interaction uncertainties. Since the detector is placed 280 m downstream of the target, it has a significantly higher number of neutrinos traversing it compared to SK. The high number of neutrino events in the detector and accurate reconstruction means ND280 has been able to constrain neutrino beam and neutrino interaction uncertainties to the $\sim 3\%$ level [67]. The data taken at ND280 is used in combination with the data at SK to improve T2K's ability to measure neutrino oscillation parameters. The data and MC simulation used at ND280 for the oscillation analysis are described in chapter 4. ND280 is a modular detector composed of several sub-detectors, the core parts of ND280 which are most relevant to the oscillation analysis are described below. A diagram of the ND280 detector and its various sub-detectors can be seen fig. 3.7. A description of the reconstruction and selection of events for the oscillation analysis will be given in chapter 4.

Fine Grain Detectors (FGDs)

Two FGDs are the central targets of ND280, with FGD1 being upstream of FGD2. Each FGD has a mass of 1.1 tonnes and is made of 15 XY planes of plastic (CH) scintillator, each plane is made of 192 scintillator bars with a reflective coating and extruded with a wavelength-shifting (WLS) fiber. The orthogonal planes allow for the directionality of a reconstructed particle to be determined. FGD2 also uses water as a target by replacing 7 of the scintillator planes with water which allows ND280 to constrain interactions on water (the target at SK). When a particle passes through the scintillator planes, energy is deposited causing the scintillator to emit light. This light then travels along a bar where a multi-pixel photon counter (MPPC) collects the light. The number of photons detected by the MPPC is proportional to the energy deposited by the particle.

Time Projection Chambers (TPCs)

The TPCs provide excellent 3D imaging of neutrino interactions and is combined with the magnetic field of the UA1 magnet to measure the momenta of particles. The momentum in conjunction with the energy deposited through ionisation in the detector allows for very good particle identification (PID). The TPCs use an Argon based gas mixture which ionises when charged particles pass through it. The electrons that are freed in the ionisation then drift through an electric field which is created by a cathode plane in the TPC. The electrons drift away from the cathode plane until they are amplified and sampled by bulk micromegas [67]. There are three TPCs in total, one upstream of FGD1, one downstream of FGD2 and one sandwiched by FGD1 and FGD2.

Pi-zero Detector (PØD)

The PØD is the most upstream sub-detector of ND280. One of the largest backgrounds when looking for electron-neutrino appearance at SK comes from NC events. The PØD was designed to to help constrain NC backgrounds, specifically those producing a π^0 which is a background to electron-neutrino appearance at SK. The PØD is constructed with alternating XY planes of scintillator bars interspersed with brass and water layers which act as the neutrino target. Each scintillator bar is read out with a single WLS fiber.

Electromagnetic Calorimeters (ECals)

The basket containing the FGDs, TPCs and PØD is surrounded by three ECals. The ECals provide near 4π coverage of the inner sub-detectors and use layers of plastic scintillators to reconstruct particles. These are interspersed with layers of lead absorbers to increase the number of interaction lengths of electromagnetic showers in the ECal. The ECals are complimentary to the sub-detectors in that they aim to reconstruct electromagnetic showers coming from interactions in any of the contained components. In particular, the downstream and Barrel Ecals are designed for tagging and reconstructing π^0s.

UA1 magnet

The ND280 detector is built within the reused UA1 magnet which provides a dipole magnetic field with a strength of 0.2 T. The magnetic field allows for precise momentum determination of particles as well as PID. In addition, the magnetic field allows for the sign of the particle's charge to be determined.

3.3 The Super-Kamiokande Detector

The far detector of the T2K experiment is the SK detector. SK is situated 295 km away from the beam target at J-PARC, on the west-coast of Japan. SK uses 50 kilotonnes of water as an active target. When charged particles above a certain momentum (known as the Cherenkov threshold) pass through this water they produce Cherenkov light which is how SK detects particles. To measure the Cherenkov light, the detector is instrumented with photo-multiplier tubes (PMTs). When a charged particle passes through the SK detector Cherenkov radiation is produced in a ring pattern which is reconstructed using the light collected by the PMTs and the position of the PMTs themselves. Electrons scatter more frequently than muons so Cherenkov rings from electrons are more blurred compared to rings from muons; examples of a muon-like ring and an electron-like ring can be seen in fig. 3.12. Tau leptons are not observed in SK as the energies of the neutrino beam is below the tau production threshold. The difference in muon-like and electron-like ring characteristics means that SK has excellent PID capabilities.

The SK detector is split into an inner and outer volume. The outer volume is imaged by 1885 outward-facing 20 cm diameter Hamamatsu PMTs and is referred to as the outer detector (OD) while the inner volume is referred to as the inner detector (ID). The OD and ID are separated by a steel structure which is lined with opaque white sheeting and absorbent black sheeting to optically isolate the ID from the OD and *vice versa*. The OD is used to veto cosmic rays and other backgrounds which is done to near 100% efficiency.

The ID is instrumented with $11,146$ 50 cm diameter Hamamatsu PMTs which gives approximately 40% PMT coverage of the ID walls. Events in the ID are collected for

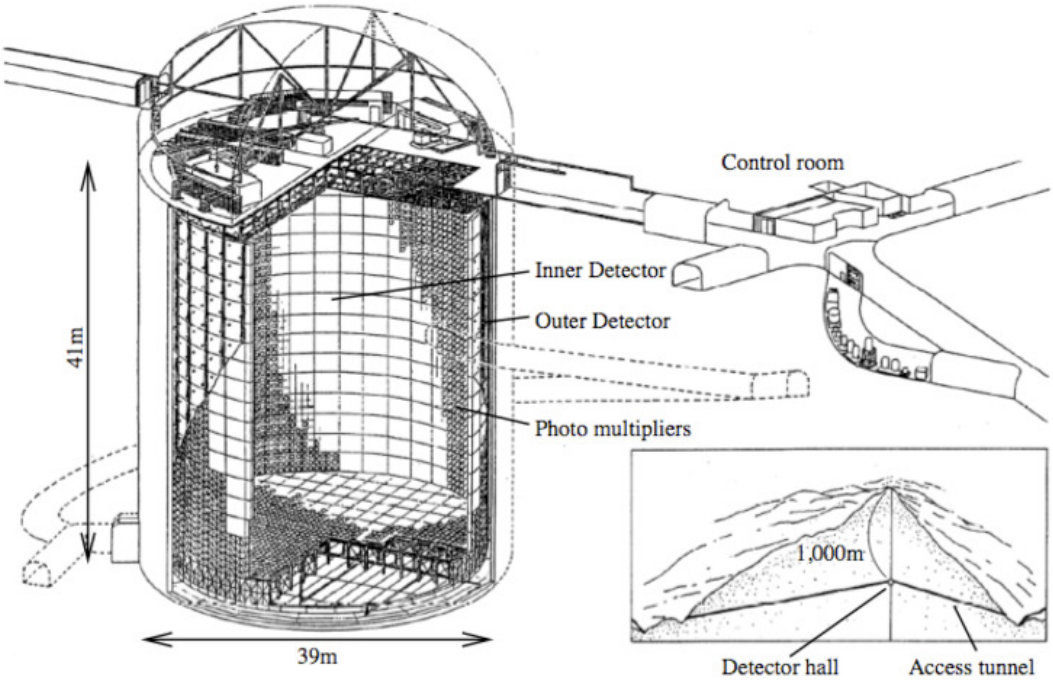

Figure 3.11: The SK detector with the Inner and Outer detectors clearly visible. The detector has an overburden of $\sim$ 1000 m and is accessed by a tunnel. Figure from [68].

use in analyses such as neutrino oscillation analyses. A detailed description of the SK detector is given in [68].

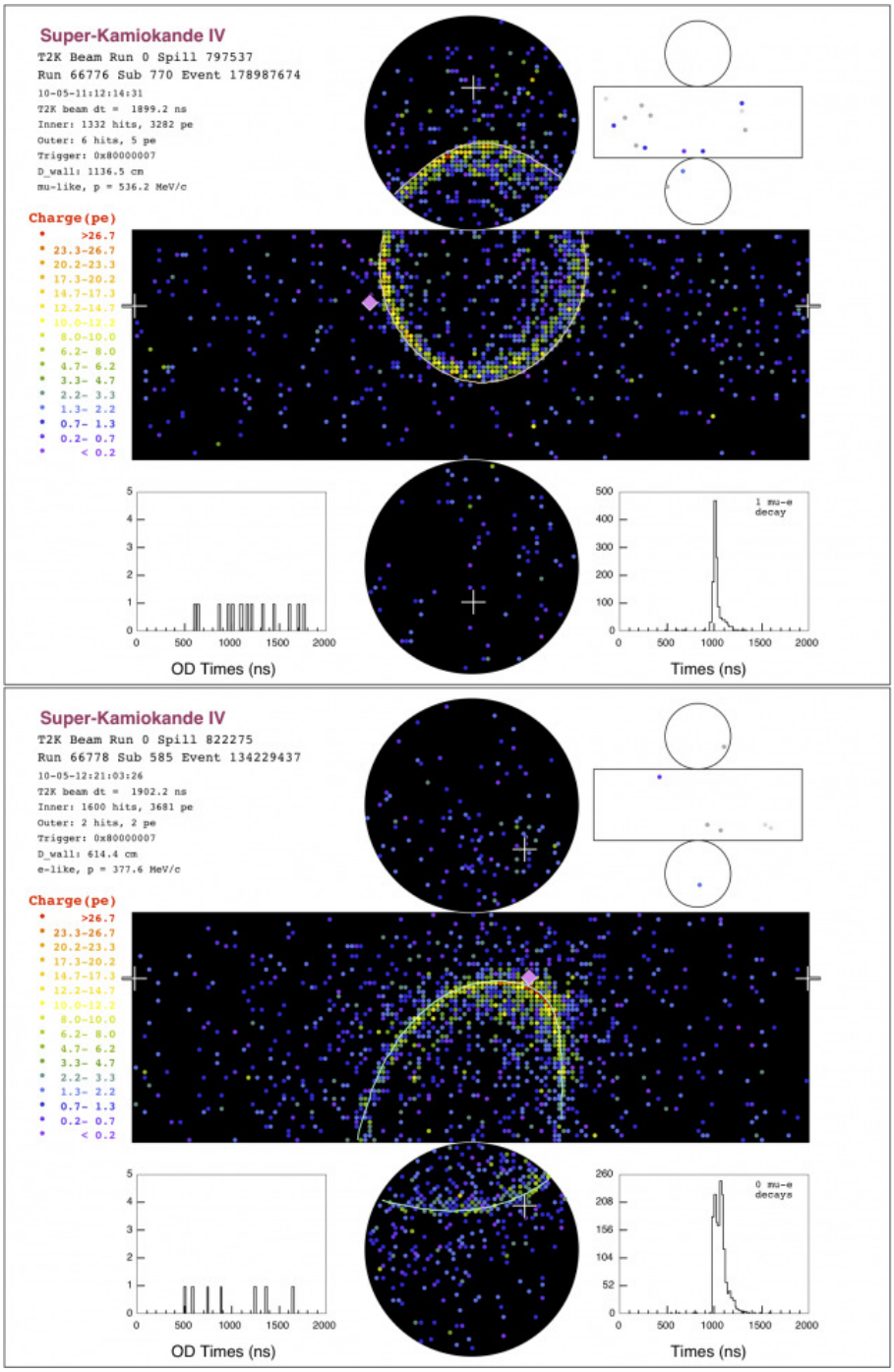

Figure 3.12: Two example event displays of the SK detector. Left is a muon-like ring and on the right is an example of an electron-like ring. The colour represents the arrival time of light at a PMT with violet corresponding to earlier times and red to later times. The size of the squares represents the number of photo-electrons detected [64].

Chapter 4

Analysis Technique

To understand how the measurements on oscillation parameters are made, this chapter describes the analysis techniques and how the various parts of the T2K experiment are used in the analysis. The oscillation analysis results presented in chapter 7 give the most recent oscillation parameter measurements from the T2K experiment. Chapter 8 will then build upon these results and show a preliminary analysis using additional data samples at SK, which should improve the constraint on oscillation parameters further. The description here will be heavily referenced later in chapter 7 and chapter 8.

4.1 Neutrino oscillation analysis

The results in chapter 7 and chapter 8 build on previous oscillation analysis results from the T2K experiment (such as [69] and [67]). The analysis techniques used for this analysis are very similar to that used for previous results. However, there have been significant improvements made to the analysis which will be highlighted. In particular, these improvements correspond to the use of larger data samples and the improved treatment of systematic (or nuisance) parameters rather than significant changes to analysis technique itself.

At its heart, the T2K oscillation analysis compares the number of predicted events for a set of parameters and compares this to the data collected at ND280 and SK. The

number of neutrino events predicted at SK and ND280 is dependent on the simulation of the neutrino flux, neutrino interaction model and detectors as well as the oscillation probability at SK. The number of events predicted at SK, $N^{\mathrm{SK}}_{\mathrm{pred}}$, is a function of neutrino energy, E_ν, and particle kinematics, $\overrightarrow{x}$, and is given by

$$N^{\mathrm{SK}}_{\mathrm{pred}}(E_{\nu,\beta}, \overrightarrow{x}) = \int dE_{\nu,\alpha}\Phi(E_{\nu,\alpha}) \times \sigma(E_{\nu,\beta}, \overrightarrow{x}) \times \epsilon(E_{\nu,\beta}, \overrightarrow{x})_{\mathrm{SK}} \times P(\nu_\alpha \rightarrow \nu_\beta), \quad (4.1)$$

and similarly the number of predicted events at ND280, $N^{\mathrm{ND280}}_{\mathrm{pred}}$, is given by

$$N^{\mathrm{ND280}}_{\mathrm{pred}}(E_{\nu,\alpha}, \overrightarrow{x}) = \int dE_{\nu,\alpha}\Phi(E_{\nu,\alpha}) \times \sigma(E_{\nu,\alpha}, \overrightarrow{x}) \times \epsilon(E_{\nu,\alpha}, \overrightarrow{x})_{\mathrm{ND280}}, \quad (4.2)$$

where α is the flavour the neutrino was produced as, β is the flavour of the at SK, Φ is the neutrino flux (how many neutrinos there are), σ is the neutrino cross section on the target mass (the probability of a neutrino interacting in the detector), ϵ_{SK} is the detector efficiency and acceptance for SK (whether an event is actually detected), $\epsilon_{\mathrm{ND280}}$ is the detector efficiency and acceptance for ND280 and $P(\nu_\alpha \rightarrow \nu_\beta)$ is the oscillation probability of a neutrino of flavour α oscillating to flavour β. The parameters which alter the predictions for the neutrino flux, neutrino interaction probability and response of the detector are referred to as nuisance parameters as they are not the parameters the analysis wishes to measure. However,to be able to measure neutrino oscillation parameters precisely an excellent understanding of these nuisance parameters is required. Therefore, a lot of time and effort is taken in ensuring that these nuisance parameters are treated with the appropriate uncertainties.

From this description, the T2K oscillation analysis can be seen to be dependent on three key aspects: the data samples used in the analysis, the nuisance parameters used and then the predictions made for a given set of nuisance and oscillation parameters. The reconstruction and data samples used at ND280 and SK are described in section 4.1.2 and section 4.1.4 respectively. How these data samples are compared to the predictions at ND280 and SK is then given in section 4.1.5. The treatment of nuisance parameters and how uncertainties are assigned to the different nuisance parameters associated with the neutrino flux, neutrino interaction model and detector effects is then covered in section 4.2. Finally, how the data, nuisance parameters and predictions are all used together in a likelihood function is then given in section 4.3.

4.1.1 Event reconstruction at ND280

As has been mentioned in chapter 3, the data at the near detector is designed to measure and constrain properties of the neutrino beam before oscillation have occured. Before describing the data that is used to make these constraints in the analysis, it is useful the key parts of the reconstruction at ND280. The simulation of the ND280 detector uses the NEUT event generator is used to simulate neutrino events which are then passed through a geomeytry of the detector in GEANT 4. Hits in different sub-detectors are then reconstructed to form tracks or showers within each sub-detector. The momentum of these tracks or showers is then calculated for different particle hypotheses. For the oscillation analyses, only ν_μ and $\bar{\nu}_\mu$ interactions which originate in FGD1 or FGD2 are included. This means that reconstruction, most of the time, will have found tracks crossing one or more of the TPCs. The TPCs allows excellent PID and momentum measurement of the particles.

Since all samples at ND280 target CC ν_μ or $\bar{\nu}_\mu$ interactions, the identification of muons is critical. Initally, the highest momentum track that starts in an FGD and crosses one of the TPCs is assumed to be a muon candidate. The sign of the muon can be determined from the magnetic field and depends on the beam is being operated in FHC or RHC mode. The differential energy loss (dE/dx) of these tracks in the TPC is compared to the expected value for different particle types. This allows muon candidates to be compared to electrons and protons and hence be rejected if found to be in good agreement with these hypotheses. Examples of the expected dE/dx curves for different particle types can be found in fig. 4.2. The momentum resolution on muons in ND280 is excellent and can be seen as a function of true muon momentum in fig. 4.1.

The number of charged pions is also an important variable used in the selection definitions for the oscillation analysis. Any additional tracks to the muon candidate are considered as pion candidates. Each track is then required to be contained in the fiducial volume of the same FGD as the muon candidate. This track can then be identified as a pion in different ways. If the track has left hits in the TPC then the dE/dx of the track is compared to different particle hypotheses. If the track has not left any hits in the TPC then hits in the FGD can be used to check whether the track is a pion. These hits

in the FGD can be used to compare the total deposited energy against track length for different particle hypotheses. In either the TPC-tagged or FGD-tagged case, the track must be in good agreement with the pion hypothesis to be accepted as a pion candidate. An additional method to tag pions is to look for delayed hits outside of the beam window can be used to search for Michel electrons from a pion. Finally, any remaining tracks in an event are reconstructed as their most probable hypothesis according to dE/dx deposited in the TPCs.

On top of the PID of the particles being used to select events, general selection cuts are applied to the events at ND280.

- **Data Quality** - all events considered for the analysis must be found to have to be within the window that a neutrino beam spill occurred at. This aims to reduce any interactions in the detector which do not originate from the neutrino beam.
- **Total multiplicity** - at least one track has to be reconstructed for an event to be considered for any of the data samples. All the samples in the oscillation analysis are CC interactions so an outgoing lepton is always expected in a signal event.
- **Fiducial Volume** - as mentioned, all events at ND280 must occur in either FGD1 or FGD2 to be used in the oscillation analysis. To reduce interactions occurring outside of the FGDs being included in the analysis a fiducial volume cut is defined. The fiducial volume of the FGDs requires the reconstructed vertex to be more than five bars away from the edge of each XY module, and the most upstream XY module of each FGD as well. At least one reconstructed track must be found to have originated within the fiducial volume of an FGD. This track must also has a segment of the track reconstructed in a TPC with a minimum of 18 clusters of hits being reconstructed. Finally, interactions in FGD1 where a second track has a reconstructed vertex originating in FGD2 are rejected.
- **Upstream and broken tracks** - if multiple tracks are found and the second highest momentum track starts more than 150 mm upstream of the highest momentum track the event is rejected. This is to prevent events where the primary track comes from the second part of a track starting upstream. Generally, broken tracks are rejected by requiring a tracks reconstructed vertex to be less than 425 mm away

from the upstream edge of the FGD. This prevents tracks starting downstream of another track in the FGD and then passing into the TPC being identified as a muon candidate. The reconstructed vertex would be therefore be misplaced due to the track being broken.

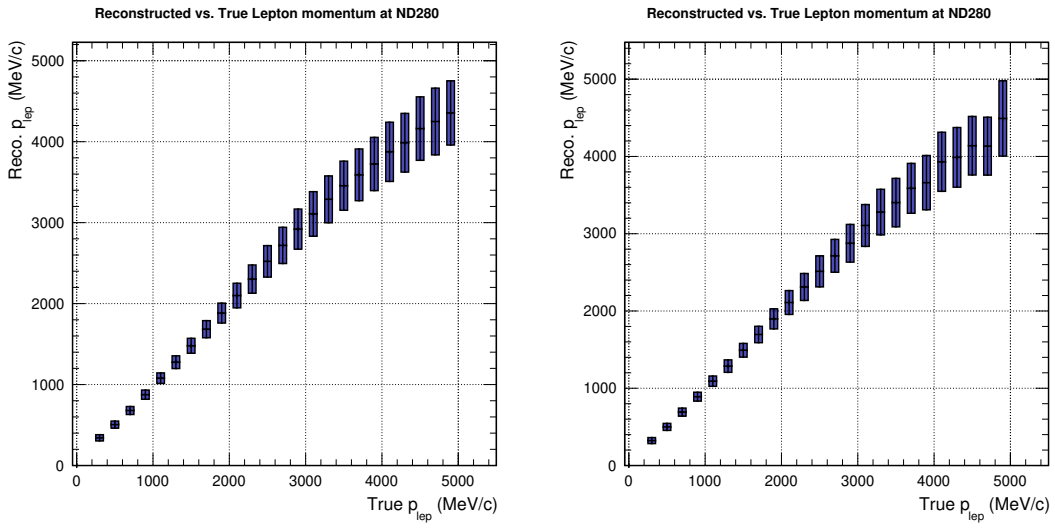

(a) FGD1 CC0π sample.

(b) FGD1 CC1π sample.

Figure 4.1: The mean reconstructed lepton momentum against true lepton momentum for events recosntructed as CC0π (left) and CC1π (right) events in FGD1. The error bars are the mean of a gaussian fitted to the reconstructed momentum distribution for each true momentum bin. In both samples, the momentum resolution for muons with true momentum less than 2 GeV is typically below 100 MeV with this steadily increasing with higher true momentum.

4.1.2 ND280 data

The use of the ND280 detector is vital in reducing the error on nuisance parameters in the T2K neutrino oscillation analysis. The number of predicted events at ND280 is not dependent on neutrino oscillation probability for this analysis. This enables nuisance parameters to be measured without the added complexity of oscillations being involved. Further to this, ND280 has significantly higher data statistics compared to SK (due to the ND280 detector being situated close to the neutrino beam source). This means the data taken at ND280 can constrain nuisance parameters associated with the neutrino beam

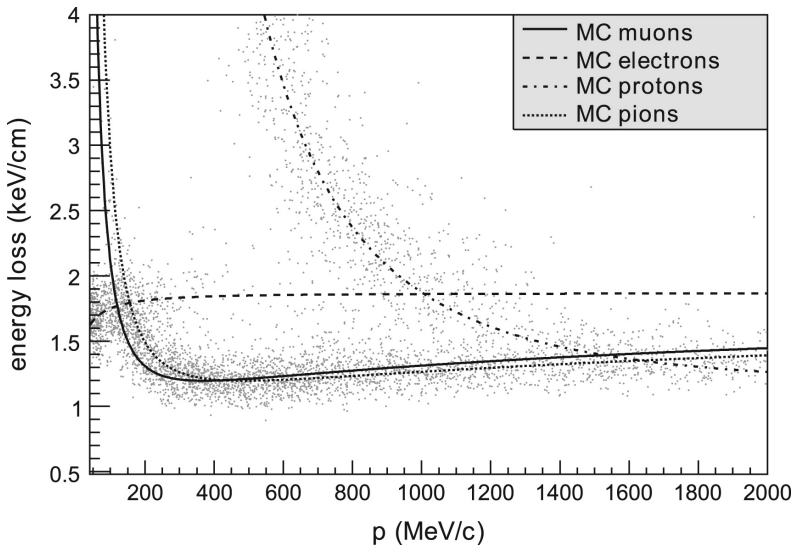

Figure 4.2: The energy loss against momentum for different particle types. The lines indicate MC expectations for different positively charged particle types and the points data points taken from the first T2K physics run. Figure taken from [62].

and neutrino interactions much more precisely than the data taken at SK could alone. In turn, this then means that the constraint on oscillation parameters is more precise.

The data collected at ND280 is categorised based on the reconstructed topology of an event and whether the data was taken whilst the beam was operating in FHC or RHC mode. There are nine selections in total at ND280 used in the oscillation analysis; three in FHC mode and six in RHC mode, all of which have a muon reconstructed as the lepton in a CC interaction. A description of how different topologies and particle types are reconstructed has already been given in section 4.1.1, so just a description of which topologies are targeted is given here. These nine topologies are:

- **FHC** ν_μ **CC**0π - one track is reconstructed as a μ^- with no other $e^\pm$, $\pi^\pm$ or π^0 candidate tracks in FHC mode
- **RHC** ν_μ **CC**0π - one track is reconstructed as a μ^- with no other $e^\pm$, $\pi^\pm$ or π^0 candidate tracks in RHC mode
- **RHC** $\bar{\nu}_\mu$ **CC**0π - one track is reconstructed as a μ^+ with no other $e^\pm$, $\pi^\pm$ or π^0 candidate tracks in RHC mode
- **FHC** ν_μ **CC**$1\pi^+$ - one track is reconstructed as a μ^- with one additional recon-

structed π^+ and no other $e^\pm$ or π^0. The π^+ can be tagged from a TPC track, from tagging a Michel electron or from tagging using FGD hit information.

- **RHC ν_μ CC1π^+** - one track is reconstructed as a μ^- and a π^+ and no other $e^\pm$ or π^0. The π^+ is identified in a similar way to the FHC ν_μ CC1π^+ selection.

- **RHC $\bar{\nu}_\mu$ CC1π^-** - one track is reconstructed as a μ^+ and a π^- is identified in a similar way to the FHC ν_μ CC1π^+ and RHC ν_μ CC1π^+. Again it is required there are is no $e^\pm$ or π^0 reconstructed as well.

- **FHC ν_μ CC-Other** - one track is reconstructed as a μ^- and do not fall into the FHC ν_μCC0π or FHC ν_μCC1π^+ selections. This sample therefore contains events with one or more π^- or with multiple π^+ identified or $e^\pm$ tracks most likely coming from a π^0.

- **RHC ν_μ CC-Other** - one track is reconstructed as a μ^- and do not fall into the RHC ν_μCC0π^+ or RHC ν_μCC1π^+ selections. Again, this can be due to the presence of a π^-, multiple π^+s or from a π^0.

- **RHC $\bar{\nu}_\mu$ CC-Other** - one track is reconstructed as a μ^+ and do not fall into the RHC $\bar{\nu}_\mu$CC0π^- or RHC $\bar{\nu}_\mu$CC1π^- selections. This can be due to the presence of a π^+, multiple π^-s or a π^0.

The event selection is only applied to events that have a reconstructed vertex in FGD1 and FGD2. The reason for there being six samples in RHC compared to three in FHC is due to the larger wrong-sign background present in RHC than FHC. This combined with the fact that the neutrino interaction cross section is larger than the anti-neutrino cross section means that the RHC samples with the wrong-sign muon have significantly more events than their FHC counterparts would. So these wrong-sign samples help to constrain the wrong-sign components of the RHC neutrino flux prediction. In the oscillation analysis these selections are binned in muon momentum and cosine of the angle between the outgoing muon and the incident neutrino direction. The binning used for each selection at ND280 is given in appendix B.1.

4.1.3 Event reconstruction at SK

The data at SK is the key to measuring neutrino oscillation parameters. The reconstruction of this data is extremely important to extract the oscillation parameters reliably. At SK, the FitQun algorithm is used to reconstruct the Cherenkov rings produced by interactions occuring in SK. FitQun uses a maximum likelihood based method to reconstruct the vertex, the number, type and momenta of particles produced from interactions in SK [70]. This is done by looking at the likelihood of the PMTs which did and did not register a hit for different topological hypotheses along with its associated kinematic variables. The results from the event reconstruction by FitQun give many variables which can be used to select events which can then use in physics analyses. Throughout this thesis, these reconstructed variables will be used frequently so it is useful to describe and define these. The list below describes some of the most useful variables for selecting events (both MC and data) for use in the oscillation analysis:

- **Fully Contained (FC)** - a fully contained event is defined as an event which has no activity in the OD. This is defined as being fewer than 16 reconstructed hits in OD PMTs.
- **Decay electrons** - decay (or Michel) electrons can be tagged in SK by looking for hits in PMTs that are delayed by 2μs (the lifetime of a muon). This is one of the most important variables for selecting data to use in the oscillation analysis.
- **Fiducial Volume** - fiducial volume cuts are made using two variables which measure an interactions distance from the ID wall. The first is the distance of the reconstructed vertex and the nearest ID wall, this will be referred to as "DWall" from now on. The second is the distance from the reconstructed vertex in the direction of the reconstructed track, this variable is referred to as "ToWall" from now on. These variables are used to define the fiducial volumes for different selections.
- **Visible Energy** - visible energy from an electro-magnetic shower to produce Cherenkov radiation. Therefore, this is proportional to the amount of light seen in the detector and can be used to reject events which are reconstructed poorly due to low amounts of Cherenkov radiation being produced.

- **Energy loss** - pions can hadronically scatter off nuclei. This causes the particles to scatter in the detector and can cause multiple Cherenkov rings. The energy loss is the amount of reconstructed energy lost between the reconstructed vertex and the point where the pion scatters to produce other Cherenkov rings.

The variables described above will be used in chapter 4 when describing the data used in the oscillation analysis as well as when describing the ν_μCC1π sample (a new data sample) in chapter 8.

In the neutrino oscillation analysis described in this chapter the reconstructed neutrino energy is used to bin each selected sample. It is through this variable that the analysis is sensitive to neutrino oscillation parameters since oscillation depend on the neutrino energy. How the reconstructed neutrino energy is calculated depends slightly on which sample an event was selected into. The data at SK will be described in section 4.1.4 but broadly these are categorised into events with no reconstructed pion and those with. For events with no reconstructed pion, the neutrino energy can be calculated assuming a CCQE interaction (i.e. two-body) and with the nucleon at rest [11]. This gives the following relationship between reconstructed neutrino energy, the reconstructed lepton momentum and the angle between the neutrino direction and the lepton:

$$E_{reco} = \frac{m_p^2 - m_n^2 - m_l^2 + 2m_n E_l}{2\left(m_n - E_l + p_l \cos\theta_{\nu l}\right)}, \tag{4.3}$$

where E_{reco} is reconstructed neutrino energy, m_p and m_n are the proton and neutron masses respectively, E_l is the lepton energy, p_l is the reconstructed lepton momentum and $\theta_{\nu l}$ is the reconstructed angle between the outgoing lepton and the neutrino direction. The residual of the reconstrcuted and true neutrino energy as a fraction of true neutrino energy for the FHC 1Rμ sample can be seen in fig. 4.3a.

Similarly, for events in SK where a charged pion is reconstructed, a CCRES interaction is assumed where the pion produced comes from a Δ^{++} resonance. Again, assuming the initial nucleon is at rest, the neutrino energy can be reconstructed using:

$$E_{reco} = \frac{m_{\Delta^{++}}^2 - m_p^2 - m_l^2 + 2m_p E_l}{2\left(m_p - E_l + p_l \cos\theta_{\nu l}\right)}, \tag{4.4}$$

where again E_{reco} is the reconstructed neutrino energy, $m_{\Delta^{++}}$, m_l and m_p are the masses of the Δ++ resonance, outgoing lepton and proton respectively, E_l is the lepton energy, p_l is

the reconstructed lepton momentum and $\theta_{\nu l}$ is the reconstructed angle between the lepton and the neutrino beam. The residual or the reconstructed and true neutrino energy as a fraction of true neutrino energy for the FHC 1ReCC1π can be seen in fig. 4.3b. It is worth mentioning that the reason why kinematic information from outgoing nucleons is not used is that these are mostly invisible in the SK detector. At the time of writing neutrons cannot be easily tagged in SK so these go unseen. Then for protons, the Cherenkov threshold is ~ 1 GeV meaning that only very energetic protons could be reconstructed in SK but the number of these events at T2K energies is very few.o

It should be noted that in eq. (4.3) and eq. (4.4) no nuclear effects altering the outgoing leptons momentum has been included. As was mentioned in section 2.4, nuclear effects can play an important role in measureing neutrino oscillation parameters. This is because nuclear effects directly impact the reconstructed neutrino energy calculations as given above. For example, when a nucleon is ejected in a nucleon interaction the binding energy of the nucleon in the nucleus should be taken into account. Binding energy is on the order of a few MeV so would shift the outgoing lepton momentum by this amount and would bias the reconstructed neutrino energy calculation if not taken into account. In the analysis, these modifications to reconstructed neutrino energy are taken into account either directly through modifying eq. (4.3) and eq. (4.4) or by modifying the lepton momentum or angle. The uncertainties related to neutrino interactions used in the analysis will be discussed in section 4.2.2.

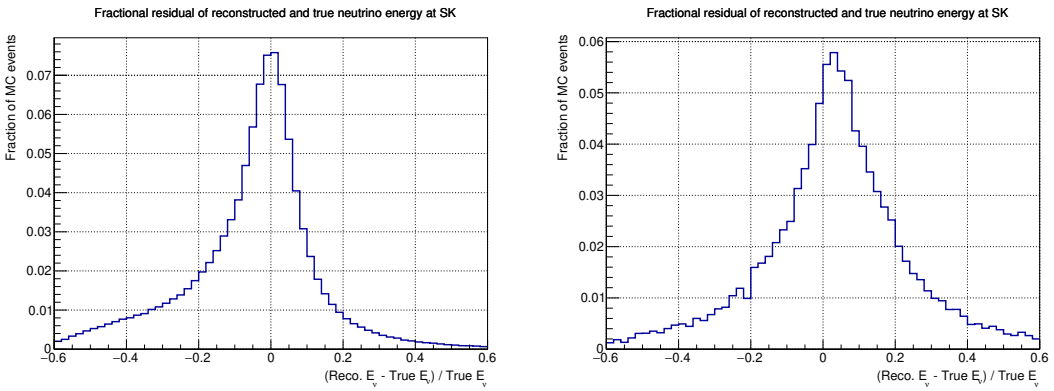

(a) FHC 1Rμ (b) FHC 1ReCC1π

Figure 4.3: Fractional residual of reconstructed and true neutrino energy for the FHC 1Rμ and FHC 1ReCC1π samples at SK.

4.1.4 SK data

Similar to the data at ND280 the data selection at SK is also categorised by topology and whether the neutrino beam was operated in FHC or RHC mode. However, due to the fact that SK is a water Cherenkov detector the topologies are primarily defined by the number of reconstructed Cherenkov rings, the PID of the ring and the number of reconstructed decay electrons. A description of how events at SK are reconstructed and important variables that are used in making the selections has already been given in section 4.1.3. The key focus of the selections are based on the number of Cherenkov rings, the PID of the ring(s) and the number of reconstructed decay electrons so these are used in the descriptions of the samples below. A fuller description of the samples including a description of fiducial volume optimisations can be found in [71]. The SK data samples currently included in the oscillation analysis are:

- **FHC 1Rμ** - one muon-like Cherenkov ring with 0 or 1 decay electrons in FHC mode.
- **FHC 1Re** - one electron-like Cherenkov ring with 0 decays electrons in FHC mode.
- **FHC 1ReCC1π** - one electron-like Cherenkov ring with 1 decay electron in FHC mode.
- **RHC 1Rμ** - one muon-like Cherenkov ring with 0 or 1 decay electron in RHC mode.
- **RHC 1Re** - one electron-like Cherenkov ring with 0 decay electrons in RHC mode.

It should be noted that the reason that there is no RHC 1ReCC1π data sample is that the π^- which would produce the associated decay electron has a high probability of being absorbed in the nucleus, so there are very few of these events would be selected. Each of these samples are then binned in kinematic variables with this binning being different for the muon-like and electron-like data samples due to the presence of different backgrounds in the samples. The muon-like samples are just binned in reconstructed neutrino energy. For electron-like samples NC interactions pose as a considerable background. Since NC and CC interactions produce particles with different kinematics, binning the samples in

different kinematic variables can help separate these interactions. To separate the signal of muon neutrinos that have oscillated to electron neutrinos and this NC background, the electron-like samples are binned in both reconstructed neutrino energy and the angle between the electron and the neutrino. The binning used for the SK data samples in the oscillation analysis can be found in appendix B.2. Studies of the addition of a new data samples at SK into the oscillation analysis are the subject of chapter 8 of thesis.

4.1.5 Statistical treatment of ND280 and SK data

In the analyses presented in chapter 7 and chapter 8 the data collected at ND280 and SK are fitted simultaneously. These data are compared to the MC prediction at each detector for a given set of nuisance and oscillation parameters. The total likelihood can be written into two separate terms; the comparison between data and the MC prediction and the contribution from nuisance parameters

$$-\log \mathcal{L}_{\text{tot}} = -\log \mathcal{L}_{\text{stat}} - \log \mathcal{L}_{\text{nuisance}}, \tag{4.5}$$

where $\mathcal{L}_{\text{tot}}$ is the total likelihood, $\mathcal{L}_{\text{stat}}$ is the contribution coming from the comparison of the MC prediction to data and $\mathcal{L}_{\text{nuisance}}$ is the contribution from nuisance parameters. The first term $\mathcal{L}_{\text{stat}}$ will be described below and the $\mathcal{L}_{\text{nuisance}}$ will be described as part of discussion of nuisance parameters in section 4.2.

The comparison between data and MC prediction, $\mathcal{L}_{\text{stat}}$, from eq. (4.5) can be split into two terms

$$-\log \mathcal{L}_{\text{stat}} = -\log \mathcal{L}_{\text{sample}} - \log \mathcal{L}_{\text{MC stat}}. \tag{4.6}$$

The first term, $\mathcal{L}_{\text{sample}}$ is a Poisson likelihood ratio comparing the predicted number of events to the number of events in the data in each analysis bin for each data sample at both SK and ND280. This sample contribution takes the form:

$$\begin{aligned} -\log \mathcal{L}_{\text{sample}} = & \sum_{\text{ND280 samples}} \sum_{\text{bins}} \left[N_{\text{pred}}^{\text{ND280}} - N_{\text{data}}^{\text{ND280}} + N_{\text{data}}^{\text{ND280}} \log \frac{N_{\text{data}}^{\text{ND280}}}{N_{\text{pred}}^{\text{ND280}}} \right] \\ & + \sum_{\text{SK samples}} \sum_{\text{bins}} \left[N_{\text{pred}}^{\text{SK}} - N_{\text{data}}^{\text{SK}} + N_{\text{data}}^{\text{SK}} \log \frac{N_{\text{data}}^{\text{SK}}}{N_{\text{pred}}^{\text{SK}}} \right], \end{aligned} \tag{4.7}$$

where N_{pred}^{ND280} and N_{pred}^{SK} are given by eq. (4.2) and eq. (4.1) and N_{data}^{ND280} and N_{data}^{SK} are the number of data events in a given sample and analysis bin for ND280 and SK respectively. The second term, $\mathcal{L}_{\text{MC stat}}$, takes into account the error coming from MC statistics at ND280 and uses the Barlow-Beeston method [72]. The Barlow-Beeston method assigns a scaling parameter for each analysis bin which scales the number of MC events in a given bin. So as not to introduce an enormous number of scaling parameters to the fit, the scaling parameters are assumed to be described by a Gaussian distribution as proposed in [73]. This approximation to the Barlow-Beeston method is very good when large numbers of Monte-Carlo events are available, which is the case for this analysis. The MC statistical uncertainty is currently only taken into account at ND280 as SK has a much larger ratio of data events to MC events due to the low number of data events.

The comparison of data to MC prediction is what drives the oscillation analysis. Typically the T2K oscillation analysis is statistics limited meaning that the greatest source of uncertainty on neutrino oscillation parameters comes from the number of data events being used in the analysis. However, at ND280 due to the large number of events $\mathcal{L}_{sample}$ has great power in constraining the uncertainties on nuisance parameters. The number of data events at SK is much smaller than at ND280 so $\mathcal{L}_{sample}$ is not as useful at constraining systematic parameters. Despite this, it is the $\mathcal{L}_{sample}$ at SK that gives the analysis its sensitivity to neutrino oscillation parameters. Due to the relatively small number of data events at SK the addition of data statistics into the oscillation analysis at SK through the introduction of new data samples can be extremely valuable in improving the constraint on neutrino oscillation parameters.

4.2 Nuisance parameters

The treatment of nuisance parameters is one of the key parts of the performing an oscillation analysis. As discussed, the number of events predicted at SK depends on the predicted neutrino flux, neutrino cross section, the detector response and the oscillation probability. Therefore, to be able to extract neutrino oscillation parameters without bias the neutrino flux, neutrino interactions and detector response all have to be modelled correctly.

Nuisance parameters are all treated in the same statistical way; through the use of constraints coming from prior uncertainties and using data to update or improve these constraints. These prior uncertainties (sometimes simply called priors) come from external datasets, calibration data and theoretical motivations. For each parameter a prior central value (the parameter value believed to be true before the fit is performed) and an uncertainty around this central value is assigned. Nearly all nuisance parameters are then modelled with a Gaussian penalty term according to their prior central value and uncertainty. For each source of nuisance parameters a covariance matrix is constructed to provide the covariance that any two parameters may have. This penalty term then takes the form:

$$-\ln \mathcal{L}_{\text{nuisance}} = \frac{1}{2} \sum_i \sum_j [x_i - \mu_i](V_{ij})^{-1}[x_j - \mu_j], \tag{4.8}$$

where V_{ij} is a covariance matrix relating parameter i to parameter j, μ_i is the prior central value of parameter i and x_i is the current value of the parameter. A term like this appears in the likelihood function for each source of nuisance parameters; one for the neutrino flux, one for neutrino interactions, one for ND280 detector systematics, one for SK detector systematics and one for prior knowledge of oscillation parameters. The study and choice of the prior central values and uncertainties is therefore an important part of the oscillation analysis and a lot of time on T2K is devoted to this. How the prior central values and uncertainty are chosen for nuisance parameters for the neutrino beam, neutrino interaction model, detector systematics as well as the prior central values and uncertainties for oscillation parameters will be discussed in the next sections. In the case where there is no clear choice for a prior uncertainty, a flat prior is used such that the parameter will only contribute to the likelihood through the $\mathcal{L}_{sample}$.

4.2.1 Neutrino Flux

An understanding of the neutrino beam produced at J-PARC is essential in predicting the number of events at ND280 and SK. The simulation of the neutrino beam consists of; the proton beam kinematics, the proton beams interaction on the target, the focusing of hadrons the magnetic horns, secondary interactions of these hadrons in the target and then the propagation of these hadrons out of the target until they decay to produce neu-

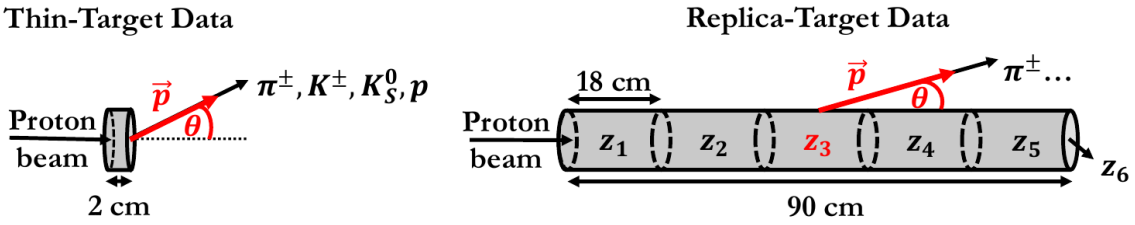

Figure 4.4: A comparison of the thin target configuration (left) and replica target configuration (right) used at the NA61 experiment. Figure taken from [78]

trinos. These processes cover a broad range of energies and physical processes so several different MC packages are used. FLUKA version 2011.2c.6 [74] [75] MC package is used to simulate the initial proton beam, the production of hadrons in the target and the subsequent re-interaction of these hadrons in the target. For the propagation of hadrons outside of the target a custom GEANT 3 simulation [76] is used. Broadly, simulating the neutrino beam at T2K can be broken down into six key areas of uncertainty: hadronic interactions, the profile and angle of the proton beam, the current and field of the magnetic horns, the alignment of the magnetic horns and target alignment, the modelling of the graphite target itself and the number of protons in the proton beam. To reduce these sources of uncertainty, data taken using the beam line monitors at J-PARC and external datasets are used.

In previous analyses the largest uncertainty at the flux peak has arisen from hadronic interactions [71]. In the analysis presented in chapter 7, this component of the neutrino flux uncertainty has been significantly reduced using external datasets from the NA61 experiment. In particular, data taken at NA61 using a replica of the target used in the T2K beamline [77] provides very useful constraints on the T2K neutrino beam. The NA61 experiment has also collected data for the T2K experiment using a thin target. The thin-target means that hadrons scatter less in the target before being measured. A comparison of the replica target and the thin target can be seen in fig. 4.4.

For the oscillation analysis, the uncertainties from different processes and parts of the neutrino beam production are converted into a set of parameters for different bins in true neutrino energy for different beam components in FHC and RHC for SK and ND280. This uncertainty on each parameter and the covariance between parameters is

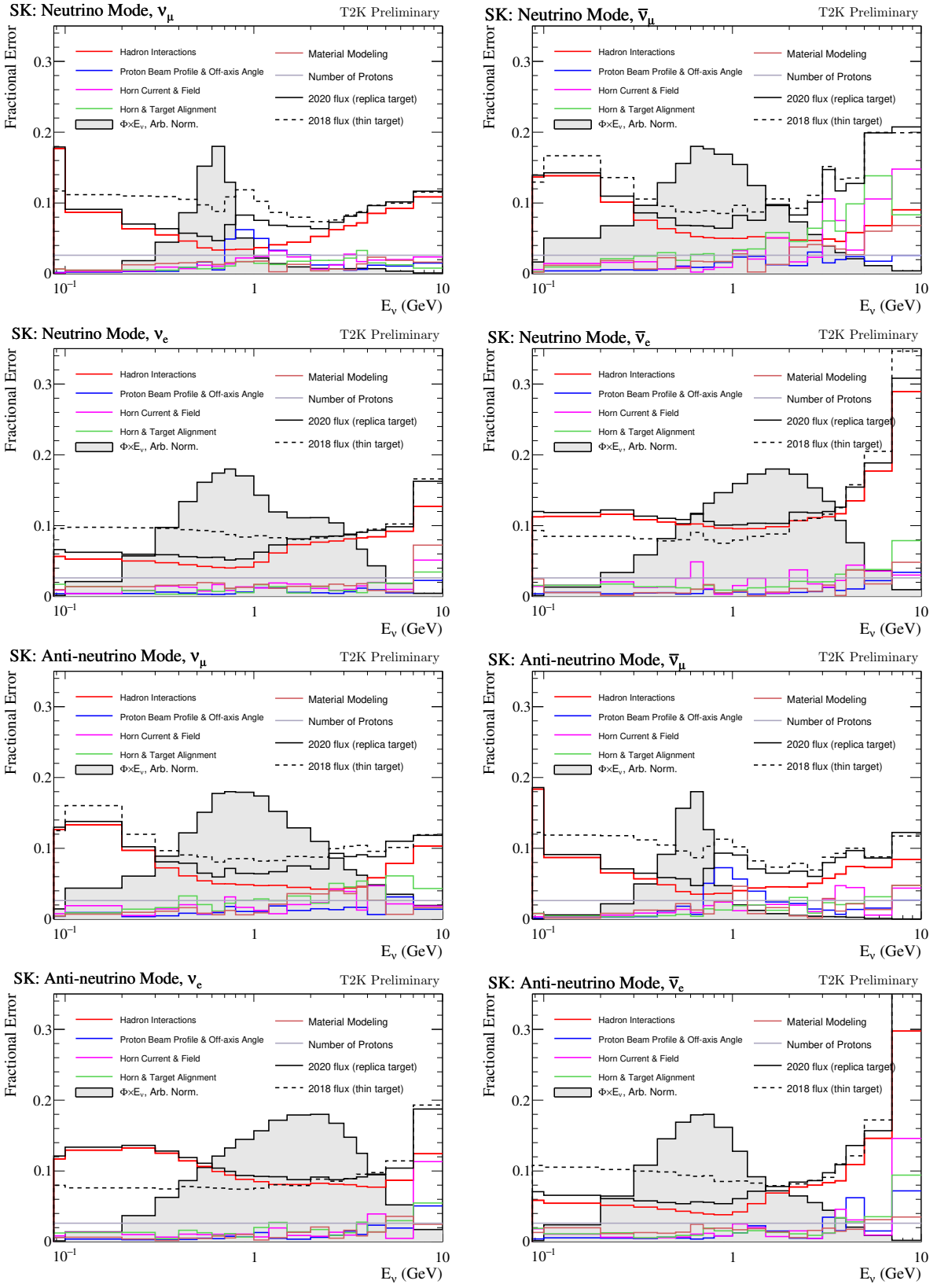

Figure 4.5: The fractional uncertainty on the neutrino beam prediction for the different neutrino flavours in both neutrino and anti-neutrino mode. The fractional uncertainty is also broken down by the source of uncertainty.

given by the covariance matrix in fig. 4.6. The binning used for ν_μ, ν_e, $\bar{\nu}_\mu$ and $\bar{\nu}_e$ for FHC and RHC can be seen in fig. 4.5. In total there are 100 parameters which vary the neutrino flux prediction; 50 for ND280 and 50 for SK. Each one of these flux systematic parameters can vary in the fit to data and vary the event rate in a true neutrino energy bin according to the covariance matrix such that the flux prediction in a true neutrino energy bin i is given by:

$$\Phi_i^{\text{pred}} = b_i \Phi_i^{\text{tuned}}, \tag{4.9}$$

where Φ_i^{pred} is the prediction in a true neutrino energy bin i, b_i is the nuisance parameter value for that true neutrino energy and Φ^{tuned}. Therefore, it can be seen that the 100 flux parameters act as normalisation parameters in a true energy range for a particular neutrino flavour and horn operating mode. The fractional uncertainty in each true neutrino bin and for different neutrino flavours for the flux prediction at SK can be seen in fig. 4.5. Figure 4.5 also shows the total fractional uncertainty using the thin target data and then the uncertainty with the addition of the replica-target data from NA61. These figures show the considerable improvement from the inclusion of the replica-target data used in this analysis.

4.2.2 Neutrino interaction model

The neutrino interaction model is a very important part of the T2K neutrino oscillation analysis. Not only is the modeling of neutrino interactions important in predicting the number of events at both ND280 and SK but also in how that energy is distributed between the initial and final-state particles. Fundamentally, neutrino oscillations depend on the neutrino energy and neutrino oscillation parameters. At neutrino experiments, neutrino interactions are reconstructed in a detector. If the mapping from true quantities (such as true neutrino energy, momentum etc.) to reconstructed quantities is incorrect or biased in some way then this will result in biasing the measurement of oscillation parameters. Therefore, ensuring that correct uncertainties are assigned to different neutrino interactions, such that the mapping of simulated to reconstructed quantities is not biased, is essential in accurately measuring neutrino oscillation parameters.

The nuisance parameters related to neutrino interaction modelling are often related

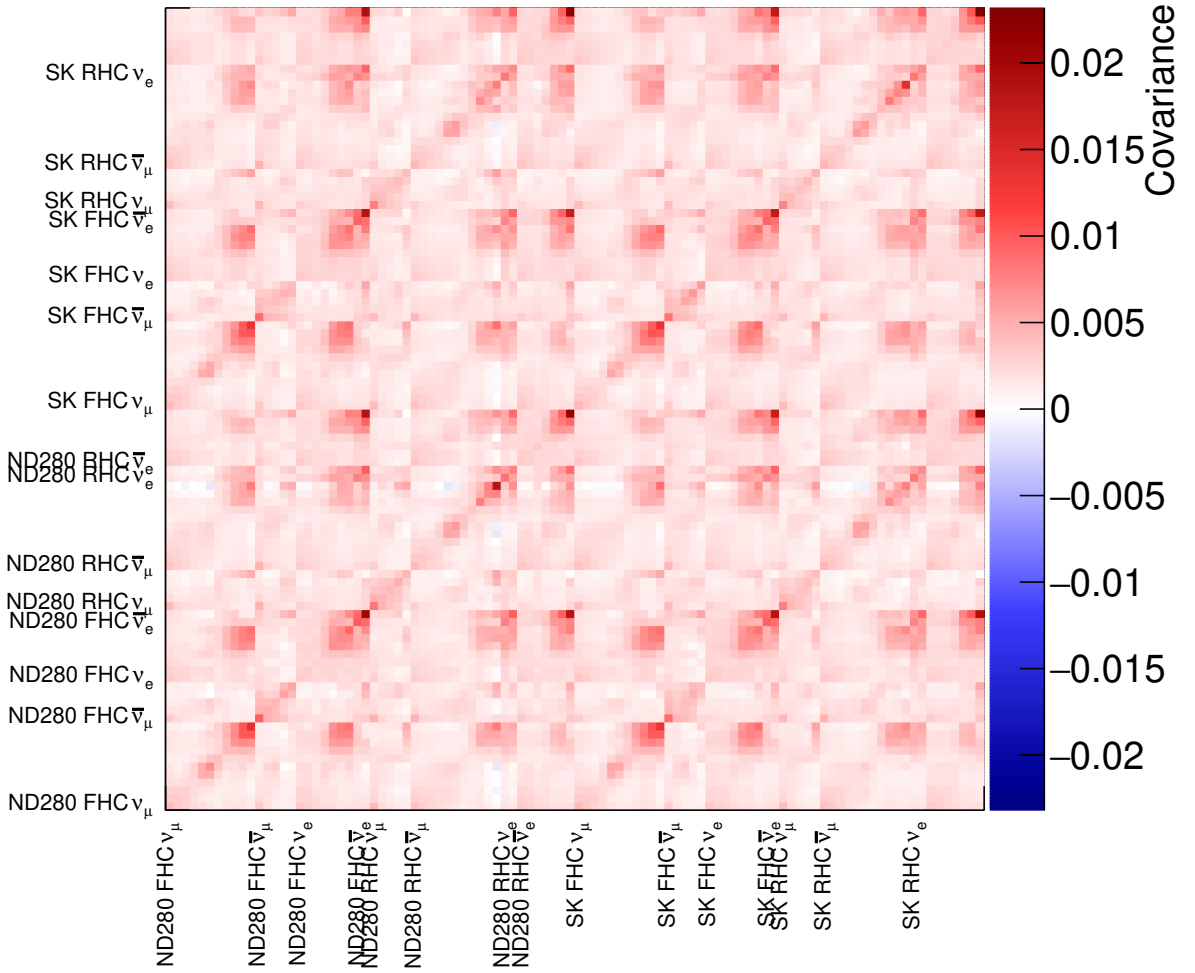

Figure 4.6: The flux covariance matrix used in the neutrino oscillation analysis. The labels show the parameters which are associated with the different detectors, horn operating modes and neutrino flavours. In general the flux covariance which are positively correlated with other flux parameters.

to theoretical uncertainties such as alternative modelling of interactions being available or are motivated by external neutrino cross-section datasets. Parameters can apply to individual neutrino interaction types, specific neutrino flavours or in a specific neutrino energy range. These uncertainties are then taken into account by altering the MC prediction for a proposed value of a nuisance parameter in the analysis. There are three types of nuisance parameters related to neutrino interaction modelling; shape parameters, normalisation parameters and parameters which can shift reconstructed values for MC events. Both shape and normalisation parameters apply a weight to the nominal MC prediction. This method is known as reweighting and is common as it allows different MC predictions to be studied without having to re-run simulations which can often be computationally expensive.

Shape parameters are used when a parameter may have a non-linear response when shifted away from its nominal value. These parameters are implemented by weighting the nominal MC prediction to match what the MC should be for a given parameter value. Since it is not computationally feasible to calculate this reweighting for every possible parameter value for each parameter, an interpolation method between points where the reweighting has been calculated is used. A continuous response is calculated by using cubic splines using the TSpline3 class in ROOT to interpolate between different points (or knots) that the response to a parameter value has been calculated at. At ND280, a spline is made for each MC event for each parameter which affects it. At SK, splines are constructed by taking the average response in an analysis bin for a particular range in true neutrino energy and creating a spline from that response. This is done for each neutrino flavour, for every systematic and then every interaction type that a systematic affects. These splines are then evaluated at the proposed value of the nuisance parameter to apply a weight to MC events. Examples of some splines used in the analysis are given in fig. 4.7.

Normalisation parameters are often used for parameters which affect rate only or where the uncertainty is on the total cross section or a cross-section ratio. The parameters change the number of events linearly as they deviate away from their prior central value. Normalisation parameters also affect all analysis bins in the same way so cannot affect particular regions of phase-space differently unlike shape parameters. Again, the

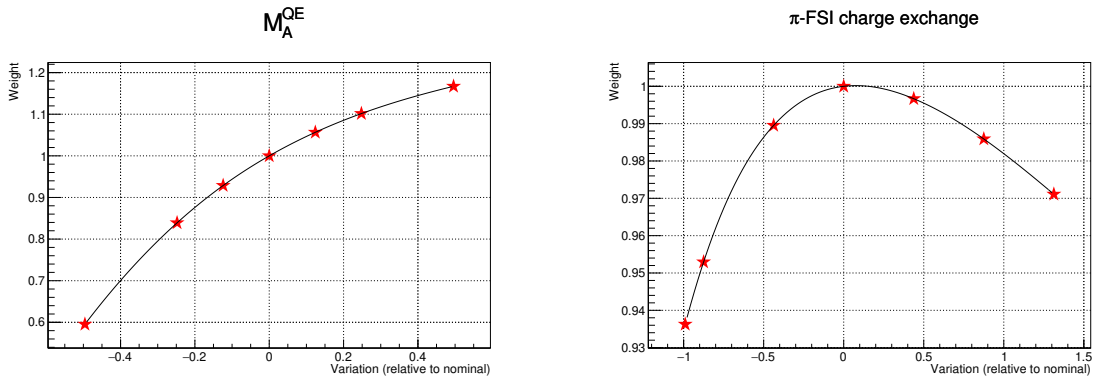

Figure 4.7: Examples of cross-section parameters splines which are used to apply systematic uncertainties in the oscillation analysis. The red markers indicate the spline knots where the exact reweighting of a parameter has been calculated at whereas the black line is the result of a cubic spline fit being used with these knots. The x-axis on these plots is the relative shift from nominal where the nominal is 0. The spline knots used are chosen to cover parameter values of at least 3σ away from a parameters prior central value.

uncertainties on these parameters come from theoretically motivated uncertainties or are motivated by measurements made with external neutrino cross-section datasets. There are 24 of the normalisation systematic parameters related to neutrino interactions used in the neutrino oscillation analysis in total.

Finally there are nuisance parameters which result in a shift in reconstructed momentum. These parameters can result in event migration between different analysis bins and in previous T2K oscillation analyses have been a leading cause of systematic uncertainty in the final oscillation results [71]. The only systematic parameters related to neutrino interactions which behave in this way in the T2K oscillation analysis are those related to binding energy. In CCQE interactions there is an uncertainty assigned to the binding energy of the nucleon in an interaction. This results in the outgoing lepton from a CCQE interaction having a different momentum and hence having a different reconstructed energy. If this binding energy is greater or smaller than what is used in the nominal simulation then the reconstructed neutrino energy will be biased. There are four of these momentum shift parameters, one each for the binding energy of nucleons in Carbon and Oxygen and for neutrino and anti-neutrino interactions.

There are currently 47 nuisance parameters used in the T2K oscillation analysis, the

full details of which would be too long for this thesis. However, below a brief description of nuisance parameters grouped by the neutrino interactions which they are designed to impact is given. When available, sources containing more detail on these systematics are given.

CCQE

- **Axial mass (M_A^{QE})** - CCQE interaction cross sections are described using three form factors which describe the structure of a nucleon; electric, magnetic and axial. The electric and magnetic form factors are constrained well by electron-scattering data [79] whereas the axial form factor is only present for neutrino-nucleon interactions. The axial form factor can be written in the dipole form as:

$$F_A(Q^2) = \frac{g_A}{\left(1 + \frac{Q^2}{M_A^{\mathrm{QE}\,2}}\right)^2}, \tag{4.10}$$

  where F_A is the axial form factor, Q^2 is the square of the 4-momentum transfer, $g_A = F_A(0)$ is well constrained from neutrino β decay [8].Therefore, the uncertainty on CCQE neutrino-nucleon interactions is taken to be from M_A^{QE}. The prior uncertainty and central value on this parameter used in the T2K oscillation analysis comes from fits to bubble chamber data [80].

- **Low Q^2 suppression** - several neutrino cross section datasets (e.g. [81]) give evidence for suppression of the CCQE cross section at low values of Q^2. Theoretically, a motivation for this suppression comes from a screening of nucleons by the nucleus. The nominal CCQE cross section used in the MC does not contain any form of Q^2 suppression. The theoretical and experimental motivations led to lead to a set of normalisation parameters in different regions of Q^2 to take this uncertainty into account.

- **Binding Energy (E_b)** - in CCQE interactions the bound nucleon in the initial state is liberated from the nucleus as a free nucleon. This means that some energy is required for the nucleon to leave the potential of the nucleus. The energy required for a nucleon to do this is called the binding energy. If the value of this binding energy is assigned incorrectly then this will lead to a bias in the reconstructed

energy calculation. For ν_μ CCQE interactions, the binding energy of the nucleon would be considered in the reconstructed energy as

$$E_\nu^{\text{reconstructed}} = \frac{m_p^2 - (m_n - E_b)^2 + m_\mu^2 + 2(m_n - E_b)E_\mu}{2\left(m_n - E_b - E_\mu + p_\mu \cos\theta_\mu\right)} \tag{4.11}$$

where m_n, m_p and m_μ are the neutron, proton and muon masses respectively, E_μ is the muon energy, p_μ is the muon momentum and $\cos\theta_\mu$ is the angle between the muon and the neutrino. It can therefore be seen that using the incorrect value of binding energy will result in a biased calculation of reconstructed neutrino energy. To take this uncertainty into account four binding energy parameters are used; two each for neutrino and anti-neutrino on C and O nuclei. These four parameters have different prior uncertainties and central values coming from constraints from electron-scattering data [82]. These parameters are correlated to ensure that the uncertainty cannot exceed 6 MeV.

2p-2h

- **2p-2h normalisations** - there are several normalisation parameters related to 2p-2h interactions. These stem from differences in model predictions for neutrino and anti-neutrino interactions [83] as well as differences in the correlations between nucleons in C and O nuclei as motivated by data taken from the CLAS experiment [84]. These uncertainties result in three normalisation parameters related to 2p-2h interactions; one for neutrinos, one for anti-neutrinos and one to account for differences in C and O nuclei.

- **2p-2h shape** - theoretical uncertainties coming from the shape of the differential cross section in energy transfer and momentum transfer are the motivation in parameters to change the 2p-2h differential cross section in different regions on energy and momentum transfer. This results in two parameters; one for C and one for O.

- **2p-2h Energy dependence** - to compliment the 2p-2h normalisation and shape parameters a series of energy dependent parameters which change the 2p-2h cross section as a function of energy are used to describe the uncertainty coming from the predictions from the Martini [85] , Nieves [86] and SuSaV2 [87] models. Four

parameters exist describing this uncertainty for neutrinos and anti-neutrinos for energies below (low) and above (high) 600 MeV.

CCRES

- **$\mathbf{C_5^A}$ and $\mathbf{M_A^{RES}}$** - similar to the M_A^{QE} parameter for CCQE interactions the M_A^{RES} and C_A^5 parameters take into account modifications to the axial form factor in CCRES interactions. The C_5^A parameter gives the normalisation of the form factor.
- **Non-resonant I-$\frac{1}{2}$ background** - as well as uncertainties related to the axial form factor in CCRES interactions, there is also a component of the CCRES cross section coming from non-resonant backgrounds. Typically, bubble chamber data does not constrain this background very well. Non-resonant pion production can result in low momentum pions which at SK can be below Cherenkov threshold so need to be modelled with appropriate uncertainty to not bias the energy reconstruction.

CC DIS and CC Multi-π

- **CC Bodek-Yang** - corrections to the CC DIS and CC Multi-π cross sections coming from fits to electron scattering data as given by Bodek and Yang [88]. These uncertainties and the development of re-weighting tools to apply this uncertainty are the topic of chapter 6.
- **CC AGKY multiplicity** - an uncertainty coming from a change in the hadronisation model used in the MC for CC Multi-π interactions is also taken into account with a systematic parameter. This is also discussed in chapter 6.
- **CC Multi-π and CC DIS normalisations** - a change of the total CC DIS and CC Multi-π cross section motivated by the difference in the prediction from NEUT and global neutrino scattering data is taken into account. This results in a normalisation uncertainty of 35% for neutrinos and 65% for anti-neutrinos and are 100% correlated with each other.

Other interactions

- **CC normalisations** - due to coulomb interactions as the lepton leaves the nucleus in a CC interaction the total CC cross section can change. The impact of coulomb interactions on CC cross sections is calculated in [89] and is found to be $\sim 2\%$ for neutrinos and $\sim 1\%$ for anti-neutrinos in the region of $400-600$ MeV and negligible outside of this region. Two normalisation parameters apply this uncertainty to MC events one for neutrinos and one for anti-neutrinos in the given energy range. These two parameters are 100% anti-correlated.

- **Electron neutrinos** - there may be uncertainties arising from ν_e or $\bar{\nu}_e$ interactions that are not present for ν_μ or $\bar{\nu}_\mu$ interactions. To ensure this uncertainty is taken into account an uncertainty on the ν_e to ν_μ and $\bar{\nu}_e$ to $\bar{\nu}_\mu$ cross sections is used. The prior uncertainty on these parameters comes from calculating corrections to form factors for electrons and radiative corrections.From the calculations in [90] two uncorrelated errors of 2% are assigned to the $\frac{\nu_e}{\nu_\mu}$ and $\frac{\bar{\nu_e}}{\bar{\nu_\mu}}$ total cross-section ratios as well as an anti-correlated 2% uncertainty mainly coming from radiative corrections.

- **Coherent pion production** - coherent pion production interactions are assigned an uncertainty of 30% based on the inspection of MINERνA data [91]. There are two fully correlated dials for CC coherent interactions on C and O as well as one for NC coherent interactions all with a 30% normalisation error.

- **NC γ and other NC interactions** - NC interactions and uncertainties associated with them are important to model correctly as they pose as backgrounds when searching for neutrino oscillations. In particular, NC1γ interactions where the $\gamma \rightarrow e^+ e^-$ can mimic electron-appearance at SK. These NC1γ interactions are given a 200% normalisation uncertainty motivated by a comparison of the MC prediction using NEUT and a different model in [92].

- **Other CC interactions** - so called CC "miscellaneous" (CC Misc) interactions such as CC interactions producing a kaon, eta, gamma and diffractive pion production give a small contribution to the event rate predictions at T2K but a conservative 100% uncertainty is still applied to these events.

π Final State Interactions

- **π Final State Interactions (FSI)** - one of the most significant difficulties in neutrino interactions is the disentangling of the effect of final state interactions of particles as they propagate through the nucleus from the physics of the initial interaction. The modelling of these interactions is difficult, however, there exist datasets that neutrino event generators can tune their models with to improve their simulations and to reduce the uncertainty on these processes. In the T2K oscillation analysis the results of tuning the NEUT FSI model to global pion scattering data [93] is used to model the systematic uncertainties arising from pion FSI. A systematic uncertainty is assigned to the different possible FSI that can occur in the NEUT model such as pion absorption, charge exchange between the pion and a nucleon, quasi-elastic scattering (for low and high momentum pions) and an uncertainty on hadron production in FSI. These uncertainties apply to all interaction modes in the MC prediction. Currently only uncertainties on pion FSI are considered. Nucleon FSI could also be included but in this analysis no nucleon information is used in the selection defintions or reconstruction.

All the systematic parameters related to neutrino interaction uncertainties used in the oscillation analysis are given in table 4.1 along with their prior central value, 1σ uncertainty, their range (where applicable), whether the parameter is implemented as a shape (spline), normalisation parameter or as a parameter which shifts an events momentum.

4.2.3 Detector systematics

There are also nuisance parameters related to how the reconstruction of interactions in a detector can vary. These uncertainties are associated with; efficiency of reconstructing and identifying particles, secondary interactions of protons and pions in the detector medium and events occurring outside of the fiducial volume. Particularly for uncertainties related to reconstruction, these parameters are informed by control samples to help to constraint them. In the oscillation analysis there are two sets of detector systematics, one for the ND280 detector and one for SK.

Parameter	Validity Range	generated value	Prior mean	Prior Error	Type	Unit
M_A^{QE}	all	1.21	1.03	0.06	shape	GeV/c^2
2p2h ν	0 <	1	flat	flat	norm.	—
2p2h $\bar{\nu}$	0 <	1	flat	flat	norm.	—
2p2h CtoO	0 <	1	1	0.2	norm.	—
2p2h C	-1–1	0	0	0	shape	—
2p2h O	-1–1	0	0	0	shape	—
2p2h Edep low E_ν	0–1	1	flat	flat	shape	—
2p2h Edep high E_ν	0–1	1	flat	flat	shape	—
2p2h Edep low $E_{\bar{\nu}}$	0–1	1	flat	flat	shape	—
2p2h Edep high $E_{\bar{\nu}}$	0–1	1	flat	flat	shape	—
Q^2 supp. 0.00-0.05 GeV^2	0–1	1	flat	flat	norm.	—
Q^2 supp. 0.05-0.10 GeV^2	0–1	1	flat	flat	norm.	—
Q^2 supp. 0.10-0.15 GeV^2	0–1	1	flat	flat	norm.	—
Q^2 supp. 0.15-0.20 GeV^2	0–1	1	flat	flat	norm.	—
Q^2 supp. 0.20-0.25 GeV^2	0–1	1	flat	flat	norm.	—
Q^2 supp. 0.25-0.50 GeV^2	0–1	1	1	0.11	norm.	—
Q^2 supp. 0.50-1.00 GeV^2	0–1	1	1	0.18	norm.	—
Q^2 supp. > 1.00 GeV^2	all	1	1	0.4	norm.	—
E_b C ν	-10–15	0	2	6	mom. shift	MeV
E_b C $\bar{\nu}$	-10–15	0	0	6	mom. shift	MeV
E_b O ν	-10–15	0	4	6	mom. shift	MeV
E_b O $\bar{\nu}$	-10–15	0	0	6	mom. shift	MeV
C_A^5	all	1.01	0.96	0.15	shape	—
M_A^{RES}	all	0.95	1.07	0.15	shape	—
I-$\frac{1}{2}$ bkg. low p_π	all	1.3	0.96	1.3	shape	—
I-$\frac{1}{2}$ bkg.	all	1.3	0.96	0.4	shape	—
CC norm ν	0 <	1	1	0.02	norm.	—
CC norm $\bar{\nu}$	0 <	1	1	0.01	norm.	—
ν_e ν_μ	0 <	1	1	0.0282843	norm.	—
$\bar{\nu}_e$ $\bar{\nu}_\mu$	0 <	1	1	0.0282843	norm.	—
CC BY DIS	all	0	0	0	shape	—
CC BY MPi	all	0	0	0	shape	—
CC AGKY Mult.	all	0	0	0	shape	—
CC Misc.	0 <	1	1	1	norm.	—
CC DIS MPi Norm ν	0 <	1	1	0.035	norm.	—
CC DIS MPi Norm $\bar{\nu}$	0 <	1	1	0.065	norm.	—
CC Coh. C	0 <	1	1	0.3	norm.	—
CC Coh. O	0 <	1	1	0.3	norm.	—
NC Coh.	0 <	1	1	0.3	norm.	—
NC 1γ	0 <	1	1	1	norm.	—
NC other near	0 <	1	1	0.3	norm.	—
NC other far	0 <	1	1	0.3	norm.	—
π-FSI QE	all	1.069	1.069	0.313	shape	—
π-FSI QE High	all	1.824	1.824	0.859	shape	—
π-FSI Hadron production	all	1.002	1.002	1.101	shape	—
π-FSI Absorption	all	1.404	1.404	0.432	shape	—
π-FSI Charge Exchange	all	0.697	0.697	0.305	shape	—

Table 4.1: A summary of the cross-section parameters used in this analysis. Coulomb corrections are omitted in this table as they take no input from the cross-section model and are applied in the calculation of reconstructed energy. It should also be noted that although a parameters range may not be explicitly restricted, the priors constrain the parameters to a finite range and if a non-physical weight is calculated it is set to 0.

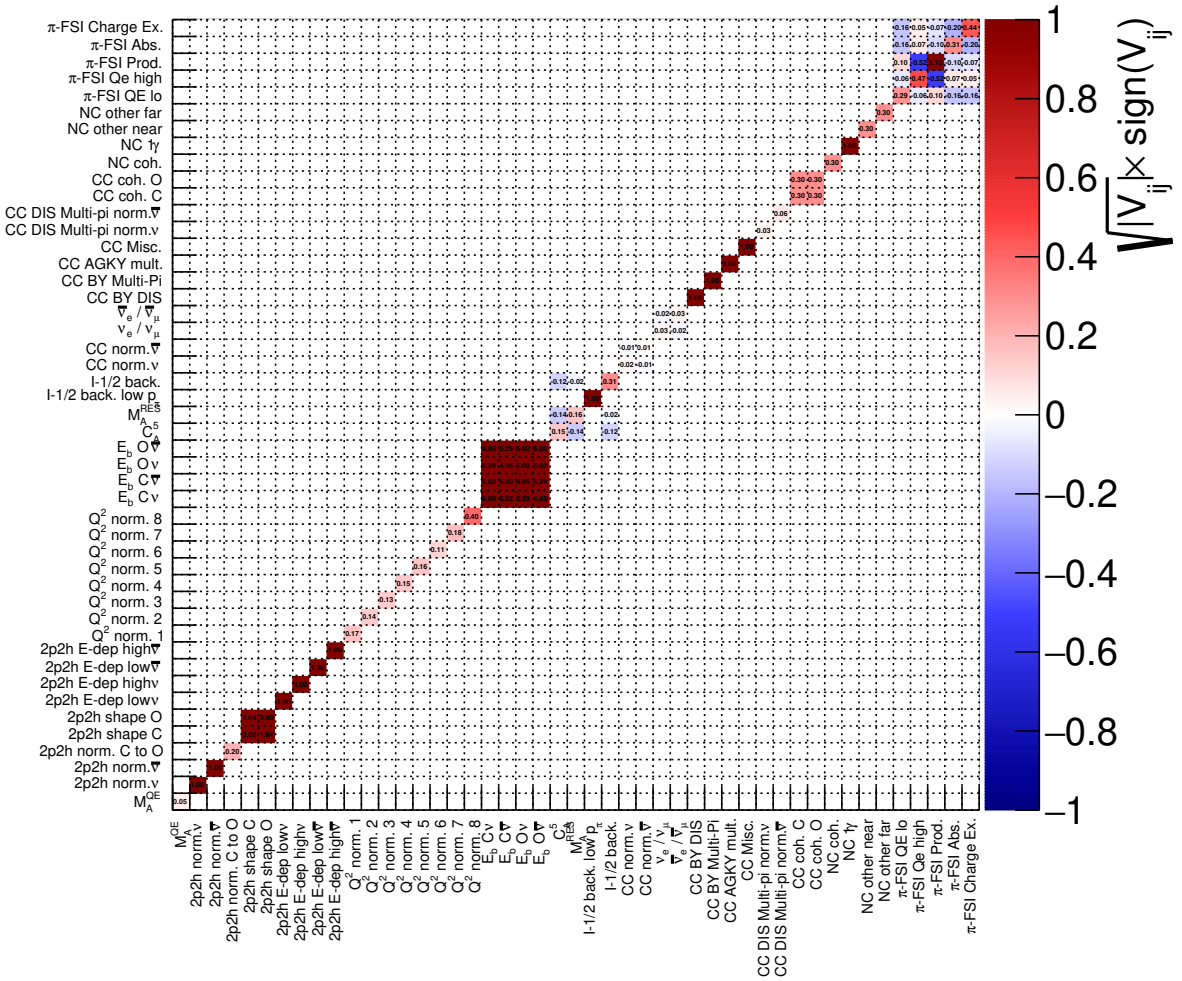

Figure 4.8: The covariance matrix used for the prior uncertainties for nuisance parameters related to neutrino interactions. The covariance is given as a fraction of the nominal value for parameters where the nominal value is not equal to zero for example for the non-resonant I-$\frac{1}{2}$ background parameter $\sqrt{V_{ij}}$ is given by the prior uncertainty 0.4 divided by the nominal value 1.3 which is $\frac{0.4}{1.3} \approx 0.31$. For parameters where the nominal value is 0 then $\sqrt{V_{ij}}$ is simply the prior uncertainty such as for the E_b parameters.One can see that in the covariance matrix used for the pre-fit is mainly diagonal.

ND280

The response of the ND280 detector and the events selected by it have several associated uncertainties related to it, such as track selection efficiency, PID, magnetic field distortion in the TPCs, momentum resolution and scale and Michel electron tagging efficiency. To account for these uncertainties in the analysis, a normalisation parameter is assigned to each analysis bin for each data sample. Each of these parameters has a nominal value of 1 and can change the number of predicted events in each bin. The uncertainty on each of these bin normalisation parameters is calculated by randomly varying the underlying detector systematics. Varying these parameters in the simulation results in a distribution of the number of events in each bin. Typically these distributions are Gaussian and if any bins do not match a Gaussian fit well then these bins are merged with a neighbouring bin. The bin merging also reduces the number of ND280 detector systematics in the analysis. This results in 574 normalisation parameters being used to describe the uncertainty in the detector response of ND280. A detailed explanation of the ND280 detector uncertainties can be found in [94] and [95].

SK

At SK a different approach to calculating the uncertainty in the detector response is used which takes advantage of the large amount data collected from atmospheric muons interacting inside SK. The detector systematics take into account the non-perfect reconstruction of event topologies in SK. To calculate this imperfection different control samples of atmospheric muon and atmospheric neutrino data are used. The detector uncertainty is parameterised as shift and smear parameters for the likelihood of different PID hypotheses and the likelihood of a particular number of Cherenkov rings. This gives the likelihood of a particular reconstructed variable to be

$$L'_m = \beta^1 L_m + \beta^0, \tag{4.12}$$

where β^0 and β^1 are the shift and smear parameters respectively and L_m is the nominal likelihood of a reconstructed variable and L'_m is the altered likelihood for that reconstructed variable. These shift and smear parameters are evaluated from atmospheric

muon and neutrino data using a Markov Chain Monte Carlo. For use in the oscillation analysis, a weight for each MC event depending on its reconstructed topology can then be calculated by making a random fluctuations from the output of the fit to atmospheric data. A binning scheme based on the data selection, neutrino flavour, whether the event is charged or neutral current and the momentum of the reconstructed lepton (if there is one) is used. The systematic parameters are thrown one million times to then build up a distribution in each bin and a covariance matrix from these throws is also made. In the oscillation analysis it is this covariance matrix which is used to apply the systematic uncertainties coming from the SK detector response. A detailed discussion of how the SK detector uncertainties can be found in [96].

In addition to this covariance made from the detector response the uncertainty from pion secondary interactions (SI) and photonuclear (PN) effects of neutrino interactions in SK are accounted for. PN uncertainties are accounted for by applying 100% uncertainty to the absorption of photons from π^0 decay. This uncertainty is only accounted for in electron-like samples since this uncertainty targets π^0s being mis-identified when looking for electron-appearance events. Then pion SI uncertainties are taken using the same dataset as is used to inform the FSI uncertainties for neutrino interactions [93] since the interaction processes and cross sections are the same for pion SI as FSI. The covariance for these effects are calculated in a similar way to the SK (and ND280) detector uncertainties in that weights are calculated by throwing systematic parameters and the change in the predicted events in each bin is then calculated and used to build a covariance matrix. The SI+PN covariance matrices is shown in fig. 4.9a and the total SK detector covariance matrix in fig. 4.9b.

4.2.4 Neutrino oscillation parameters

Although it seems strange to have neutrino oscillation parameters listed as nuisance parameters for a neutrino oscillation analysis, the T2K experiment is not sensitive to all oscillation parameters. Therefore, parameters which T2K is not sensitive to act as nuisance parameters for the parameters that T2K can measure more accurately. In addition, the assignment of prior uncertainties on oscillation parameters is an important topic and

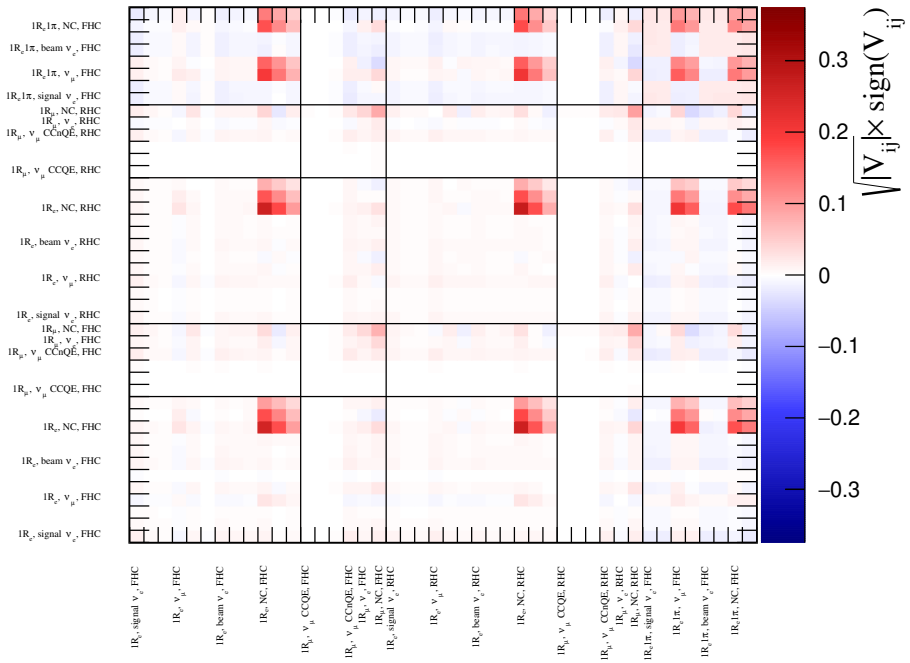

(a) SI + PN error matrix

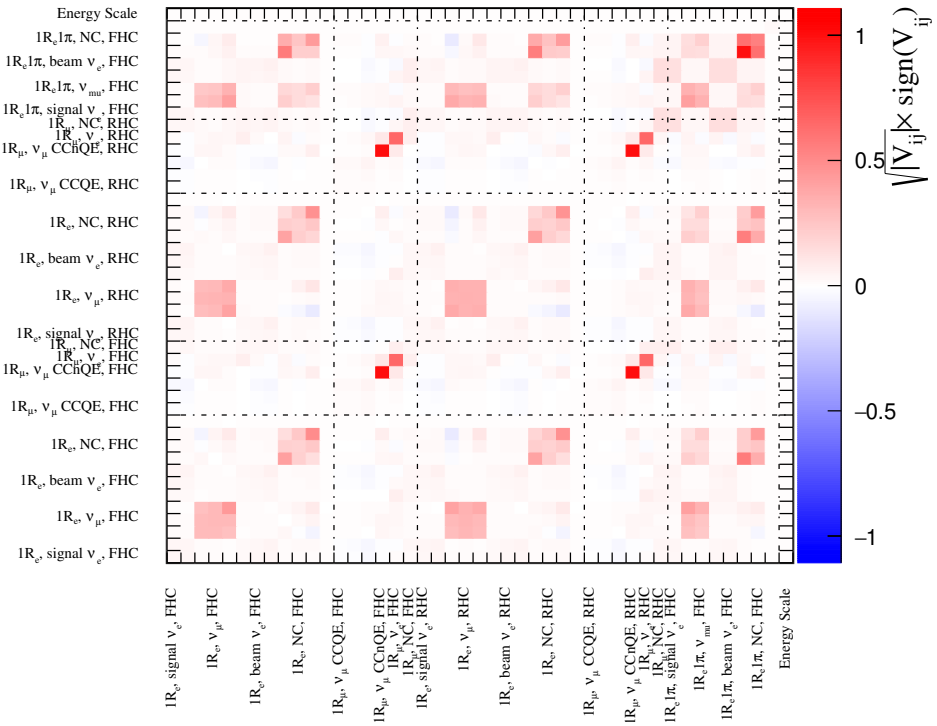

(b) The full SK detector covariance matrix used for the latest T2K neutrino oscillation analysis. A total of 44 parameters for all SK samples are used.

Table 4.2: The central values and uncertainties for $\sin^2\theta_{12}$, $\sin^2\theta_{13}$ (when results are quoted as using the 'reactor constraint") and Δm^2_{12}.

Oscillation parameter	Best-fit value
$\sin^2\theta_{12}$	0.307 ± 0.013
$\sin^2\theta_{13}$	$(2.18 \pm 0.07) \times 10^{-2}$
Δm^2_{12}	$(7.53 \pm 0.18) \times 10^{-5}$ eV^2

if done incorrectly could bias the final results on oscillation parameters. The T2K experiment searches for muon neutrino disappearance and electron neutrino appearance which are primarily sensitive to the θ_{13}, θ_{23}, Δm^2_{32} and δ_{CP} oscillation parameters. Therefore, the mixing angle θ_{12} and mass splitting Δm^2_{21} act as nuisance parameters. The prior uncertainties on the $\sin^2\theta_{13}$, $\sin^2\theta_{23}$ and δ_{CP} oscillation parameters (i.e. the oscillation parameters that are measured by T2K) are taken to be flat. The effect of having a flat prior in $\sin\delta_{\text{CP}}$ rather than δ_{CP} will be shown later in chapter 7. For the oscillation parameters which T2K is not primarily sensitive to (θ_{12} and Δm^2_{21}) the prior uncertainty and central values are taken from [26]. No correlation between oscillation parameters is considered in the prior. A special case exists for the θ_{13} mixing angle since this oscillation parameter is measured well by reactor neutrino experiments. As was discussed section 2.3.2, a prior uncertainty and central value can be taken from the PDG world-average to increase T2K's sensitivity to electron-neutrino appearance. This central value and uncertainty is used in a Gaussian prior like that in eq. (4.8), with the central values and uncertainties given in table 4.2. The results in chapter 7 will present results using a flat prior on $\sin^2\theta_{13}$ and using the constraint from neutrino reactor experiments which will be labelled as "reactor constraint".

4.3 T2K Likelihood function

The core part of the neutrino oscillation analysis, which brings together the statistical treatment of the data described in section 4.1.5 and the treatment of nuisance parameters as described in section 4.2, is the likelihood function. The likelihood function contains terms comparing the MC prediction and data in a Poisson likelihood term for both ND280

(where an MC statistics term is also included) and SK. The likelihood function also then includes all nuisance parameters in the form of Gaussian terms like eq. (4.8) but for all the different sources of systematic uncertainty; neutrino flux, neutrino interactions, SK detector response, ND280 detector response and the prior uncertainties taken on oscillation parameters. The point of the likelihood function is to establish what set of neutrino oscillation parameters and nuisance parameter values give the best fit to the data at ND280 and SK given our prior knowledge of uncertainties on the nuisance parameters. In practice the lower the value of the negative logarithm of the likelihood function, the better the MC prediction matches the data. In a fit, a balance between systematic parameter values improving the agreement between the MC prediction and data (minimising the sample contribution) and the systematic parameter value agreeing with the prior uncertainty and central value assigned to it (minimising the contribution to the likelihood from the Gaussian penalty terms) is found. The full likelihood function, or rather the negative logarithm of the likelihood function, is given in eq. (4.13).

$$
\begin{aligned}
-\log(\mathcal{L}_{\text{total}}) = & -\log \mathcal{L}^{\text{ND280}}_{\text{sample}} - \log \mathcal{L}^{\text{ND}}_{\text{MC stat.}} \\
& -\log \mathcal{L}^{\text{SK}}_{\text{sample}} \\
& -\log \mathcal{L}_{\text{nuisance}} \\
= & \sum_{\text{bins}} \left[N^{\text{ND280}}_{\text{pred}} - N^{\text{ND280}}_{\text{data}} + N^{\text{ND280}}_{\text{data}} \log \frac{N^{\text{ND280}}_{\text{data}}}{N^{\text{ND280}}_{\text{pred}}} + \frac{(\beta_i - 1)^2}{2\sigma^2_{\beta_i}} \right] \\
& + \sum_{\text{bins}} \left[N^{\text{SK}}_{\text{pred}} - N^{\text{SK}}_{\text{data}} + N^{\text{SK}}_{\text{data}} \log \frac{N^{\text{SK}}_{\text{data}}}{N^{\text{SK}}_{\text{pred}}} \right] \\
& + \sum_{i}^{\text{flux}} \sum_{j}^{\text{flux}} \frac{1}{2} (X_i - \mu_i)(V^{\text{flux}}_{ij})^{-1}(X_j - \mu_j) \\
& + \sum_{i}^{\text{xsec}} \sum_{j}^{\text{xsec}} \frac{1}{2} (X_i - \mu_i)(V^{\text{xsec}}_{ij})^{-1}(X_j - \mu_j) \\
& + \sum_{i}^{\text{SK det}} \sum_{j}^{\text{SK det}} \frac{1}{2} (X_i - \mu_i)(V^{\text{SK det}}_{ij})^{-1}(X_j - \mu_j) \\
& + \sum_{i}^{\text{ND det}} \sum_{j}^{\text{ND det}} \frac{1}{2} (X_i - \mu_i)(V^{\text{ND det}}_{ij})^{-1}(X_j - \mu_j) \\
& + \sum_{i}^{\text{osc}} \sum_{j}^{\text{osc}} \frac{1}{2} (X_i - \mu_i)(V^{\text{osc}}_{ij})^{-1}(X_j - \mu_j)
\end{aligned}
\tag{4.13}
$$

The terms $N^{\text{SK}}_{\text{pred.}}$ and $N^{\text{ND280}}_{\text{pred.}}$ are the number predicted events in an analysis bin for a set of neutrino oscillation and nuisance parameters at SK and ND280 as given by

eq. (4.1) and eq. (4.2). $N_{\text{data}}^{\text{SK}}$ and $N_{\text{data}}^{\text{ND280}}$ are the number of data events in an analysis bin at SK and ND280. Then for nuisance parameters X_i is the current parameter value, μ_i is the prior central value and V_{ij} is the covariance matrix describing the covariance between parameters for a given source of systematic uncertainty. There is a covariance matrix for each of the sources of systematic uncertainty where V_{ij}^{flux} is for the neutrino flux (fig. 4.6), V_{ij}^{xsec} is for neutrino interaction uncertainties (fig. 4.8), $V_{ij}^{\text{SK det.}}$ is for the SK detector response (fig. 4.9b), $V_{ij}^{\text{ND280 det.}}$ is for the ND280 detector response and V_{ij}^{osc} is for the priors on the oscillation parameters (as described in section 4.2.4). The β and σ_β parameters in poisson likelihood term of eq. (4.13) are to take into account of the MC stat uncertainty at ND280 as mentioned in section 4.1.5. How the likelihood function is used to find the neutrino oscillation parameters (and nuisance parameters) which best match the data at SK and ND280 is the discussion of the next chapter.

4.4 Fake Data Studies

Once the systematic model and inputs to an analysis have all been decided on, it is important to check that the analysis is robust to sources of systematic uncertainties. This is established through fits to several fake data sets. Each fake data set is created by reweighting the nominal MC prediction for each sample, at both the ND280 and SK, to an alternative model for neutrino interactions. For example, a fake data set could be made by using alternative form factors for CCQE interactions which would change the number of CCQE interactions as well as the kinematics of CCQE events. The systematic model for the analysis does not explicitly have an parameter to take the uncertainty from changing nucleon form factors for CCQE interactions into account. However, the hope is that the systematic model has been prescribed sufficient uncertainty to describe this fake data well. If a fit to this fake data extracts the same results on oscillation parameters as an Asimov fit then this indicates that the analysis is robust to the fake data. Several fake data sets are chosen based on theoretical and data-driven motivations. It was found for the analysis presented in chapter 7 that no fit to fake data was found to give a significant bias on oscillation parameters. The largest change in the 1D credible intervals of δ_{CP} was found to be 0.073 to the left edge and 0.080 to the right edge. The fake data studies

performed for the oscillation analysis presented in chapter 7 can be found in [97]. In chapter 8 a study using fake data will be used to show the importance of the CC Multi-π and CC DIS systematic uncertainties that have been developed.

Chapter 5

Markov Chain Monte Carlo

In the previous chapter, the general analysis technique employed by the T2K experiment to measure neutrino oscillation parameters was described. At its heart this uses the likelihood function described in section 4.3, however, the technique used to evaluate this likelihood and how it is used extract the best-fit parameter values and uncertainties has not been discussed yet. For the analyses presented in chapter 7 and chapter 8 a Markov Chain Monte Carlo (MCMC) technique is used to sample the likelihood and to then extract the best-fit parameters and their uncertainties. MCMC will be explained in section 5.1 and more details on the checks performed on the output Markov chains are given in section 5.2. After this, how constraints on parameters are actually made are described in section 5.3. Finally, validations of the fitting framework performed before starting fits to data are described in section 5.5. For all of the results shown in this thesis the Markov Chain 3-flavour (MaCh3) analysis framework is used.

5.1 Markov Chain Monte Carlo

The Monte Carlo technique is a well established method of approximating a function or distribution through the use of random number generation [98]. A classic example of the use of Monte Carlo methods is the approximation of the integral of a function by seeing what fraction of randomly generated points is less than the functions value

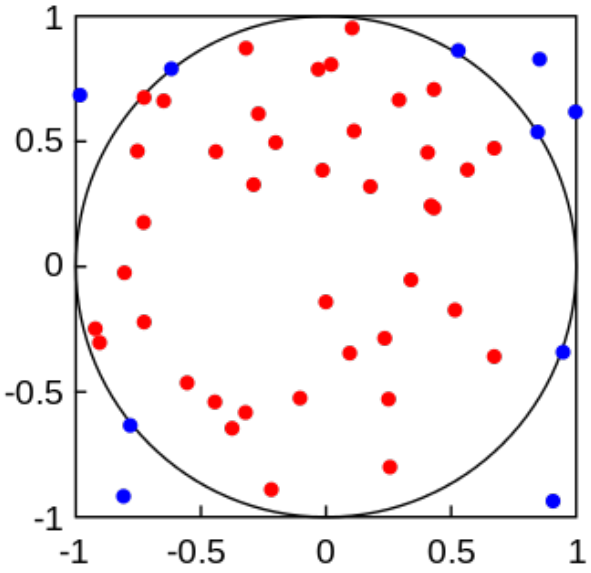

Figure 5.1: An example of random sampling being used to estimate π by estimating the area of a circle. The red points all fall into the area of the circle and hence the integral and the blue points are those that do not fall within the circle. Figure taken from [100]

as shown in fig. 5.1. In the case of the neutrino oscillation analyses presented in this thesis, the MCMC technique is used to approximate the full likelihood function for a set of oscillation and nuisance parameters. The MCMC technique uses the same ideas as the Monte Carlo technique; that a function and its properties can be approximated through sampling. The key part of MCMC is that a Markov chain is used to sample parameter values rather randomly sampling across all possible parameter values. A Markov chain samples a function by proposing different parameter values based on their likelihood and the current values. Therefore, the proposed parameter values used to sample the function are based on this local position rather than the global parameter space as in random sampling (like the example in fig. 5.1). The algorithm used in the analyses in this thesis is the Metropolis-Hastings algorithm [99] and is discussed in section 5.1.1. The MCMC technique is particularly useful for the T2K neutrino oscillation analysis because the likelihood function used has an extremely high number of dimensions; there are 574 ND detector systematics, 45 SK detector systematic parameters, 100 systematic parameters related to the neutrino flux, 48 related to neutrino interaction uncertainties and then the six neutrino oscillation parameters. This 773-dimensional likelihood is difficult to solve analytically which is why the MCMC technique is so useful here.

The MCMC technique lends itself to the Bayesian view of statistics and in particular Bayesian inference. In the case here the likelihood function described in section 4.3 describes the probability of neutrino oscillation parameters and nuisance parameters being true given the observed data

$$\mathcal{L}_{\text{Total}} = P(\vec{\theta}|D), \tag{5.1}$$

where $\mathcal{L}_{\text{Total}}$ is the total likelihood function given in eq. (4.13), $\vec{\theta}$ are all model parameters (including nuisance parameters) and D is the data. Using Bayes theorem, this can be rewritten in terms of a joint probability between the parameter values given the data and the probability of parameter values being true according to prior knowledge on that parameter such that

$$P(\vec{\theta}|D) \propto P(D|\vec{\theta})P(\theta) \tag{5.2}$$

where the proportionality sign arises as this statement is true up to some normalisation constant (sometimes interpreted as the probability of observing the data and is never required to be evaluated in this analysis).

Following on from this Bayesian view, the likelihood function introduced in the previous chapter can be identified as the posterior distribution (or simply the posterior). When the posterior distribution is binned in a particular parameter then it is referred to as a posterior density. Posterior, posterior density and likelihood function will all be used interchangeably throughout this thesis. The aim of the analysis is to build this posterior distribution and to establish its properties which is done through the use of MCMC.

The aim of any MCMC method is to have a chain where the steps taken are representative of the function that is trying to be approximated. To approximate the function in question, the Markov chain must sample the underlying distribution such that it does not depend on the current step number. Once this has been achieved the chain is said to be stationary and ensures that the Markov chain is sampling from the underlying distribution independently so that it can be approximated with enough samples. To be able to achieve this the algorithm used to propose parameter values in the Markov chain must to satisfy some key statistical conditions. An in-depth discussion of MCMC techniques and Bayesian inference in general is beyond the scope of this thesis (in-depth discussion on these topics can be found in [101] and [98] for example) but the key properties underpinning MCMC are:

- **Irreducibility** - from any starting point there is a non-zero probability of reaching any other point given enough steps. This is essentially requiring that a chain can reach any part of the parameter space.
- **Aperiodicity** - a chain cannot repeat itself in a periodic fashion. This would mean that the chain is not sampling the parameter space in an independent manner and so would not approximate the function it was sampling.
- **Recurrence** - once the chain has reached a stationary distribution (such that the probability of a step no longer depends on the starting position) then all subsequent steps will be samples of that stationary distribution. Another way of expressing this is that there exists a non-infinite time for which a chain can return to any previous step once it is stationary.

There are many different MCMC algorithms which satisfy these conditions and which can be used to sample functions or distributions. Different algorithms may be more or less applicable depending on the distribution it is trying to approximate so some care must be taken when deciding which algorithm to use. In the case of the analyses presented in this thesis the Metropolis-Hastings algorithm is used.

5.1.1 Metropolis-Hastings algorithm

MCMC algorithms propose sets of parameter values, or locations in the functions parameter space, to evaluate the function at. These proposals and parameter values are often referred to as "steps" and the MCMC is often described as "stepping" through the parameter space of a function. These proposals then have some probability of being accepted, where the position in the parameter space is updated and new step proposals are made from there, or rejected, where the position in parameter space is kept the same and new step proposals are made from the same position. The algorithm employed in this oscillation analysis is the Metropolis-Hastings algorithm [99], which is perhaps the best known MCMC algorithm. The way that the Metropolis-Hastings proposes steps is following:

1. **Calculate current likelihood** - calculate the likelihood (using eq. (4.13)) at the current step.

2. **Propose new step** - propose a new step by throwing parameter values. For this analysis, a Gaussian proposal function centered at the current parameter values is used to propose new parameter values. The width of this Gaussian is determined by the prior uncertainty on parameters and prior correlation between parameters (which was described in section 4.2). The width can also be adjusted for each parameter by scaling this width. This changing of the proposal functions width is known as step-size tuning and will be discussed in section 5.2.

3. **Calculate proposed likelihood** - calculate the likelihood (using eq. (4.13)) at the proposed step.

4. **Accept or reject step** - in the Metropolis-Hastings algorithm the acceptance probability of a step is based on the likelihood at the current step and the proposed step. In mathematical terms the acceptance probability, α, is given by

$$\alpha = min\left(1, \frac{\mathcal{L}_{\text{proposed}}}{\mathcal{L}_{\text{current}}}\right), \tag{5.3}$$

   where $\mathcal{L}_{\text{proposed}}$ is the likelihood at the proposed step, $\mathcal{L}_{\text{current}}$ is the likelihood at the current step and the *min* function returns the smallest of the two values only. A random number thrown from a uniform distribution between 0 and 1 is then generated. If the random number is below the acceptance probability then the step is accepted. This means that steps where the proposal is to go to a position with a higher likelihood are always accepted.

5. **Update chain** - if a step is accepted then update all parameter values to this accepted position. All these parameter values are saved and appended to the chain. Conversely proposed steps with lower likelihoods are only sometimes accepted with probability α.

6. **Repeat** - repeat this process. If the step has been accepted then the current position will be updated to the proposed position.

A schematic of these steps of the Metropolis-Hastings algorithm is shown in fig. 5.2.

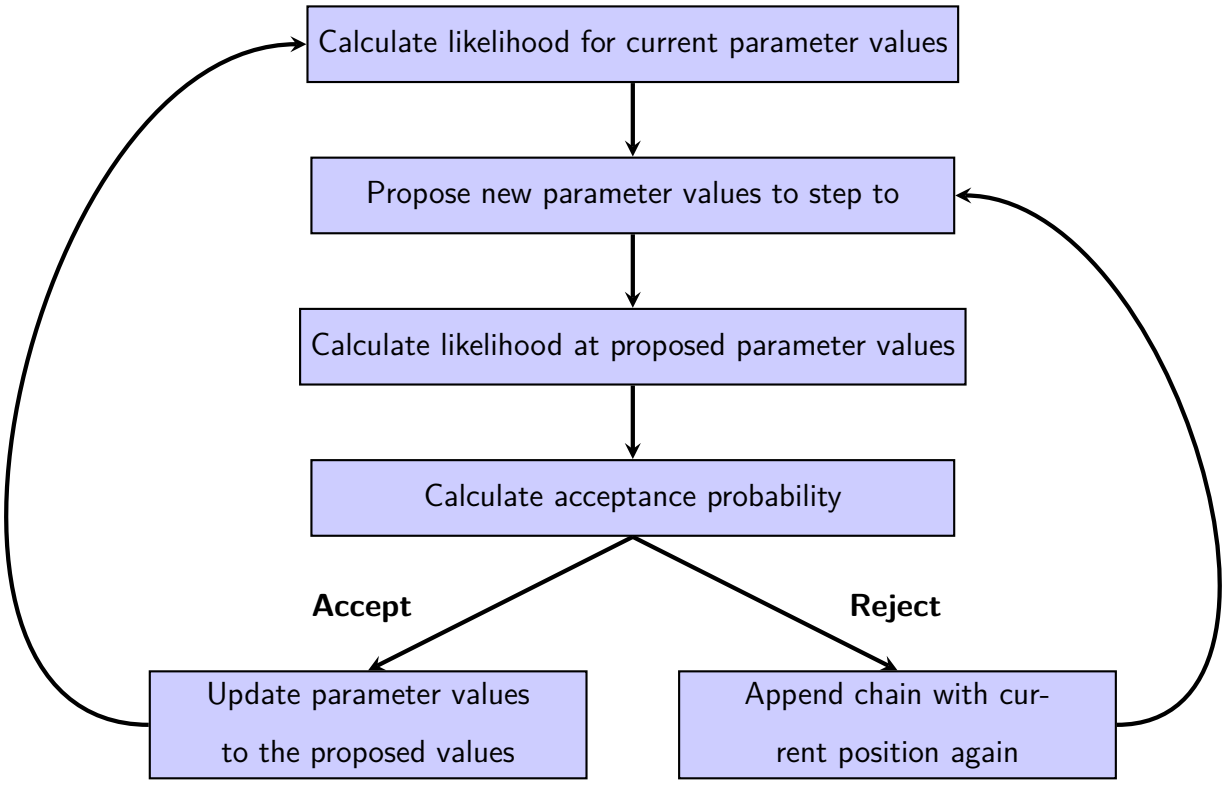

Figure 5.2: A schematic showing the key steps of the Metropolis-Hastings algorithm. This processes is repeated until the number of desired steps have been taken.

5.2 Chain diagnostics

Although the Metropolis-Hastings algorithm is well known to satisfy the requirements of an MCMC algorithm, it is important to verify that the Markov chains being used for an analysis are behaving as anticipated. In particular it is important to check that the acceptance ratio and the correlation between steps have reached stable and sensible values.

5.2.1 Burn-in

As described, Markov Chains are required to reach a stationary state for them to sample the T2K likelihood function (or any function) in an unbiased way. At this stationary state the chain has "forgotten" where it started (i.e. the step probability does not depend on the number of steps any more). However, when running a Markov Chain there will be some time before the chain has reached this stationary state. The period before the chain

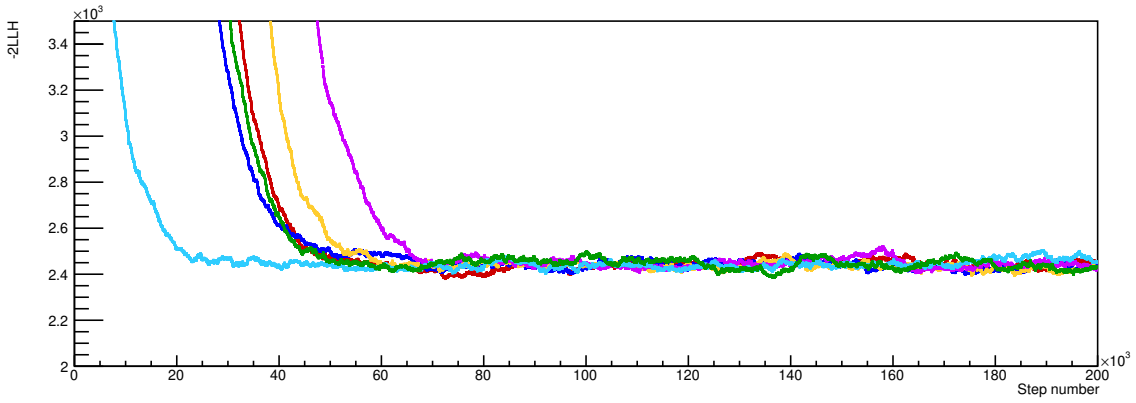

Figure 5.3: The negative LLH of several chains against the number of steps taken. It can clearly be seen that the chains all converge to similar values of the likelihood after $\sim 100 \times 10^3$ steps. The negative LLH often gives very high values initially as initial parameter values can be very unlikely.

has reach a stationary state is called the "burn-in" period and in the case of the T2K analysis is typically on the order of $\sim 100,000$ steps. The burn-in period can be seen clearly in fig. 5.3. When the Markov Chains are used to extract parameter values these steps are disregarded as they are not sampling from the stationary distribution so will not give an accurate representation of the function being sampled. The burn-in period is defined by looking at the logarithm of the likelihood as the step number increases. Once the likelihood value has converged to a relatively stable value then this indicates that the chain has reached a stationary distribution. Additional checks where different burn-in sizes are used when making the results to ensure that the burn-in does not impact the results.

5.2.2 Auto-correlations

A useful variable to consider when looking at chain diagnostics is autocorrelation. Although in a stationary state a Markov chain will be sampling the steps from the same stationary distribution, steps can still be slightly correlated with each other. Autocorrelation is a measure of how correlated a step is with previous steps; in other words this is a measure of how independent steps are. The autocorrelation of particular variable (or

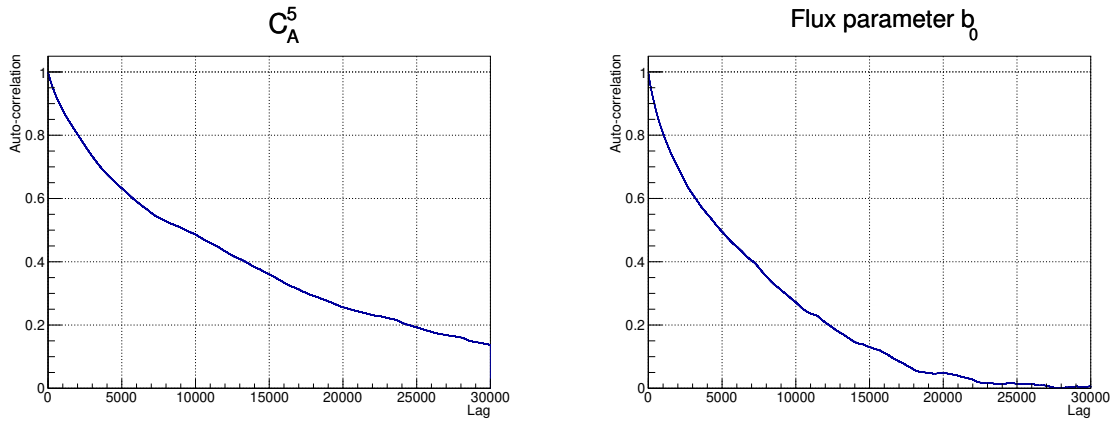

Figure 5.4: Auto-correlation vs. lag for two different nuisance parameters. The autocorrelation decreases as lag increases and is below 0.2 for a lag of 30,000 which what the step size tuning procedure aims for.

set of variables, C_Y, is calculated by using the following formula [98]:

$$C_Y = \frac{\sum_i^{N-l}(Y_i - \hat{Y})(Y_{i+l} - \hat{Y})}{\sum_i^N (Y_i - \hat{Y})^2}, \tag{5.4}$$

where N is the number of steps in a Markov Chain, i is the current step in the chain, Y is the current value of a parameter, $\hat{Y}$ is the mean of a parameter value and l is the lag which is used to look at how correlated steps are at some other position in the chain. For the T2K oscillation analysis an autocorrelation below 0.2 after a lag of 30,000 steps is aimed for across all parameters. To ensure the autocorrelation reaches this target the Markov chain step-sizes can be tuned. For each proposed step the step size in each dimension can be altered to make sure parameter values are being proposed efficiently. If the autocorrelation for a parameter is high, this is often a sign that the step-size is too small so the step size can be increased such that a parameter is sampled more efficiently. An example of the autocorrelation of some parameters is shown in fig. 5.4.

As well as being informative about when a Markov chain has reached stationary distribution, autocorrelation gives the number of total steps necessary to make levels of statistical statements on parameter values. A greater number of samples of the T2K likelihood function will result in a more accurate description of its properties. Therefore, a greater number of steps in a Markov chain will result in more accurate measures of parameter values. However, because each step in a Markov chain is not fully independent the autocorrelation between steps has to be taken into account in estimating the total

number of steps required. To estimate the required number of steps to make statistical statements, for a given autocorrelation and lag, the number of independent steps outside of some probability value can be used, which is given by

$$n = \frac{n_{\text{steps}}(1-\delta)}{l} \tag{5.5}$$

where n is the number of independent steps outside of the credible region given by δ, l is a given lag for some level of autocorrelation and n_{steps} is the number of steps required. For the T2K oscillation analysis, statements on oscillation parameters at $3\,\sigma$ are desirable so δ would be 0.9973. For the fits to data shown in chapter 7 over 150 million steps (post burn-in) were used to make constraints on oscillation parameters. Using eq. (5.5) and a lag of $30,000$ this means there are ~ 50 independent steps outside of the $3\,\sigma$ probability region which is significantly more than needed to make statements at the $3\,\sigma$ significance level. However, the number of independent steps given in eq. (5.5) is only an estimate and in practice the stability of $3\,\sigma$ limits is used to double-check that enough Markov chain steps have been performed. How statistical statements and limits are constructed from the resultant Markov chain will be described in more detail in section 5.3. If the contours are stable when subtracting a significant number of Markov chain steps then this indicates that surplus number of steps has been achieved. Similarly for the Asimov fits shown at the end of this chapter and in chapter 8 the number of steps used are more than great enough to make $2\,\sigma$ statements on oscillation parameters.

5.3 Making measurements of parameters

When sufficiently long Markov chains have been made, these can then be used to extract parameter values and uncertainties which are the most likely given the data and prior systematic uncertainties. The Markov chains sample the likelihood function and build a posterior probability distribution which is the estimate of the likelihood function. This distribution has 773 dimensions which is quite unwieldy. To get from this high number of dimensions to the constraints on parameter values the posterior distribution needs to be projected into marginal posterior densities to give constraints on individual parameters. The way that this is done in this analysis is through marginalisation which is a common statistical technique [26].

5.3.1 Marginalisation of nuisance parameters

The marginalisation of the posterior distribution allows constraints on individual parameters to be made. For a neutrino oscillation analysis the constraints on oscillation parameters are the dimensions of interest, however, nuisance parameters make up the majority of the dimensions of the posterior distribution. Marginalisation can be performed by integrating the posterior over all parameters except for the one of interest. Similarly, for 2D results marginalisation is done by integrating all but the two parameters of interest. The marginalised likelihood can be written as

$$\mathcal{L}_{marg}(o) = \int \mathcal{L}_{tot}(o, f) df, \tag{5.6}$$

where o are the parameters of interest, f are nuisance parameters, $\mathcal{L}_{marg}$ is the marginalised posterior and $\mathcal{L}_{tot}$ is the full posterior distribution. These marginalised posteriors are then binned to give 1D or 2D histograms from which the constraints on parameter values can be extracted. Whether the results for a parameter is given in 1D or 2D will result in slightly different best-fit values and credible intervals due to marginalisation effects. An example of marginalisation in 2D compared to 1D is given in fig. 5.5.

5.3.2 Best-fit values and credible intervals

Once the posterior density distribution has been marginalised, parameter values and their constraints can be measured. To extract parameter values the bin with the highest posterior density in the marginal distribution is chosen. This point is known as the Highest Posterior Density Point (HPDP) and is used as the best-fit values in the results shown in chapter 7 and chapter 8. The uncertainties on parameter values are given a Credible Interval (CI) which gives the range of parameter values which contains a certain fraction of marginal posterior density. These intervals are calculated by finding the bins with the highest posterior density and summing them until the sum reaches a value α, where α is the value for which the CI is quoted for. Typically, CIs are given for 68%, 90% and 99% of the posterior density. These CI then mean that:

$$\int_{\theta_1}^{\theta_2} P(\vec{\theta}|D) d\vec{\theta} = \alpha, \tag{5.7}$$

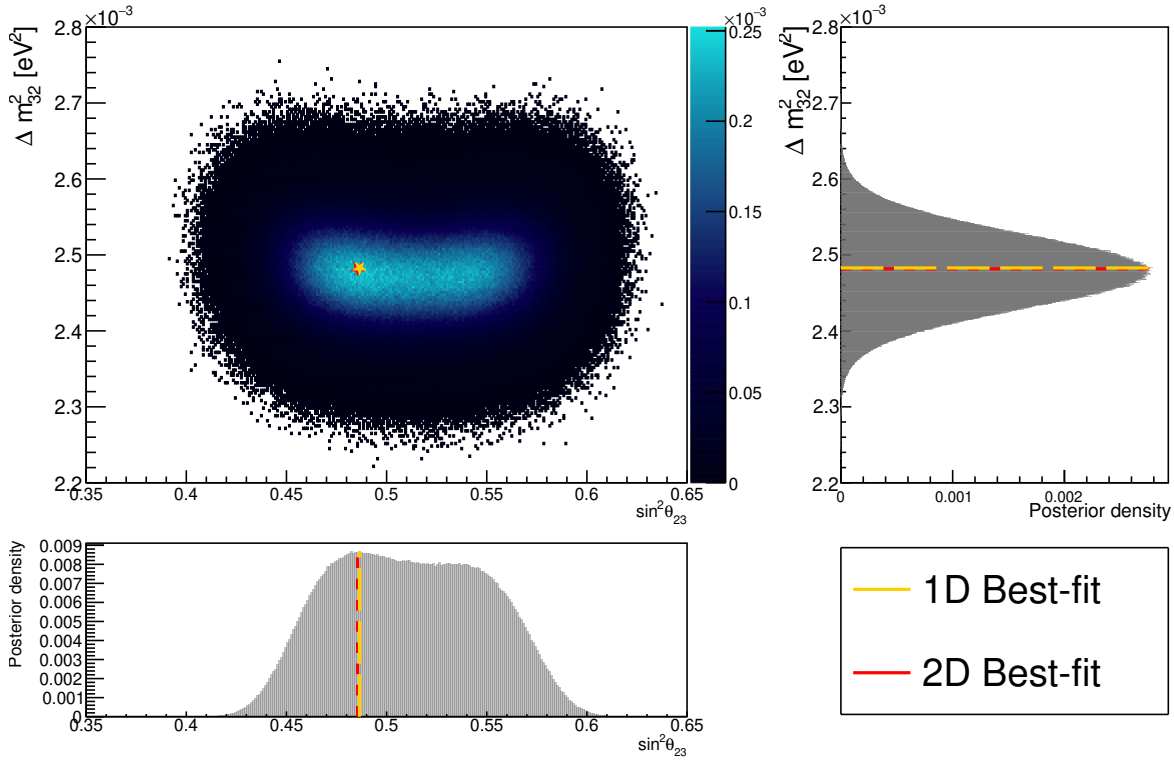

Figure 5.5: An example of 1D and 2D marginalised posterior distributions which also highlight the slight different in parameter value with the highest value in the posterior distribution.

where $\vec{\theta}$ are the set of all parameters used in the likelihood function and D is the data taken at ND280 and SK, θ_1 and θ_2 give the edges of the CI and, again, α is the fraction of posterior probability the CI is quoted for. It is worth noting that due to the normalisation of the posterior distribution, the integral over the full range of any parameter will always give one.

For non-Gaussian parameters the technique described of constructing CIs can result in non-contiguous CIs . Therefore, difficulty in plotting the uncertainty on these parameters can be difficult. For these parameters the mean of the 1D posterior distribution and RMS are used for the best-fit value and 68% confidence interval. This problem does not arise for any oscillation parameters and is only present for a handful of parameters.

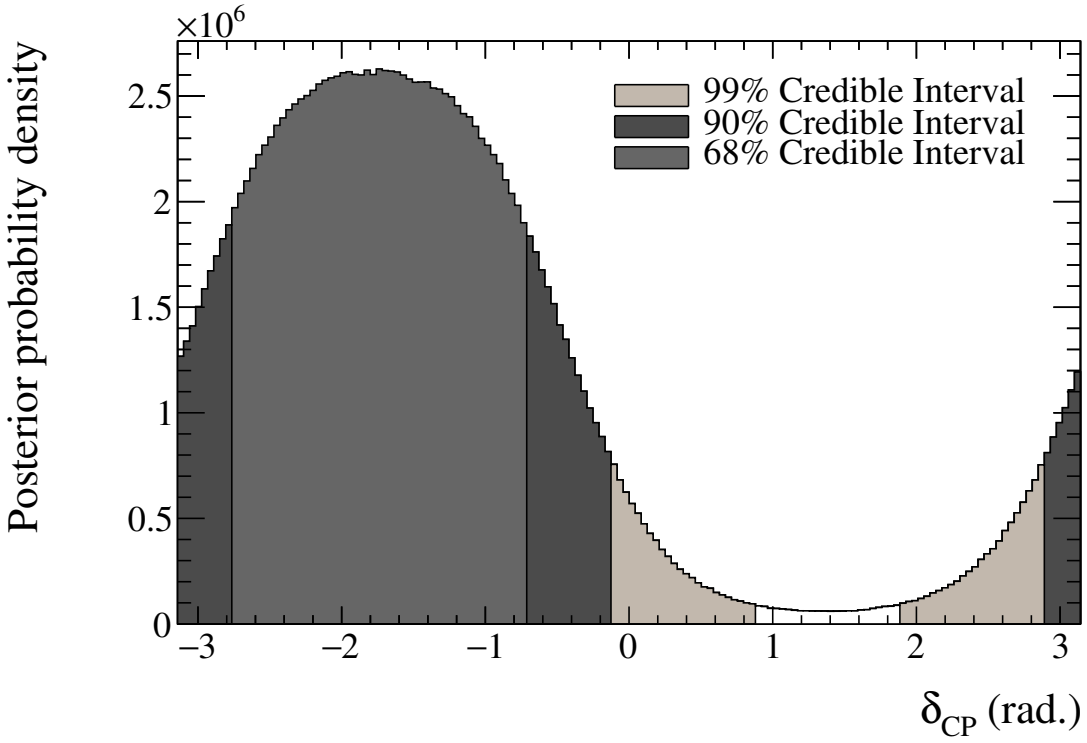

Figure 5.6: An example of 1D CI on δ_{CP} marginalised over both mass hierarchies.

5.3.3 Reweighting of priors

An incredibly useful tool at the disposal of analyses which use Markov chains is the ability to reweight steps in the chains to effectively run with a different prior constraint on a parameter. As long as the posterior from the Markov chain sufficiently covers parameter values, then steps in the Markov chain can be given a weight to simulate the use of a different prior constraint. The use of a prior changes the probability of the Markov chain sampling in certain regions of parameter space. Therefore, reweighting steps based on their parameter values results in the same change in posterior density as using a different prior would. The weight used to do this is simply the ratio of the desired prior to the prior currently used for a parameter at every step in the Markov chain. For example, if a flat prior is used for a parameter then the effect of changing to a Gaussian prior on that parameter could be checked by reweighting steps in the chain with the correct Gaussian weight. In the T2K oscillation analysis, this technique is very useful to study two effects; the impact of using a constraint on θ_{13} coming from reactor neutrino experiments as well as the impact of using a different prior on δ_{CP}.

As mentioned in section 2.3.2, reactor neutrino experiments give excellent constraints on the θ_{13} neutrino oscillation parameter. Electron-neutrino appearance probability depends on this mixing angle and therefore using the constraints from reactor experiments allows T2K to be more sensitive to the value of δ_{CP}. The reweighting of the prior on θ_{13} is a handy trick which saves on computational time as a second fit does not need to be performed using a different prior on θ_{13}. Instead of running a new fit, the steps can simply be reweighted from the original chain based on using a Gaussian prior on θ_{13} taken from the PDG [26].

The second utility of reweighting of steps in the chain is to see the effect of using a different prior constraint on δ_{CP}. It is common practice in Bayesian analyses to study the impact of the choice of prior constraints on parameters of interest to ensure that the choice of prior belief is not impacting the final result significantly. For the T2K neutrino oscillation analysis the parameter of key interest is δ_{CP}, so the impact of changing from having a prior flat across values of δ_{CP} compared to having a prior flat in $\sin\delta_{\mathrm{CP}}$ (which is how δ_{CP} appears in the electron-neutrino appearance probability) is investigated to make sure this has no significant impact. A comparison of using these two priors will be shown in chapter 7.

5.4 Computational improvements

The number of steps required for an MCMC analysis is large. This combined with the high number of systematic parameters means that the computational requirements of an oscillation analysis can be very large. To be able to run an analysis more efficiently and ultimately faster I made significant changes to parts of the MaCh3 framework. This work is particularly important for the results in chapter 8 where adding a data samples into the analysis increases the computational requirements. There are two main areas that have been optimised in the MaCh3 framework; that related to the loading of the TSpline3 objects for cross-section parameters and then calculation of the response to systematic parameters.

The loading of the TSpline3 objects which are used to calculate the response of many

cross-section parameters (as described in section 4.2.2) results in the RAM required to run a Markov chain to be high. For SK MC, this results in 9 GB of RAM being required to load all of the splines. However, not all of the splines that exist have a response to systematic parameters. A TSpline3 object exists for a particular bin (usually in true and reconstructed neutrino energy), for each cross-section parameter and for every interaction mode which a systematic effects. In the case that there are no MC events in an analysis bin a TSpline3 object still exists but its response is completely flat (i.e. it returns a value of one at whatever value it is evaluated at). Particularly for the electron-like samples at SK, where the splines are binned in true neutrino energy, reconstructed neutrino energy and the reconstructed angle between the out-going lepton and incoming neutrino, this results in a number of bins which do not have any MC events contained in them. This results in many splines which all have an identical flat response at a value of one but are all loaded into memory for use in the analysis. Not only do these flat splines occupy more space in memory but they also get evaluated only to return a weight of one and hence unnecessarily increases computation time for each Markov chain step. This problem will only get worse with the addition of more samples into the analysis so improving the treatment of these flat spline objects is important for future analyses as well as current ones. In order to do this, I restructured the spline loading in the MaCh3 framework such that flat splines were identified in the loading and were set to all point to the same flat spline response rather than being actually loaded into memory. Further to this, when splines are evaluated if the spline is known to be flat a weight of 1 is returned rather than the spline being evaluated. These improvements along with other minor optimisations in the code lead to a 30% decrease in RAM usage at SK and 40% decrease in the time taken per Markov chain step. The change in time per step are shown in fig. 5.7.

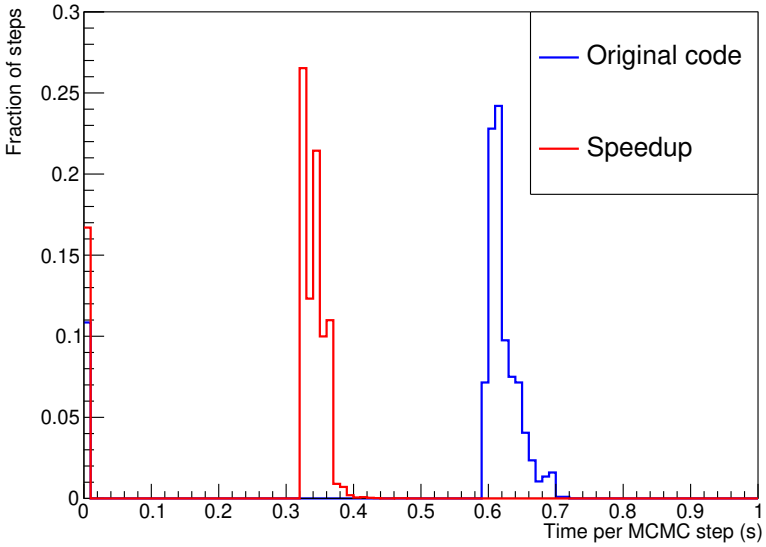

Figure 5.7: A comparison of the step time per MCMC step before and after improvements to the code were made. The step time is reduced by $\sim 40\%$.

5.5 Validation of fitter

Once all the inputs to the analysis have been constructed it is essential to ensure that the analysis framework behaves correctly before fitting to real data. Validations of the analysis framework are done in three main ways; cross-checking with other analysis frameworks used by the T2K experiment, likelihood scans and fits to fake data known as Asimov fits.

5.5.1 Cross-checks with other analysis frameworks

In the T2K experiment there are a total of three analysis frameworks which are used to extract oscillation parameters from data. The three analyses all use slightly different analysis techniques and independent code bases and are therefore an excellent way to look for bugs or unexpected behaviour in one analysis framework (assuming the probability that all three analysis frameworks have identical bugs is very small!). The Markov chain analysis framework described in this chapter is called Markov-Chain-3-flavour (MaCh3) and is used for all the results shown in this thesis. The other two analysis frameworks are P-theta [102] and VALOR [103]. There are two main ways that cross-checks are performed across the fitting groups. Firstly, the event rate prediction at SK for each

fitting group are compared; if these event rates are not found to be in good agreement this indicates a bug or discrepancy in the fitters. Secondly, varying systematic parameter values and making sure that the change in event rate prediction and the predicted event rate spectra at SK for different parameter values is consistent across frameworks ensures that systematic parameters have been implemented consistently.

5.5.2 Likelihood Scans

Another method for validating the analysis framework is to calculate the likelihood of different oscillation parameters using MC that was made with a known set of oscillation parameters. If the analysis framework and the likelihood calculation has been implemented correctly, the minimum of the negative logarithm of the likelihood will be at the oscillation parameter values used to generate the MC. This is an excellent way in checking that the analysis framework is behaving as expected. To make likelihood scans the likelihood of a set of oscillation parameters is computed. This is repeated for many different sets of parameter values until a likelihood surface has been built. Likelihood scans are performed in 1D or 2D of the oscillation parameters with nuisance parameters fixed to their prior central values. Examples of likelihood scans for a given set of oscillation parameters are given in section 5.5.2 and section 5.5.2.

5.5.3 Asimov fits

The natural next step from likelihood scans is to then start running Markov Chains but using a set of fake data inputs. These fake data inputs are simply the predicted event rate spectra at SK that have been made using a known set of oscillation parameters and systematic parameter values set to their prior central values. Again, if the fitting framework is working correctly then the best-fit parameter values returned by the fitter should be very close to the parameter values used to make the fake data. These Asimov fits are often labelled by the set of oscillation parameters used to generate them. The sets of oscillation parameters commonly used are given in table 5.1. The results from an Asimov fit using the oscillation parameters labelled A (referred to as Asimov A) are

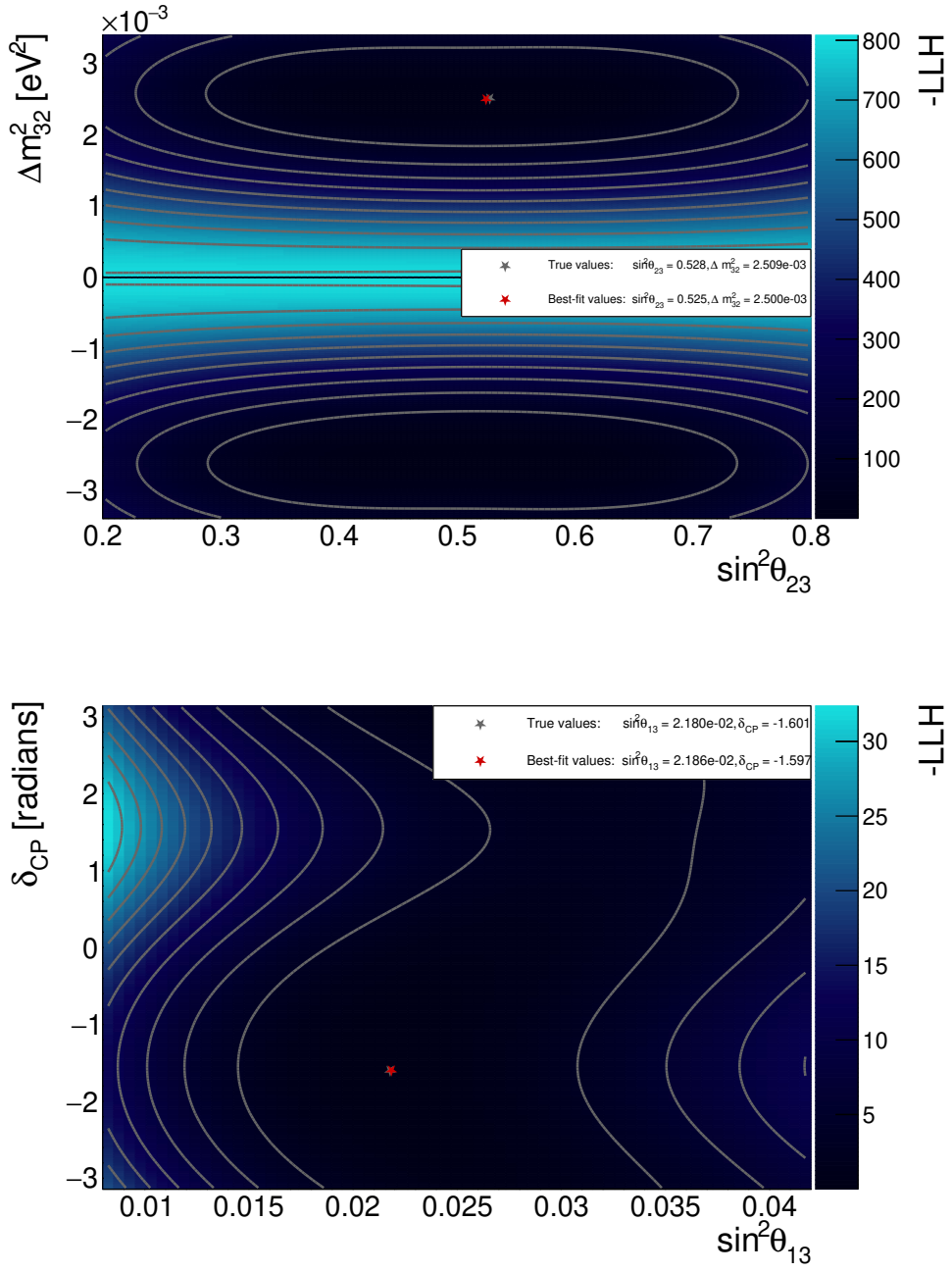

Figure 5.8: 2D likelihoods scan for Δm^2_{32} vs. $\sin^2\theta_{23}$ (top) and θ_{13} vs. δ_{CP} (bottom). The best-fit values found in the likelihood scans are extremely close to the input oscillation parameter values indicating that the likelihood calculation is working correctly. The contours indicate values of constant likelihood.

shown below for Δm^2_{32} vs. $\sin^2\theta_{23}$ and δ_{CP} vs. $\sin^2\theta_{13}$ in fig. 5.9. Systematic parameters values and uncertainties are set to their best-fit values from a fit to near detector data only. Separate Asimov fits are performed to validate that the fitting at the near detector is working as expected but these were not performed by myself so will not be discussed.

The constraints given from a fit to an Asimov dataset also give the sensitivity of an analysis to that set oscillation parameters. They show you the results of a fit if your data were exactly as expected for a given set of parameter values. In this way, Asimov fits serve the dual purpose of validating the fitting framework and giving the expected sensitivity if the set of oscillation parameters used were true in nature. In chapter 8 an Asimov fit will be used to show the potential sensitivity gained from adding new data samples at SK into the T2K neutrino oscillation analysis. Asimov data set will then also be used to show the potential bias that can occur in a neutrino oscillation analysis if neutrino cross-section parameters are not modelled with appropriate uncertainties.

Table 5.1: Oscillation parameter values used for Asimov A fits.

Parameter	value
$\sin^2\theta_{12}$	0.307
$\sin^2\theta_{23}$	0.528
$\sin^2\theta_{13}$	0.0218
Δm^2_{21}	7.53×10^{-5}
Δm^2_{32}	2.509×10^{-3}
δ_{CP}	-1.601

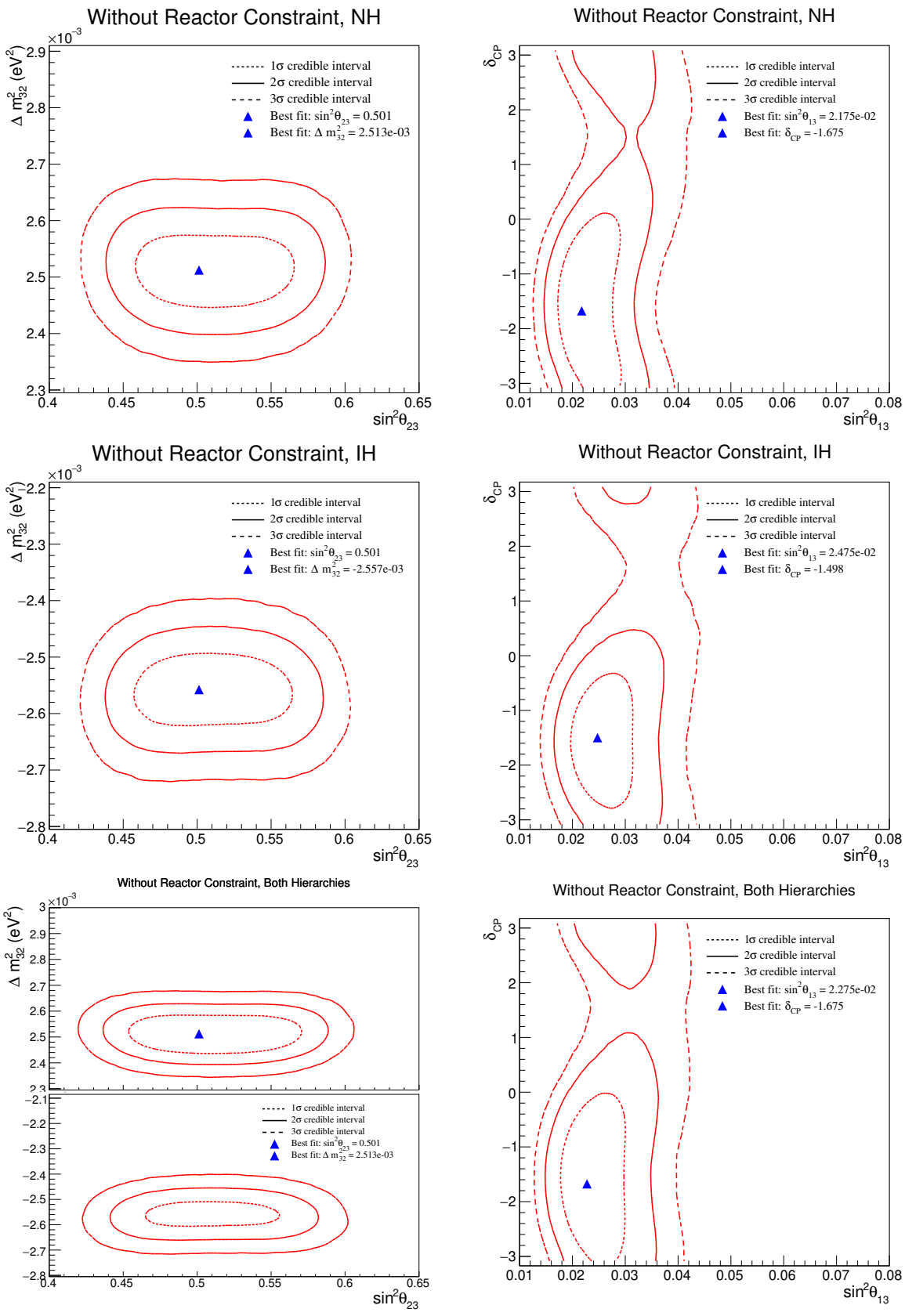

Figure 5.9: 2D constraints on oscillation parameters from an Asimov A fit. Good agreement is found between the input oscillation parameter values and the best fit values retrieved from the fit. The top plots show constraints marginalised over the normal mass hierarchy, middle over inverted mass hierarchy and bottom over both mass hierarchies.

Chapter 6

Neutrino Interaction Uncertainties for the T2K Oscillation analyses

Modelling neutrino interactions and their associated uncertainties are some of the most important aspects of a neutrino oscillation analysis. If appropriate uncertainties are not assigned to the MC predictions used for the analysis, then there may not be enough freedom in the fit to describe the observed data. Especially for oscillation analyses, if the nuisance parameters related to neutrino interactions are unable to describe the data well, then the neutrino oscillation parameters extracted from the fit will be biased. The study of neutrino interactions and how changes to the MC prediction may impact the oscillation analysis results is a very important part of the T2K experiment. For every iteration of the oscillation analysis, updates to the MC and the associated uncertainties are made in order to make more accurate measurements of neutrino oscillation parameters. These updates can be motivated in various ways; theorists may come up with a new model which can be used in MC generators, experiments (including T2K) may publish new cross-section measurements which highlight limitations or preferences to models, or might simply be known that the model used in previous analyses can be improved upon. For example, as the T2K experiment takes more data, the uncertainty coming from the neutrino interaction model will become a greater fraction of the uncertainty on neutrino oscillation parameters. Therefore, there will be a greater motivation to reduce uncertainties on the neutrino interaction model as more data is collected at T2K (and even more

so for future experiments such as DUNE and Hyper-K).

It is also important to consider which uncertainties may become more important for future T2K analyses. In future oscillation analyses, an additional data sample at SK which targets CCRES interactions will be included at SK. A description of this sample and preliminary sensitivity studies with this sample included will be given in chapter 8. As will be shown in chapter 8, this sample includes a significant amount of CCRES, CC Multi-π and CC DIS interactions. The contribution of these interactions are much larger in this new sample compared to the other five sample at SK. Therefore, updates to the uncertainties used for these interactions will be required for the inclusion of this new sample in the oscillation analysis. To this end, new uncertainties for CC Multi-π and CC DIS interactions have been developed. This chapter will describe the development of new uncertainties for CC Multi-π and CC DIS interactions, their motivation and their behaviour in a fit to data.

6.1 Deep Inelastic scattering

Before discussing the new uncertainties designed for CC Multi-π and CC DIS interactions, a more detailed description of CC Multi-π and CC DIS interactions is necessary. The discussion will start with a general description of DIS interactions and how multi-π interactions differ will be highlighted. As has already been described in section 2.4, DIS interactions involve the interaction of neutrinos and the quarks which make up nucleons. These interactions can occur on both the valence quarks and the sea quarks which all make up a particular nucleon. In the generation of DIS events in MC simulations, there are three major parts; the cross-section calculation, the distribution of momenta within the struck nucleon and then the hadronisation of outgoing particles. These three key processes will be described for the NEUT neutrino interaction generator, which is what the T2K experiment uses to generate its MC predictions.

Before looking at how DIS interactions are generated in more detail, it is useful to define some very handy kinematic variables which will be referenced throughout the rest of this chapter. Arguably the two most important variables for DIS are Bjorken-x and

Bjorken-y. Bjorken-x can be thought of as the fraction of momentum that the struck quark inside a nucleon carries and Bjorken-y the fraction of neutrino energy transferred to the hadronic system. From Bjorken-x and Bjorken y the four-momentum transfer squared, Q^2, and the invariant mass of the hadronic system, W, can be calculated. The formula for each of these variables is given below, taken from [11]

$$x = \frac{Q^2}{2p_{nuc} \cdot (p_\nu - p_{lep})}, \tag{6.1}$$

$$y = 1 - \frac{E_{lep}}{E_\nu}, \tag{6.2}$$

$$Q^2 = -(p_\nu - p_{lep})^2, \tag{6.3}$$

$$W^2 = m_{nuc}^2 + 2m_{nuc}E_\nu y(1-x), \tag{6.4}$$

where x is Bjorken-x, y is Bjorken-y, Q^2 is the four-momentum transfer squared, W^2 is the invariant hadronic mass, p_{nuc}, p_ν, p_{lep} are the four-momenta of the nucleon, neutrino and lepton respectively, E_{lep} and E_ν are the lepton and neutrino energy respectively and m_{nuc} is the mass of the nucleon.

The differential cross section of an interaction gives the probability of an interaction occurring. In the generation of DIS events in NEUT the cross section is used to give the probability of a neutrino of a given energy interacting for a particular neutrino interaction mode. For DIS interactions, the cross section used is taken from [104] which gives a double differential cross section in Bjorken-x and Bjorken-y. This double differential cross section for CC neutrino DIS interactions is given in eq. (6.5) from [105] as well as the general definitions of Bjorken-x and Bjorken-y in eq. (6.1) and eq. (6.2).

$$\begin{aligned}
\frac{d\sigma^2}{dxdy} = & \frac{G_F^2 M_N E_\nu}{\pi \left(1 + Q^2/M_W^2\right)^2} \\
& \times \left\{ \left(y^2 x + \frac{m_l^2 y}{2E_\nu M_N} \right) F_1 \right. \\
& + \left[\left(1 - \frac{m_l^2}{4E_\nu^2} \right) - \left(1 + \frac{M_N x}{2E_\nu} \right) y \right] F_2 \\
& \pm \left[xy \left(1 - \frac{y}{2} \right) - \frac{m_l^2 y}{4E_\nu M_N} \right] F_3 \\
& + \frac{m_l^2 \left(m_l^2 + Q^2\right)}{4E_\nu^2 M_N^2 x} F_4 \\
& \left. - \frac{m_l^2}{E_\nu M_N} F_5 \right\},
\end{aligned} \tag{6.5}$$

where G_F is Fermi's constant, M_N is the nucleon mass, E_ν is the neutrino energy, Q^2 is four-momentum tranfser squared, M_W is the W-boson mass, x is Bjorken-x, y is Bjorken-y, and F_i are the structure functions used to describe the momentum distribution of quarks within a nucleon. This then simplifies using Callan-Gross and Albright-Jarlskog relations [105]; $F_2 = 2xF_1$, $F_4 = 0$ and $2xF_2 = F_5$.

The structure functions in eq. (6.5) are calculated from Parton Distribution Functions (PDFs). These PDFs can be interpreted as the distribution of the fraction of total momentum of the nucleon carried by different species of quarks. PDFs have been measured experimentally by a variety of experiments over the years, such as NuTeV and CCFR [106]. The PDFs which NEUT use are the GRV98LO PDFs [107]. The PDFs used can have a significant impact on the differential cross section of DIS interactions.

The DIS model in NEUT splits into two parts; one with events $1.3 < W < 2.0$ GeV/c^2 and one with events where $W > 2.0$ GeV/c^2. The lower W part of the model describes multi-π interactions and the higher W DIS interactions. To generate multi-π and DIS interactions, different approaches for calculating the number of hadrons, or multiplicity, of an interaction are used. It is worth saying that these definitions for multi-π and DIS interactions are specific to the NEUT generator and other neutrino event generators such as GENIE [108] and NuWro [109] have different definitions.

For multi-π interactions a custom hadronisation model is used to describe the multiplicity of interactions. This hadronisation model uses KNO scaling [110] as well as fits to bubble chamber data [111] and will be described in more detail in section 6.3.2. All hadrons produced in these interactions except for the outgoing nucleon are considered to be pions. To avoid double counting multi-π interactions producing single pions and resonant pion production, events where the number of hadrons ≥ 3 are only considered for multi-π interactions (events where the number of hadrons is less than 3 are rethrown in the MC generation). This means that the multi-π cross section is equal to the cross section given in eq. (6.5) multiplied by the fraction of events with the number of hadrons ≥ 3. The momenta of the hadrons is then assigned by decay by the phase-space. Due to the fact that multi-π interactions require at least two pions to be produced, if the fraction of events with more than or less than two pions changes so does the multi-π cross section. This means that a change in the multiplicity in pions produced (by changing the

hadronisation model) will change the cross section of multi-π interactions. The multiplicity model also has a knock on effect to interactions producing pions through resonant interactions. In NEUT (and other neutrino event generators) resonant pion production always produces a single pion. Therefore, a change to the fraction of events producing a single pion will change the number of events which get produced through resonant pion interactions. This makes the systematic uncertainty on the multiplicity model used also interesting to CCRES dominated samples.

The other part of the DIS model are high W interactions. For DIS interactions with $W > 2$, NEUT uses PYTHIA 5.72 [112], a popular generator that is used for high-energy interactions producing many particles. PYTHIA 5.72 uses the Lund string model [113] to describe the hadronisation of particles and is designed to describe interactions at these higher values of W. Since these DIS interactions occur at higher W and typically higher energies these interactions do not have the same level of importance for modelling resonant pion interactions correctly.

6.2 Deep Inelastic scattering at T2K

The T2K experiment uses a neutrino beam with a peak energy of 0.6 GeV. At this energy, DIS interactions are not the most prevalent interactions, instead, interactions such as CCQE, 2p-2h and CCRES are the most common. However, CC Multi-π and CC DIS interactions will still contain oscillated neutrinos so are also signal events. As discussed in **??** the reconstructed neutrino energy assumes either CCQE or CCRES interactions for events at SK depending on the sample. For any CC Multi-π and CC DIS interactions at SK this results in a difference between the true neutrino energy and the reconstructed energy. Therefore, CC Multi-π and CC DIS interactions must be modelled accurately so that oscillation parameters can be extracted without bias. To be able to do this, nuisance parameters related to these interactions must be properly modelled and their uncertainties properly assigned. It is therefore important at T2K that CC Multi-π and CC DIS interactions are modelled correctly to ensure that the data can be properly described by the MC predictions in the analysis.

6.2.1 CC Multi-π and CC DIS at ND280

The data at ND280 has great power to reduce the uncertainty on nuisance parameters related to neutrino interactions (as well as the neutrino flux). In turn, this then means that the predictions at SK have much smaller uncertainties associated with them as the data at ND280 has constrained many nuisance parameters. Conversely, if ND280 cannot describe the data well, this twill be propagated to the MC predictions at SK which will result in oscillation parameters being measured poorly or incorrectly. This is why it is important that the nuisance parameters in a fit can correctly account for the uncertainties which may be present in data.

The samples used at ND280 for the oscillation analysis have already been introduced in section 4.1.2. At ND280, CC Multi-π and CC DIS interactions mainly occupy the CC-1π and CC-Other samples at ND280. Particularly for the CC-1π sample, CC Multi-π and CC DIS interactions pose as a background to the CCRES interactions which the sample aims to constrain. CC Multi-π and CC DIS interactions can be mistaken for CCRES interactions in the case that one or more of the pions produced are absorbed through FSI, or if particles are misidentified or are not identified. CC Multi-π and CC DIS interactions can also be constrained more directly though the CC-Other sample at ND280 which targets events with more than one charged pion, a π^0 or a photon. Many pions can be produced in CC Multi-π and CC DIS interactions, so it is likely that these events are selected in the CC-Other sample. Comparisons of true CCRES, CC Multi-π and CC DIS interactions for the CC-1π^+ and CC-Other samples at ND280 can be seen in fig. 6.1. As can be seen in these figures, both the FGD1 CC1π and CC-Other FHC samples contain large components of CCRES, CC Multi-π and CC DIS interactions.

6.2.2 CC Multi-π and CC DIS at SK

The five samples at SK that are used in the neutrino oscillation analysis have already been outlined in section 4.1.4. Similarly to ND280, these data samples are not primarily composed of CC Multi-π and CC DIS interactions and these interactions act as backgrounds to other signals. The 1ReCC1π sample is the only sample at SK to target CCRES in-

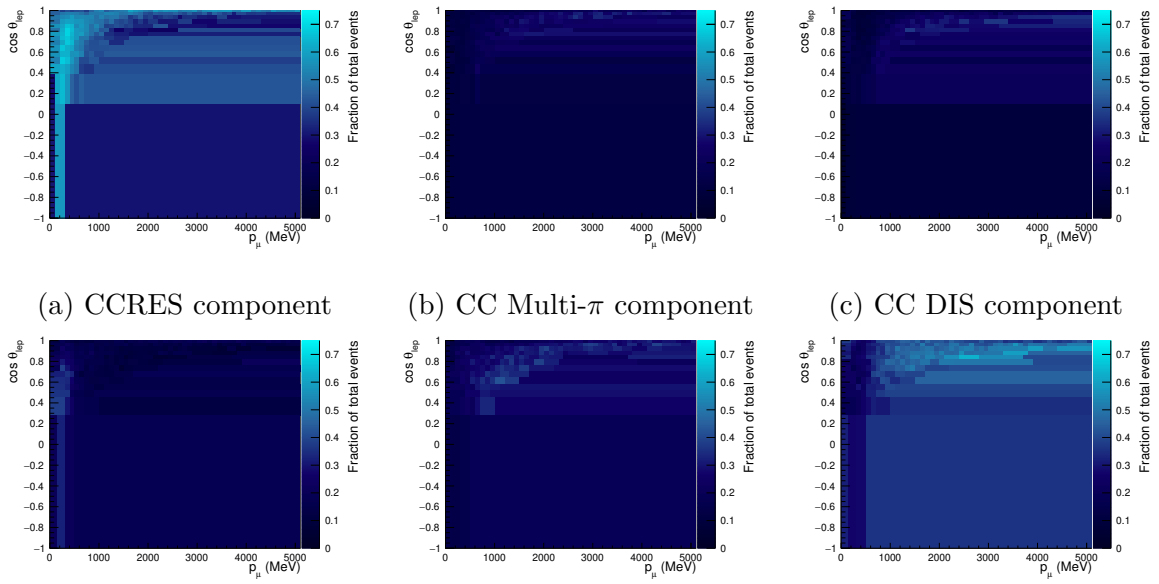

(a) CCRES component (b) CC Multi-π component (c) CC DIS component

(d) CCRES component (e) CC Multi-π component (f) CC DIS component

Figure 6.1: CCRES, CC Multi-π and CC DIS components for the FGD1 CC1π (top) and CC Other (bottom) FHC samples. The z-axis is the fraction of events of a given interaction that make up the nominal MC prediction in each bin.

teractions and since it is an electron-like sample this sample has few events in it. In the future, samples at SK which target CCRES interactions will be included in the oscillation analysis. A discussion of this sample and the importance of CC Multi-π and CC DIS interactions to it will be discussed in chapter 8. The plan to include this sample in the oscillation analysis is one of the key motivations for developing new nuisance parameters for CC Multi-π and CC DIS interactions.

6.3 Improved nuisance parameters for CC Multi-π and CC DIS interactions

As described above, although CC Multi-π and CC DIS interactions are not the most prevalent interaction type at T2K energies, they play an important role in ensuring that oscillation parameters are extracted without bias. In the analysis, how this manifests itself is ensuring that CC Multi-π and CC DIS interactions are assigned appropriate uncertainties in the MC simulation. This then means that the fit is able to correctly account

for any differences between the data and MC predictions. In previous neutrino oscillation analyses, CC Multi-π and CC DIS interactions have had an uncertainty applied to them, however, as more data has been taken and as the neutrino interaction model has grown more complicated, new CC Multi-π and CC DIS uncertainties have been developed. Similarly, with the plan to include the ν_μCC1π sample at SK into the oscillation analysis these uncertainties need to be revisited. The uncertainty used in previous neutrino oscillation analyses will be described so as to highlight where improvements have been made and then a description of the new uncertainties that have been used in the latest analysis.

6.3.1 Previous uncertainty

In previous neutrino oscillation analyses, CC Multi-π, CC DIS, CC interactions producing Kaons, Etas and photons were all grouped together and treated with the same uncertainty. The uncertainty used was based on external data [114], which showed the total uncertainty on DIS interactions at $\sim$ 4GeV is $\sim$ 10%. It was known that this uncertainty should be larger at lower energies so the uncertainty was parameterised as

$$\delta_{\text{CC-Other}} = \frac{0.4}{E_\nu}, \tag{6.6}$$

where $\delta_{\text{CC-Other}}$ is the uncertainty on an interactions and E_ν is the true neutrino energy of an interaction. On first inspection, it appears that this uncertainty will go to infinity at low true neutrino energy but there is a cut off at $\sim$ 0.6 GeV, below which there are no interactions as the cross section for these interactions becomes zero.

The uncertainty used for CC DIS and CC Multi-π interactions in previous analyses has a few limitations. Firstly, the uncertainty is applied to CC Multi-π, CC DIS as well as CC interactions producing Kaons, Etas and photons. This means that all these interactions are 100% correlated in the fit and have the same uncertainty applied to them, despite potentially posing as different backgrounds in different samples in the analysis. If CC Multi-π, CC DIS and these other CC interactions need to change in different ways in a fit to data, then this uncertainty cannot account for this. If the difference between these interactions is large then this may result in a bias in the extracted oscillation parameter results. Secondly, CC Multi-π and CC DIS interactions use different models in MC simulations. Ideally, the uncertainties on processes for CC Multi-π and CC DIS

interactions would be treated independently. Thirdly, the energy dependence of this uncertainty is quite simplistic and does not take into account more recent models and theoretical work.

6.3.2 New nuisance parameters for the oscillation analysis

As has been described, the uncertainty used for CC Multi-π and CC DIS interactions in previous oscillation analyses had limitations. Since CC Multi-π and CC DIS interactions will become more important to the T2K analysis with the addition of the FHC ν_μCC1π sample at SK, it is desirable to make improvements to how the uncertainty on these interactions is implemented. In the description in section 6.1, two sources of uncertainty have been highlighted in the calculation of the cross section; the PDFs and the multiplicity model. These sources resulted in six new nuisance parameters being created and used in the analysis; three shape parameters and three normalisations parameters.

Corrections by Bodek and Yang

Using different PDFs result in different cross sections for CC Multi-π and CC DIS interactions. In NEUT, two versions of the GRV98LO PDFs are available. One of these versions of the PDFs has been adapted using several corrections taken from fits to photoproduction data and electron scattering data [88]. The motivation of the authors performing these fits was to make the PDFs able to describe both low and high Q^2 interactions such that (long-baseline) neutrino experiments can use them more reliably in their analyses. To make these corrections, the authors, Bodek and Yang, propose changes to the scaling of the PDFs. These corrections include several terms to include higher order QCD effects, as well as a factors which are applied to all PDFs to allow them to describe low Q^2 interactions. The new scaling variable used in these corrections, which is used instead of Bjorken-x in the structure functions:

$$x \rightarrow \xi_W = \frac{2x(Q^2 + M_f^2 + B)}{Q^2\left[1 + \sqrt{1 + (2Mx)^2/Q^2}\right] + 2Ax}, \tag{6.7}$$

where x is Bjorken-x, M_f is the final mass of the quark, M is the mass of the nucleon, Q^2 is the usual four-momentum transfer squared and A and B are parameters used in

the fit to electron scattering and photo-production data. There are two factors applied to the PDFs so that they are able to describe low Q^2 data, one for valence quarks and one for sea quarks which are

$$K_{sea} = \frac{Q^2}{Q^2 + C_s}, \tag{6.8}$$

$$K_{valence} = \left[1 - G_D^2(Q^2)\right] \left(\frac{Q^2 + C_{v2}}{Q^2 + C_{v1}}\right), \tag{6.9}$$

where Q^2 is the usual four-momentum transfer squared, G_D is the proton elastic form factor and C_s, C_{v1} and C_{v2} are parameters used in the fit to data. These K factors are found for u and d quarks separately. In total, there are eight parameters which modify the GRV98LO PDFs. From now on these corrected PDFs will be referred to as "Bodek-Yang" corrections or "BY" corrections. The BY corrections are the model which is used for the nominal MC predictions for the T2K experiment. The other available version of the PDFs are the version of the GRV98LO PDFs which have not had corrections applied to them. These PDFs will be referred to as "without BY" or "no BY" from now on. The predictions for BY corrections and no BY corrections for CC Multi-π and CC DIS are shown in fig. 6.2.

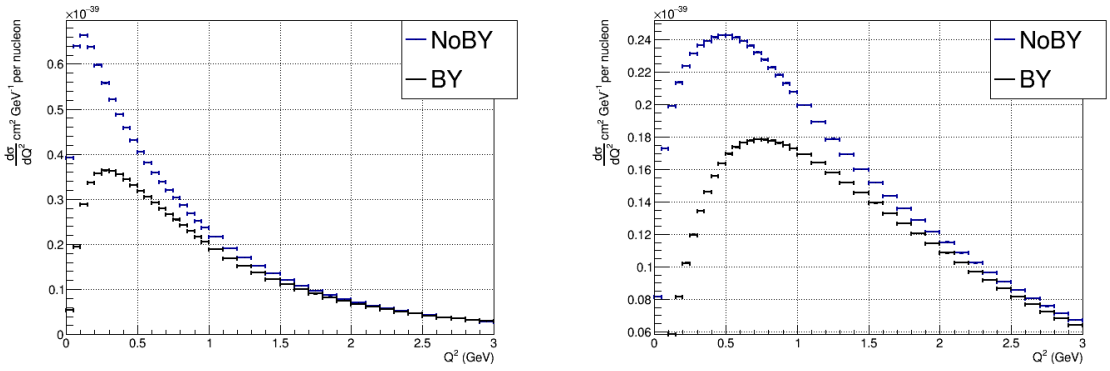

(a) ν_μ CC Multi-π on water

(b) ν_μ CC DIS on water

Figure 6.2: Comparisons of the cross sections in MC events using PDFs with BY corrections and without (No BY). A significant difference can be seen in the low Q^2 region for both CC Multi-π and CC DIS interactions.

The choice of which PDFs to use, results in different MC predictions for CC Multi-π and CC DIS interactions since the cross section changes. The BY corrected version of the PDFs should be more reliable for neutrino interactions since they have been tuned to lower energy interactions, however, most of the data used is from electron scattering data

which will not constrain the axial part of neutrino interactions. Similarly, other PDFs are available that could be used to simulate DIS interactions, again, these will change the predictions for CC DIS and CC Multi-π interactions. Therefore, although the BY corrected PDFs are more appropriate to use for neutrino interactions, it is still important to model uncertainties around the MC predictions from these PDFs. Unfortunately, the eight parameters in the BY corrections are published without errors and without correlations between the parameters. Practically, this makes it hard to use the parameters as a way of changing the MC predictions. Instead it was decided to use the difference between the predictions using the BY corrected PDFs and the PDFs without BY corrections as the 1σ uncertainty and use this to parameterise the uncertainty on CC DIS and CC Multi-π interactions.

To be able to apply an uncertainty to CC DIS and CC Multi-π interactions in a neutrino oscillation analysis, the MC prediction needs to be reweighted to account for a change in model used to make the prediction. This reweighting was done by making a set of binned inputs for C, O and H targets and for ν_μ, ν_e, $\bar{\nu}_\mu$ and $\bar{\nu}_e$ interactions. Each input was made by taking the ratio of MC simulations made without BY corrections to with BY corrections in Q^2 and true E_ν in nucleon frame. These two kinematic variables were used as the largest difference between the cross sections using the different PDFs is seen in Q^2. True E_ν in nucleon frame was also used to reduce the impact of nuclear effects on the reweighting. Since the neutrino oscillation analysis at T2K only uses lepton kinematics in the fit binning, the focus on the reweighting was to produce a reliable uncertainty in lepton kinematics only. Although changes to the PDFs will also create changes to the prediction of energy of outgoing hadrons, the reweighting will not accurately reproduce outgoing hadron kinematics. Examples of these inputs can be seen in fig. 6.3. All the inputs used for the different targets and neutrino flavours can be found in appendix A.1. When calculating the weight to apply to an event the kinematics of that event are found and the relevant bin of the input is then used. Linear interpolation is used between bins to make the reweighting less dependent on the choice of binning used for the inputs. The weight to apply to an event is then calculated by:

$$w = 1 + n \cdot x, \tag{6.10}$$

where w is the weight to be applied to the nominal MC predictions, n is the value returned

from the input histogram bin and x is the value associated with the nuisance parameter which is in units of σ and varies from -3 to $+3$ with 0 corresponding to the nominal MC prediction.

The difference between the predictions made with BY corrections and without can be large especially at low Q^2 which results in large weights being applied to the MC simulations in the reweighting. The uncertainty is applied symmetrically around the nominal MC prediction, so particularly at regions of low Q^2 shifts of -2 or -3 σ away from nominal would result in a negative cross section. To avoid this, if a negative cross section is found from the reweighting a weight of value one is returned instead. In an oscillation analysis, this prevents the nuisance parameters going to unphysical values and means that only the penalty term will contribute to the likelihood calculation since the MC prediction will not be modified.

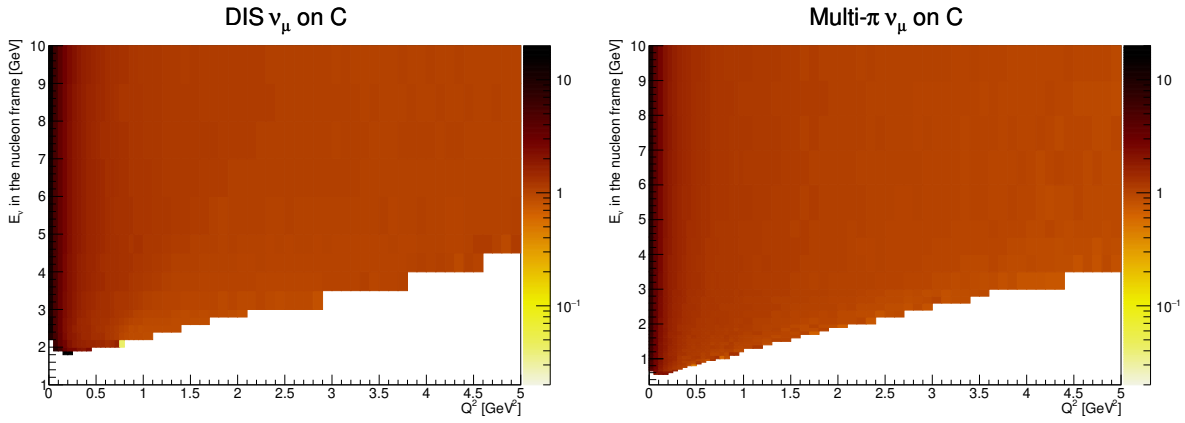

Figure 6.3: Example of inputs used for reweighting the MC prediction in the fit. The area of large difference comes in regions of low Q^2. This can be seen as the largest weights in the inputs can be seen in these regions.

To check that the reweighting was behaving well, MC events made with BY corrections reweighted to be equivalent to no BY were compared with MC events made without BY corrections. Some of these checks can be seen in fig. 6.4. Generally, the reweighting works reasonably well and captures the majority of the difference between the two PDFs. There are some regions at the edge of phase-space where the reweighted prediction does not match the MC generated with the other PDFs and this is believed to be because of non-overlapping phase-space between the two models. Considering that where the reweighting does not work perfectly the difference in the cross section is of order

$\sim 10^{-41}\text{cm}^{-2}$ the reweighting was considered more than good enough to encapsulate the uncertainty on CC DIS and CC Multi-π interactions coming from using BY corrections and not using BY corrections. Additional plots comparing the reweighting of MC events with those generated without BY corrections are given in appendix A.2.

Two uncertainties from the difference in using PDFs with BY corrections and without are used in the neutrino oscillation analysis; one for CC DIS and one for CC Multi-π. Since CC Multi-π and CC DIS interactions act as different backgrounds in different samples in the oscillation analysis, these two uncertainties are uncorrelated when used in a fit. These two uncertainties are implemented as shape parameters in the fit with there response across a $\pm 3\sigma$ range from the nominal prediction is described by a cubic spline. Examples of the splines used are shown in fig. 6.5. The changes to the predictions at ND280 and SK will be shown in section 6.3.3.

NEUT multi-pion multiplicity uncertainties

The other part of the DIS model at T2K that can change the MC prediction is the choice of the multiplicity model used. As has already been discussed, for high W DIS interactions PYTHIA 5.72 is used to calculate the multiplicity of an interaction whereas for low W (multi-π) interactions a custom model is used. Particularly for the multiplicity model for multi-π interactions, since this is tuned to experimental data there is an uncertainty associated with the model. For example, both NEUT and GENIE use a custom model based on KNO scaling [110] to simulate hadronisation for multi-π interactions. However, these hadronisation models are tuned to slightly different bubble chamber data so result in different multiplicities in simulations. KNO scaling is an experimentally observed phenomenon that the average multiplicity in an interactions is linear with the logarithm of W^2 i.e.:

$$< n_{multiplicity} >= \alpha + \beta \cdot \ln(W^2). \tag{6.11}$$

where $< n_{multiplicity} >$ is the mean average multiplicity in an interaction, W^2 is the invariant hadronic mass squared and α and β are two coefficients that come from fitting to bubble chamber data. In NEUT the multiplicity model for multi-π interactions uses $\alpha = 0.06$ and $\beta = 1.22$. Whereas in GENIE, the AGKY multiplicity model is used [115]

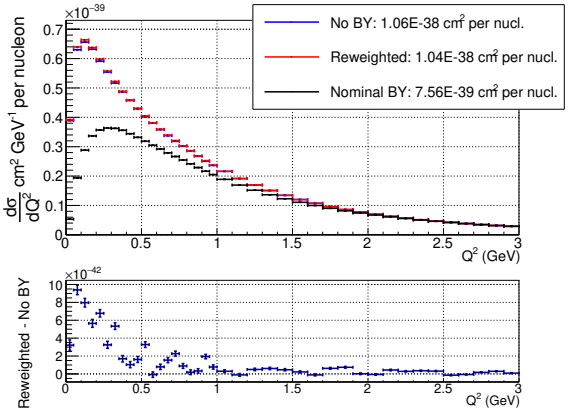

(a) ν_μ CC Multi-π BY in Q^2

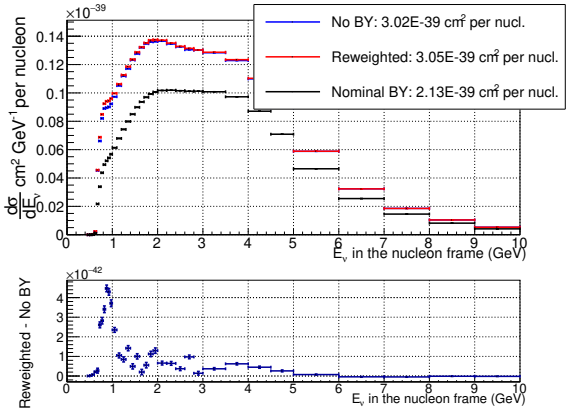

(b) ν_μ CC Multi-π BY in E_ν in the nucleon frame

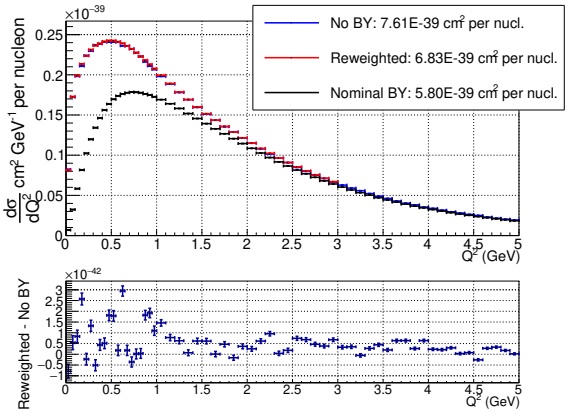

(c) ν_μ CC DIS BY in Q^2

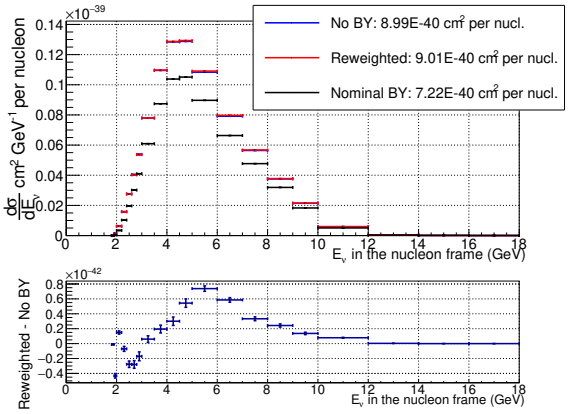

(d) ν_μ CC DIS BY in E_ν in the nucleon frame

Figure 6.4: Comparisons of MC events reweighted from using BY corrections to without BY corrections using the inputs given in fig. 6.3 for ν_μ CC Multi-π (top) and CC DIS (bottom) interactions on water. Comparisons are given in the two variables the inputs were made in i.e. Q^2 (left) and E_ν in the nucleon frame (right). The lower panels in all the plots show the difference between reweighted MC and that generated without BY corrections. Generally the reweight MC matches well with MC events that were generated without BY corrections however some differences arise a low Q^2 and low E_ν in the nucleon frame. However, these differences are small and in a region where the cross sections are very small originally. To aid in the comparisons the integral of each distribution is given in the legend for the MC events made with BY corrections, the reweighted ones and those generated without BY corrections to the PDFs.

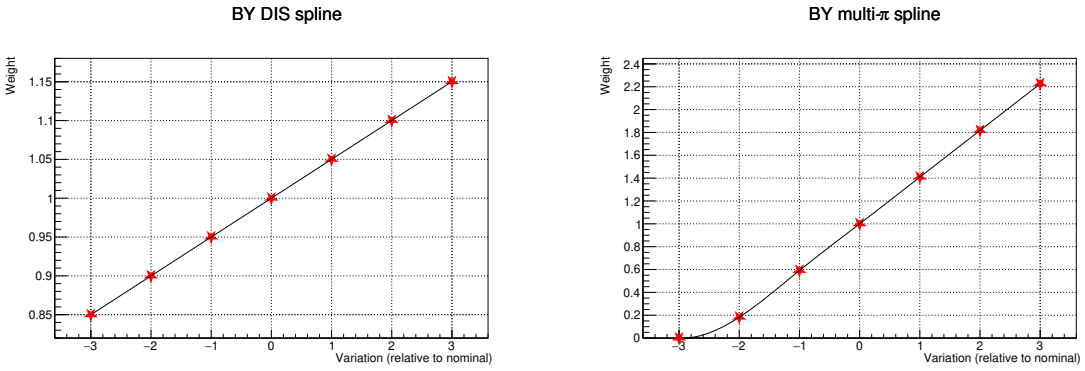

Figure 6.5: Examples of splines used for the BY uncertainty for CC DIS (left) and CC Multi-π (right) interactions. These splines exhibit typical behaviour in returning weights larger than one for positive variations relative to nominal and negative for variations less than zero. The red stars indicate the spline knot positions.

to generate the multiplicity of multi-π interactions. The AGKY model also uses different α and β values depending on the nucleon and neutrino flavour. Since multi-π interactions can only have two or more pions, a change in the multiplicity will result in a change in the cross section since only events with two or more pions are kept in the simulation. Therefore, a systematic parameter which changes the CC Multi-π cross section based on changing the multiplicity model in NEUT to the AGKY model that GENIE uses has been developed. This uncertainty is implemented using a set of inputs which give the ratio of the CC Multi-π cross section for ν_e, ν_μ, $\bar{\nu}_e$ and $\bar{\nu}_\mu$ as a function of true neutrino energy. Again, like the uncertainty from BY corrections, the difference between the models is taken as the one σ uncertainty around the default NEUT CC Multi-π prediction. For use in the oscillation analysis events have to be reweighted to change the MC prediction. To do this the ratio of the two cross sections is taken from the appropriate bin in true neutrino energy from the input for a particular neutrino flavour. The inputs used for this reweighting can be seen in fig. 6.6 and were provided by Christophe Bronner and were made by generating MC with NEUT using the α and β coefficients from the AGKY model. This uncertainty was implemented in the neutrino oscillation analysis as a shape parameter through the use of cubic splines. Examples of the splines for this multiplicity uncertainty used at SK can be seen in fig. 6.7. There is no comparison available for reweighted events and those made with the AGKY multiplicity model in NEUT as the model has not been fully implemented yet.

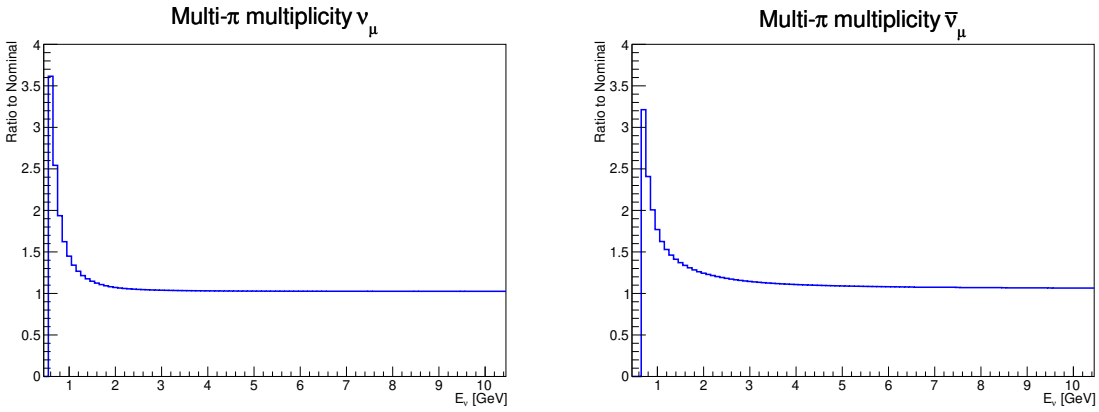

Figure 6.6: Examples of inputs used for reweighting MC predictions based on uncertainties on the CC Multi-π multiplicity model. The weights are taken from the ratio of predictions using the AGKY multiplicity model to the nominal NEUT prediction. The x-axis is true neutrino energy.

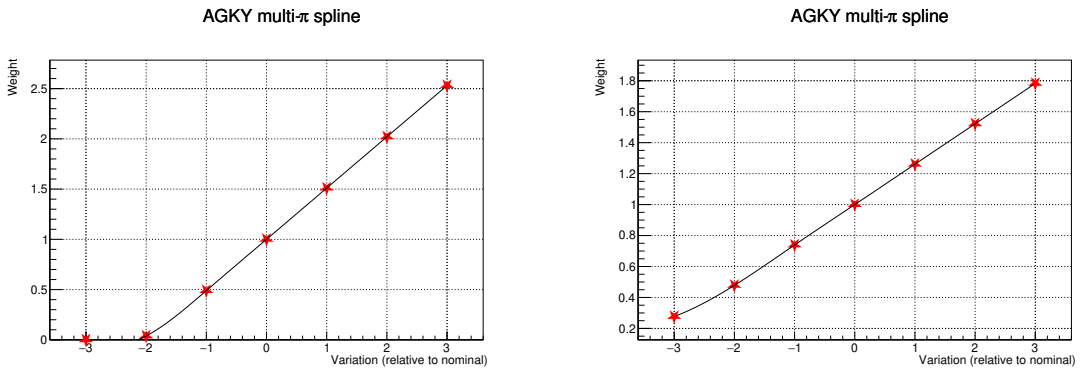

Figure 6.7: Examples of the splines response to the AGKY reweighting at different parameter values.

Additional normalisation uncertainties

As well as the new shape parameters described above, some additional normalisation parameters have been included. These include separate normalisation for neutrino and antineutrino interactions. These normalisations apply to both CC DIS and CC Multi-π interactions together and are motivated by the fact that the NEUT CC inclusive cross section differs from the PDG world-average at high energies [26]. An uncertainty of 3.5% is applied for neutrino and 6.5% for antineutrino interactions. Furthermore, since in the new uncertainties for CC Multi-π and CC DIS no longer include CC interactions including Kaons, Etas and photons, an additional normalisation parameter which accounts for an uncertainty in these interactions was added into the analysis. A conservative 100% uncertainty is given to this normalisation.

6.3.3 Impact on MC predictions

To show the impact that the uncertainties have on the predictions at ND280 and SK MC predictions for a variety of different nuisance parameters values have been made. These can be seen in fig. 6.8 and fig. 6.9 for the FGD1 CC1π and CC-Other FHC samples at ND280 and fig. 6.10 for SK, these are only shown for the shape parameters.

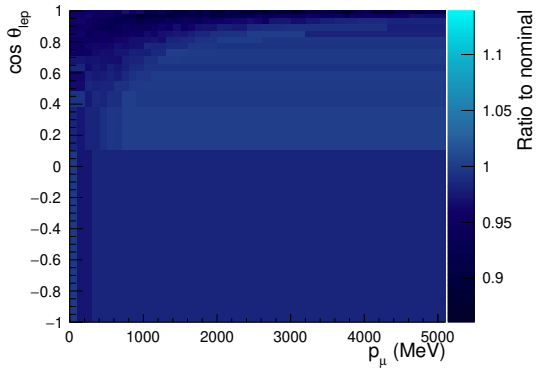

(a) -1σ BY CC Multi-π

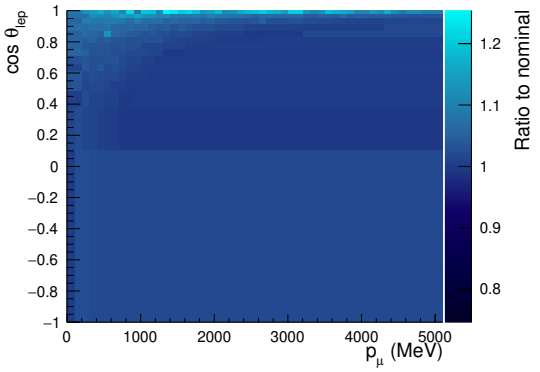

(b) $+1\sigma$ BY CC Multi-π

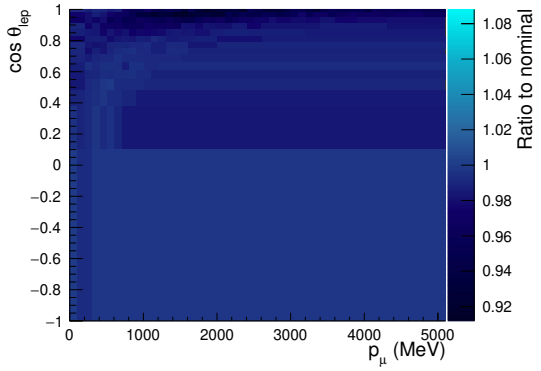

(c) -1σ BY CC DIS

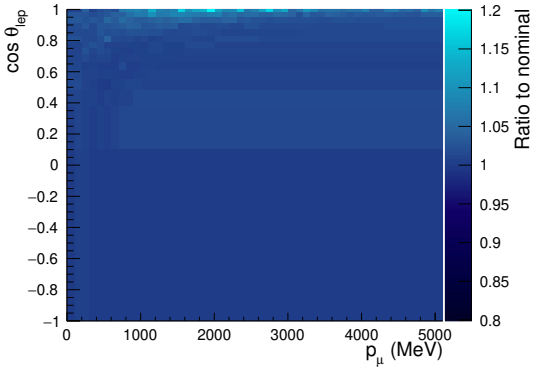

(d) $+1\sigma$ BY CC DIS

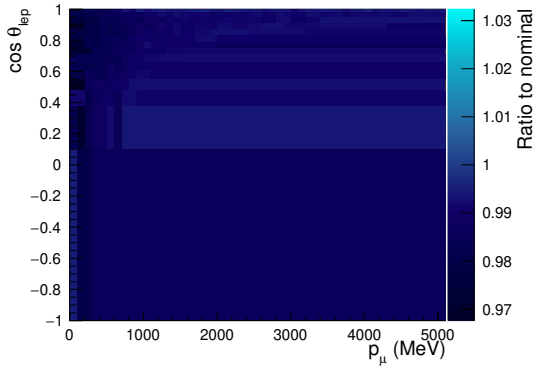

(e) -1σ CC Multi-π multiplicity

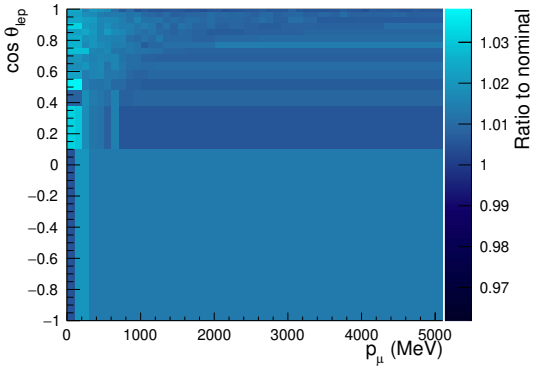

(f) $+1\sigma$ CC Multi-π multiplicity

Figure 6.8: The impact of the new uncertainties on CC DIS and CC Multi-π interactions on the FGD1 CC-1π FHC sample at ND280. The impact is shown as a ratio to the nominal MC prediction and for variation of $+1\sigma$ and -1σ.

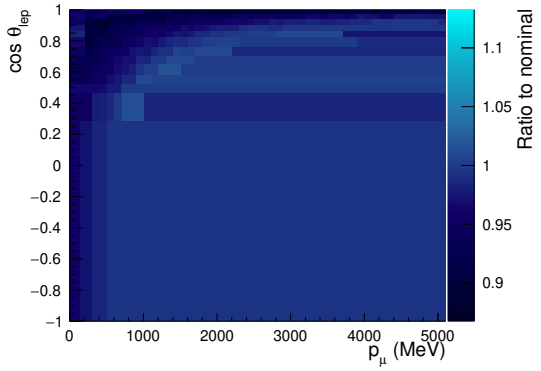

(a) -1σ BY CC Multi-π

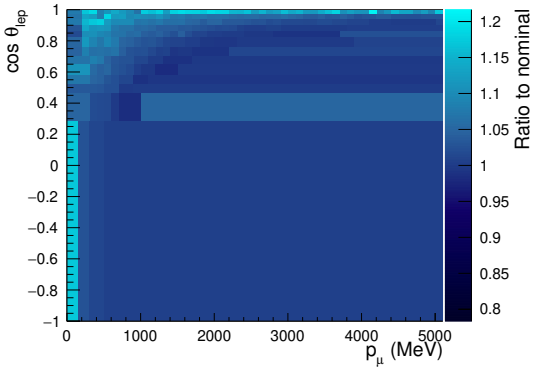

(b) $+1\sigma$ BY CC Multi-π

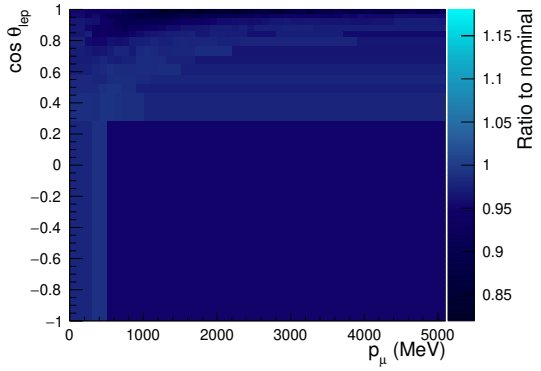

(c) -1σ BY CC DIS

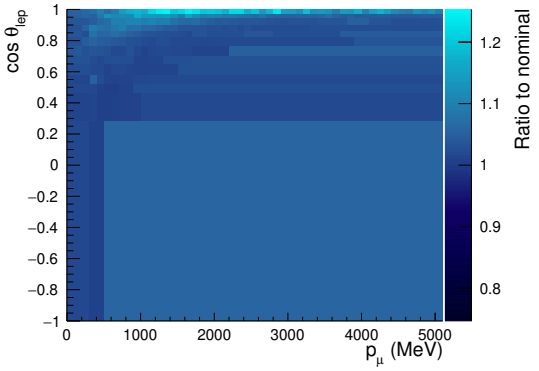

(d) $+1\sigma$ BY CC DIS

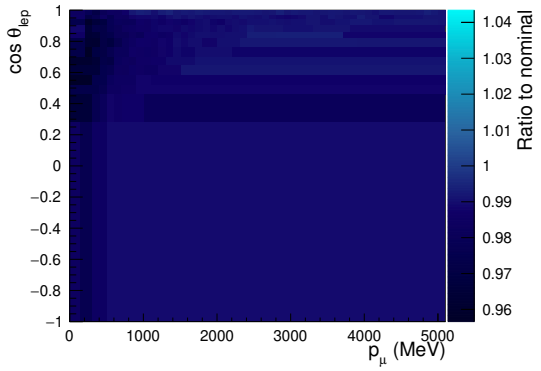

(e) -1σ CC Multi-π multiplicity

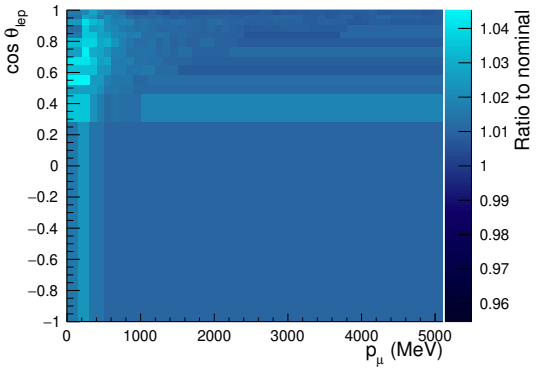

(f) $+1\sigma$ CC Multi-π multiplicity

Figure 6.9: The impact of the new uncertainties on CC DIS and CC Multi-π interactions on the FGD1 CC-Other FHC sample at ND280. The impact is shown as a ratio to the nominal MC prediction and for variation of $+1\sigma$ and -1σ.

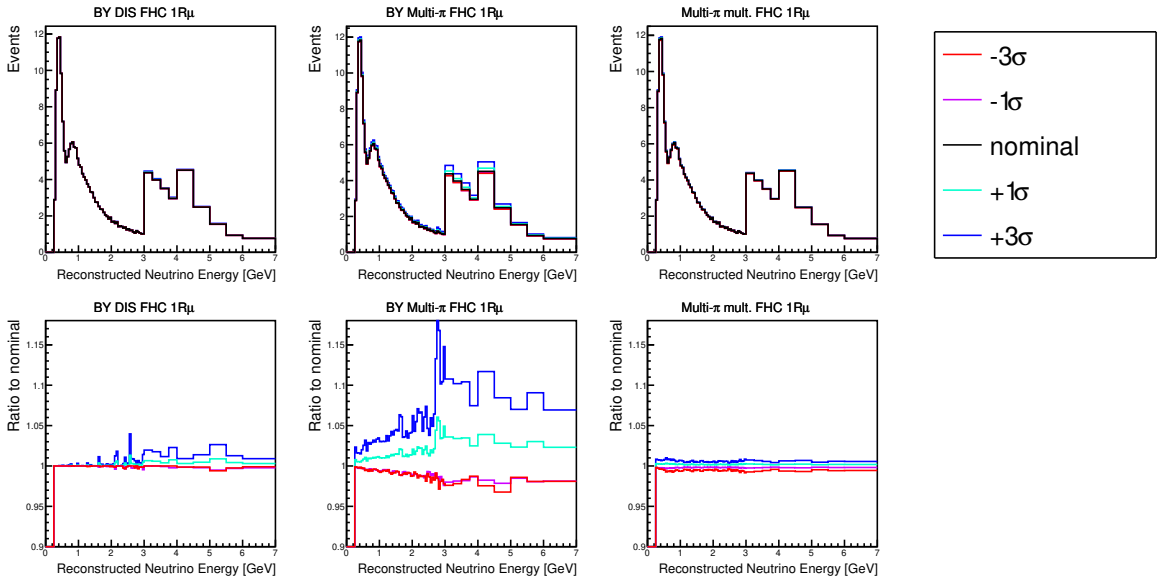

Figure 6.10: Variations of the three new systematic parameters for CC DIS and CC Multi-π interactions and how they affect the FHC 1Rμ MC prediction at SK. It can be seen that the parameters which affect CC Multi-π interactions have the largest impact since there are more CC Multi-π interactions predicted for this sample than CC DIS interactions.

6.4 Behaviour of parameters in a fit to data

The new uncertainties used in the latest neutrino oscillation have been highlighted above. These parameters have been used in a fit to data from which neutrino oscillation parameters were extracted. The oscillation parameter constraints from this fit are the subject of the next chapter. It is also interesting to look at the post-fit parameter values from the fit to data to ensure that none of the parameters have gone to unexpected values. To this end, the post-fit nuisance parameter values related to cross section parameters are shown in fig. 6.11. Their post-fit values are shown from a fit to ND280 data only as well as a joint fit of ND280 and SK data. Interestingly, the constraint on the new uncertainties becomes weaker when SK is also fitted. This implies that there is some difference in the preferred values of the parameters between ND280 and SK and results in a larger uncertainty. Alternatively, it could be that these CC DIS and CC Multi-π parameters anticorrelate with SK detector systematics which are only present in the joint ND280 and SK fit. The difference between the ND280 and the joint ND280 and SK fit highlights the importance in improved systematic treatment to CC DIS and CC Multi-π

interactions. If there was not sufficient freedom in the systematic parameters to show this difference between the ND280 and SK then the parameters would be applied to SK at values which don't agree with the SK data and could cause a bias in the oscillation parameters.

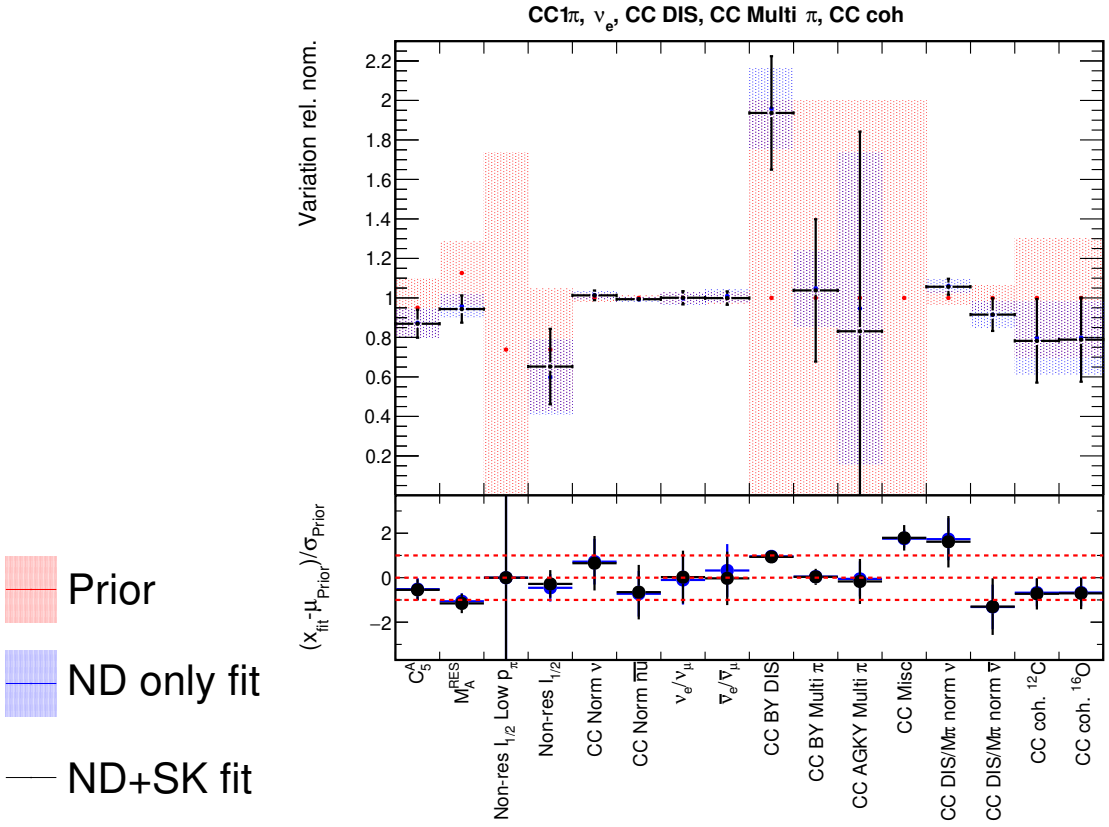

Figure 6.11: Parameter value comparisons pre-fit (i.e. at prior central values) (red), post a fit to ND280 data only (blue) and then post a joint-fit of ND280 and SK data (black). The joint-fit has very similar post-fit parameter values compared to the ND280 only data fit as the ND280 data provides a much larger constrain on parameters.

6.5 Summary

This chapter has described DIS interactions and how they pose as important backgrounds to signals in the oscillation analysis. In order to account for the uncertainties related to CC Multi-π and CC DIS interactions at T2K, a new set of uncertainties related to these interactions were developed. These new uncertainties improve upon the old uncertainties in that they now account for CC Multi-π and CC DIS interactions having different

uncertainties as well as targeting specific parts of the simulation of these interactions in NEUT. An uncertainty on the PDFs used to calculate the cross section for CC DIS and CC Multi-π interactions has now been implemented where the uncertainty is motivated by the corrections made by Bodek and Yang to the GRV98LO PDFs. Also an uncertainty is now applied to CC Multi-π interactions based on a change in the multiplicity model which ultimately changes the number of events which produce more than one pion. The importance of these new uncertainties to an oscillation analysis with an additional sample included at SK will be shown in chapter 8.

Chapter 7

Neutrino Oscillation analysis using runs 1–10

The technique described in chapter 4 and chapter 5 as well as the new neutrino cross-section systematics related to CC Multi-π CC DIS interactions described in chapter 6 are all brought together in the fit to data presented in this chapter. The results shown here are the most recent and most sensitive measurements of neutrino oscillation parameters from the T2K experiment. The improvement in precision comes from both increased data statistics as well as many improvements to the modelling of nuisance parameters including the improved treatment of CC DIS interaction uncertainties described in chapter 6. At the time of the analysis, all the available POT at ND280 and SK were used in the analysis. The POT accumulated and beam power for each run of the J-PARC neutrino beamline can be seen in fig. 7.1. Before showing the constraints on neutrino oscillation parameters the data used in the analysis will be described along with the MC predictions for each data sample. Then two sets of oscillation parameter results will be shown; one using a flat prior on $\sin^2\theta_{13}$ (without reactor constraint) and one using a Gaussian prior on $\sin^2\theta_{13}$ (with reactor constraint). MC predictions of the spectra for each sample from the post-fit will then be show in section 7.5 through the use of posterior predictive distributions. Tests of the use of the prior constraint on δ_{CP} will then be checked by showing comparisons of data fits using a flat prior on δ_{CP} versus using a flat prior on $\sin\delta_{\mathrm{CP}}$. Finally, a discussion of the key findings of the results which particular emphasis on δ_{CP} is given.

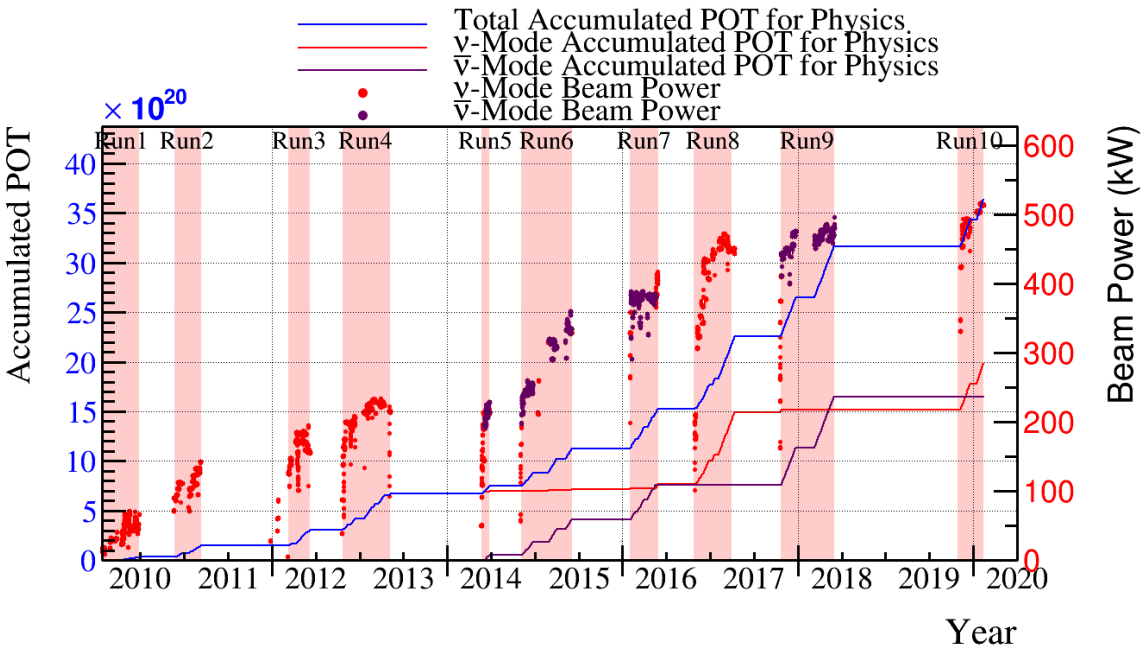

Figure 7.1: The beam power, running period and POT accumulated for each run of the J-PARC beamline. Runs 1–10 can be seen to span 10 years of data taking. Figure from [116].

7.1 Data and MC predictions at ND280

The analysis presented in this chapter utilises all the data currently available at ND280. Previous analyses [71] have used runs 2–6 but this analyses includes runs 7–9 as well which results in an increase of $\sim 100\%$ in the data used in the analysis. The increase in data at the ND280 should allow nuisance parameters to be even more precisely constrained compared to previous analyses. In turn, reduced uncertainties on nuisance parameters will result in better constraints on the neutrino oscillation parameters T2K aims to measure. The pre-fit MC and data distributions projected in lepton momentum for each FHC sample at ND280 can be seen in fig. 7.2. In fig. 7.2 it can be seen that the CC0π samples are mainly CCQE interactions (as expected) with a considerable component of 2p-2h as well as some CCRES interactions where the pion is not reconstructed. The CC1π samples are mainly predicted to be composed of CCRES interactions with a considerable component of CC Multi-π and CC DIS interactions. This component of CC Multi-π and CC DIS in the CC1π samples is why having appropriate uncertainties for these interactions is important for modelling CCRES interactions correctly and is part of the

motivation for the new uncertainties described in chapter 6. Then the CC-Other sample be seen to be mainly CC Multi-π and CC DIS interactions with some NC interactions as well. Both the CC0π and CC-Other samples can be seen to typically under predict the data pre-fit while the CC1π sample has reasonable agreement with the data pre-fit. Other 1D and 2D pre-fit MC and data comparisons can be found in appendix C.1.

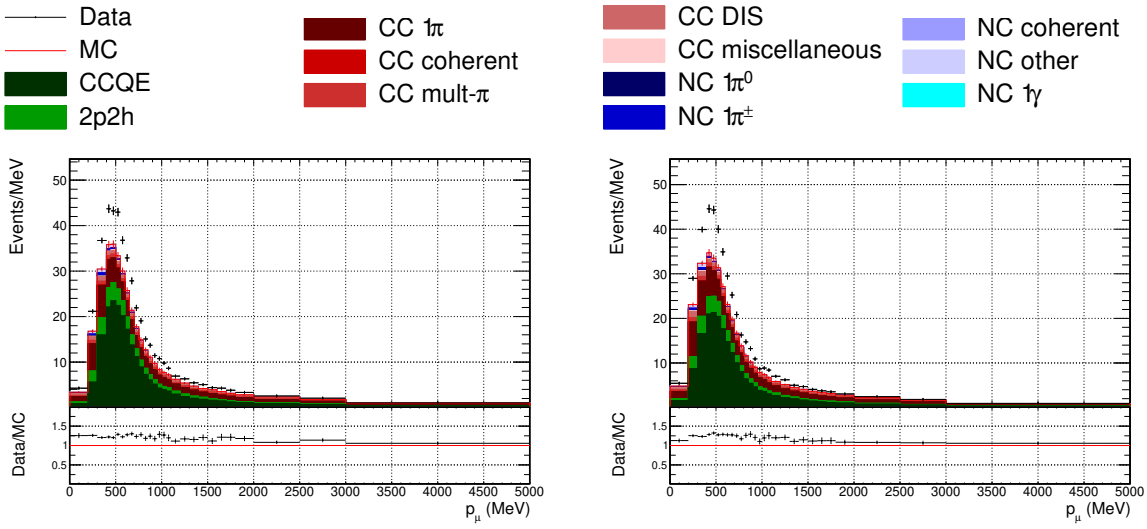

(a) FGD1 FHC ν_μ 0π

(b) FGD2 FHC ν_μ 0π

(c) FGD1 FHC ν_μ 1π

(d) FGD2 FHC ν_μ 1π

(e) FGD1 FHC ν_μ Other

(f) FGD2 FHC ν_μ Other

Figure 7.2: Pre-fit p_μ projections of data and nominal MC broken down by interaction mode for FHC selections. The FGD1 samples can be seen on the left and FGD2 on the right. Figures taken taken [117].

7.2 Data and MC predictions at SK

The data at SK used in this analysis includes the full run 1-10 dataset collected at SK which is all the data currently available. Runs 1-4, 8 and 10 were all performed in FHC operating mode and account for a total of 19.664 $\times$ 10^{20} POT. The remaining runs (5-7 and 9) were all performed in RHC operating mode and account for a further 16.3456 $\times$ 10^{20} POT. The data selected in each of the SK data samples described in chapter 4 is given in fig. 7.3 and is overlaid onto the MC prediction with nuisance parameter values from a fit to ND280 data only.. Compared to the previous T2K oscillation analysis the data presented here uses an additional $\sim$ 30% POT in FHC mode with the POT taken in RHC mode being the same between the two analyses. A summary of the number of events in each data sample and the POT in FHC and RHC mode can be seen in table 7.1. The unoscillated and oscillated event rate predictions for each sample at SK, broken-down by neutrino flavour and interaction mode, before and after a fit to the data at ND280 can be found in appendix C.2.

Table 7.1: The total number of data events for each SK selection for runs 1-10.

Selection	Run 1-10 POT	Events in Data
FHC 1Rμ		318
FHC 1Re	19.644×10^{20}	94
FHC 1ReCC1π		14
RHC 1Rμ	16.34556×10^{20}	137
RHC 1Re		16

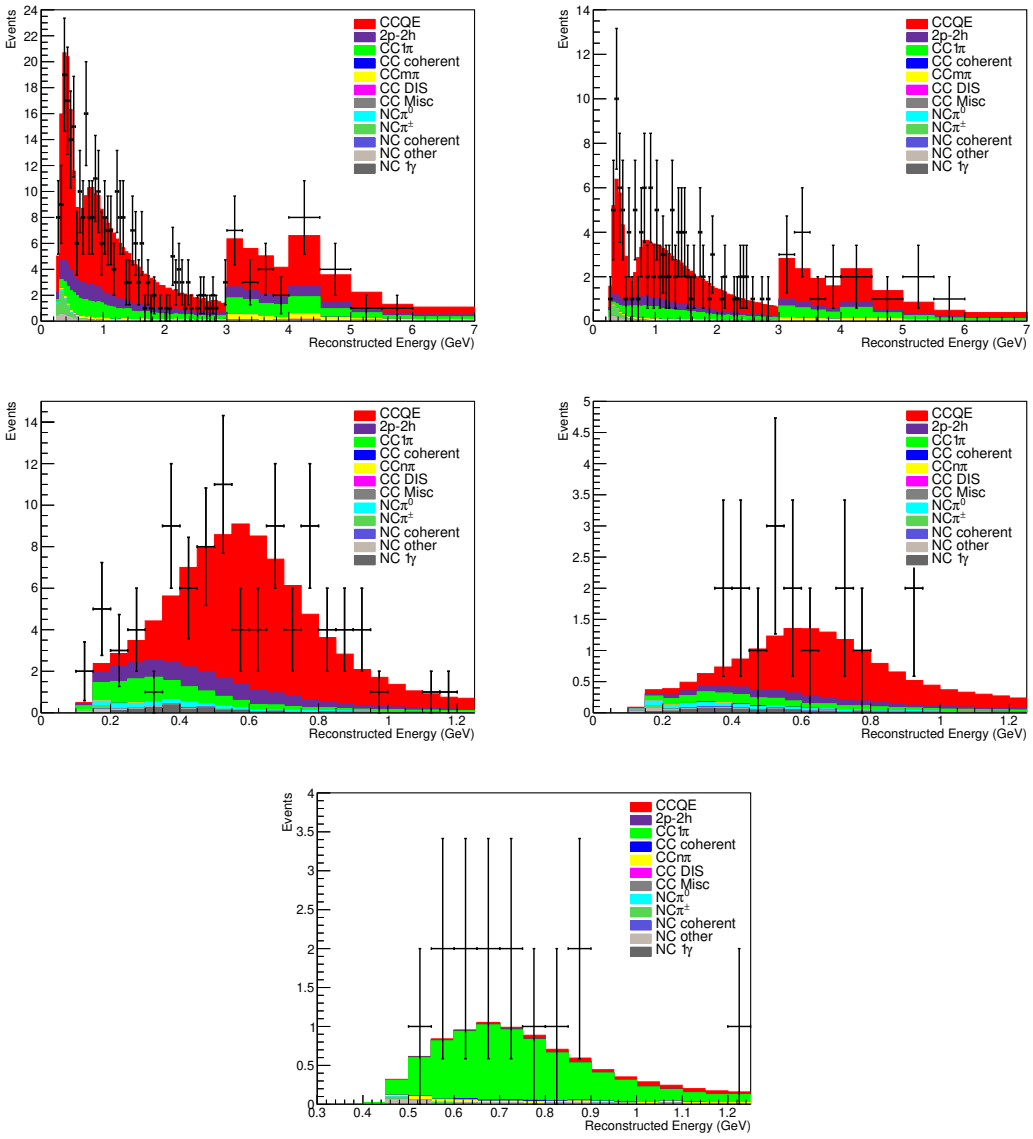

Figure 7.3: The MC prediction for each data sample at SK with the data overlaid. Top left is the FHC 1Rμ sample, top right FHC 1Re sample, middle left RHC 1Rμ, middle right the RHC 1Re sample and bottom the FHC 1ReCC1π sample.

7.3 Fits to T2K data only (without reactor constraint)

The first results presented are obtained from a joint fit to data at ND280 and SK using a flat prior on $\sin^2\theta_{13}$ and a Gaussian prior on $\sin^2\theta_{12}$ and Δm^2_{21} from the PDG best fit [26]. This means for the neutrino oscillation parameters that T2K is sensitive to, the sensitivity comes only from T2K data and not from any prior knowledge of their values and uncertainties. These results are less sensitive to the neutrino oscillation parameters which describe electron neutrino appearance in particular since this process is highly dependent on the θ_{13} mixing parameter. The results using the PDG constraint on $\sin^2\theta_{13}$ will be shown in section 7.4.

7.3.1 Oscillation parameter constraints

The constraints on oscillation parameters are presented as credible intervals which have been calculated from the Markov chains used for the analysis. These credible intervals are presented both in 2D for Δm^2_{32} vs. $\sin^2\theta_{23}$ and δ_{CP} vs. $\sin^2\theta_{13}$ as well as 1D. Due to marginalisation effects (which are described in section 5.3.1) these can differ slightly from the 2D credible intervals. In addition, 1D and 2D credible intervals are given marginalised over all values of Δm^2_{32} , such that both mass orderings are marginalised over, marginalised over just the normal hierarchy (NH) ($\Delta m^2_{32} > 0$) and marginalised over just the inverted hierarchy ($\Delta m^2_{32} < 0$). The results for individual mass orderings as well as marginalised over both can be interesting since the mass ordering is still unknown and neutrino oscillation parameters can change fairly significantly between hierarchies.

2D Credible Intervals

2D credible intervals are useful in seeing not only the constraints on individual oscillation parameters but also how they correlate with other parameters. In particular, 2D plots of Δm^2_{32} vs. $\sin^2\theta_{23}$ (the two main parameters which describe muon neutrino disappearance) and δ_{CP} vs. $\sin^2\theta_{13}$ (the two main parameters which describe electron neutrino appearance) are useful in seeing how these parameters relate to each other.

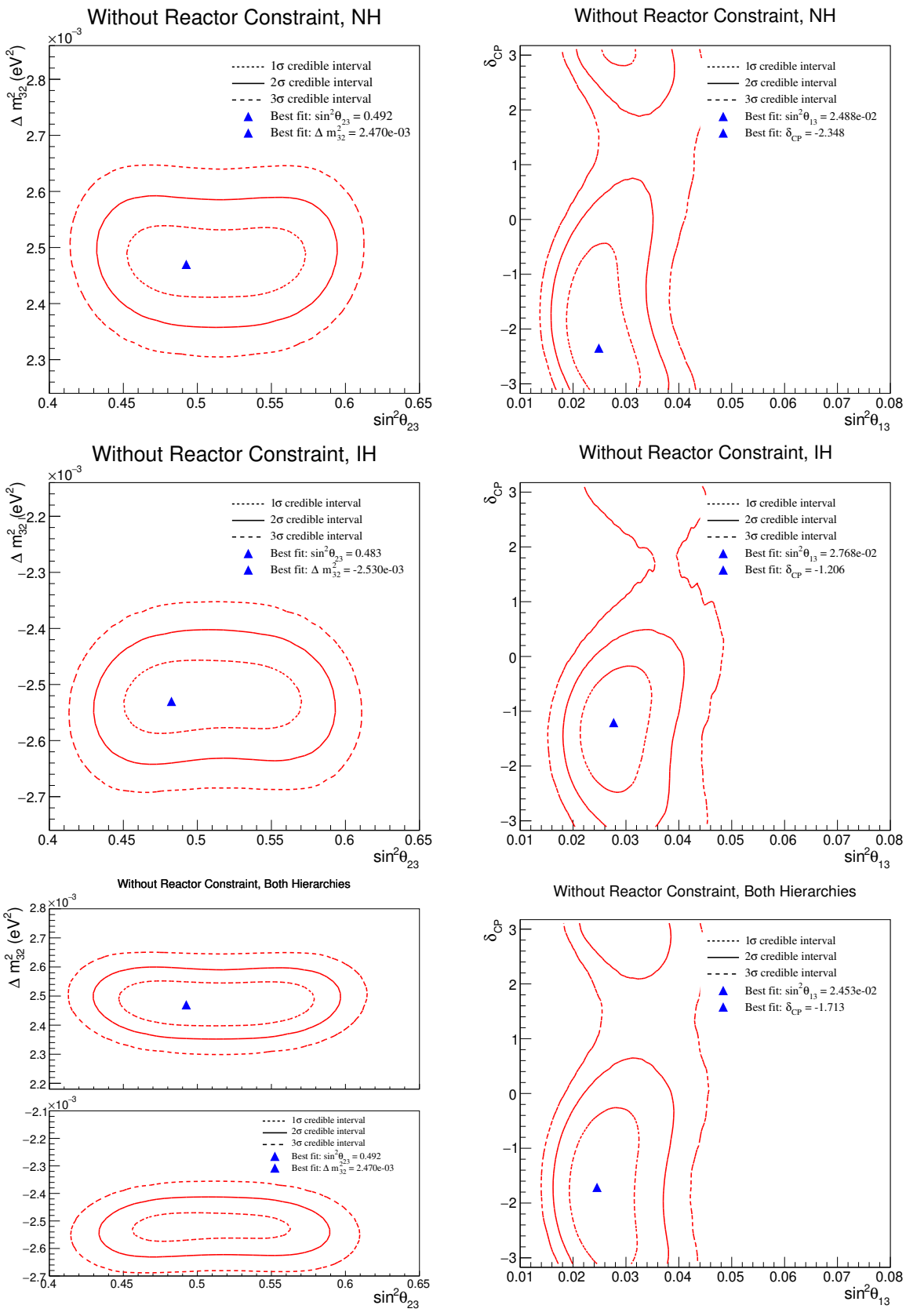

Figure 7.4: Data-fit results without reactor constraint: 2D credible intervals for Δm^2_{32} vs. $\sin^2\theta_{23}$ (left) and δ_{CP} vs. $\sin^2\theta_{13}$ (right) marginalised over NH (top), IH (middle) and both mass orderings (bottom).

1D Credible Intervals

The 2D constraints above can then be marginalised over to produce 1D constraints on oscillation parameters. Again, 1D distributions are shown marginalised over both mass ordering, marginalised over just the NH and also marginalised over just the IH. 1D credible intervals are shown for $\sin^2\theta_{13}$ and δ_{CP} in fig. 7.5 and Δm^2_{32} and $\sin^2\theta_{23}$ in fig. 7.6.

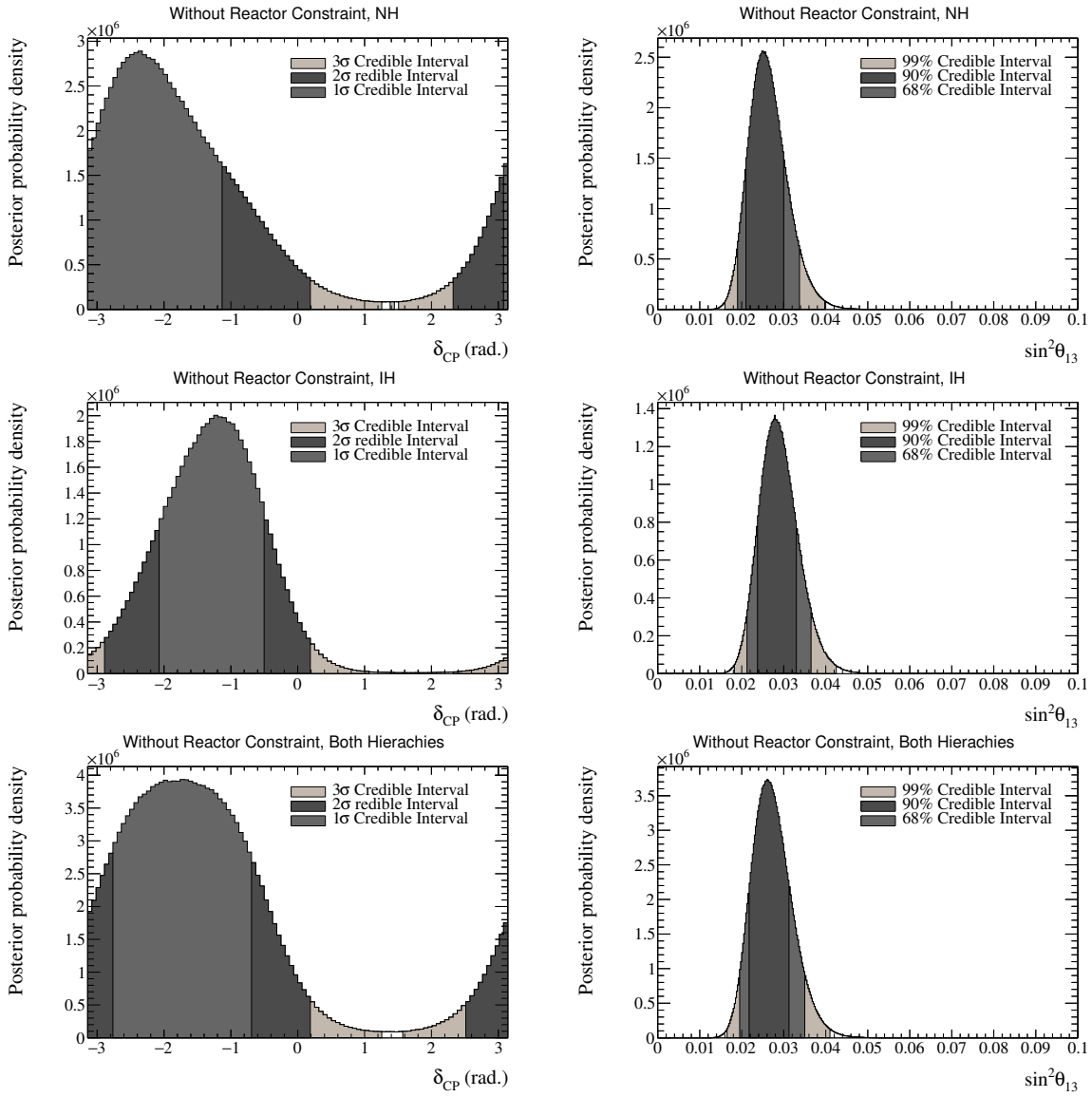

Figure 7.5: Data-fit results without reactor constraint: 1D credible intervals on δ_{CP} (left) and $\sin^2\theta_{13}$ (right) marginalised over NH (top), IH (middle) and both mass orderings (bottom).

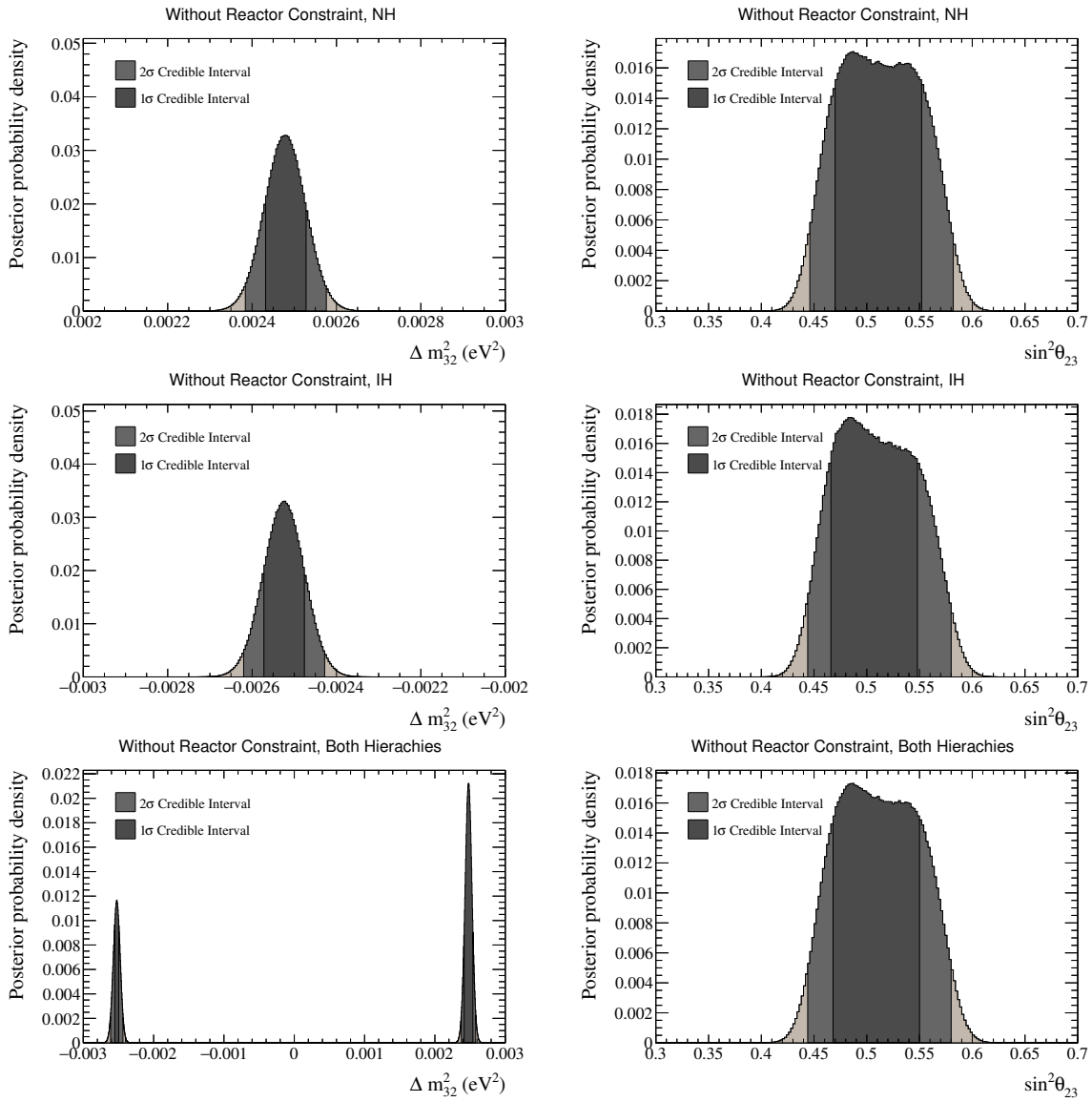

Figure 7.6: Data-fit results without reactor constraint: 1D credible intervals on Δm^2_{32} (left) and $\sin^2\theta_{23}$ (right) marginalised over NH (top), IH (middle) and both mass orderings (bottom).

7.4 Fit to T2K Data with reactor constraint

As has been described in section 4.2.4 a prior constraint on $\sin^2\theta_{13}$ can be used in the analysis using the latest results from the PDG [26]. The use of this external constraint allows T2K to measure oscillation parameters more precisely especially those related to electron neutrino appearance. Due to correlations between oscillation parameters the use

of a prior on $\sin^2\theta_{13}$ can also impact the constraints on other neutrino oscillation parameters. Therefore, the oscillation parameter constraints and best-fit parameter values are slightly different when made using a prior from reactor experiments compared to not using this prior, although in this case we find the two sets of results very compatible with each other.

7.4.1 Oscillation parameter constraints

2D Credible Intervals

2D credible intervals in Δm^2_{32} vs. $\sin^2\theta_{23}$ and δ_{CP} vs. $\sin^2\theta_{13}$ are shown in fig. 7.7. The constraints on disappearance parameters is very similar to that without the reactor constraint except that the best-ft value for $\sin^2\theta_{23}$ is now above $\sin^2\theta_{23}= 0.5$. As mentioned in section 2.2.6, muon neutrino disappearance suffers from octant degeneracy which results in very symmetric results around $\sin^2\theta_{23}= 0.5$ for the result shown without reactor constraints. When the reactor constraint is applied, the additional sensitivity coming from electron neutrino appearance events (which is dependent on $\sin^2\theta_{23}$) allows the octant degeneracy to be partially lifted. This results in more asymmetric constraints around $\sin^2\theta_{23}= 0.5$.

For the appearance parameters in fig. 7.7, the increased constraint from using the reactor prior is significant. The credible intervals for $\sin^2\theta_{13}$ become very similar to that of the prior which is expected due to the fact that reactor experiments are more sensitive to the θ_{13} mixing parameter than T2K is. In turn this then reduces the uncertainty on δ_{CP} which can be seen to be constrained more tightly compared to without reactor constraint.

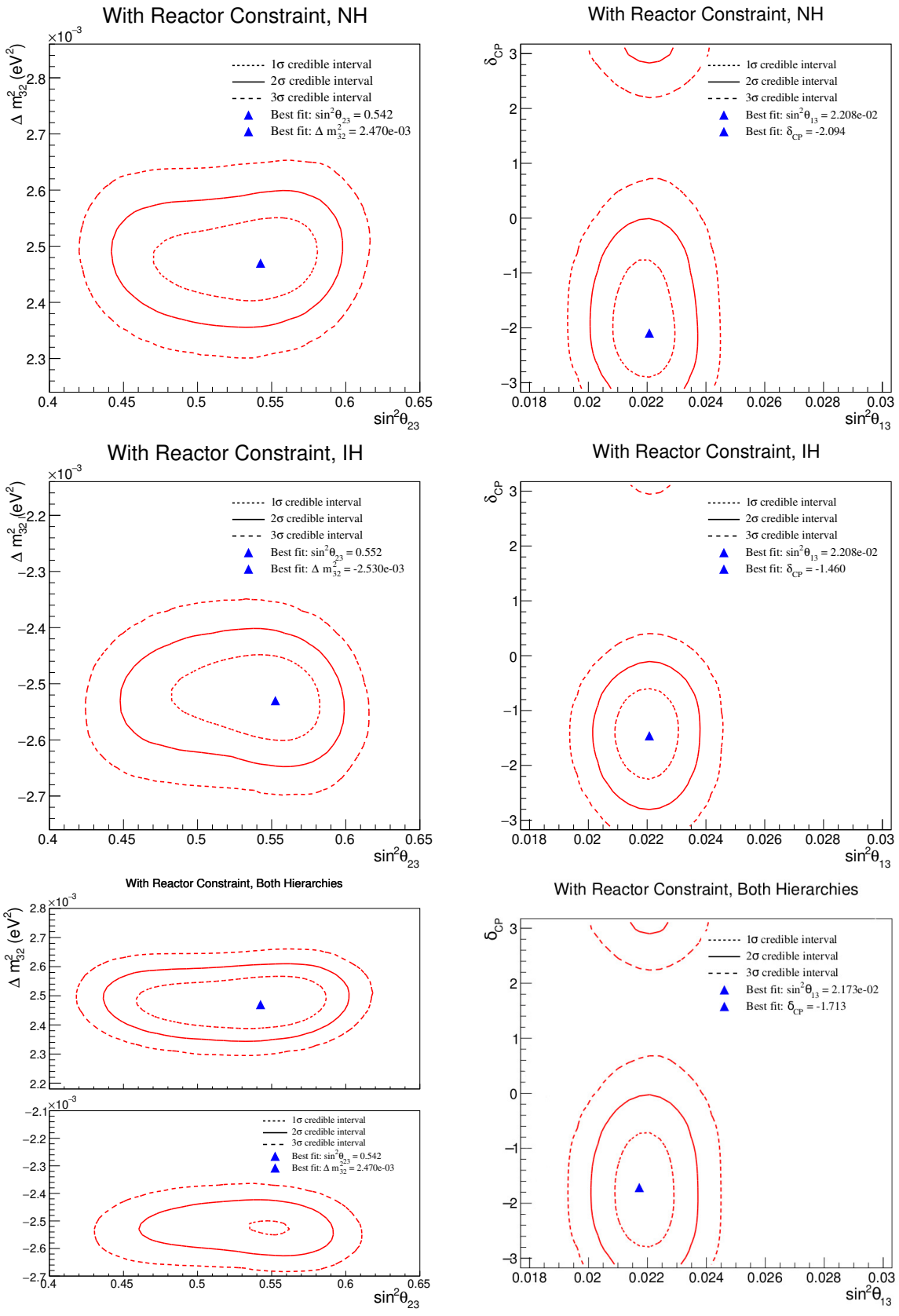

Figure 7.7: Data-fit results with reactor constraint: 2D credible intervals for Δm^2_{32} vs. $\sin^2\theta_{23}$ (left) and δ_{CP} vs. $\sin^2\theta_{13}$ (right). Credible intervals are shown marginalised over the NH (top). marginalised over the IH (middle) and marginalised over both hierarchies (bottom).

1D Credible Intervals

The 1D credible intervals for a data fit with reactor constraint can be seen in fig. 7.8 for electron appearance parameters and fig. 7.9 for the disappearance parameters.

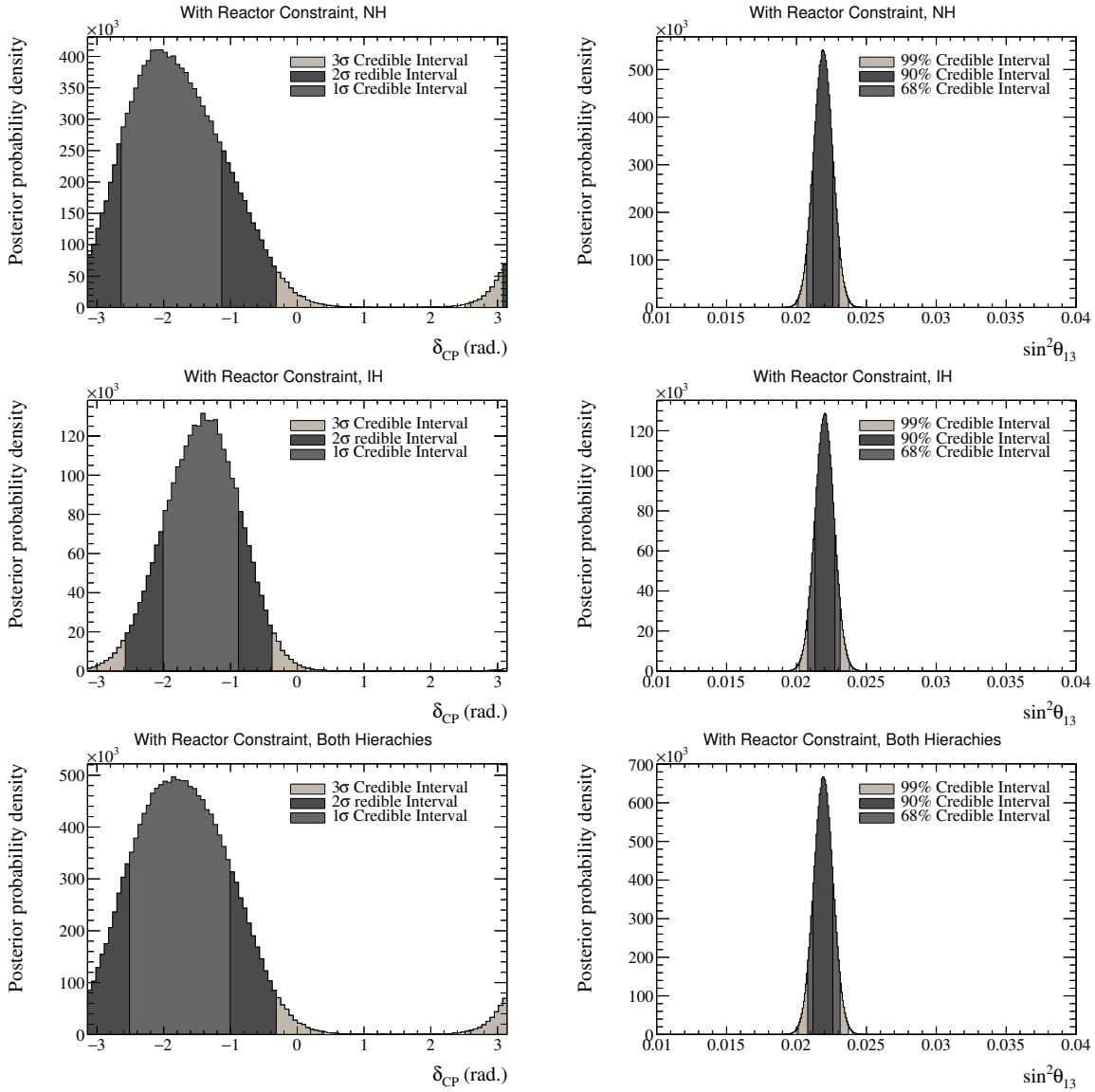

Figure 7.8: Data-fit results with reactor constraint: 1D credible intervals on δ_{CP} and $\sin^2\theta_{13}$. The $\sin^2\theta_{13}$ credible intervals are very similar to the Gaussian prior from the reactor experiments.

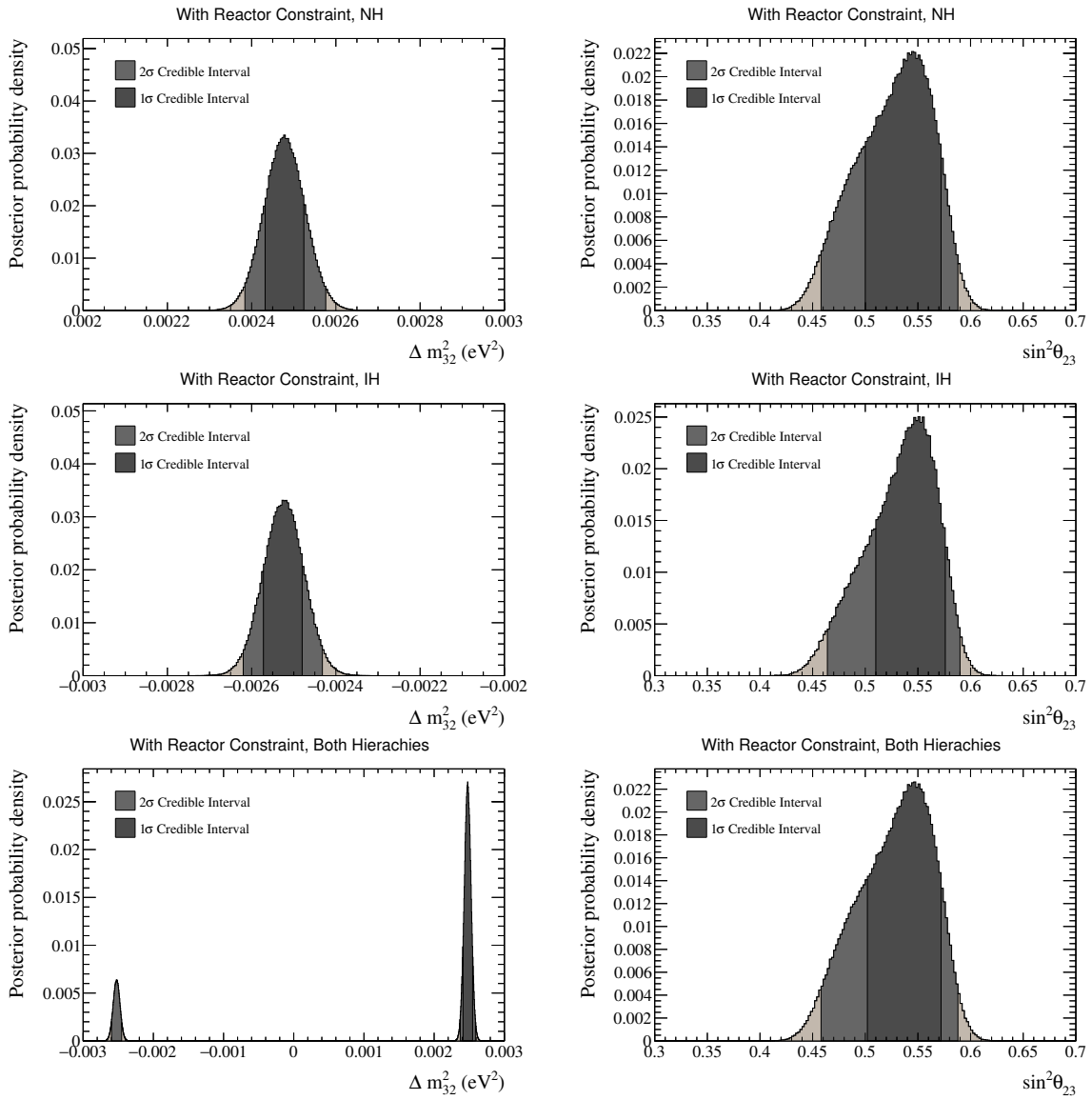

Figure 7.9: Data-fit results with reactor constraint: 1D credible intervals on Δm^2_{32} (left) and $\sin^2\theta_{23}$ (right) marginalised over NH (top), IH (middle) and both mass orderings (bottom).

7.5 Comparison of results with Data

The Markov chains from the fit to data can also be used to build a mean prediction for the SK samples as well as an uncertainty around this mean prediction. This is done by randomly sampling from steps in the Markov chains and calculating the oscillated spectrum for each SK sample using all parameter values at this step. Doing this many

times builds a distribution of the predicted number of events in each analysis bin from which a mean prediction and RMS can be extracted. The mean predictions and the RMS from the posterior prediction in each bin are then used to construct a 1σ uncertainty band error on the mean prediction in each bin. These distributions are known as posterior predictive distributions and are a useful tool for looking at the post-fit parameter values from the fit and comparing them to the data at SK. Posterior distributions for each sample at SK using the neutrino oscillation parameter results using reactor constraints are shown in fig. 7.10 and fig. 7.11. Figure 7.11 shows the same as fig. 7.10 but with the ratio taken to the unoscillated prediction for each data sample at SK. These posterior predictive distributions show good agreement between the post-fit parameter values and the SK data.

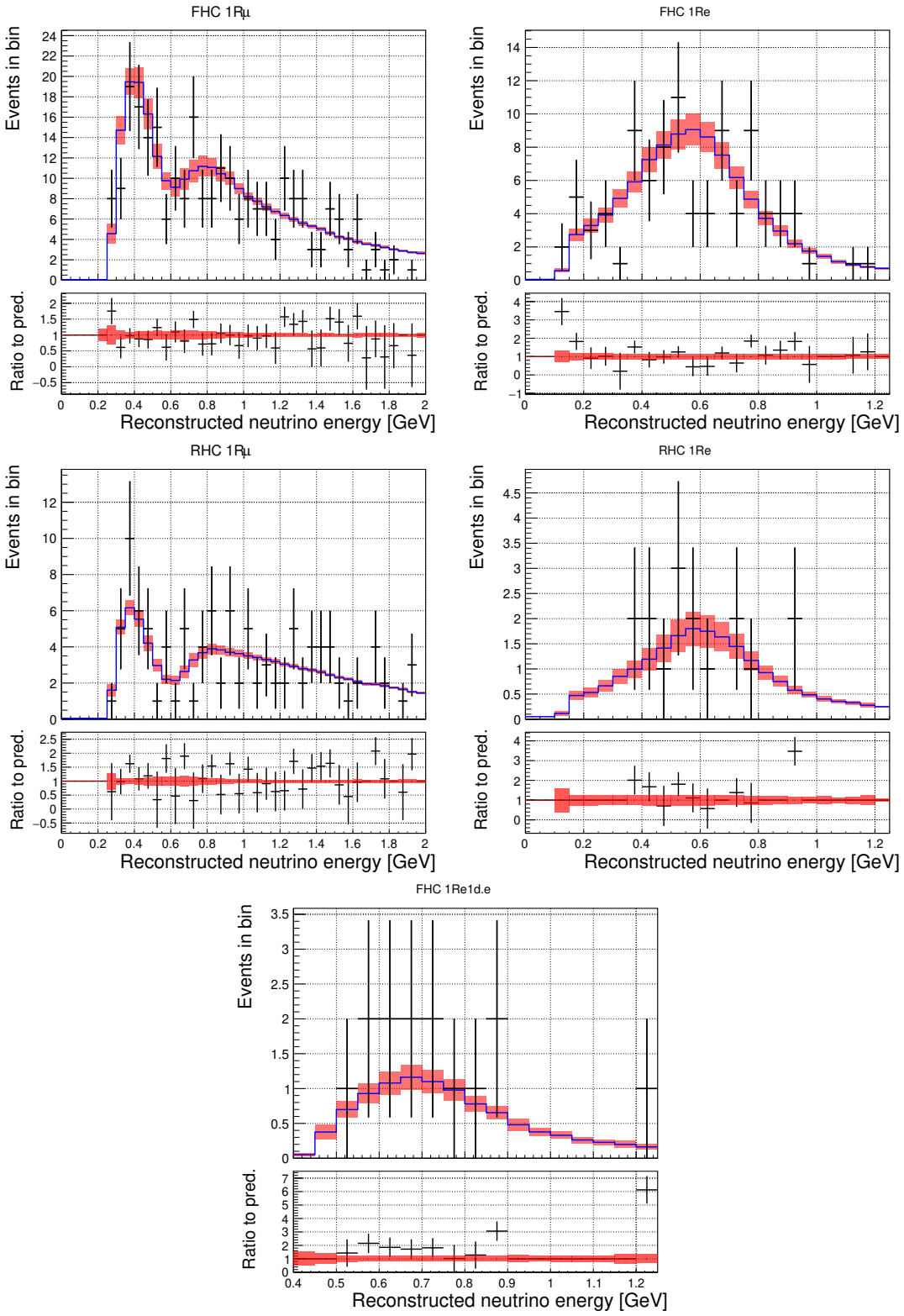

Figure 7.10: Post-fit distribution (blue) and one sigma error band (red) with run 1–10 data (black) for each SK selection overlaid. Posterior predictive distributions are made using a Markov chain from a joint SK and ND280 fit. The post-fit distribution and errors are made by taking the mean and RMS from a posterior predictive distribution in each bin.

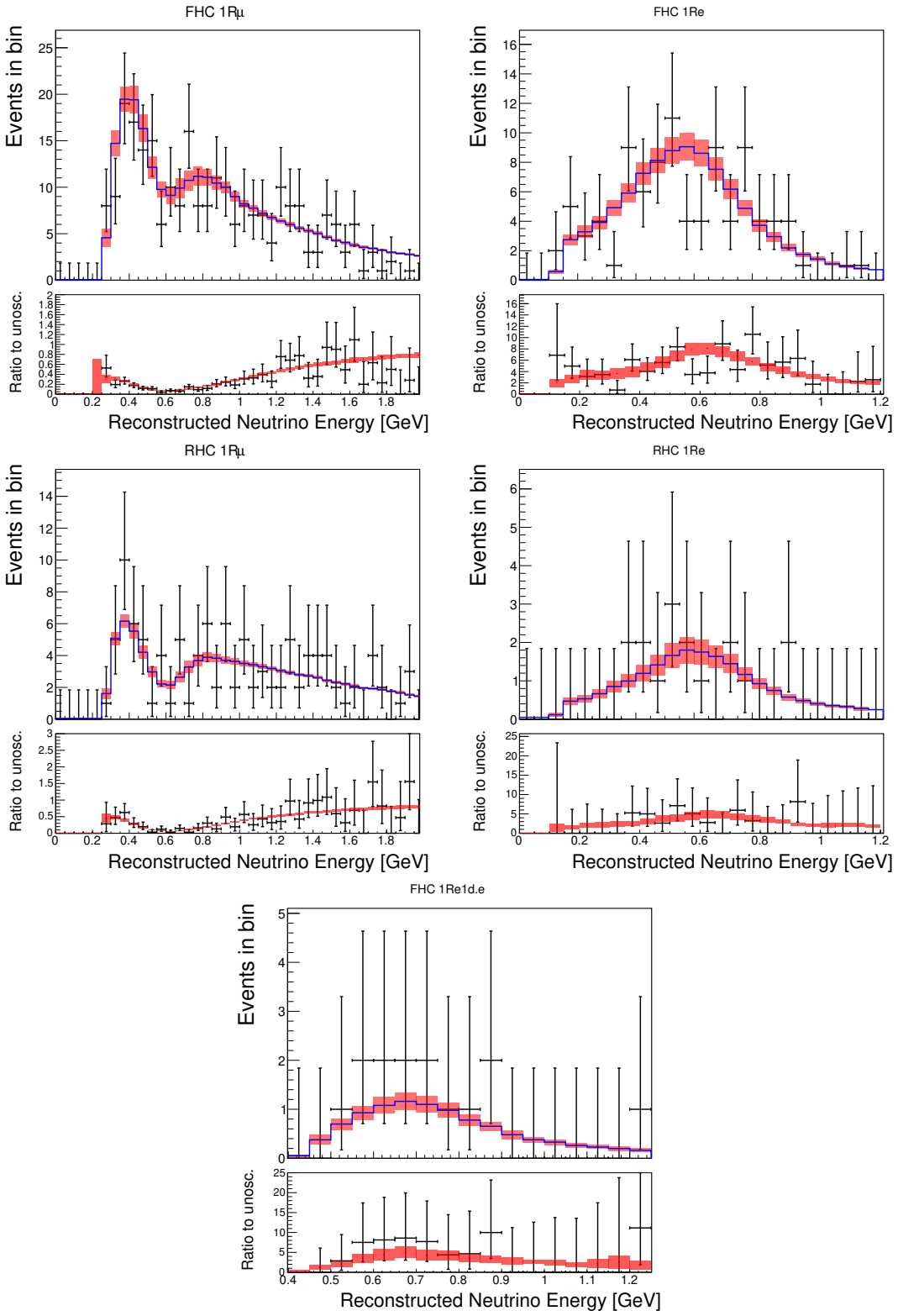

Figure 7.11: Post-fit distribution (blue) and one sigma error band (red) with run 1–10 data (black). Posterior predictive distributions are made using a Markov chain from a joint SK and ND fit. The post-fit distribution and errors are made by taking the mean and RMS from a posterior predictive distribution in each bin. The data error bars in this figure are Poisson errors rather than $\sqrt{N}$ as in fig. 7.10.

7.6 Studies on the prior constraint used on δ_{CP}

In Bayesian analyses it is common practice to check that the use of the prior constraint used on a parameter of interest is not affecting the final statements on parameter values significantly. In the case of this analysis, the neutrino oscillation parameter of interest which T2K is least sensitive to (so where the choice of prior could have the largest impact) is δ_{CP}. To estimate the size of the effect from the choice of prior on the final statements on δ_{CP}, the credible intervals found using a prior constraint which is flat across all values of δ_{CP} and a prior constraint which is flat in $\sin\delta_{\mathrm{CP}}$ are compared. The motivation for using a flat prior in $\sin\delta_{\mathrm{CP}}$ is that in the neutrino oscillation probability for electron neutrino appearance (given in eq. (2.49)) is dependent on $\sin\delta_{\mathrm{CP}}$ rather than δ_{CP}. Therefore, a check on the use of a prior on the δ_{CP} versus how the parameter appears in the neutrino oscillation probability seems like a sensible check to make.

Similarly to how the constraints on neutrino oscillation parameters are made using different prior constraints on $\sin^2\theta_{13}$ for without reactor constraints and with, the change in prior on δ_{CP} to $\sin\delta_{\mathrm{CP}}$ is done by reweighting step based on the value of the old prior and new prior. This means that additional Markov chains do not need to be made for the studies on the prior constraint used on δ_{CP} and the existing chains can simply be reweighted. The 1D posterior distributions for δ_{CP} using a prior flat in δ_{CP} and flat in $\sin\delta_{\mathrm{CP}}$ can be seen in fig. 7.12. The results from using a prior constraint flat in $\sin\delta_{\mathrm{CP}}$ is broadly consistent with those made from using a prior flat in δ_{CP}.

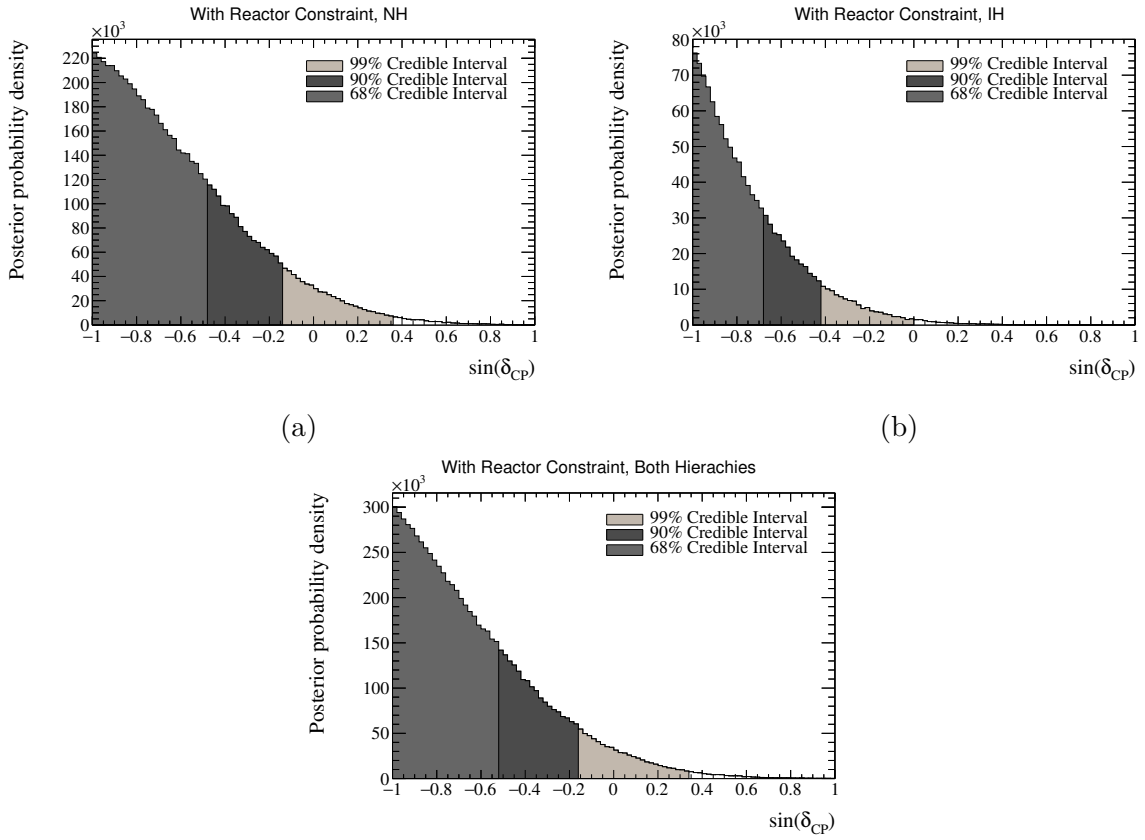

Figure 7.12: 1D $\sin\delta_{\mathrm{CP}}$ credible intervals with a prior flat in $\sin\delta_{\mathrm{CP}}$ (rather than flat in δ_{CP}) for the normal hierarchy, inverted hierarchy and both hierarchies (bottom). It can be seen that in $\sin\delta_{\mathrm{CP}}$ that values close to 1 are excluded at 99% and values around -1 are preferred which is consistent with previous results shown. It can also be seen that $\sin\delta_{\mathrm{CP}} = 0$ is still disfavoured at 90% even under this change in prior.

7.7 Summary of results

The results shown above are the latest and most precise oscillation parameter results from the T2K collaboration. To summarise the results, 2D plots of Δm^2_{32} vs. $\sin^2\theta_{23}$ and δ_{CP} vs. $\sin^2\theta_{13}$ with the credible intervals and best-fit values for both with and without the reactor constraint prior being used are given in fig. 7.13. In particular it is worth highlighting what can be said open the open questions in neutrino oscillations; the octant of θ_{23}, the mass ordering and the value of δ_{CP}. The question of the value of δ_{CP} will be discussed in more detail in section 7.7.1.

Regarding the octant of θ_{23}, the results shown without the reactor constrained prior prefer the lower octant of θ_{23} ($\sin^2\theta_{23} < 0.5$) for the NH and IH and also when $\sin^2\theta_{23}$ is marginalised over both mass hierarchies. However it should be noted that the credible intervals without the reactor constraint for the disappearance parameters are almost symmetric around $\sin^2\theta_{23}= 0.5$ so the preference for the lower or upper octant is not high. When the reactor constraint is used the upper octant is preferred for the NH, IH and when both hierarchies are marginalised over. Furthermore, the credible intervals can now be seen to be asymmetric about $\sin^2\theta_{23}= 0.5$. This is expected since the use of the reactor constraint prior constraint the electron neutrino appearance probability which allows the octant degeneracy to be partially lifted. Probabilities for the octant of θ_{23} are given in table 7.3.

For constraints on the mass hierarchy the results all generally prefer the normal hierarchy. This can be seen in a few ways; firstly the best-fit point for $\sin^2\theta_{23}$ vs. Δm^2_{32} when marginalised across both hierarchies can be seen to be in the normal hierarchy ($\Delta m^2_{32} > 0$) and secondly the credible intervals occupy a much smaller region of phase-space both for Δm^2_{32} vs. $\sin^2\theta_{23}$ and for δ_{CP} vs. $\sin^2\theta_{13}$ which indicates that fewer oscillation parameter values are likely in the IH. To be more quantitative, probabilities for the normal and inverted orderings are given in table 7.3.

The constraints on all the neutrino oscillation parameters that the T2K experiment is sensitive to is given in the form of a "triangle plot", which are shown in Bayesian analyses, in fig. 7.14. This plot shows all the 2D and 1D credible intervals for the oscillation

parameters.

Table 7.2: The 1D best-fit parameter values and $1\,\sigma$ credible interval from this analysis. For the best-fit value of Δm^2_{32} for both orderings the 1σ range within the mass ordering where the best-fit is in is quoted.

Osc. Par.	without RC					
	NH		IH		both	
	HPD	$1\,\sigma$ CI	HPD	$1\,\sigma$ CI	HPD	$1\,\sigma$ CI
$\sin^2\theta_{13}$ ($\times 10^3$)	2.49	2.10–3.00	2.79	2.385–3.30	2.61	2.18–3.13
δ_{CP}	-2.37	-1.13–π	-1.23	-2.07–-0.50	-1.73	-2.76–-0.69
$\sin^2\theta_{23}$	0.487	0.470 – 0.552	0.483	0.466–0.548	0.487	0.468–0.550
Δm^2_{32} ($\times 10^3$)	2.48	2.43–2.53	-2.52	-2.58–-2.48	2.48	2.42–2.54

Osc. Par.	with RC					
	NH		IH		both	
	HPD	$1\,\sigma$ CI	HPD	$1\,\sigma$ CI	HPD	$1\,\sigma$ CI
$\sin^2\theta_{13}$ ($\times 10^3$)	2.19	2.12–2.26	2.20	2.13–2.28	2.19	2.12–2.26
δ_{CP}	-2.04	-2.64–-1.13	-1.41	-2.01–-0.88	-1.85	-2.51–-1.01
$\sin^2\theta_{23}$	0.545	0.500–0.572	0.551	0.510–0.576	0.547	0.502–0.572
Δm^2_{32} ($\times 10^3$	2.48	2.43–2.53	-2.53	-2.58–-2.48	2.48	2.41–2.55

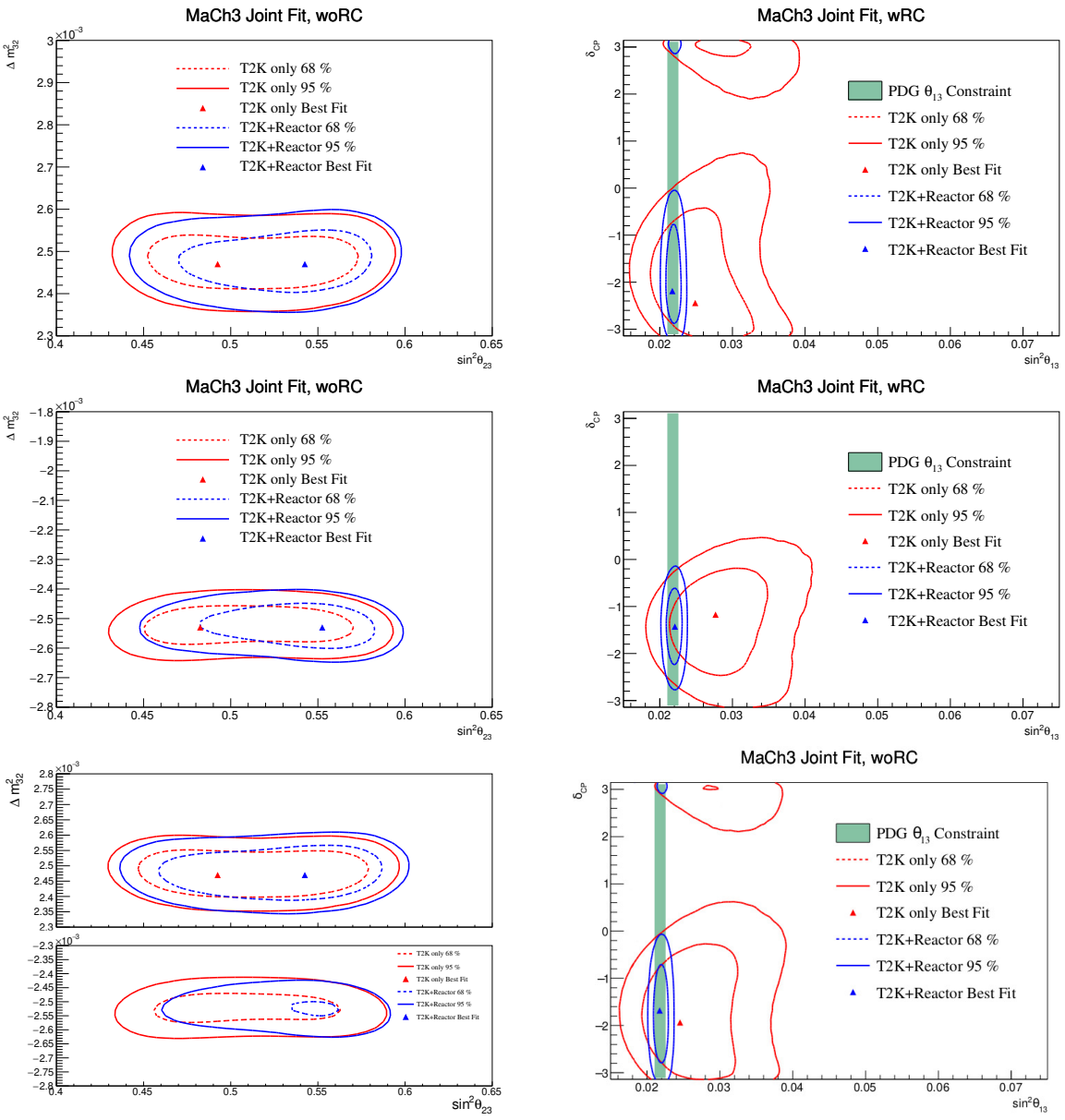

Figure 7.13: A comparison of 2D constraints on oscillation parameters with and without the reactor constrained prior being used.

Table 7.3: Posterior probabilities from T2K data fits for normal and inverted hierarchies, as well as upper and lower octants. The probabilities are calculated by calculating the fraction of Markov chain steps in each region of parameter-space.

without RC			
	$\sin^2\theta_{23} < 0.5$	$\sin^2\theta_{23} > 0.5$	Sum
NO ($\Delta m^2_{32} > 0$)	0.260	0.387	0.647
IO ($\Delta m^2_{32} < 0$)	0.152	0.201	0.353
Sum	0.412	0.588	1.000
with RC			
	$\sin^2\theta_{23} < 0.5$	$\sin^2\theta_{23} > 0.5$	Sum
NO ($\Delta m^2_{32} > 0$)	0.195	0.613	0.808
IO ($\Delta m^2_{32} < 0$)	0.035	0.157	0.192
Sum	0.230	0.770	1.000

7.7.1 Discussion of δ_{CP}

As has been mentioned in earlier chapters, the value of δ_{CP} is of particular interest because of its importance to CP violation in the neutrino sector. The results outlined here prefer CP non-conserving values and exclude these values (0 and or π) at the 90% significance level and almost at 2σ. In fact, the results from the oscillation analysis prefer values of δ_{CP} which are much closer to $-\pi/2$ radians meaning they prefer the maximal amount of CP-violation available. To visualise this more easily, radial plots of the 1D constraints on δ_{CP} using the reactor constraint are given in fig. 7.16. Another way to phrase that CP violation is at a maximal amount is that electron neutrino appearance for neutrino and antineutrinos are maximally different for a set of oscillation parameters. Again, this can be visualised more easily in fig. 7.15 which show the oscillation spectra for the 1Re samples at SK for FHC and RHC mode using the best-fit oscillation parameters and different values of δ_{CP}. These results give a tantilising hint of CP-violation in neutrinos and more precise measurements of δ_{CP} will be made over the coming years to precisely determine its value.

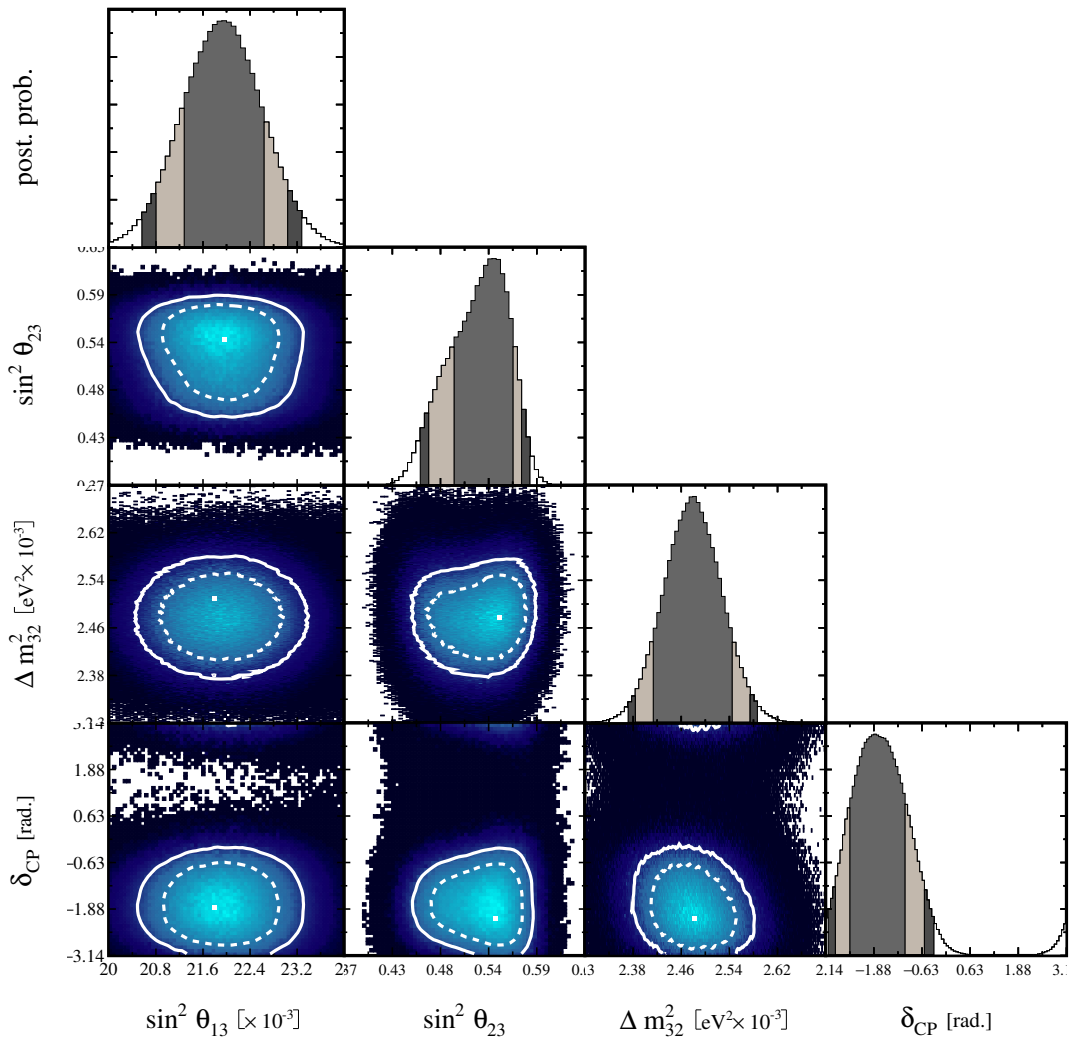

Figure 7.14: A "bayesian triangle" plot showing the 68% (dashed) and 90% (solid) credible intervals for the data fit using the reactor constraint. This shows all four oscillation parameters that the T2K experiment is sensitive in 2D and also 1D.

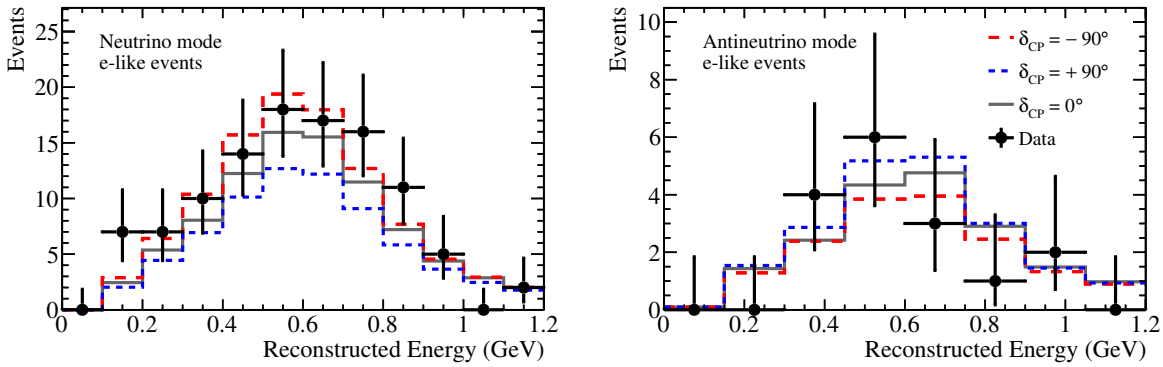

Figure 7.15: Oscillated predictions for the 1Re sample at SK for FHC mode (left) and RHC mode (right). The predictions use the best-fit oscillation parameters with reactor constraint. The predicted spectra for different values of δ_{CP} (0, $-\pi/2$ and $+\pi/2$) are also shown which highlights that the T2K results prefer a value of $-\pi/2$. This can naively be seen by eye from the better agreement between the data points and the $\delta_{\mathrm{CP}} = -\pi/2$ prediction for FHC and RHC mode.

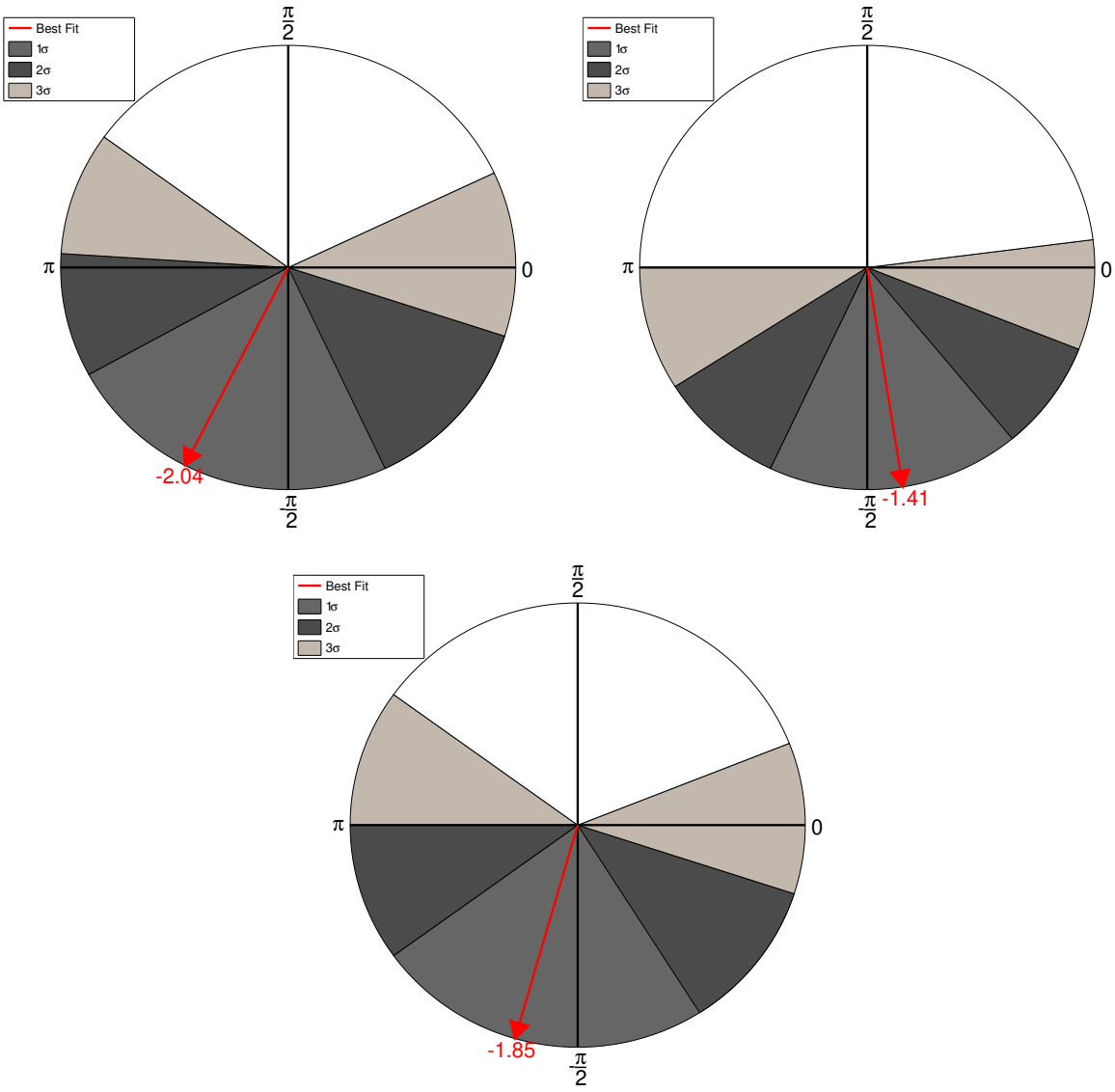

Figure 7.16: Radial plots showing the 1D constraints on δ_{CP} using the reactor constraint. For the NH (top left), IH (top right) and marginalised across both mass hierarchies (bottom). In all cases the best-fit value prefers a value close to $-\pi/2$. It can also be seen that the CP-conserving values of 0 and π are disfavoured at $\sim 2\sigma$ for all cases. Another interesting note is that large regions of δ_{CP} are disfavoured at more than 3σ.

Chapter 8

Oscillation Analysis including the ν_μ CC1π^+ data sample at Super-Kamiokande

The analysis presented in chapter 7 is the latest oscillation analysis result from the T2K experiment. Going forward, the T2K experiment wishes to improve its constraints on oscillation parameters in order to answer key open questions about neutrino oscillation parameters. In the current analysis, the largest source of uncertainty comes from statistical uncertainties due to a lack of data events at SK. Therefore, naively increasing the statistics used in the analysis should result in improved constraints on neutrino oscillation parameters. One way to do this is to simply continue to take more data which will increase the data across all data samples. However, another way to increase the data statistics into an analysis is to include new data samples into the analysis. This chapter focuses on preliminary studies of adding a new data sample at SK. The sample added into the analysis targets ν_μ CC1π^+ events at SK in FHC mode. A brief description of how these events are selected at SK and why the oscillation analysis will benefit from including them will be given in section 8.1. Then MC predictions at SK of the sample will be shown will be shown in section 8.2. The potential improvement in oscillation parameter constraints will be demonstrated through the use of an Asimov fit in section 8.3. Finally, the relevance of the new systematic parameters described in chapter 6 to this

sample will be demonstrated through a fake data fit in section 8.4.

8.1 ν_μCC1π event selection

As described in chapter 3, the T2K experiment has a neutrino flux which is peaked at $\sim$ 0.6 GeV which maximises the muon neutrino disappearance probability for the baseline of the T2K experiment. The other impact of this is that most of the neutrino interactions in ND280 and SK are likely to be CCQE interactions. Therefore, most of the data samples at SK target these CCQE interactions in their selection criteria and hence these interactions are the dominant interaction in the MC predictions. For example the FHC 1Rμ sample at SK is predicted to be $\sim$ 60% CCQE interactions (which can be seen in the event rate tables in appendix C). However, as neutrino energy increases so does the total cross section. This means that despite the T2K flux being suppressed at higher energies, a significant number of events can come from energies above the neutrino flux peak. As neutrino energy increases, the differential cross sections of CCRES, CC Multi-π and CC DIS interactions also increase. In fact, at $\sim$ 1 GeV CCRES interactions have the largest differential cross section which can be seen in fig. 8.2. Including these higher energy interactions in the neutrino oscillation analysis presents the opportunity to include a significant increase to the total data statistics used.

A new data sample which targets ν_μ CCRES interactions has been designed over the last few years in the T2K collaboration. This ν_μCC1π sample includes these interactions above the T2K neutrino flux peak and is consequently much richer in CCRES, CC Multi-π and CC DIS interactions than other samples at SK. The final state topology that this sample aims to select at SK is where there is at least one sharp Cherenkov ring and one decay electron or two decay electrons. These sharp Cherenkov rings can correspond to either the muon or the pion and the decay electrons can come from one of or both the muon and pion. A cartoon of an event this data sample aims to select is given in fig. 8.1. The design and optimisation of the selection for the ν_μCC1π data sample has been performed in previous years and is described in [118] in detail. The selection criteria for the ν_μCC1π sample are as follows:

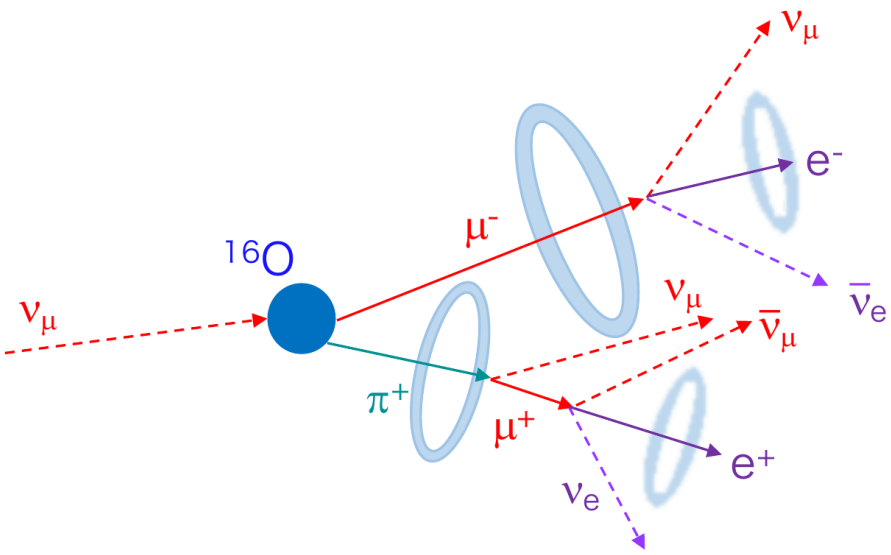

Figure 8.1: A cartoon of a ν_μCC1π signal event where a CCRES interaction producing a muon and pion above Cherenkov threshold. The light blue rings are Cherenkov rings. Figure taken from [118].

- **Pre-selection cuts** - an event must be classed as fully contained in the reconstruction (the definition of a fully contained event at SK was described in section 3.3). In addition to this, a cut on the visible energy of an event is made to reduce NC backgrounds. Any event with a visible energy above 30 MeV will pass the pre-selection phase.

- **Exclusion of other SK samples** - a masking cut to exclude events which are selected into other samples at SK ensures no events are double counted. To do this any event must have at least one reconstructed Cherenkov ring or more than one reconstructed decay electron. This will exclude all events from the other 5 SK samples.

- **Number of decay electrons** - one or two decay electrons are reconstructed in the detector. This forms a key part of the event selection in looking for event topologies with a muon and a charged pion in the final state.

- **Fiducial Volume cut** - to avoid including events where the reconstruction is poor in SK, a fiducial volume cut is applied. This removes event close to the inner detector wall where the reconstruction can be poor as well as any entering backgrounds from the outer detector or outside of the detector entirely. To apply this fiducial

volume cut the DWall parameter is used (which is described in section 3.3). For events reconstructed with one decay electron a DWall cut of > 80 cm is used. Then for two decay electrons a DWall cut of > 50 cm is used.

- **Ring shape and fit quality cuts** - Since this sample targets charged-current muon neutrino interactions with a pion in the final state the reconstructed rings are all muon-like (i.e. sharp) and not e-like. The muon produced in the CC interaction will (obviously) produce a muon-like ring and if the charged pion in above Cherenkov threshold then an additional ring is produced. Since charged pions and muons have very similar masses and the same charge, the Cherenkov profile of a pion is extremely similar to that of a muon. Therefore, if both the muon and pion are above Cherenkov threshold both rings will be sharp. For the reconstruction of events in this sample, both rings are assumed to have a pion-like Cherenkov profile. To implement these cuts on the ring shape two likelihood ratios are looked at. The first looks at the ratio of the likelihood that an event has two sharp rings (pion-like) to the likelihood of the event being e-like. The cut also has a dependence on the reconstructed pion momentum. Slightly different optimised cuts are found for events with one and two decay electrons.

$$\ln \frac{\mathcal{L}_{\pi\pi}}{\mathcal{L}_e} > -400 + 1.2p_\pi, \tag{8.1}$$

$$\ln \frac{\mathcal{L}_{\pi\pi}}{\mathcal{L}_e} > -400 + 1.0p_\pi, \tag{8.2}$$

where $\mathcal{L}_{\pi\pi}$ is the likelihood from the fit to two pion-like rings, $\mathcal{L}_e$ is the likelihood of a fit to a single e-like ring and p_π is the reconstructed pion momentum. eq. (8.1) is used for events with one reconstructed decay electron and eq. (8.2) for events with two reconstructed decay electrons. The second part of this cut is comparing the likelihood of the two pion-like rings fit to best fit from any other combination of two rings from different particle hypotheses. The optimised cuts from this are given below and again are different for events with one or two reconstructed decay electrons.

$$\ln \frac{\mathcal{L}_{\text{best other 2-ring fit}}}{\mathcal{L}_{\pi\pi}} < 340, \tag{8.3}$$

$$\ln \frac{\mathcal{L}_{\text{best other 2-ring fit}}}{\mathcal{L}_{\pi\pi}} < 310, \tag{8.4}$$

where $\mathcal{L}_{\text{best other 2-ring fit}}$ is the likelihood of the best fit using other two ring hypotheses and eq. (8.3) is used for events with one reconstructed decay electron and eq. (8.4) for events with two reconstructed decay electrons.

- **Energy loss cut** - for events with one reconstructed decay electron, NCπ^+ interactions pose as a potential background to signal events. To reduce this background a cut on the energy loss of the two reconstructed rings is performed. NC events do not produce an outgoing lepton so the number of detector photo-electrons of these events is typically lower compared to CC interactions. Any events with one decay electron and an energy loss of less than 300 MeV are rejected from the selection.

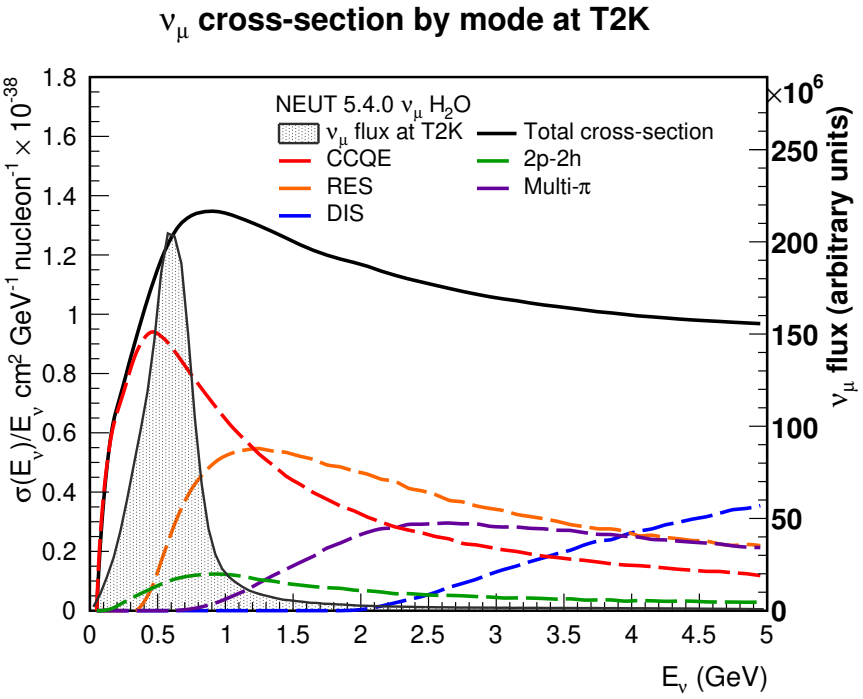

Figure 8.2: The ν_μ differential cross section as a function of neutrino energy on H_2O for different neutrino interactions. The T2K neutrino flux is also shown to compare the energy range that the T2K experiment operates at. At the T2K flux peak energy of $\sim$ 0.6 GeV CCQE can be seen to have the highest interaction probability. Then above this energy the CCQE differential cross section decreases and the differential cross sections of other interaction modes increase. In particular CCRES and CC Multi-π become significant at $\sim$ 1GeV.

8.2 MC predictions at SK for the FHC ν_μCC1π sample

Once the selection has been made the next step towards including the ν_μCC1π data sample into the oscillation analysis is including this sample in the analysis framework. To do this I made the required changes in the MaCh3 framework such that the sample and all of its associated reconstructed quantities could be read into the analysis. This enables MC predictions to be made for this sample at SK as well studies of how nuisance and oscillation parameters impact this prediction. The oscillated and unoscillated prediction for the ν_μCC1π sample can be see in fig. 8.3 as well as a breakdown of the sample by interactions mode and beam component in table 8.1 and table 8.2. The final state topologies of the ν_μCC1π sample and how these correspond to neutrino interaction mode in the MC prediction are shown in fig. 8.4.

As can be seen from the MC predictions in fig. 8.3, table 8.2 and table 8.1 the ν_μCC1π SK sample is dominated by CCRES and CC Multi-π interactions. This makes the sample unique at SK as the other samples are muon-like samples are primarily composed of CCQE interactions. As has been discussed in chapter 6, CC Multi-π and CC DIS interactions pose as backgrounds to correctly modelling CCRES interactions. Since the ν_μCC1π sample has such a large component of CCRES interactions, the CC Multi-π and CC DIS shape parameters that I developed are particularly important for this sample. If the CCRES component of the ν_μCC1π sample is not accurately modelled then this will result in the neutrino oscillation parameters found in the oscillation analysis being biased. The impact of mismodeling CC Multi-π and CC DIS interactions will be shown in section 8.4.

Table 8.1: Unoscillated event rate predictions for the ν_μCC1π sample at SK. The large contributions from CCRES and CC Multi-π interactions show the importance of these modes in accurately predicting these samples at SK.

	ν_μ	ν_e	$\bar{\nu}_\mu$	$\bar{\nu}_e$	ν_e signal	$\bar{\nu}_e$ signal	Total
CCQE	25.42687	0.00033	1.39410	0.00000	0.00000	0.00000	26.82130
CC1π	225.21755	0.02489	3.97616	0.00010	0.00000	0.00000	229.21870
CC coh.	4.93386	0.00042	0.31473	0.00004	0.00000	0.00000	5.24905
CCnπ	29.41624	0.00922	1.19486	0.00013	0.00000	0.00000	30.62045
CC DIS	7.83680	0.00623	0.14092	0.00004	0.00000	0.00000	7.98399
NCπ^0	0.16545	0.00859	0.00669	0.00037	0.00000	0.00000	0.18110
NC$\pi^{+/-}$	1.45884	0.05226	0.07783	0.00442	0.00000	0.00000	1.59336
NC coh.	0.00000	0.00000	0.00000	0.00000	0.00000	0.00000	0.00000
NC other	4.45422	0.16903	0.19291	0.01542	0.00000	0.00000	4.83158
2p-2h	4.44002	0.00000	0.37528	0.00000	0.00000	0.00000	4.81530
NC 1γ	0.00000	0.00000	0.00000	0.00000	0.00000	0.00000	0.00000
CC Other	1.74314	0.00000	0.09557	0.00000	0.00000	0.00000	1.83871
Sample totals	305.09299	0.27097	7.76904	0.02052	0.00000	0.00000	
Total	313.15352						

Table 8.2: Oscillated event rate predictions for the ν_μCC1π sample at SK using the Asimov A oscillation parameters. The large contributions from CCRES and CC Multi-π interactions after oscillations have been applied show the importance of these modes in accurately predicting these samples at SK.

	ν_μ	ν_e	$\bar{\nu}_\mu$	$\bar{\nu}_e$	ν_e signal	$\bar{\nu}_e$ signal	Total
CCQE	11.33579	0.00033	0.86889	0.00000	0.00094	0.00001	12.20596
CC1π	85.03231	0.02337	2.85806	0.00009	0.13512	0.00002	88.04898
CC coh.	1.67585	0.00038	0.19762	0.00004	0.00373	0.00000	1.87762
CCnπ	23.93404	0.00891	0.99200	0.00013	0.00691	0.00002	24.94201
CC DIS	7.39895	0.00617	0.13381	0.00004	0.00050	0.00001	7.53948
NCπ^0	0.16545	0.00859	0.00669	0.00037	0.00000	0.00000	0.18110
NC$\pi^{+/-}$	1.45884	0.05226	0.07783	0.00442	0.00000	0.00000	1.59336
NC coh.	0.00000	0.00000	0.00000	0.00000	0.00000	0.00000	0.00000
NC other	4.45422	0.16903	0.19291	0.01542	0.00000	0.00000	4.83158
2p-2h	2.01991	0.00000	0.24437	0.00000	0.00000	0.00002	2.26430
NC 1γ	0.00000	0.00000	0.00000	0.00000	0.00000	0.00000	0.00000
CC Other	1.45758	0.00000	0.07881	0.00000	0.00000	0.00000	1.53639
Sample totals	138.93295	0.26905	5.65099	0.02052	0.14720	0.00008	
Total	145.02079						

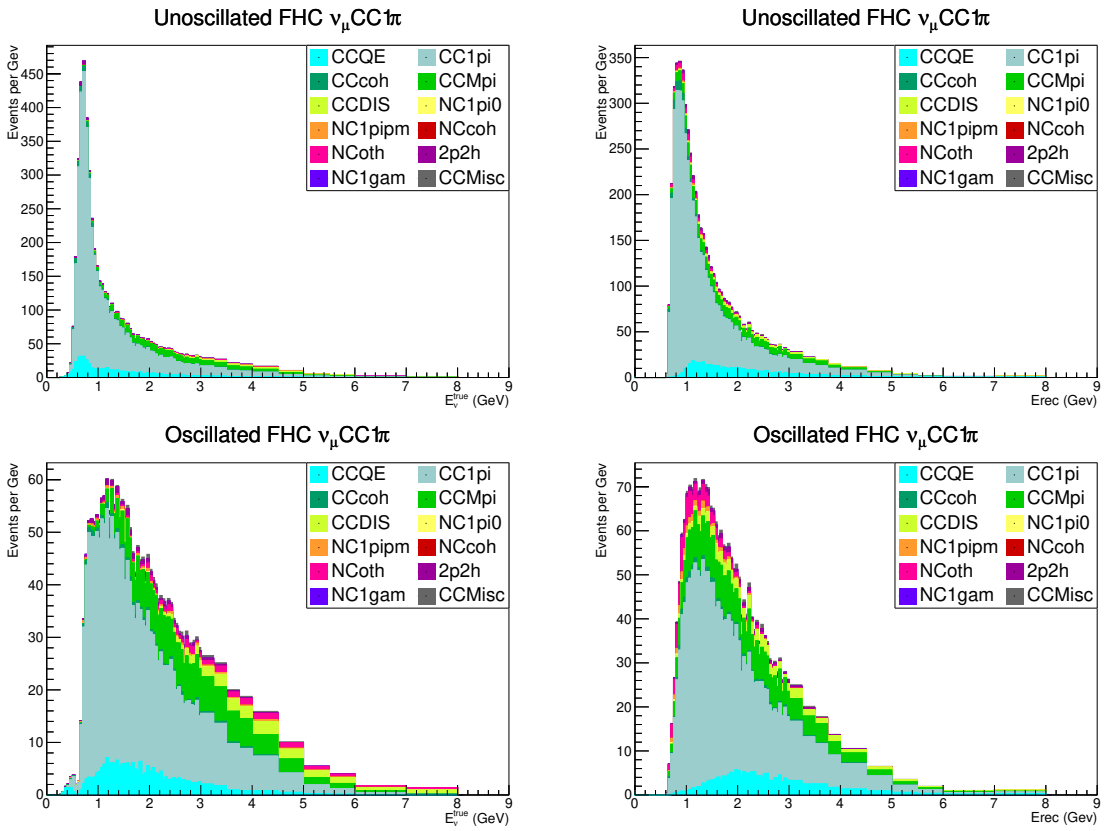

Figure 8.3: Predictions of the ν_μCC1π sample at SK in true neutrino energy (left) and reconstructed neutrino energy (right). The top plots are the predictions without oscillations and the lower plots are using the Asimov A neutrino oscillation parameters. The plots are broken down by each interaction mode.

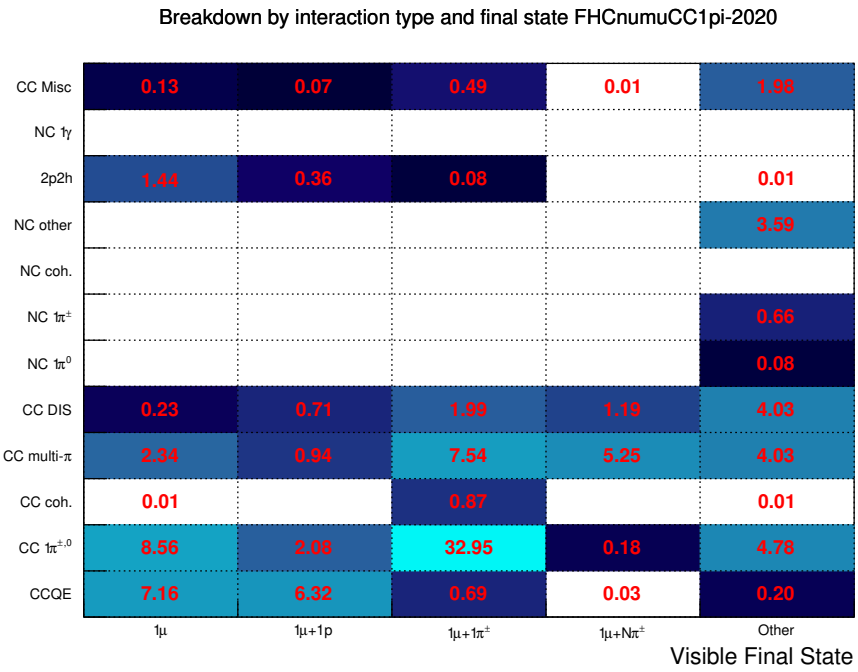

Figure 8.4: A comparison of the neutrino interaction modes and visible final state topologies for oscillated events in the ν_μCC1π sample at SK using the Asimov A oscillation parameters. The number of events in each bin corresponds to a percentage of all the events in the sample. The overlap between CCRES interactions and visible $1\mu + 1\pi$ can be seen to be by far the largest component of the sample as expected. No secondary particles are considered in these topology definitions.

8.3 Improved sensitivity to oscillation parameters

As well as increasing the statistics used in the oscillation analysis, the ν_μCC1π sample has the additional benefit of being sensitive to oscillation parameters at a higher neutrino energy than the other samples at SK. This means that this sample is sensitive to different oscillation effects so can give additional sensitivity to some oscillation parameters. Since the ν_μCC1π sample is a muon-like sample, it will be most sensitive to the oscillation parameters responsible for muon neutrino disappearance i.e. θ_{23} and Δm^2_{32}. In particular, the higher energy neutrinos in the sample is helpful in constraining Δm^2_{32} and hence also the mass ordering. To demonstrate how values Δm^2_{32}, θ_{23} and the mass ordering impacts the ν_μCC1π sample the predictions for various oscillation parameters is given in fig. 8.5.

The predictions in fig. 8.5 show how the MC distribution changes for different values of Δm^2_{32}, θ_{23} and the mass ordering. In particular, the impact that Δm^2_{32} can have on the shape of the MC predictions can be quite large. The impact of θ_{23} on the prediction can also be quite large but this mainly has an impact closer to the oscillation maximum (0.6GeV) where there are fewer events in the ν_μCC1π sample. The low number of statistics at these lower energies means that this sample is less sensitive to θ_{23} than it is to Δm^2_{32}. From these different MC predictions, it is expected that the addition of ν_μCC1π sample into the T2K oscillation analysis should aid in reducing the uncertainty on the Δm^2_{32} mass splitting. It should also be stressed that the fact that the other muon-like samples at SK constrain θ_{23} well, makes the ν_μCC1π sample complimentary to the current samples. To study the sensitivity increase from the addition of the ν_μCC1π sample into the oscillation analysis further, an Asimov fit with this sample included has been performed. As described in section 5.5.3, an Asimov fit firstly validates that the fitting framework works as expected and secondly gives the expected sensitivity of an analysis to the inputted parameter values. By comparing the Asimov contours presented in section 5.5.3 with an Asimov fit with the ν_μCC1π sample included the expected increase in sensitivity can be estimated.

For the Asimov fit, the nuisance parameters used were the same as those used in fits to data described in chapter 4 and chapter 7 and the Asimov A oscillation parameter values given in table 5.1 were used. As of yet, the SK detector systematic uncertainties for

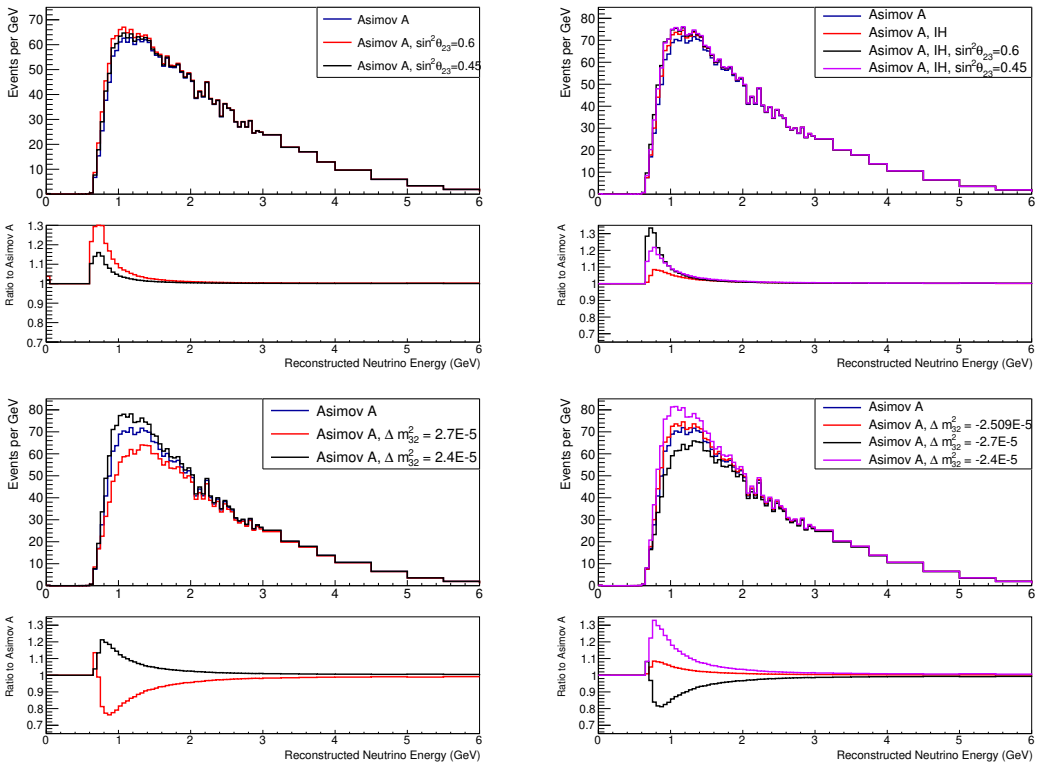

Figure 8.5: Predicted spectra for the ν_μCC1π sample at SK using different neutrino oscillation parameters. To compare the oscillated spectra these predictions are also given as a ratio to the prediction using the Asimov A neutrino oscillation parameter values. For the different predictions if a neutrino oscillation parameter has been changed from the Asimov A set then the value is given and any predictions labelled "IH" are for the inverted hierarchy and have the sign of Δm^2_{32} set to be negative.

the ν_μCC1π sample are not available. Therefore, no detector uncertainties are applied in this Asimov fit for the ν_μCC1π sample at SK. Despite this caveat, the Asimov fit should still serve as an indication as to whether the addition of the ν_μCC1π sample will increase the T2K experiments sensitivity to neutrino oscillation parameters. The results of this Asimov fit and comparisons to the Asimov fit without the ν_μCC1π sample included (which has already been shown in section 5.5.3) are shown in fig. 8.6 and fig. 8.7.

The comparison between the Asimov fit with and without the ν_μCC1π sample at SK included shows the expected impact that the ν_μCC1π sample will have on the oscillation analysis (if the Asimov A set of neutrino oscillation parameters were true in nature). The first thing to notice is that the introduction of the ν_μCC1π sample has no visible impact to the appearance contours shown in fig. 8.6. This behaviour is expected since the ν_μCC1π sample is a muon-like sample and so should not give any considerable sensitivity to δ_{CP} or $\sin^2\theta_{13}$. In contrast, the ν_μCC1π sample does have a visible impact on the disappearance contours. In both $\sin^2\theta_{23}$ and Δm^2_{32} the 1σ and 2σ credible intervals have changed, albeit it in fairly small ways. Since the ν_μCC1π sample contains interactions of typically higher energy than the other muon-like samples at SK, it is sensitive to different oscillation effects. Therefore, it is not unexpected that the shape of the contours and in the credible intervals change slightly. To make the impact on $\sin^2\theta_{23}$ and Δm^2_{32} clearer, 1D posterior densities are shown in fig. 8.7.

The 1D posterior distributions in fig. 8.7 show the impact on $\sin^2\theta_{23}$ which can now been seen to be minimal. There is a small shift in the position of both the 1σ and 2σ credible intervals, however this is only at the level on one bin width, and the actual width of the credible intervals do not change. In fact, for the case where only the inverted hierarchy is marginalised over the credible intervals are identical with and without the ν_μCC1π sample. This is not unexpected since the ν_μCC1π sample has events which are usually above the oscillation maximum so the samples sensitivity to $\sin^2\theta_{23}$ is not very large. On the other hand, the Δm^2_{32} posterior density with the addition of the ν_μCC1π sample can be see to have shifted slightly and also both the 1σ and 2σ credible regions can be seen to have shrunk. This is seen for the case were the mass hierarchies are marginalised over individually and when both mass hierarchies are marginalised over. The reduction in the credible interval region in Δm^2_{32} is the main indication of where the

ν_μCC1π sample can improve the sensitivity of the T2K neutrino oscillation analysis.

The comparison of an Asimov fit with and without the ν_μCC1π sample at SK indicates that this sample is expected to increase the sensitivity of the T2K oscillation analysis. This improvement mainly manifests itself in the uncertainty on Δm^2_{32} being slightly reduced. These Asimov fits are slightly limited in scope since they only show the improvement in sensitivity to neutrino oscillation parameters values used as the input, however, the fact that these fits show an improved constraint on Δm^2_{32} is an encouraging sign that the ν_μCC1π sample will help constraint neutrino oscillation parameters in fit to data. The increased sensitivity from this sample is the main role of the ν_μCC1π sample into the oscillation analysis, however, the sample also plays an important role for testing systematic uncertainties. The FHC 1ReCC1π sample was the only sample at SK for the run 1–10 data fit presented in chapter 7 to target interactions with pions. Since this sample is an e-like sample it does not contain many events. The addition of the ν_μCC1π sample at SK provides a higher statistics sample which also targets interactions with pions. This sample will be be less statistics limited so provides an good resource for looking at the impact of systematics effects related to charged pions as well as providing additional constraint to systematics in the fit. In this way, the ν_μCC1π sample at SK plays a dual role in the oscillation analysis.

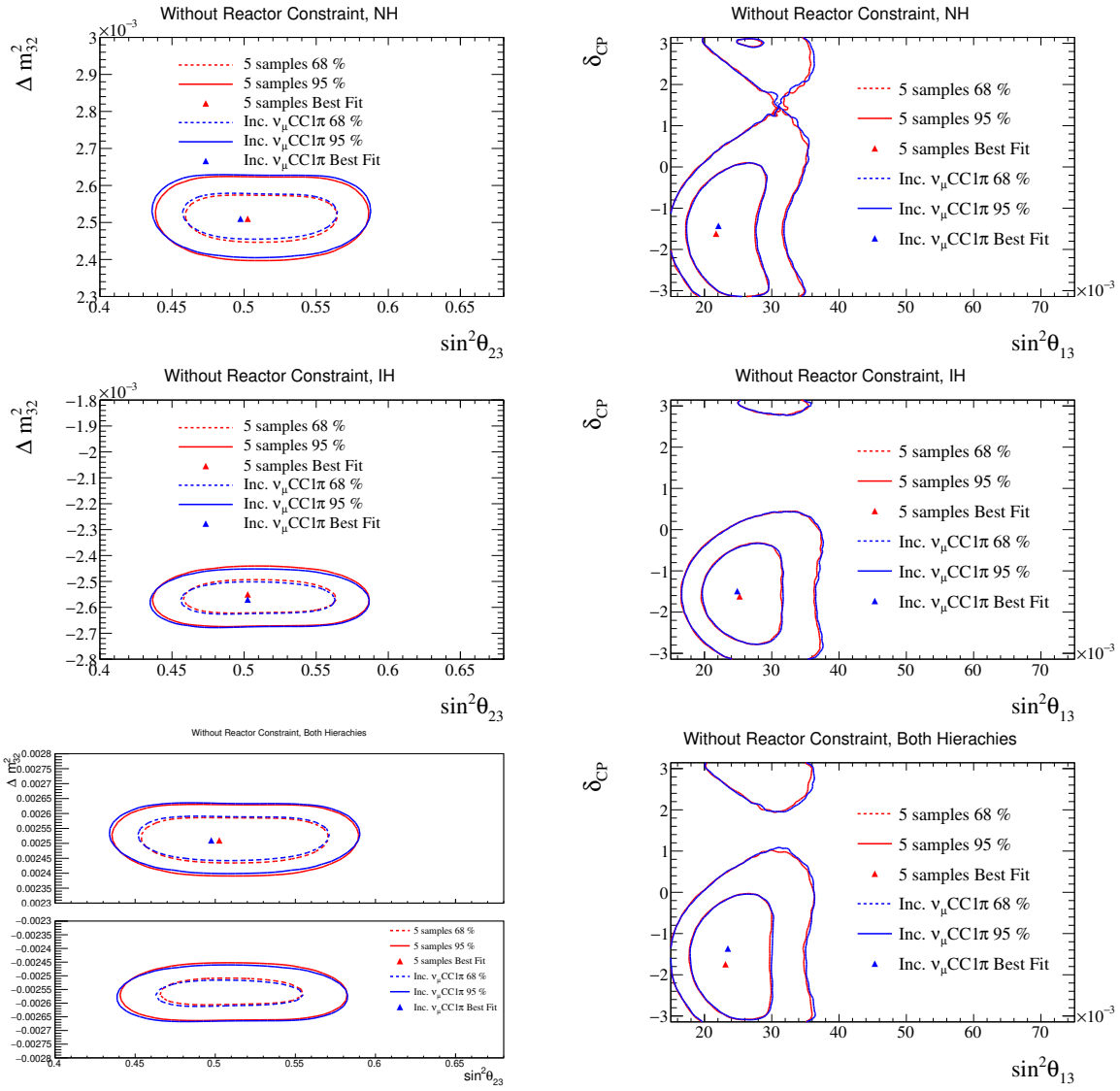

Figure 8.6: A comparison of the CIs from an Asimov fit using five SK samples and also including the ν_μCC1π sample. The CIs show a small increase in the sensitivity to Δm^2_{32} and a minor broadening of the uncertainty on θ_{23}. These are all shown not using the reactor constraint on θ_{13}.

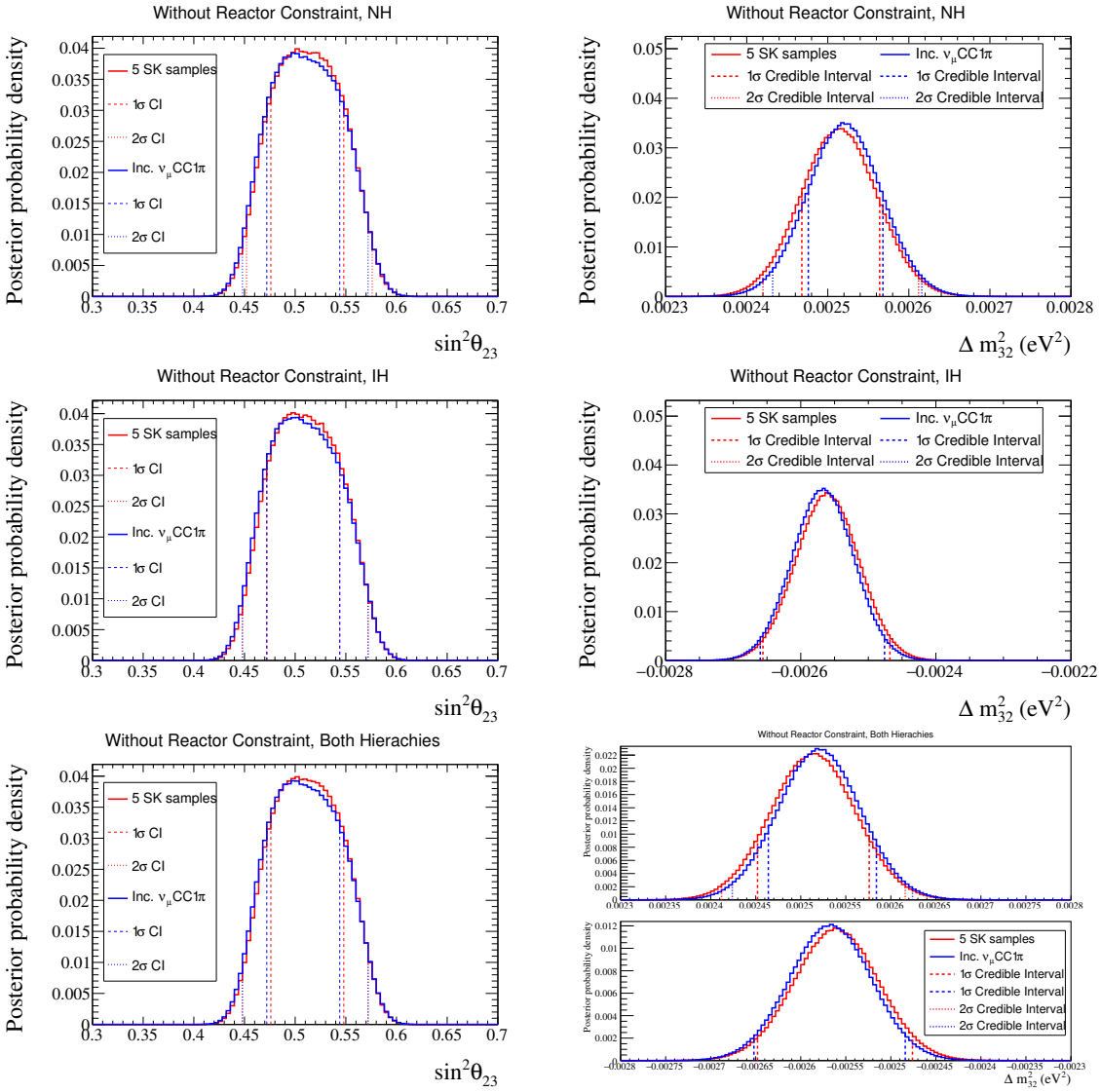

Figure 8.7: 1D CIs for an Asimov fit using five SK samples and one also using the ν_μCC1π sample at SK. It is now clearer in 1D that the Δm^2_{32} uncertainty decreases slightly but the θ_{23} constraint is very similar in both except for a small shift in the CIs.

8.4 Effect of mismodeling CC Multi-π and CC DIS interactions

The ν_μCC1π sample contains events which have originated from interactions with an energy typically higher than the other SK samples used in the T2K neutrino oscillation analysis. This means that the composition of the neutrino interactions which make up this sample are considerably different compared to other samples. In particular, the event rates shown in table 8.2 show the largest contributions to this sample from CCRES and CC Multi-π interactions. Furthermore, the fraction of CC DIS events predicted, although fairly low, is significantly higher compared to the other SK samples. Similarly, since the signal for the ν_μCC1π sample is targeting CCRES interactions CC Multi-π and CC DIS interactions become important in ensuring that CCRES interactions are not mismodelled. As has been described in chapter 6, CC Multi-π and CC DIS pose as background to the CC1π sample at ND280. This is even more important for the ν_μCC1π sample as the largest neutrino interaction which makes up this sample is CCRES. Therefore, if the CC Multi-π and CC DIS backgrounds are not properly accounted for, the prediction for the ν_μCC1π sample at SK will be incorrect and result in biased oscillation parameters being extracted. To demonstrate this effect a Fake Data Study (FDS) has been performed.

Fake data studies are typically performed to look at the impact of a change in the nominal MC at ND280 and SK and whether the nuisance parameters in the oscillation analysis can adequately account for this change in MC. Often, the changes in the MC looked at in fake data studies are considered extreme and are stress tests of the nuisance parameters used in the analysis. In other words, fake data studies are designed to look at "how does the analysis framework behave if nature is very different to our nominal MC". To study the impact of mismodeling CC Multi-π and CC DIS, MC with variations to the Bodek-Yang shape and CC Multi-π multiplicity parameters (as described in chapter 6) have been used as the data for the analysis. The use of this modified MC as the data coins the term "fake data" and this will be used when describing this modified MC. The fake data for this study was made by making MC predictions with the Bodek-Yang and CC Multi-π multiplicity parameters simultaneously to $+1\sigma$ which represents a significant change to the nominal MC. All other nuisance parameters were set to their prior central

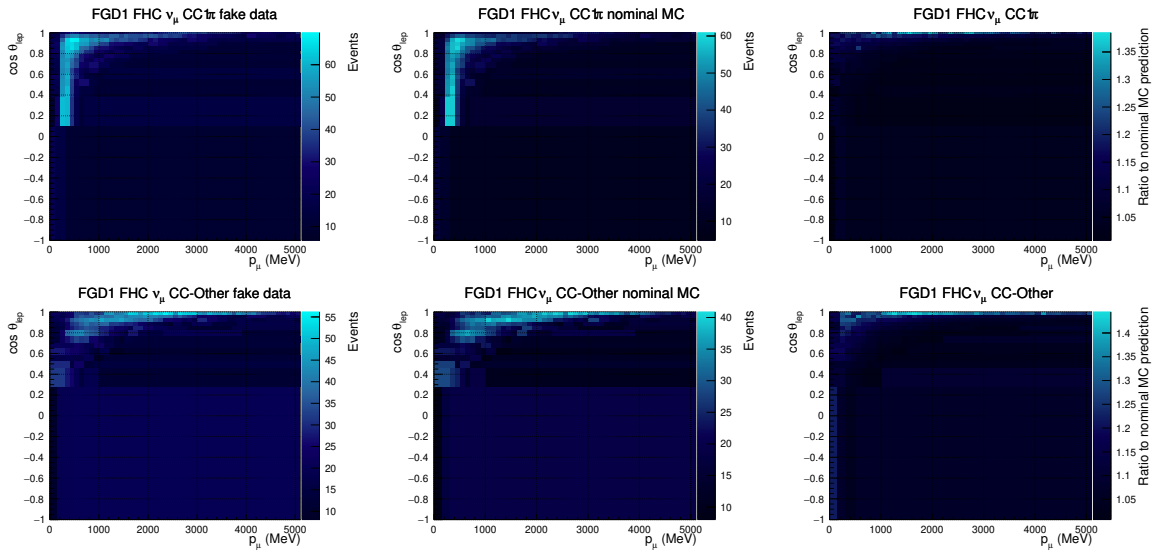

Figure 8.8: The fake data (left) and nominal MC (middle) at ND280 used in the FDS as well as the ratio of the fake data to the nominal MC (right) for the FGD1 CC1π and CC-Other samples in FHC. The fake data varies from the nominal MC most in the CC1π and CC-Other samples since these samples contain the most CC Multi-π and CC DIS interactions. The fake data, nominal MC and their ratios for all samples at ND280 are shown in appendix D.1.

values and the Asimov A set of neutrino oscillation parameters were used for the MC predictions at SK. These predictions and the ratio to the MC predictions, which were made with all other nuisance parameters set to their prior central value, for the CC-1π and CC-Other samples at ND280 and for all samples at SK can be seen in fig. 8.8, fig. 8.9, fig. 8.11 and fig. 8.10. So that the fit cannot account for this change to the nominal MC, the Bodek-Yang and CC Multi-π shape parameters are fixed both at ND280 and SK. This aims to show the impact of what would happen in the oscillation analysis if the data varied from our nominal model of CC DIS and CC Multi-π and the Bodek-Yang and CC Multi-π multiplicity parameters were not included in the fit.

The expectation from this FDS is that the fit will not return the neutrino oscillation parameters or nuisance parameter values which were used to make fake data inputs. Instead, the fit will attempt to describe the difference between the nominal MC with the limited freedom it has. This will result in both the nuisance parameters and neutrino oscillation parameters being used to describe the difference in CC DIS and CC Multi-π between the nominal MC and the fake data. What this results in is a bias in the nuisance

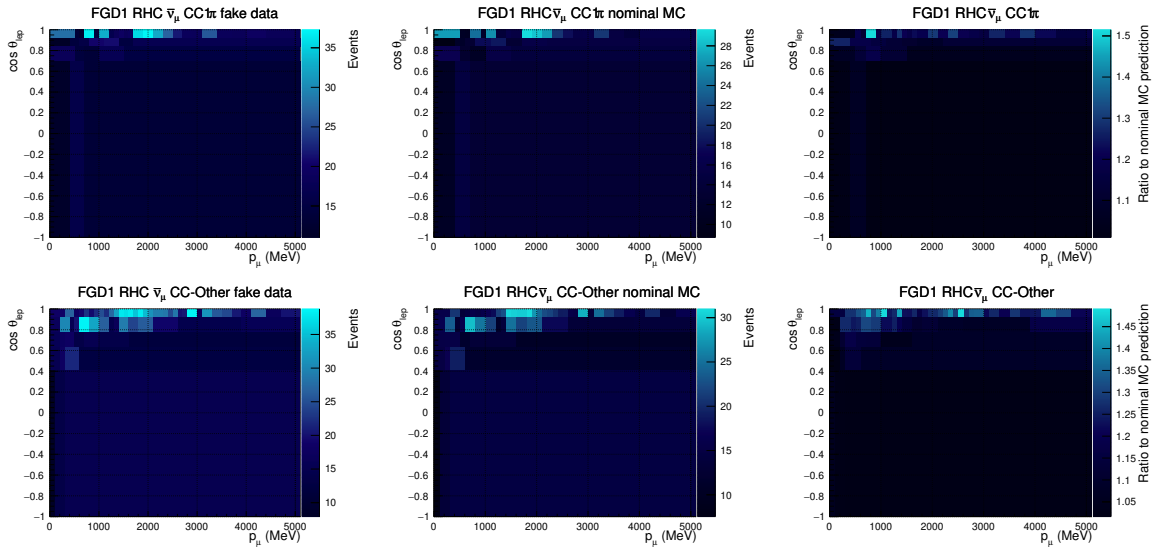

Figure 8.9: The fake data (left) and nominal MC (middle) at ND280 and the ratio of the fake data to the nominal MC (right) for the FGD1 CC0π, CC1π and CC-Other samples in RHC. The largest differences are in the CC1π and CC-Other samples since these samples contain more CC Multi-π and CC DIS interactions. The fake data, nominal MC and their ratios for all samples at ND280 are shown in appendix D.1.

parameters and, most crucially, the neutrino oscillation parameters returned in the fit. As this fake data study investigates the impact of CC DIS and CC Multi-π interactions, the areas where CC DIS and CC Multi-π interactions are important are expected to be the cause of this bias. It has been mentioned several times that CC Multi-π interactions pose as a background to CCRES interactions at the T2K experiment, so changes in CC Multi-π in the FDS are expected to cause a change in the nuisance parameters which describe uncertainties associated with CCRES interactions. Since the ν_μCC1π sample at SK is predominantly predicted to be CCRES interactions this will then lead to a bias in the neutrino oscillation parameters extracted from the fit. In addition, the normalisation parameters associated with higher energy interactions are expected to attempt to describe the difference in the nominal MC and the fake data. Therefore, the CC Multi-π, CC DIS and CC Misc. normalisation parameters as well as the high energy flux parameters are expected to be biased. These biases are also expected to result in a bias in the extract neutrino oscillation parameters. In particular, a change in the flux parameters will result in a change in the prediction for all samples so the bias in oscillation parameters will not be purely as a result of mismodeling of CCRES interactions in the ν_μCC1π sample.

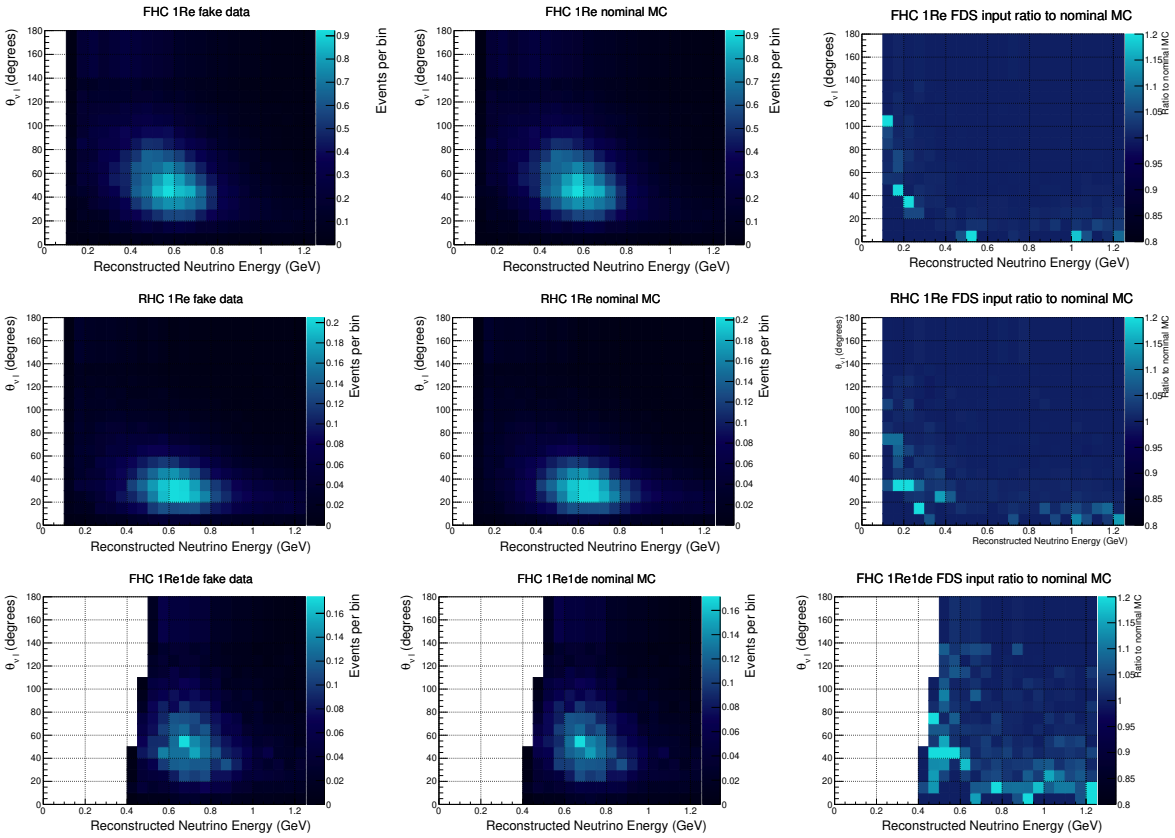

Figure 8.10: The fake data (left) and nominal MC (middle) at SK used in the FDS as well as the ratio of the fake data to the nominal MC (right) for each sample at SK. The fake data varies from the nominal MC most in the two samples which target interactions with a pion.

The results from the FDS are shown in figs. 8.12 to 8.17. For all of these results, comparisons to an Asimov fit using the Asimov A neutrino oscillation parameters and with nuisance parameter values set to their prior central value. The Asimov A oscillation parameter values are given in **??**. Figure 8.12 compares the oscillation parameter constraints from the Asimov fit and the FDS. The bias in the oscillation parameters is clear in the disappearance parameters in particular, where the contours are significantly different. The constraints in δ_{CP} vs. $\sin^2\theta_{13}$ also differ but not as significantly. The ν_μCC1π sample at SK is expected to be a significant bias in the disappearance parameters because CCRES interactions make up a large fraction of the predicted number of events for this sample. Therefore, the mismodeling of CC Multi-π and CC DIS interactions can cause nuisance parameters related to CCRES interactions to be biased. This then results in the MC prediction of the ν_μCC1π sample at SK to be biased and then oscillation param-

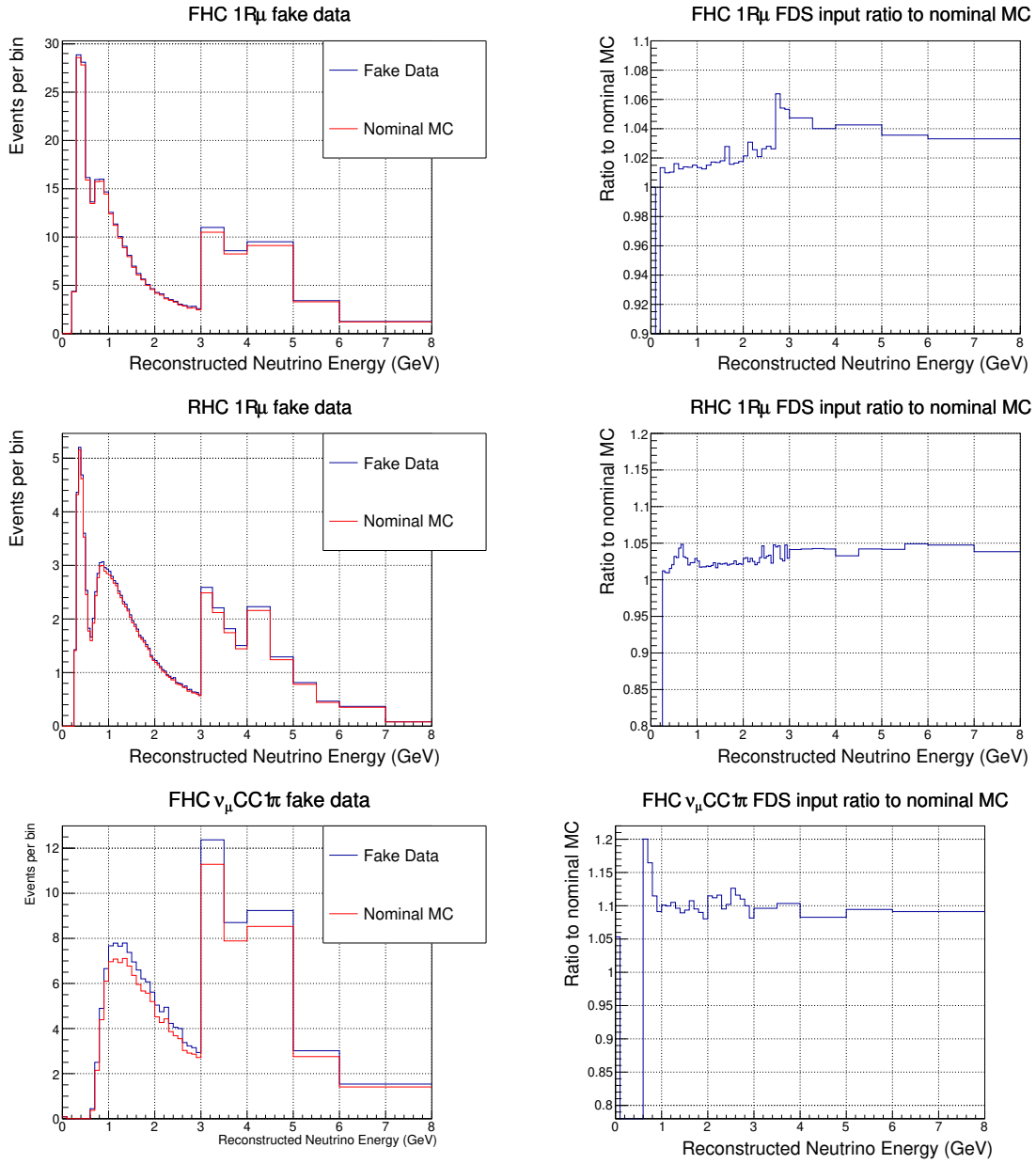

Figure 8.11: The fake data and nominal MC (left) at SK used in the FDS as well as the ratio of the fake data to the nominal MC (right) for each sample at SK. The fake data varies from the nominal MC most in the two samples which target interactions with a pion which is expected as CC Multi-π and CC DIS interactions are a larger background in these sample. In particular, there is a large difference in the ν_μCC1π fake data compared to the nominal MC prediction.

eters to be extracted incorrectly. It can be seen in fig. 8.13 that the nuisance parameters related to neutrino interactions show that this is indeed the case. Nuisance parameters related to CCQE and 2p-2h are not impacted in the FDS but for nuisance parameters

related to CCRES (such as M_{RES}^{A} and C_{5}^{A}) return parameter values which are different to their input values. In fig. 8.13 the 2p2h energy dependent parameters have been removed as these paramters are very poorly constrained.

One of the other observations of the FDS is that the flux parameters are also impacted by the mismodeling of CC Multi-π and CC DIS. Since CC Multi-π and CC DIS have the larger cross sections at higher neutrino energies, the mismodeling of these interactions can lead to nuisance parameters related to the higher energy neutrino flux predictions can be impacted. This can be seen quite clearly in figs. 8.14 to 8.17 for the nuisance parameters for the higher energy component of the neutrino flux are pulled above their inputted values. The flux parameters are pulled to these higher values as without the CC DIS and CC Multi-π shape parameters the fit cannot account for the larger CC DIS and CC Multi-π in the fake data. It can also be seen in that some nuisance parameters that are related to the lower energy flux predictions are also found to be at a greater value than their inputted values in the FDS. Although there does not seem to be any immediate reason for this since CC DIS and CC Multi-π interactions should have a very minimal impact at lower energies, since nuisance parameters for the neutrino flux are often positively correlated these lower energy nuisance parameters are increases since the higher energy flux prediction has to increase. The flux parameters will impact the predictions for all samples so these biases are likely to be the cause of the slight change in the appearance contours as well as contributing to the change in the disappearance contours.

The results from the FDS clearly indicate the importance of the CC DIS and CC Multi-π shape parameters that have been developed for the T2K neutrino oscillation analysis. Without these parameters included in the analysis a fit to data, where CC DIS and CC Multi-π interactions are significantly different to the nominal MC prediction, results in biased nuisance and oscillation parameters being extracted. In particular, nuisance parameters related to the modelling of CCRES interactions are incorrectly described which is especially important for making accurate predictions of the ν_{μ}CC1π sample at SK. In addition, the nuisance parameters related to modelling the high energy neutrino flux prediction are forced to be increased due to the lack of freedom without the CC Multi-π and CC DIS shape parameters included in the analysis. The combination of nuisance

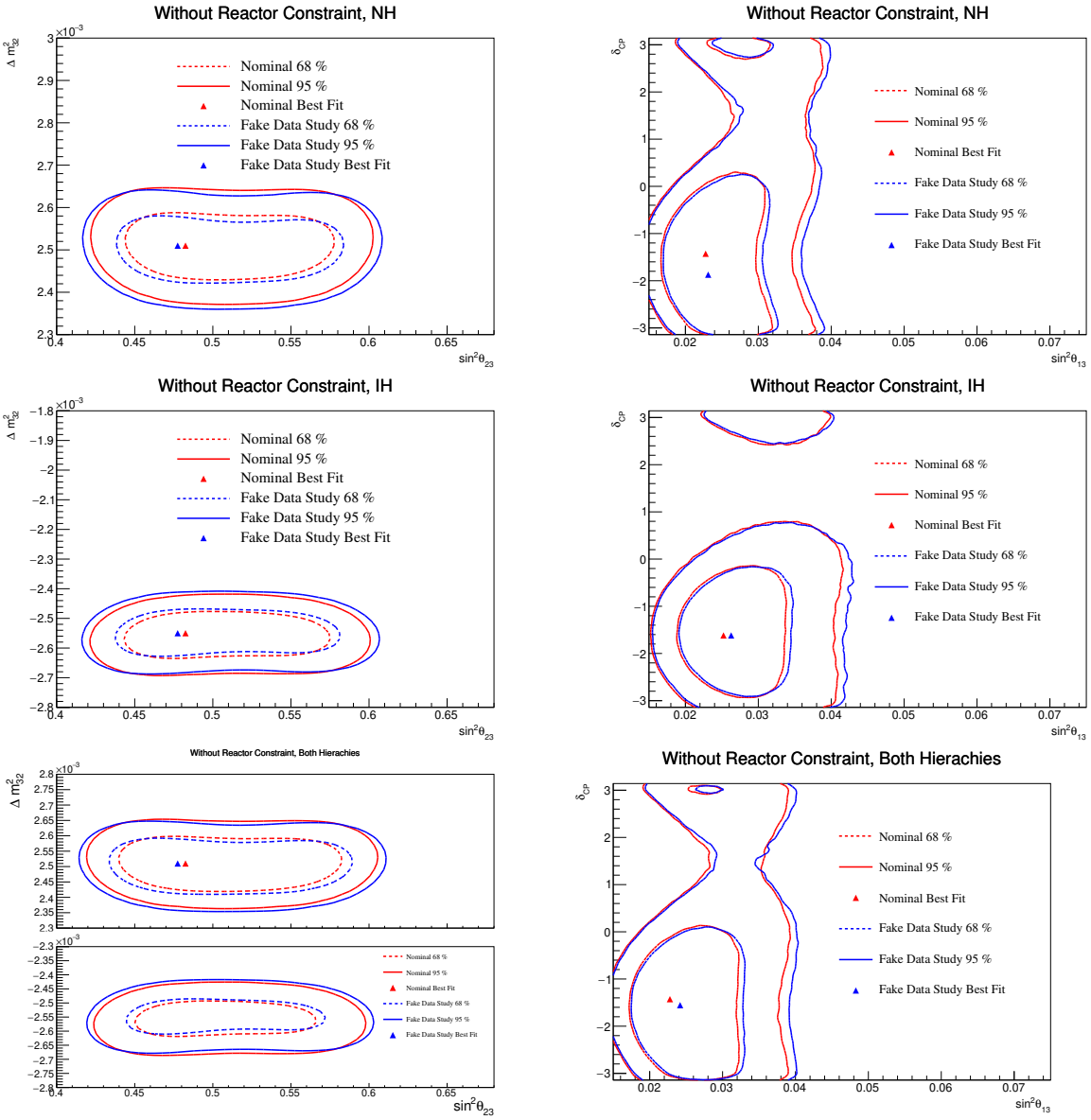

Figure 8.12: A comparison of the results on oscillation parameters from a FDS and an Asimov fit. The change in the credible intervals indicates the bias introduced by the change to CC Multi-π and CC DIS interactions in the fake data.

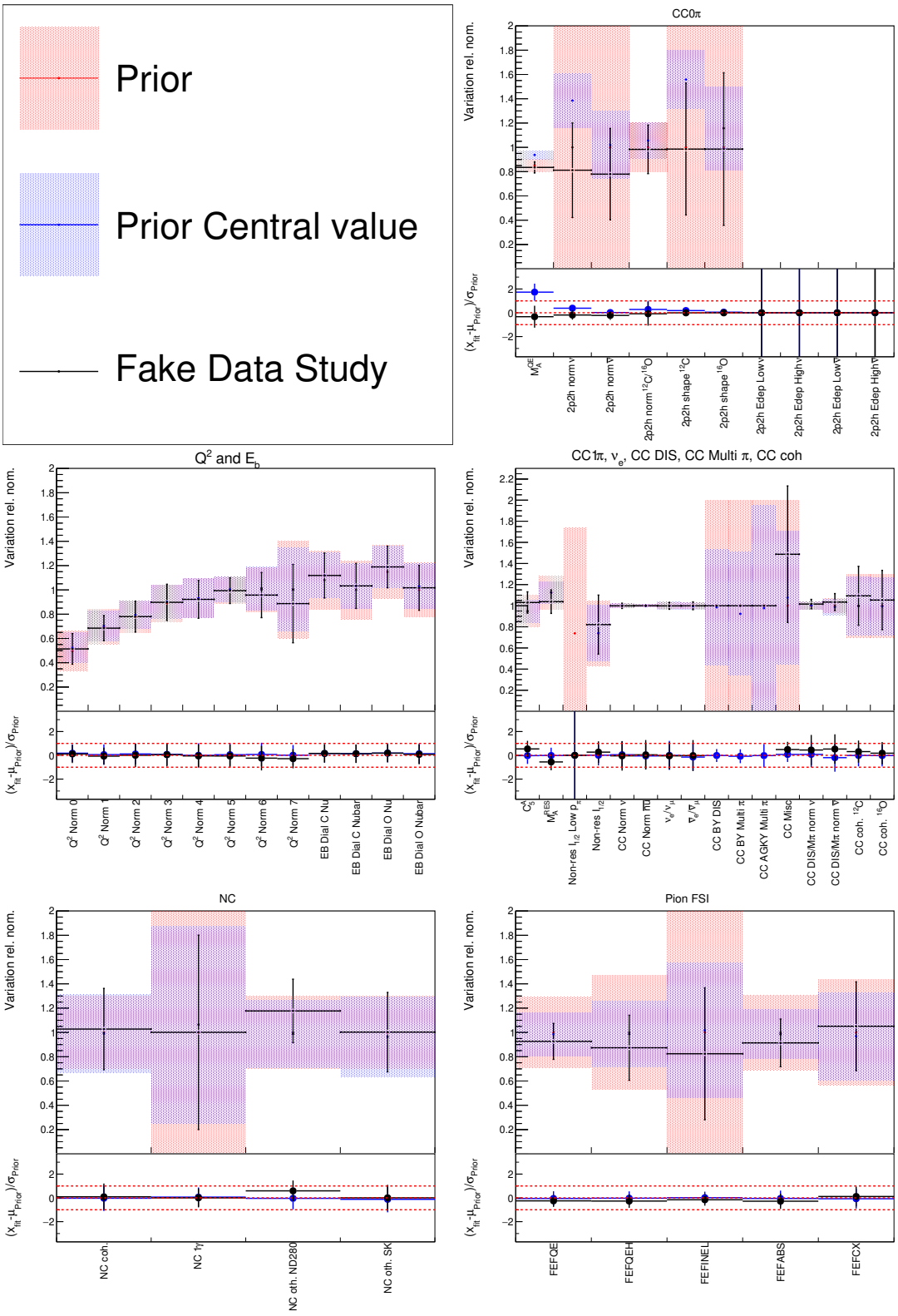

Figure 8.13: Comparison of the parameter values for the FDS and an Asimov fit where parameter values are set to their prior central values. The nuisance parameters related to CCRES interactions as well as the CC Multi-π, CC DIS and CC Misc. normalisation parameters can be seen to have moved from their inputted prior central values which indicates a bias in these parameters.

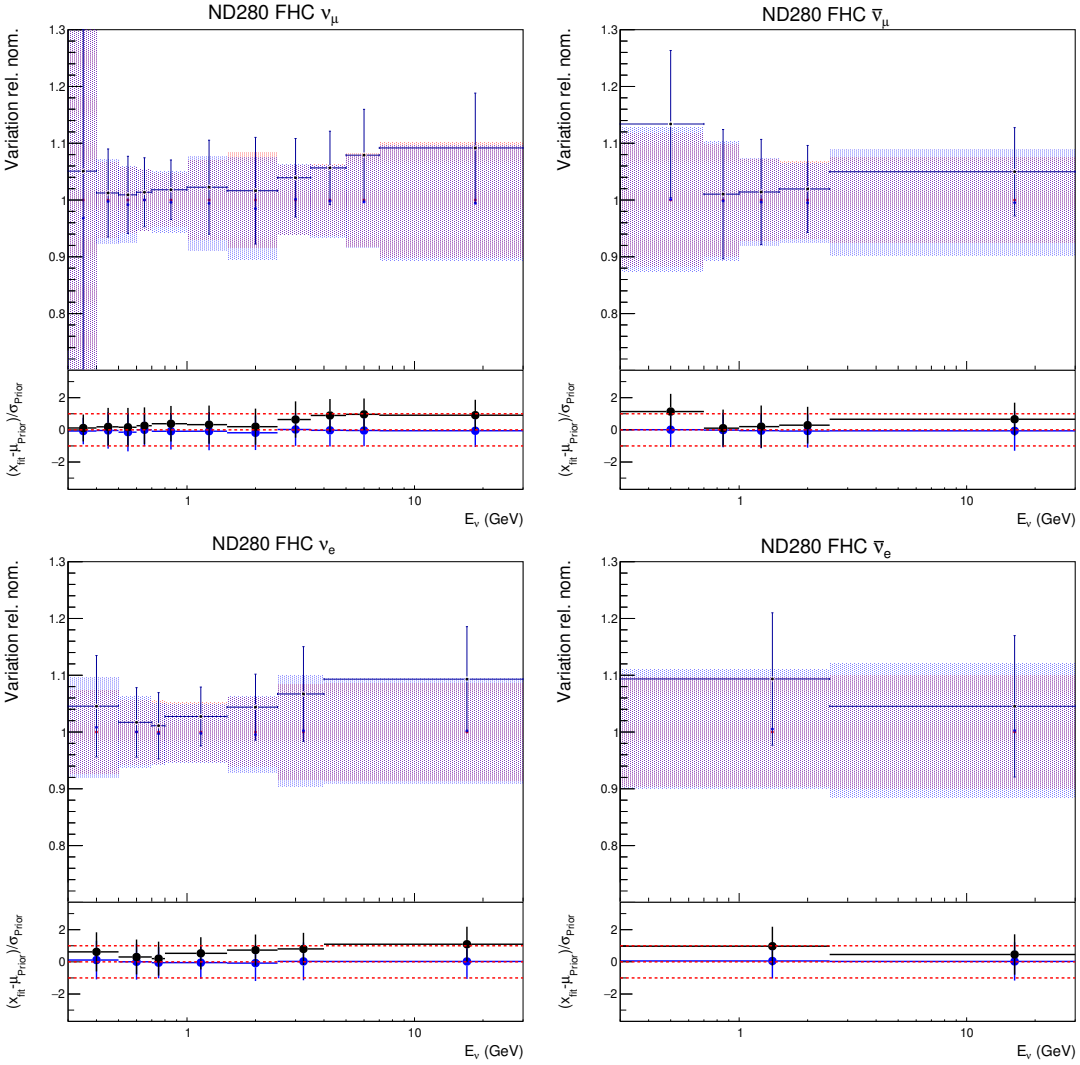

Figure 8.14: A comparison of the parameter values for the FDS and an Asimov fit where parameter values are set to their prior central values. Here the parameters relating to the neutrino flux in FHC mode at ND280 are shown. Each parameter related to a different normalisation parameter covering a range of true neutrino energy given by the x-axis.

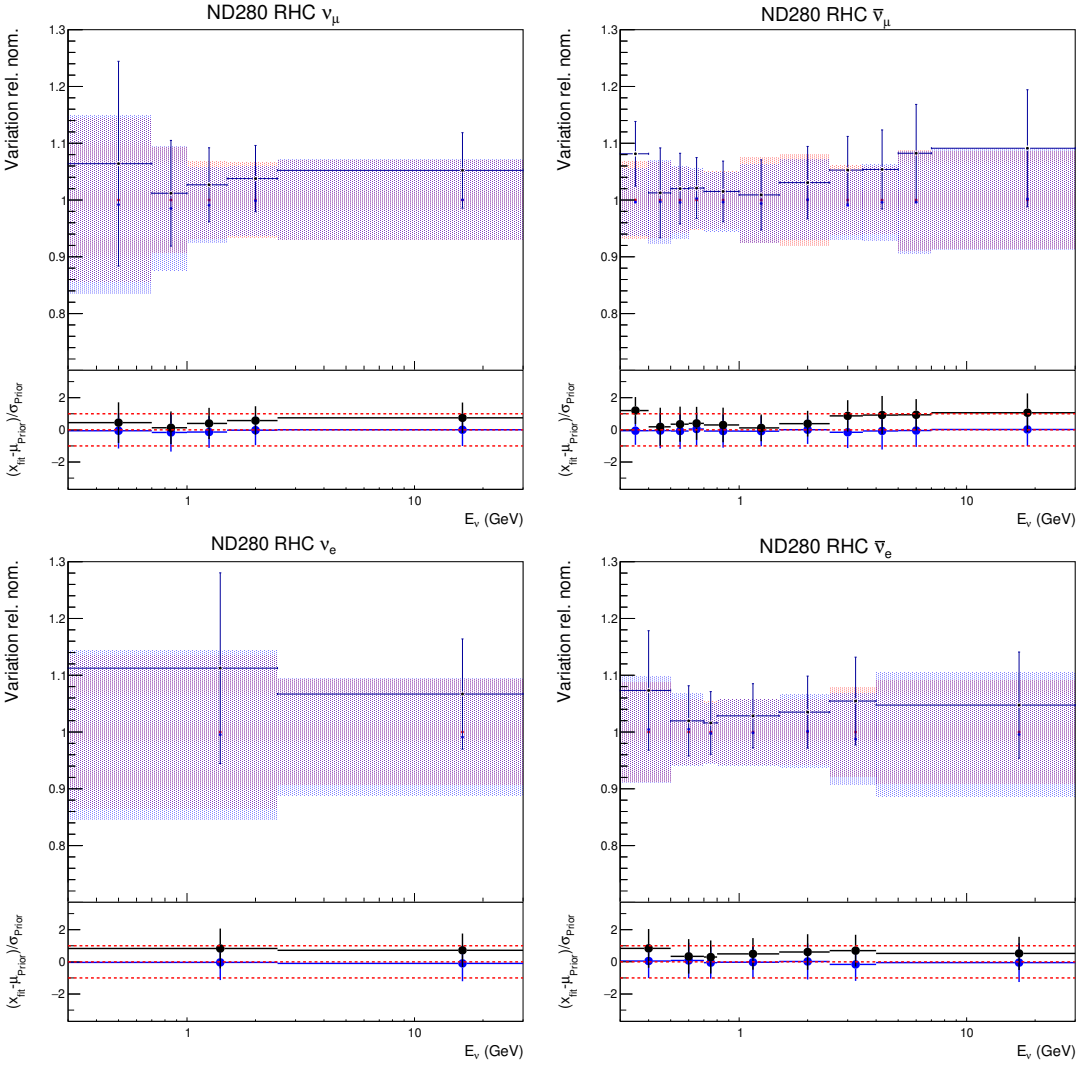

Figure 8.15: Comparison of the parameter values for the FDS and an Asimov fit where parameter values are set to their prior central values. Here the parameters relating to the neutrino flux in RHC mode at ND280 are shown. Each parameter related to a different normalisation parameter covering a range of true neutrino energy given by the x-axis.

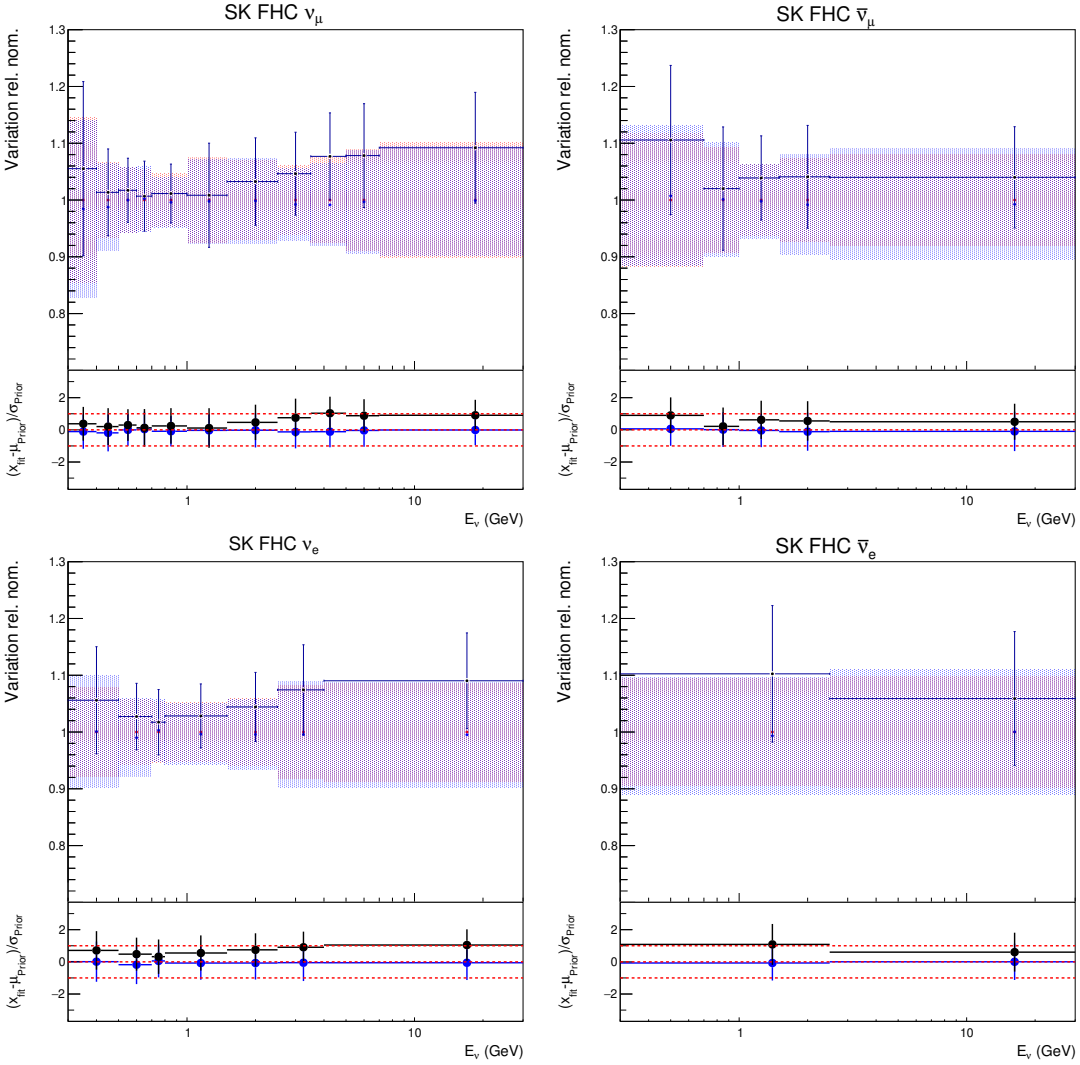

Figure 8.16: Comparison of the parameter values for the FDS and an Asimov fit where parameter values are set to their prior central values. Here the parameters relating to the neutrino flux in FHC mode at SK are shown. Each parameter related to a different normalisation parameter covering a range of true neutrino energy given by the x-axis.

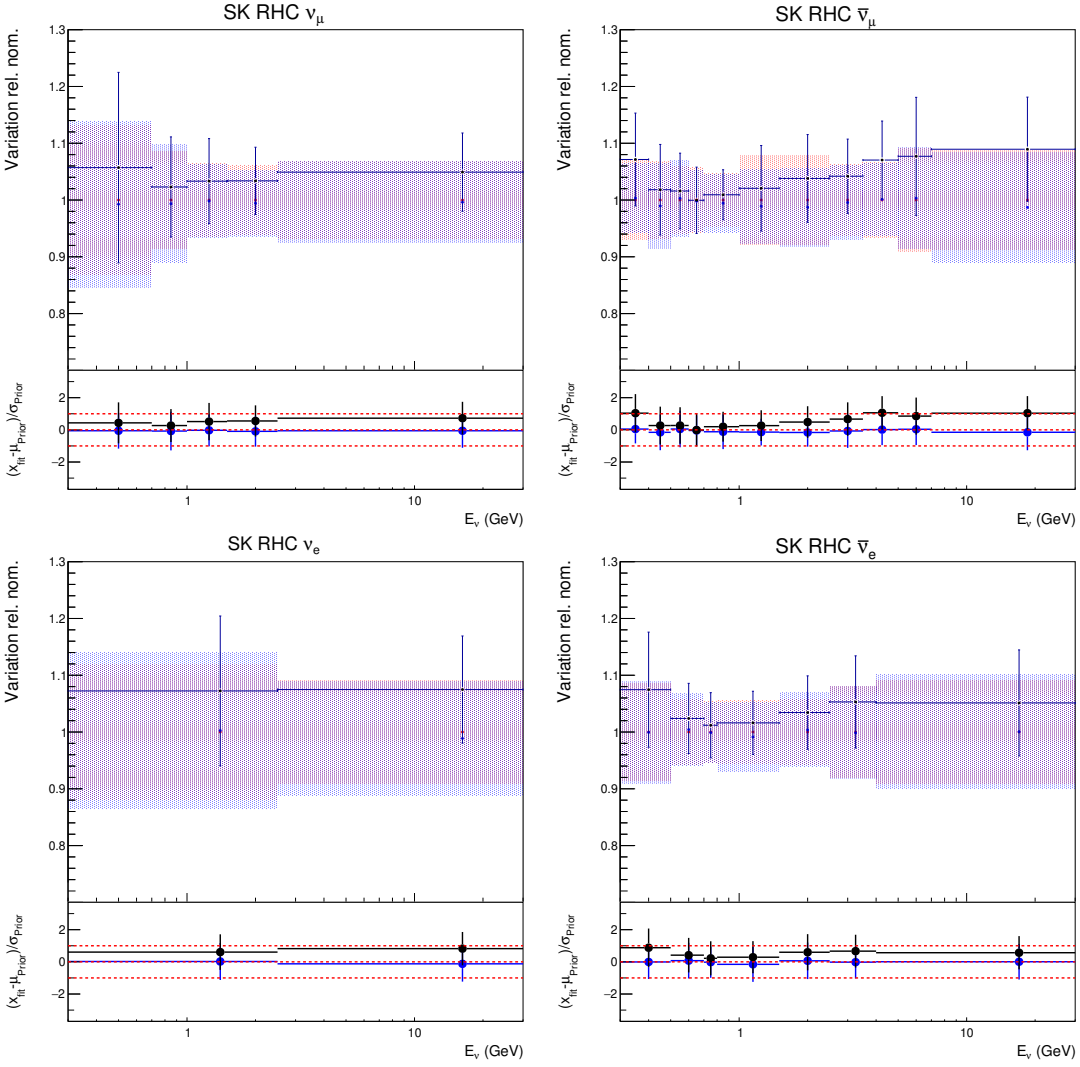

Figure 8.17: Comparison of the parameter values for the FDS and an Asimov fit where parameter values are set to their prior central values. Here the parameters relating to the neutrino flux in RHC mode at SK are shown. Each parameter related to a different normalisation parameter covering a range of true neutrino energy given by the x-axis.

parameters for CCRES and the neutrino flux predictions then causes the extracted neutrino oscillation parameters to be biased since the MC prediction at SK is incorrect. In a fit to real data (i.e. those collected at ND280 and SK), if CC Multi-π and CC DIS interactions were significantly different to the nominal MC predictions used at T2K and the CC DIS and CC Multi-π shape parameters were not used in the analysis, then the statements made on neutrino oscillation parameters would be biased. Particularly as future fits to data will include the ν_μCC1π sample at SK, these CC DIS and CC Multi-π shape parameters are vital in ensuring that neutrino oscillation parameters are extracted correctly.

8.5 Summary

In this chapter, the impact of adding the ν_μCC1π sample at SK into the oscillation analysis has been shown. An Asimov fit with preliminary inputs has been presented and shows the potential gains in sensitivity to neutrino oscillation parameters from adding this sample into the analysis. The ν_μCC1π sample is sensitive to neutrino oscillation parameters which impact muon neutrino disappearance. This increase in sensitivity mainly manifests itself through an increase in the precision on Δm^2_{32} which should also increase T2K experiments sensitivity to the neutrino mass ordering. The next iteration of the T2K oscillation analysis will include the data from the ν_μCC1π sample in the oscillation analysis.

A breakdown of the ν_μCC1π sample has also been shown which highlights that it is comprised of interactions which occur at typically higher energies than the other samples at SK in the oscillation analysis. Therefore, the events which make up this sample are expected to be predominantly CCRES and CC Multi-π interactions. The large contribution of these CCRES and CC Multi-π interactions set the ν_μCC1π sample apart from the other muon-like samples at SK which are dominated by CCQE interactions. This means that for the ν_μCC1π sample the CC DIS and CC Multi-π shape parameters are important in accurately making predictions at SK and ultimately making constraints on oscillation parameters.

To highlight the importance of the CC DIS and CC Multi-π parameters in the oscillation analysis a FDS has been performed. In this FDS, MC predictions where the CC DIS and CC Multi-π interactions were significantly different to the nominal MC prediction were used as data. Then, crucially, the fit was not allowed to vary the CC DIS or CC Multi-π shape parameters in the fit from its prior central value. This then led to a bias in nuisance parameter values related to CCRES, CC Multi-π, CC DIS and the neutrino flux especially at higher neutrino energies. Ultimately this then also created a bias in the oscillation parameters extracted from the fit. The FDS clearly shows the importance of the CC Multi-π and CC DIS shape parameters in making accurate measurements of neutrino oscillation parameters.

Chapter 9

Conclusion and outlook

This thesis has focused on the latest results from the T2K oscillation analysis with improved systematic uncertainties related to interactions involving final state hadrons from CC Multi-π and CC DIS interactions. The addition of the FHC ν_μCC1π sample into the analysis was then shown as well as the important role that these new CC Multi-π and CC DIS systematics play for this sample.

The latest T2K data-fit results using the MaCh3 framework which uses Markov Chain Monte Carlo were presented in chapter 7. This analysis used all the available data at the time at both ND280 and SK and included the improved CC Multi-π and CC DIS systematic uncertainties that I developed. The analysis technique used for measuring neutrino oscillation parameters at the T2K experiments and the Markov Chain Monte Carlo techniques used by the MaCh3 framework in chapter 4 and chapter 5. The results from this analysis are the latest and most sensitive results to neutrino oscillation parameters from the T2K experiment. The results disfavour CP-conservation in the neutrino sector at the 90% level, giving a possible indication of CP-violation. To establish whether this indication is real the results need to be improved on going forward. To improve on the current results, the statistical and systematic uncertainties in the current analysis need to be reduced.

One way to reduce the statistical uncertainty on the measurement of neutrino oscillation parameters is by including additional data samples such as the FHC ν_μCC1π

sample. The potential improvement to the sensitivity of the T2K experiment was shown in chapter 8. Although the size of the improvement to the sensitivity is not large from the addition of this sample, there was a noticeable improvement in the measurement of Δm^2_{32}. The additional sensitivity from this sample will increase as the T2K experiment continues to take more data. The ν_μCC1π sample also has a second role in the analysis by being an important check of systematics related to CCRES, CC Multi-π and CC DIS interactions. The importance of the new CC Multi-π and CC DIS systematics described in chapter 6 to an analysis including the FHC ν_μCC1π sample was shown by looking at fake data studies in chapter 8. This fake data study clearly showed that in the situation where nature is significantly different to the nominal predictions for CC Multi-π and CC DIS interactions, these new systematics are crucial to measuring neutrino oscillation parameters without bias. The next T2K oscillation analysis plans to include the ν_μCC1π sample in data fits. Before this can happen, new systematics related to CCRES interactions will have to be developed. The new systematics that have been described in chapter 6 will be the basis for the systematics related to CC Multi-π and CC DIS interactions for the next analysis.

Experiments measuring neutrino oscillation parameters are at an exciting point in history. The results from the T2K experiment give an indication of CP-violation in the neutrino sector. Current generation experiments such as T2K and NOvA will strive to keep improving their results in the coming years by taking more data and improving systematic uncertainties. These experiments should be able to give strong statements on the octant, mass ordering and CP-violation in neutrino oscillations. However, these experiments will not have the statistical power to make $5\,\sigma$ statements to answer these key questions. In the near future, the Hyper-K and DUNE experiments will add greatly to the picture painted by T2K and NOvA and will measure neutrino oscillation parameters with unprecedented precision. The PMNS parameterisation of neutrino oscillations will be scrupulously tested and, if CP-violation exists, the magnitude of CP-violation in the neutrino sector will be determined. All of these measurements will contribute greatly to the field of Particle Physics by understanding what Physics lays beyond the Standard Model and how matter came to be.

Bibliography

[1] Patrick Dunne. *Latest Neutrino Oscillation Results from T2K*. July 2020. DOI: 10.5281/zenodo.4154355. URL: https://doi.org/10.5281/zenodo.4154355.

[2] K. Abe et al. "The T2K Experiment". In: *Nucl. Instrum. Meth. A* 659 (2011), pp. 106–135. DOI: 10.1016/j.nima.2011.06.067. arXiv: 1106.1238 [physics.ins-det].

[3] Q. R. Ahmad et al. "Direct evidence for neutrino flavor transformation from neutral current interactions in the Sudbury Neutrino Observatory". In: *Phys. Rev. Lett.* 89 (2002), p. 011301. DOI: 10.1103/PhysRevLett.89.011301. arXiv: nucl-ex/0204008.

[4] Y. Fukuda et al. "Evidence for oscillation of atmospheric neutrinos". In: *Phys. Rev. Lett.* 81 (1998), pp. 1562–1567. DOI: 10.1103/PhysRevLett.81.1562. arXiv: hep-ex/9807003.

[5] Serguei Chatrchyan et al. "Observation of a New Boson at a Mass of 125 GeV with the CMS Experiment at the LHC". In: *Phys. Lett. B* 716 (2012), pp. 30–61. DOI: 10.1016/j.physletb.2012.08.021. arXiv: 1207.7235 [hep-ex].

[6] Georges Aad et al. "Observation of a new particle in the search for the Standard Model Higgs boson with the ATLAS detector at the LHC". In: *Phys. Lett. B* 716 (2012), pp. 1–29. DOI: 10.1016/j.physletb.2012.08.020. arXiv: 1207.7214 [hep-ex].

[7] Cush MissMJ. *Standard Model of Elementary particles*. [Online; accessed 19-July-20021]. 2019. URL: %5Curl%7Bhttps://en.wikipedia.org/wiki/File:Standard_Model_of_Elementary_Particles.svg%7D.

[8] Carlo Giunti and Chung W. Kim. *Fundamentals of Neutrino Physics and Astrophysics*. 2007. ISBN: 978-0-19-850871-7.

[9] Antonio Riotto. "Theories of baryogenesis". In: *ICTP Summer School in High-Energy Physics and Cosmology*. July 1998, pp. 326–436. arXiv: hep-ph/9807454.

[10] Enrico Fermi. "Tentativo di una teoria dell'emissione dei raggi beta". In: *Ric. Sci.* 4 (1933), pp. 491–495.

[11] M. Thompson. *Modern Particle Physics*. Modern Particle Physics. Cambridge University Press, 2013. ISBN: 9781107034266. URL: https://books.google.co.uk/books?id=BV1sAAAAQBAJ.

[12] C. S. Wu et al. "Experimental Test of Parity Conservation in β Decay". In: *Phys. Rev.* 105 (1957), pp. 1413–1414. DOI: 10.1103/PhysRev.105.1413.

[13] R. P. Feynman and Murray Gell-Mann. "Theory of Fermi interaction". In: *Phys. Rev.* 109 (1958). Ed. by L. M. Brown, pp. 193–198. DOI: 10.1103/PhysRev.109.193.

[14] G. Danby et al. "Observation of High-Energy Neutrino Reactions and the Existence of Two Kinds of Neutrinos". In: *Phys. Rev. Lett.* 9 (1962), pp. 36–44. DOI: 10.1103/PhysRevLett.9.36.

[15] K. Kodama et al. "Observation of tau neutrino interactions". In: *Phys. Lett. B* 504 (2001), pp. 218–224. DOI: 10.1016/S0370-2693(01)00307-0. arXiv: hep-ex/0012035.

[16] Patrick Janot and Stanisław Jadach. "Improved Bhabha cross section at LEP and the number of light neutrino species". In: *Physics Letters B* 803 (Apr. 2020), p. 135319. ISSN: 0370-2693. DOI: 10.1016/j.physletb.2020.135319. URL: http://dx.doi.org/10.1016/j.physletb.2020.135319.

[17] Elliot Leader and Enrico Predazzi. *An Introduction to Gauge Theories and Modern Particle Physics*. Vol. 2. Cambridge Monographs on Particle Physics, Nuclear Physics and Cosmology. Cambridge University Press, 1996. DOI: 10.1017/CBO9780511622601.

[18] Ziro Maki, Masami Nakagawa, and Shoichi Sakata. "Remarks on the unified model of elementary particles". In: *Prog. Theor. Phys.* 28 (1962), pp. 870–880. DOI: 10.1143/PTP.28.870.

[19] B. Pontecorvo. "Neutrino Experiments and the Problem of Conservation of Leptonic Charge". In: *Zh. Eksp. Teor. Fiz.* 53 (1967), pp. 1717–1725.

[20] Boris Kayser. "Neutrino physics". In: *eConf* C040802 (2004). Ed. by Joanne Hewett et al., p. L004. arXiv: hep-ph/0506165.

[21] P. Langacker et al. "On the Mikheev-Smirnov-Wolfenstein (MSW) Mechanism of Amplification of Neutrino Oscillations in Matter". In: *Nucl. Phys. B* 282 (1987), pp. 589–609. DOI: 10.1016/0550-3213(87)90699-7.

[22] Kaoru Hagiwara, Naotoshi Okamura, and Ken-ichi Senda. "The earth matter effects in neutrino oscillation experiments from Tokai to Kamioka and Korea". In: *JHEP* 09 (2011), p. 082. DOI: 10.1007/JHEP09(2011)082. arXiv: 1107.5857 [hep-ph].

[23] R. Wendell. *Prob3++ software for computing three flavour neutrino*. URL: http://www.phy.duke.edu/~raw22/public/Prob3.

[24] Tomas Nosek. "Effects of Matter in Neutrino Oscillations and Determination of Neutrino Mass Hierarchy at Long-baseline Experiments". Other thesis. Dec. 2016. arXiv: 1612.09132 [hep-ph].

[25] A.D. Sakharov. "Violation of CP Invariance, C asymmetry, and baryon asymmetry of the universe". In: *Sov. Phys. Usp.* 34.5 (1991), pp. 392–393. DOI: 10.1070/PU1991v034n05ABEH002497.

[26] P.A. Zyla et al. "Review of Particle Physics". In: *PTEP* 2020.8 (2020), p. 083C01. DOI: 10.1093/ptep/ptaa104.

[27] C. Jarlskog. "A Basis Independent Formulation of the Connection Between Quark Mass Matrices, CP Violation and Experiment". In: *Z. Phys. C* 29 (1985), pp. 491–497. DOI: 10.1007/BF01565198.

[28] Hisakazu Minakata, Hiroshi Nunokawa, and Stephen Parke. "Parameter degeneracies in neutrino oscillation measurement of leptonicCPandTviolation". In: *Physical Review D* 66.9 (Nov. 2002). ISSN: 1089-4918. DOI: 10.1103/physrevd.66.093012. URL: http://dx.doi.org/10.1103/PhysRevD.66.093012.

[29] "Deep Underground Neutrino Experiment (DUNE), Far Detector Technical Design Report, Volume I Introduction to DUNE". In: *JINST* 15.08 (2020), T08008. DOI: 10.1088/1748-0221/15/08/T08008. arXiv: 2002.02967 [physics.ins-det].

[30] K. Abe et al. "The Hyper-Kamiokande Experiment - Snowmass LOI". In: *2022 Snowmass Summer Study*. Sept. 2020. arXiv: 2009.00794 [physics.ins-det].

[31] S. Pascoli, S. T. Petcov, and Antonio Riotto. "Connecting low energy leptonic CP-violation to leptogenesis". In: *Phys. Rev. D* 75 (2007), p. 083511. DOI: 10.1103/PhysRevD.75.083511. arXiv: hep-ph/0609125.

[32] C. Hagedorn et al. "CP Violation in the Lepton Sector and Implications for Leptogenesis". In: *Int. J. Mod. Phys. A* 33.05n06 (2018), p. 1842006. DOI: 10.1142/S0217751X1842006X. arXiv: 1711.02866 [hep-ph].

[33] Kevin J. Kelly et al. "Neutrino mass ordering in light of recent data". In: *Phys. Rev. D* 103.1 (2021), p. 013004. DOI: 10.1103/PhysRevD.103.013004. arXiv: 2007.08526 [hep-ph].

[34] Fengpeng An et al. "Neutrino Physics with JUNO". In: *J. Phys. G* 43.3 (2016), p. 030401. DOI: 10.1088/0954-3899/43/3/030401. arXiv: 1507.05613 [physics.ins-det].

[35] Stephen Parke. "Theoretical Aspects of the Quantum Neutrino". In: *28th International Symposium on Lepton Photon Interactions at High Energies*. Singapur: WSP, 2020, pp. 116–127. DOI: 10.1142/9789811207402_0008. arXiv: 1801.09643 [hep-ph].

[36] W.C. Haxton, R.G. Hamish Robertson, and Aldo M. Serenelli. "Solar Neutrinos: Status and Prospects". In: *Annual Review of Astronomy and Astrophysics* 51.1 (Aug. 2013), pp. 21–61. DOI: 10.1146/annurev-astro-081811-125539. URL: https://doi.org/10.1146%2Fannurev-astro-081811-125539.

[37] G. Ranucci et al. "Borexino". In: *Nucl. Phys. B Proc. Suppl.* 91 (2001). Ed. by J. Law, R. W. Ollerhead, and J. J. Simpson, pp. 58–65. DOI: 10.1016/S0920-5632(00)00923-3.

[38] M. G. Aartsen et al. "Measurement of Atmospheric Neutrino Oscillations at 6–56 GeV with IceCube DeepCore". In: *Phys. Rev. Lett.* 120.7 (2018), p. 071801. DOI: 10.1103/PhysRevLett.120.071801. arXiv: 1707.07081 [hep-ex].

[39] Y. Fukuda et al. “Measurements of the solar neutrino flux from Super-Kamiokande’s first 300 days”. In: *Phys. Rev. Lett.* 81 (1998). [Erratum: Phys.Rev.Lett. 81, 4279 (1998)], pp. 1158–1162. DOI: 10.1103/PhysRevLett.81.1158. arXiv: hep-ex/9805021.

[40] Aldo Serenelli. “Alive and well: a short review about standard solar models”. In: *Eur. Phys. J. A* 52.4 (2016), p. 78. DOI: 10.1140/epja/i2016-16078-1. arXiv: 1601.07179 [astro-ph.SR].

[41] Raymond Davis Jr., Don S. Harmer, and Kenneth C. Hoffman. “Search for neutrinos from the sun”. In: *Phys. Rev. Lett.* 20 (1968), pp. 1205–1209. DOI: 10.1103/PhysRevLett.20.1205.

[42] F. P. An et al. “Observation of electron-antineutrino disappearance at Daya Bay”. In: *Phys. Rev. Lett.* 108 (2012), p. 171803. DOI: 10.1103/PhysRevLett.108.171803. arXiv: 1203.1669 [hep-ex].

[43] Y. Abe et al. “Reactor electron antineutrino disappearance in the Double Chooz experiment”. In: *Phys. Rev. D* 86 (2012), p. 052008. DOI: 10.1103/PhysRevD.86.052008. arXiv: 1207.6632 [hep-ex].

[44] J. K. Ahn et al. “Observation of Reactor Electron Antineutrino Disappearance in the RENO Experiment”. In: *Phys. Rev. Lett.* 108 (2012), p. 191802. DOI: 10.1103/PhysRevLett.108.191802. arXiv: 1204.0626 [hep-ex].

[45] K. Eguchi et al. “First results from KamLAND: Evidence for reactor anti-neutrino disappearance”. In: *Phys. Rev. Lett.* 90 (2003), p. 021802. DOI: 10.1103/PhysRevLett.90.021802. arXiv: hep-ex/0212021.

[46] Tomoyuki Konno et al. “Online monitoring system for Double Chooz experiment”. In: Dec. 2009, pp. 622–628. DOI: 10.1109/NSSMIC.2009.5401999.

[47] Bedrich Roskovec. “Latest Reactor Neutrino Oscillation Results from the Daya Bay Experiment”. In: *PoS* ICHEP2020 (2021), p. 170. DOI: 10.22323/1.390.0170.

[48] T. K. Gaisser and M. Honda. “FLUX OF ATMOSPHERIC NEUTRINOS”. In: *Annual Review of Nuclear and Particle Science* 52.1 (Dec. 2002), pp. 153–199. DOI: 10.1146/annurev.nucl.52.050102.090645. URL: https://doi.org/10.1146%2Fannurev.nucl.52.050102.090645.

[49] M. G. Aartsen et al. “Determining neutrino oscillation parameters from atmospheric muon neutrino disappearance with three years of IceCube DeepCore data”. In: *Phys. Rev. D* 91.7 (2015), p. 072004. DOI: 10.1103/PhysRevD.91.072004. arXiv: 1410.7227 [hep-ex].

[50] N. G. Cooper. “Los Alamos Science, Number 25 – 1997: Celebrating the neutrino”. In: (Dec. 1997). DOI: 10.2172/569122. URL: https://www.osti.gov/biblio/569122.

[51] P. Adamson et al. “Improved search for muon-neutrino to electron-neutrino oscillations in MINOS”. In: *Phys. Rev. Lett.* 107 (2011), p. 181802. DOI: 10.1103/PhysRevLett.107.181802. arXiv: 1108.0015 [hep-ex].

[52] M. A. Acero et al. “First Measurement of Neutrino Oscillation Parameters using Neutrinos and Antineutrinos by NOvA”. In: *Phys. Rev. Lett.* 123.15 (2019), p. 151803. DOI: 10.1103/PhysRevLett.123.151803. arXiv: 1906.04907 [hep-ex].

[53] Alex Himmel. *New Oscillation Results from the NOvA Experiment*. July 2020. DOI: 10.5281/zenodo.4142045. URL: https://doi.org/10.5281/zenodo.4142045.

[54] Yasuhiro Nakajima. *Recent results and future prospects from Super- Kamiokande*. June 2020. DOI: 10.5281/zenodo.4134680. URL: https://doi.org/10.5281/zenodo.4134680.

[55] *Five Sample Joint Oscillation Analysis with T2K Run1–10 Data*. https://t2k.org/docs/technotes/397/version-1-6-3-_____-2020-11-19-for-collaboration-review. Accessed: 2021-07-19.

[56] Y. Hayato. “NEUT”. In: *Nucl. Phys. B Proc. Suppl.* 112 (2002). Ed. by J. G. Morfin, M. Sakuda, and Y. Suzuki, pp. 171–176. DOI: 10.1016/S0920-5632(02)01759-0.

[57] Kevin Scott McFarland. “Neutrino Interactions”. In: *61st Scottish Universities Summer School in Physics: Neutrinos in Particle Physics, Astrophysics and Cosmology (SUSSP61)*. Apr. 2008. arXiv: 0804.3899 [hep-ex].

[58] Teppei Katori and Marco Martini. “Neutrino–nucleus cross sections for oscillation experiments”. In: *J. Phys. G* 45.1 (2018), p. 013001. DOI: 10.1088/1361-6471/aa8bf7. arXiv: 1611.07770 [hep-ph].

[59] Omar Benhar and Noemi Rocco. "Nuclear Effects in Neutrino Interactions and their Impact on the Determination of Oscillation Parameters". In: (2013). DOI: 10.48550/ARXIV.1310.3869. URL: https://arxiv.org/abs/1310.3869.

[60] K. Abe et al. "The T2K Experiment". In: *Nucl. Instrum. Meth. A* 659 (2011), pp. 106–135. DOI: 10.1016/j.nima.2011.06.067. arXiv: 1106.1238 [physics.ins-det].

[61] K. Abe et al. "Improved constraints on neutrino mixing from the T2K experiment with $\mathbf{3.13 \times 10^{21}}$ protons on target". In: *Phys. Rev. D* 103.11 (2021), p. 112008. DOI: 10.1103/PhysRevD.103.112008. arXiv: 2101.03779 [hep-ex].

[62] K. Abe et al. "The T2K experiment". In: *Nuclear Instruments and Methods in Physics Research Section A: Accelerators, Spectrometers, Detectors and Associated Equipment* 659.1 (2011), pp. 106–135. ISSN: 0168-9002. DOI: https://doi.org/10.1016/j.nima.2011.06.067. URL: https://www.sciencedirect.com/science/article/pii/S0168900211011910.

[63] Kirk T McDonald. "An Off-axis neutrino beam". In: (Nov. 2001). arXiv: hep-ex/0111033.

[64] *T2K Experiment Photo Gallery: Super-Kamiokande*. http://t2k-experiment.org/photo/super-kamiokande/. Accessed: 2021-02-17.

[65] *T2K Experiment General Plots: INGRID near detector*. https://t2k.org/docs/plotsx/general/nd280/ingrid/latest_diagram/front_note_png/view. Accessed: 2022-03-25.

[66] K. Abe et al. "T2K neutrino flux prediction". In: *Phys. Rev. D* 87.1 (2013). [Addendum: Phys.Rev.D 87, 019902 (2013)], p. 012001. DOI: 10.1103/PhysRevD.87.012001. arXiv: 1211.0469 [hep-ex].

[67] K. Abe et al. "Constraint on the matter–antimatter symmetry-violating phase in neutrino oscillations". In: *Nature* 580.7803 (2020). [Erratum: Nature 583, E16 (2020)], pp. 339–344. DOI: 10.1038/s41586-020-2177-0. arXiv: 1910.03887 [hep-ex].

[68] Y. Fukuda et al. "The Super-Kamiokande detector". In: *Nucl. Instrum. Meth. A* 501 (2003). Ed. by V.A. Ilyin, V.V. Korenkov, and D. Perret-Gallix, pp. 418–462. DOI: 10.1016/S0168-9002(03)00425-X.

[69] K. Abe et al. "Search for CP Violation in Neutrino and Antineutrino Oscillations by the T2K Experiment with 2.2×10^{21} Protons on Target". In: *Phys. Rev. Lett.* 121.17 (2018), p. 171802. DOI: 10.1103/PhysRevLett.121.171802. arXiv: 1807.07891 [hep-ex].

[70] M. Jiang et al. "Atmospheric Neutrino Oscillation Analysis with Improved Event Reconstruction in Super-Kamiokande IV". In: *PTEP* 2019.5 (2019), 053F01. DOI: 10.1093/ptep/ptz015. arXiv: 1901.03230 [hep-ex].

[71] K. Abe et al. "Improved constraints on neutrino mixing from the T2K experiment with $\mathbf{3.13 \times 10^{21}}$ protons on target". In: (Jan. 2021). arXiv: 2101.03779 [hep-ex].

[72] Roger J. Barlow and Christine Beeston. "Fitting using finite Monte Carlo samples". In: *Comput. Phys. Commun.* 77 (1993), pp. 219–228. DOI: 10.1016/0010-4655(93)90005-W.

[73] J.S. Conway. "Incorporating Nuisance Parameters in Likelihoods for Multisource Spectra". In: (Mar. 2011). Comments: Presented at PHYSTAT 2011, CERN, Geneva, Switzerland, January 2011, to be published in a CERN Yellow Report, 115–120. 6 p. DOI: 10.5170/CERN-2011-006.115. arXiv: 1103.0354. URL: https://cds.cern.ch/record/1333496.

[74] Alfredo Ferrari et al. "FLUKA: A multi-particle transport code (Program version 2005)". In: (Oct. 2005). DOI: 10.2172/877507.

[75] T. T. Böhlen et al. "The FLUKA Code: Developments and Challenges for High Energy and Medical Applications". In: *Nucl. Data Sheets* 120 (2014), pp. 211–214. DOI: 10.1016/j.nds.2014.07.049.

[76] René Brun et al. "GEANT Detector Description and Simulation Tool". In: (Oct. 1994). DOI: 10.17181/CERN.MUHF.DMJ1.

[77] N. Abgrall et al. "Pion emission from the T2K replica target: method, results and application". In: *Nucl. Instrum. Meth. A* 701 (2013), pp. 99–114. DOI: 10.1016/j.nima.2012.10.079. arXiv: 1207.2114 [hep-ex].

[78] Tomislav Vladisavljevic. "Constraining the T2K Neutrino Flux Prediction with 2009 NA61/SHINE Replica-Target Data". In: *Prospects in Neutrino Physics*. Apr. 2018. DOI: 10.5281/zenodo.1300546. arXiv: 1804.00272 [physics.ins-det].

[79] L. Alvarez-Ruso et al. “NuSTEC White Paper: Status and challenges of neutrino–nucleus scattering”. In: *Prog. Part. Nucl. Phys.* 100 (2018), pp. 1–68. DOI: 10.1016/j.ppnp.2018.01.006. arXiv: 1706.03621 [hep-ph].

[80] Callum Wilkinson. “Constraining neutrino interaction uncertainties for oscillation experiments”. PhD thesis. Sheffield U., June 2015.

[81] P. A. Rodrigues et al. “Identification of nuclear effects in neutrino-carbon interactions at low three-momentum transfer”. In: *Phys. Rev. Lett.* 116 (2016). [Addendum: Phys.Rev.Lett. 121, 209902 (2018)], p. 071802. DOI: 10.1103/PhysRevLett.116.071802. arXiv: 1511.05944 [hep-ex].

[82] Arie Bodek and Tejin Cai. “Removal Energies and Final State Interaction in Lepton Nucleus Scattering”. In: *Eur. Phys. J. C* 79.4 (2019), p. 293. DOI: 10.1140/epjc/s10052-019-6750-3. arXiv: 1801.07975 [nucl-th].

[83] M. Martini et al. “Neutrino and antineutrino quasielastic interactions with nuclei”. In: *Phys. Rev. C* 81 (2010), p. 045502. DOI: 10.1103/PhysRevC.81.045502. arXiv: 1002.4538 [hep-ph].

[84] C. Colle et al. “Extracting the mass dependence and quantum numbers of short-range correlated pairs from $A(e, e'p)$ and $A(e, e'pp)$ scattering”. In: *Phys. Rev. C* 92.2 (2015), p. 024604. DOI: 10.1103/PhysRevC.92.024604. arXiv: 1503.06050 [nucl-th].

[85] A. Nikolakopoulos et al. “Mean field approach to reconstructed neutrino energy distributions in accelerator-based experiments”. In: *Phys. Rev. C* 98.5 (2018), p. 054603. DOI: 10.1103/PhysRevC.98.054603. arXiv: 1808.07520 [nucl-th].

[86] Juan Nieves et al. “2p2h Excitations, MEC, Nucleon Correlations and Other Sources of QE-like Events”. In: *JPS Conf. Proc.* 12 (2016), p. 010002. DOI: 10.7566/JPSCP.12.010002.

[87] J. E. Amaro et al. “Neutrino-Nucleus scattering in the SuSA model”. In: (June 2021). arXiv: 2106.02857 [hep-ph].

[88] Arie Bodek and Un-ki Yang. “A Unified model for inelastic e - N and nu - N cross-sections at all Q**2”. In: *AIP Conf. Proc.* 792.1 (2005). Ed. by Wesley H. Smith and Sridhara R. Dasu, pp. 257–260. DOI: 10.1063/1.2122031. arXiv: hep-ph/0508007.

[89] Jonathan Engel. "Approximate treatment of lepton distortion in charged current neutrino scattering from nuclei". In: *Phys. Rev. C* 57 (1998), pp. 2004–2009. DOI: 10.1103/PhysRevC.57.2004. arXiv: nucl-th/9711045.

[90] Melanie Day and Kevin S. McFarland. "Differences in Quasi-Elastic Cross-Sections of Muon and Electron Neutrinos". In: *Phys. Rev. D* 86 (2012), p. 053003. DOI: 10.1103/PhysRevD.86.053003. arXiv: 1206.6745 [hep-ph].

[91] A. Higuera et al. "Measurement of Coherent Production of $\pi^{\pm}$ in Neutrino and Antineutrino Beams on Carbon from E_{ν} of 1.5 to 20 GeV". In: *Phys. Rev. Lett.* 113.26 (2014), p. 261802. DOI: 10.1103/PhysRevLett.113.261802. arXiv: 1409.3835 [hep-ex].

[92] E. Wang et al. "Photon emission in neutral current interactions at the T2K experiment". In: *Phys. Rev. D* 92.5 (2015), p. 053005. DOI: 10.1103/PhysRevD.92.053005. arXiv: 1507.02446 [hep-ph].

[93] E. S. Pinzon Guerra et al. "Using world charged $\pi^{\pm}-$nucleus scattering data to constrain an intranuclear cascade model". In: *Phys. Rev. D* 99.5 (2019), p. 052007. DOI: 10.1103/PhysRevD.99.052007. arXiv: 1812.06912 [hep-ex].

[94] *T2K Technical Note 273:Muon anti-neutrino and neutrino Charge-Current multiple pion selections in anti-neutrino mode.* https://t2k.org/docs/technotes/273/t2k-tn-273-v2. Accessed: 2022-04-04.

[95] *T2K Technical Note 407:FHC muon neutrino charged current and multiple pion sample in the ND280 tracker for the 2020 oscillation analysis inputs: Run* $2+3+4+8$ *with P6T NEUT MC.* https://t2k.org/docs/technotes/407/v1p3. Accessed: 2022-04-04.

[96] *T2K Technical Note 318:Fit to Super-K Atmospheric Neutrino Data for Optimization of the fiTQun Fiducial Volume Cuts and Estimation of Detector Uncertainties.* https://t2k.org/docs/technotes/318/v2r2. Accessed: 2022-04-04.

[97] *T2K Technical Note 396:Fake-data studies for the 2020 oscillation analysis.* https://t2k.org/docs/technotes/396. Accessed: 2022-04-11.

[98] S. Brooks et al. *Handbook of Markov Chain Monte Carlo*. Chapman & Hall/CRC Handbooks of Modern Statistical Methods. CRC Press, 2011. ISBN: 9781420079425. URL: https://books.google.co.uk/books?id=qfRsAIKZ4rIC.

[99] W. K. Hastings. "Monte Carlo Sampling Methods Using Markov Chains and Their Applications". In: *Biometrika* 57 (1970), pp. 97–109. DOI: 10.1093/biomet/57.1.97.

[100] Mysid Yoderj. *Monte Carlo Integragtion*. [Online; accessed 19-July-20021]. 2014. URL: %5Curl%7Bhttps://en.wikipedia.org/wiki/File:MonteCarloIntegrationCircle.svg%7D.

[101] W.R. Gilks, S. Richardson, and D. Spiegelhalter. *Markov Chain Monte Carlo in Practice*. Chapman & Hall/CRC Interdisciplinary Statistics. Taylor & Francis, 1995. ISBN: 9780412055515. URL: https://books.google.co.uk/books?id=TRXrMWY%5C_i2IC.

[102] Andrew Chappell. "CP violation and neutrino mass ordering at the T2K experiment". PhD thesis. Warwick U., Apr. 2019.

[103] Wing Yan Ma. "Five sample joint neutrino/antineutrino oscillation analysis in T2K". PhD thesis. Imperial Coll., London, 2017. DOI: 10.25560/58946.

[104] S. Kretzer and M. H. Reno. "Tau neutrino deep inelastic charged current interactions". In: *Phys. Rev. D* 66 (2002), p. 113007. DOI: 10.1103/PhysRevD.66.113007. arXiv: hep-ph/0208187.

[105] Carl H. Albright and C. Jarlskog. "Neutrino Production of m+ and e+ Heavy Leptons. 1." In: *Nucl. Phys. B* 84 (1975), pp. 467–492. DOI: 10.1016/0550-3213(75)90318-1.

[106] Un-Ki Yang et al. "Measurements of F_2 and $xF_3^{\nu} - xF_3^{\bar{\nu}}$ from CCFR ν_μ−Fe and $\bar{\nu}_\mu$−Fe data in a physics model independent way". In: *Phys. Rev. Lett.* 86 (2001), pp. 2742–2745. DOI: 10.1103/PhysRevLett.86.2742. arXiv: hep-ex/0009041.

[107] M. Glück, E. Reya, and A. Vogt. "Dynamical parton distributions revisited". In: *Eur. Phys. J. C* 5 (1998), pp. 461–470. DOI: 10.1007/s100520050289. arXiv: hep-ph/9806404.

[108] C. Andreopoulos et al. "The GENIE Neutrino Monte Carlo Generator". In: *Nucl. Instrum. Meth. A* 614 (2010), pp. 87–104. DOI: 10.1016/j.nima.2009.12.009. arXiv: 0905.2517 [hep-ph].

[109] Jaroslaw A. Nowak. "Wroclaw neutrino event generator". In: *Phys. Scripta T* 127 (2006). Ed. by T. Ohlsson et al., pp. 70–72. DOI: 10.1088/0031-8949/2006/T127/025. arXiv: hep-ph/0607081.

[110] Z. Koba, Holger Bech Nielsen, and P. Olesen. "Scaling of multiplicity distributions in high-energy hadron collisions". In: *Nucl. Phys. B* 40 (1972), pp. 317–334. DOI: 10.1016/0550-3213(72)90551-2.

[111] S. J. Barish et al. "Study of Neutrino Interactions in Hydrogen and Deuterium. 1. Description of the Experiment and Study of the Reaction Neutrino d –> mu- p p(s)". In: *Phys. Rev. D* 16 (1977), p. 3103. DOI: 10.1103/PhysRevD.16.3103.

[112] Torbjörn Sjöstrand. "The Pythia event generator: Past, present and future". In: *Computer Physics Communications* 246 (2020), p. 106910. ISSN: 0010-4655. DOI: https://doi.org/10.1016/j.cpc.2019.106910. URL: https://www.sciencedirect.com/science/article/pii/S0010465519302899.

[113] Hans-Uno Bengtsson and Torbjorn Sjostrand. "The Lund Monte Carlo for Hadronic Processes: Pythia Version 4.8". In: *Comput. Phys. Commun.* 46 (1987), p. 43. DOI: 10.1016/0010-4655(87)90036-1.

[114] P. Adamson et al. "Neutrino and Antineutrino Inclusive Charged-current Cross Section Measurements with the MINOS Near Detector". In: *Phys. Rev. D* 81 (2010), p. 072002. DOI: 10.1103/PhysRevD.81.072002. arXiv: 0910.2201 [hep-ex].

[115] T. Yang et al. "A Hadronization Model for Few-GeV Neutrino Interactions". In: *Eur. Phys. J. C* 63 (2009), pp. 1–10. DOI: 10.1140/epjc/s10052-009-1094-z. arXiv: 0904.4043 [hep-ph].

[116] *T2K Experiment General Plots: Beam power and data taking.* https://t2k.org/docs/plotsx/frequentlyupdated/Beam/2020-02-12. Accessed: 2022-03-25.

[117] *T2K Technical Note 395:ND280 fit for 2020 oscillation analyses.* https://t2k.org/docs/technotes/395/banff-mach3-nd-fit-v3. Accessed: 2021-07-16.

[118] Tomoyo Yoshida. "A study of single charged-pion production events at Super-Kamiokande induced by charged-currents interactions of T2K-beam muon neutrinos". PhD thesis. Tokyo Institue of Technology, Mar. 2020.

Appendix A

Neutrino Interaction Uncertainties

This appendix contains complementary plots for the new systematic uncertainties developed in chapter 6. These include the inputs used for the reweighting of CC Multi-π and CC DIS to describe the uncertainty on the Bodek-Yang corrections in appendix A.1. A variety of additional validation plots showing how the reweighting behaves in different kinematic variables and for different neutrino flavours and target materials is given in appendix A.2.

A.1 BY inputs

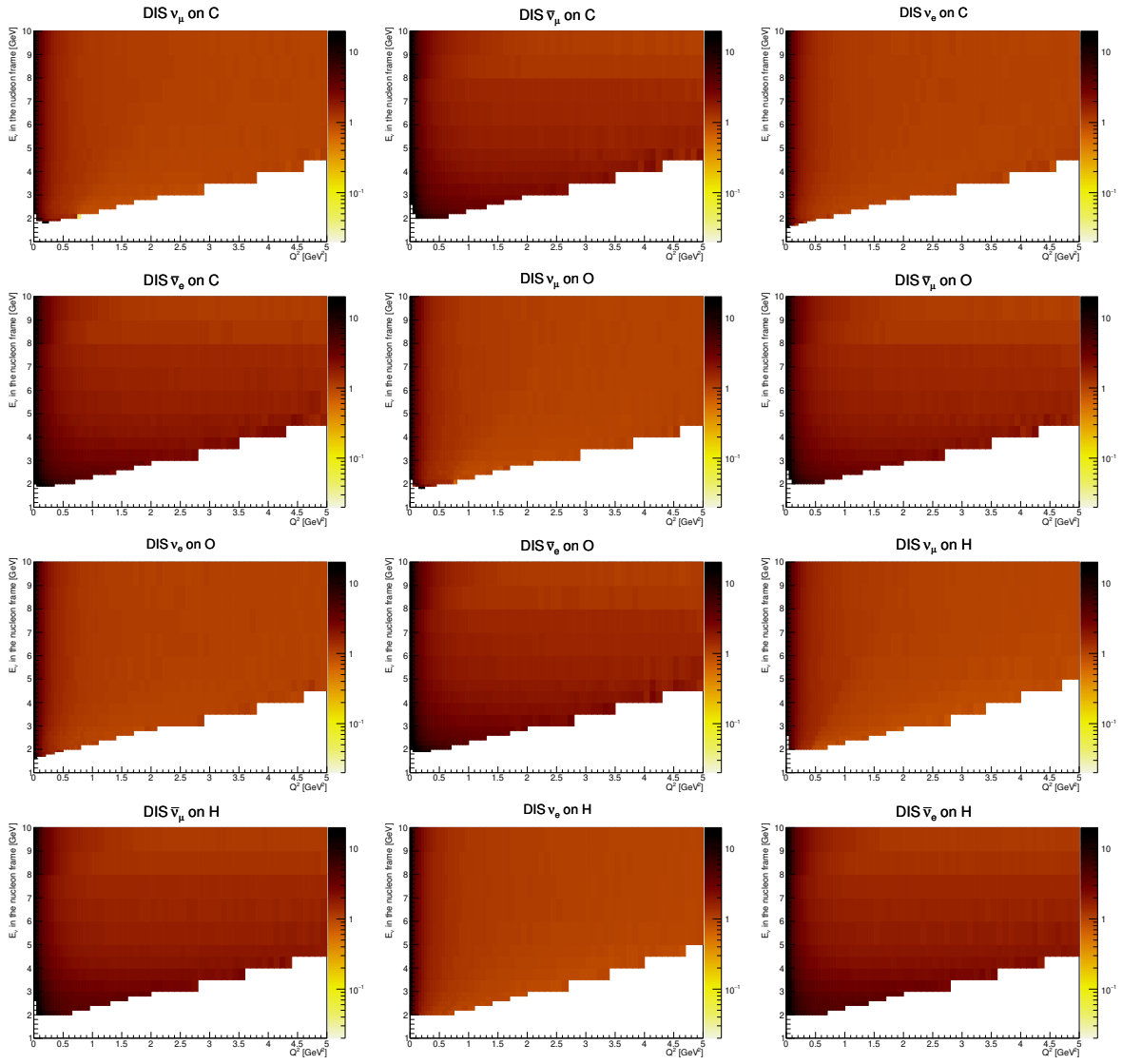

Figure A.1: All the inputs for different nuclei and neutrino flavours for applying an uncertainty based on the BY corrections for CC DIS interactions. The general feature across all inputs are the large weights at low Q^2 values. The inputs extend to much larger values of both Q^2 and E_ν in the nucleon frame but are zoomed in on here to show the key features.

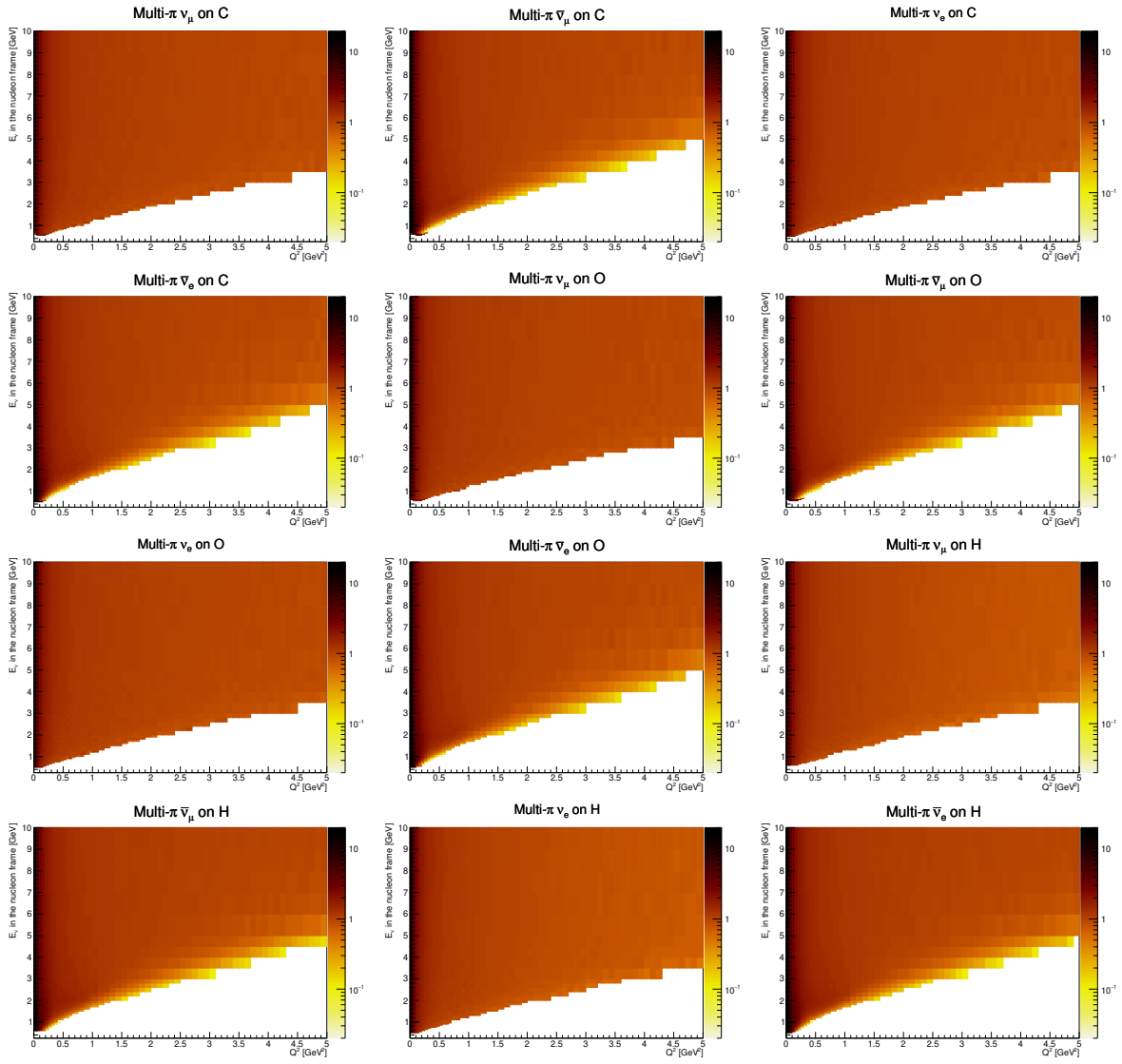

Figure A.2: All the inputs for different nuclei and neutrino flavours for applying an uncertainty based on the BY corrections for CC Multi-π interactions. The general feature across all inputs are the large weights at low Q^2 values. The inputs extend to much larger values of both Q^2 and E_ν in the nucleon frame but are zoomed in on here to show the key features.

A.2 Bodek-Yang reweighting validations

Below are many plots comparing the reweighting from interactions made with BY corrections to those made without BY corrections. In general, the reweighting does well in reproducing the cross-section of events generated without BY corrections but there are some regions of phase-space that do not behave perfectly. This is thought to be due to non-overlapping phase-space between the two models in particular regions of Bjorken-x and Bjorken-y. The reweighting behaves well in lepton kinematics which are the kinematic variables that the neutrino oscillation analysis is binned in. The reweighting was thought to be sufficiently accurate for describing the uncertainty on CC DIS and CC Multi-π interactions. It is worth noticing that usually the difference between the reweighted MC and MC generated without BY corrections is much smaller than the difference between events generated with BY corrections and those generated without BY corrections. Therefore, the reweighting does performs well at applying the uncertainty to interactions. The validation plots are shown for interactions on water in appendix A.2.1 and CH in appendix A.2.2 for each neutrino flavour in Q^2, E_ν in the nucleon frame, Bjorken-x and Bjorken-y.

A.2.1 H2O

A.2.2 CH

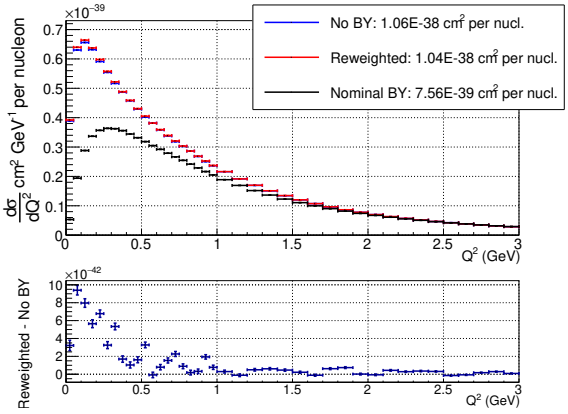

(a) ν_μ CC Multi-π BY in Q^2

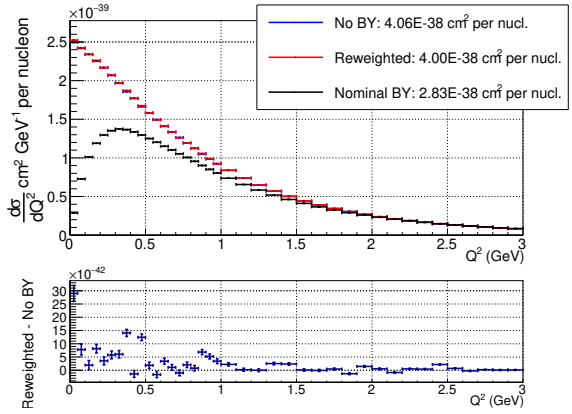

(b) ν_e CC Multi-π BY in Q^2

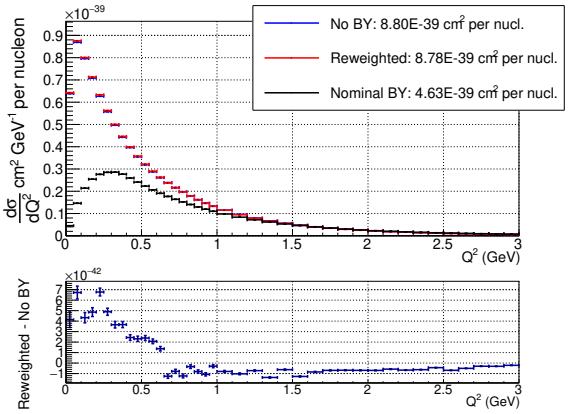

(c) $\bar{\nu}_\mu$ CC Multi-π BY in Q^2

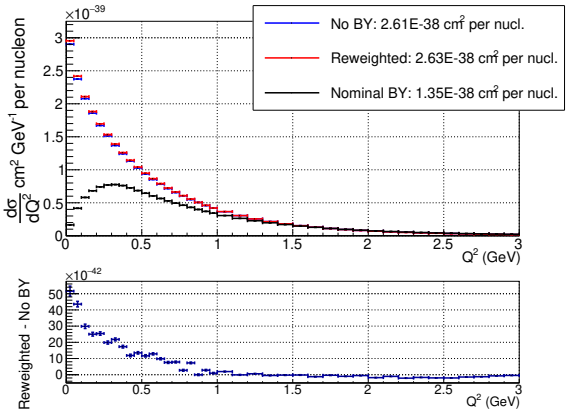

(d) $\bar{\nu}_e$ CC Multi-π BY in Q^2

Figure A.3: Comparisons of MC events reweighted from using BY corrections to without BY corrections using the inputs given in fig. 6.3 for CC Multi-π interactions on water for ν_μ, ν_e, $\bar{\nu}_\mu$ and $\bar{\nu}_e$. Comparisons are given in Q^2. The lower panels in all the plots show the difference between reweighted MC and that generated without BY corrections.

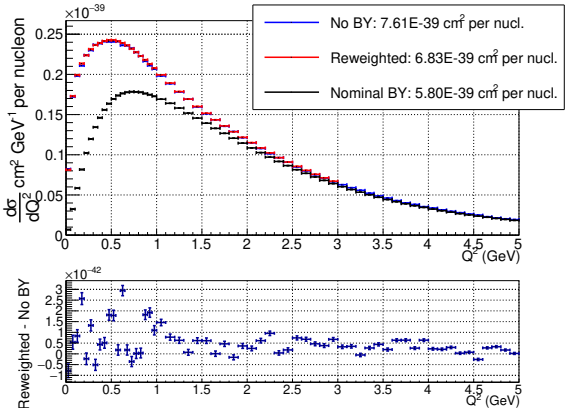

(a) ν_μ CC DIS BY in Q^2

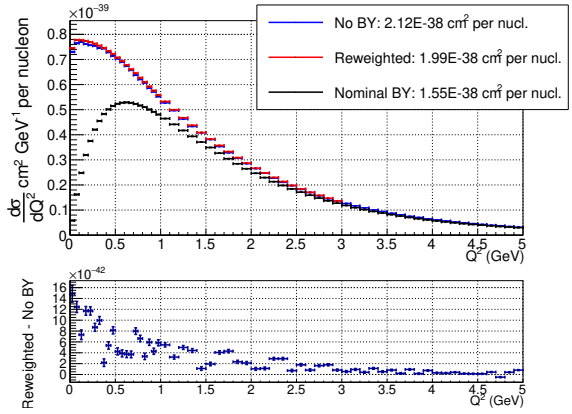

(b) ν_e CC DIS BY in Q^2

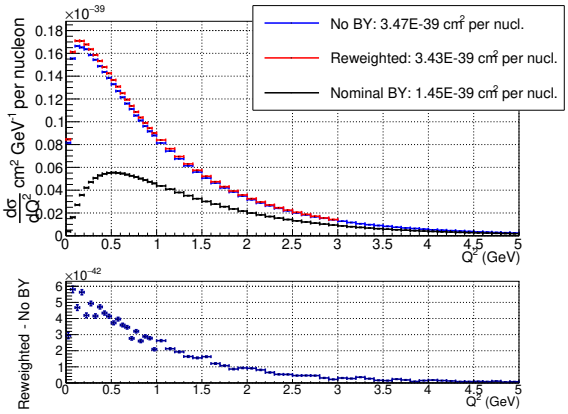

(c) $\bar{\nu}_\mu$ CC DIS BY in Q^2

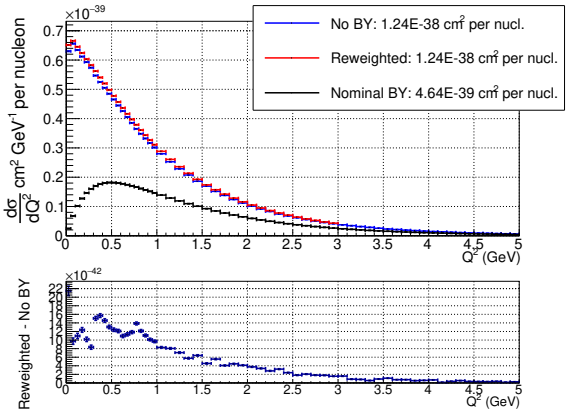

(d) $\bar{\nu}_e$ CC DIS BY in Q^2

Figure A.4: Comparisons of MC events reweighted from using BY corrections to without BY corrections using the inputs given in fig. 6.3 for CC DIS interactions on water for ν_μ, ν_e, $\bar{\nu}_\mu$ and $\bar{\nu}_e$. Comparisons are given in Q^2. The lower panels in all the plots show the difference between reweighted MC and that generated without BY corrections.

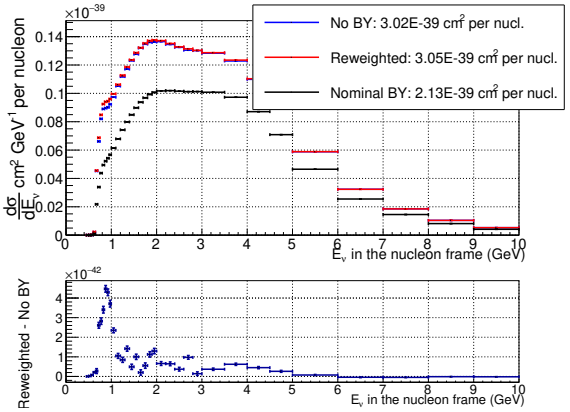

(a) ν_μ CC Multi-π BY in E_ν

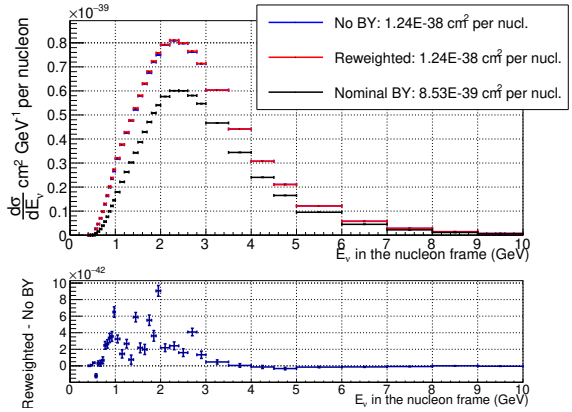

(b) ν_e CC Multi-π BY in E_ν

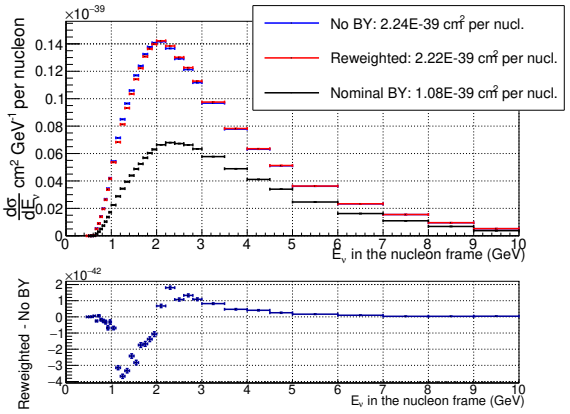

(c) $\bar{\nu}_\mu$ CC Multi-π BY in E_ν

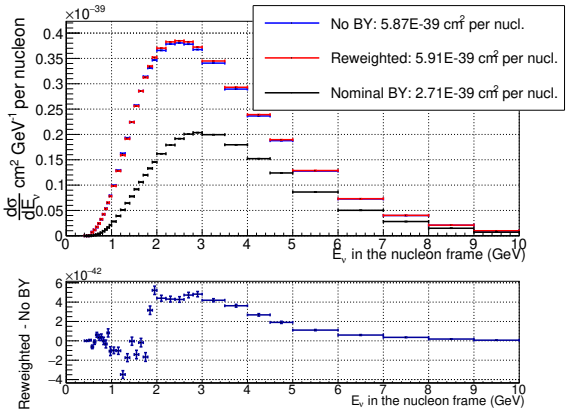

(d) $\bar{\nu}_e$ CC Multi-π BY in E_ν

Figure A.5: Comparisons of MC events reweighted from using BY corrections to without BY corrections using the inputs given in fig. 6.3 for CC Multi-π interactions on water for ν_μ, ν_e, $\bar{\nu}_\mu$ and $\bar{\nu}_e$. Comparisons are given in E_ν. The lower panels in all the plots show the difference between reweighted MC and that generated without BY corrections.

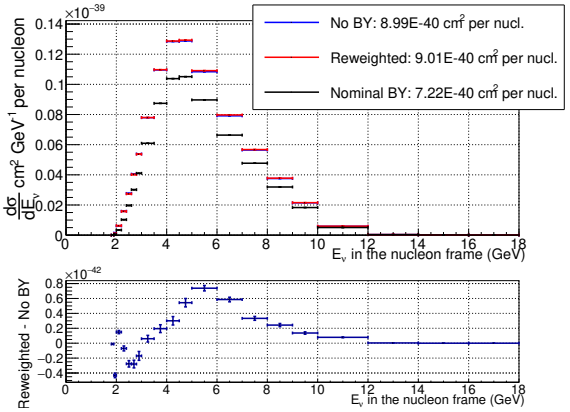

(a) ν_μ CC DIS BY in E_ν

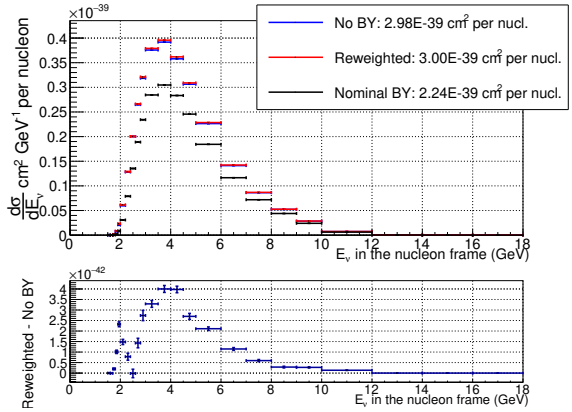

(b) ν_e CC DIS BY in E_ν

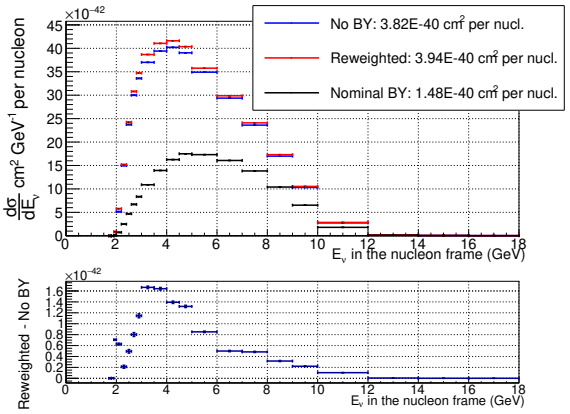

(c) $\bar{\nu}_\mu$ CC DIS BY in E_ν

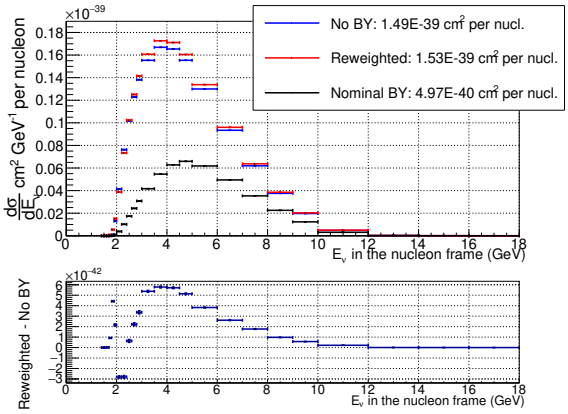

(d) $\bar{\nu}_e$ CC DIS BY in E_ν

Figure A.6: Comparisons of MC events reweighted from using BY corrections to without BY corrections using the inputs given in fig. 6.3 for CC DIS interactions on water for ν_μ, ν_e, $\bar{\nu}_\mu$ and $\bar{\nu}_e$. Comparisons are given in E_ν. The lower panels in all the plots show the difference between reweighted MC and that generated without BY corrections.

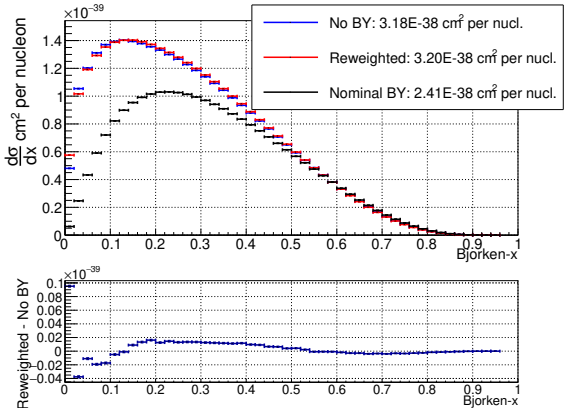

(a) ν_μ CC Multi-π BY in Bjorken-x

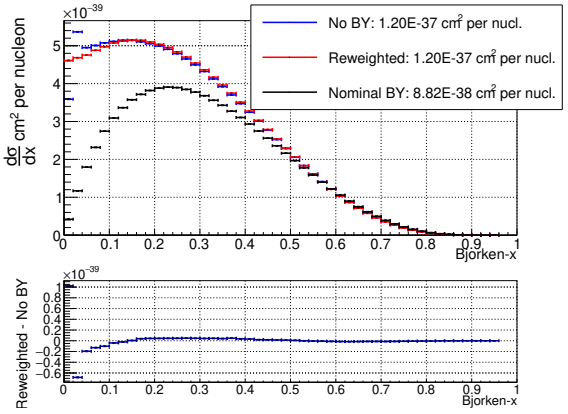

(b) ν_e CC Multi-π BY in Bjorken-x

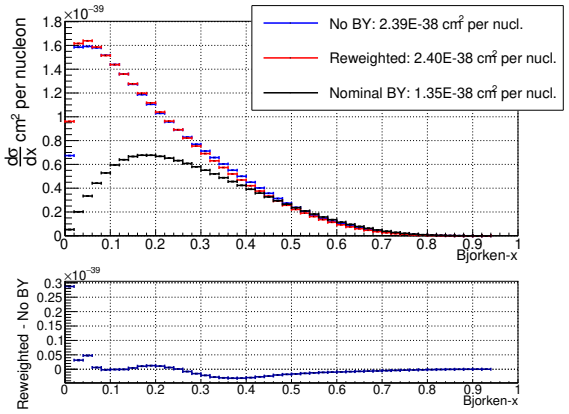

(c) $\bar{\nu}_\mu$ CC Multi-π BY in Bjorken-x

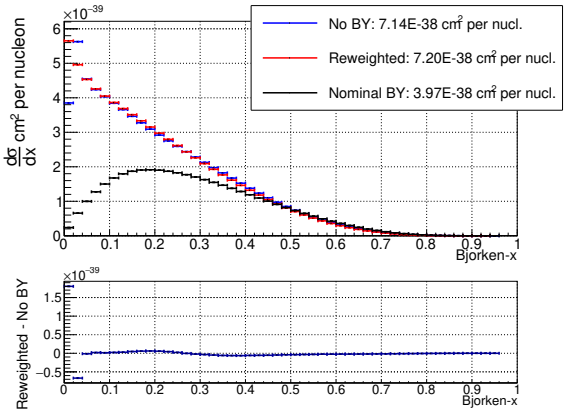

(d) $\bar{\nu}_e$ CC Multi-π BY in Bjorken-x

Figure A.7: Comparisons of MC events reweighted from using BY corrections to without BY corrections using the inputs given in fig. 6.3 for CC Multi-π interactions on water for ν_μ, ν_e, $\bar{\nu}_\mu$ and $\bar{\nu}_e$. Comparisons are given in Bjorken-x. The lower panels in all the plots show the difference between reweighted MC and that generated without BY corrections.

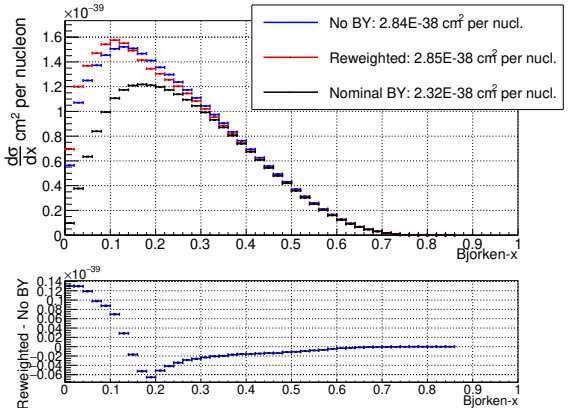

(a) ν_μ CC DIS BY in Bjorken-x

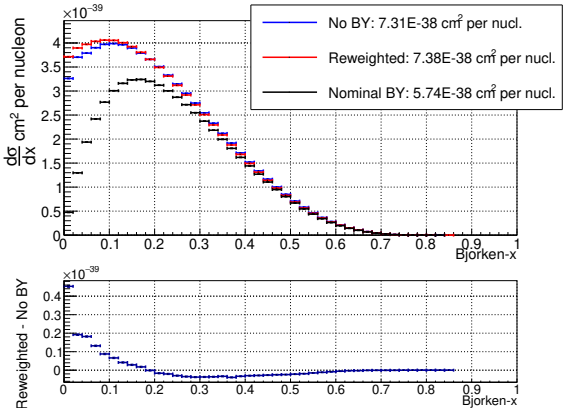

(b) ν_e CC DIS BY in Bjorken-x

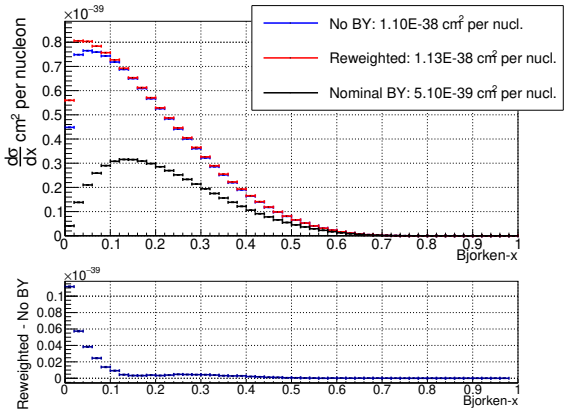

(c) $\bar{\nu}_\mu$ CC DIS BY in Bjorken-x

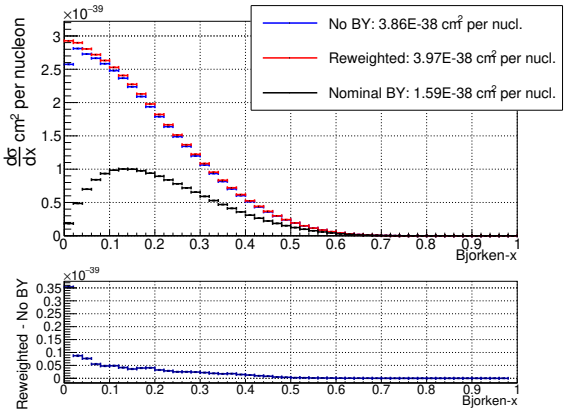

(d) $\bar{\nu}_e$ CC DIS BY in Bjorken-x

Figure A.8: Comparisons of MC events reweighted from using BY corrections to without BY corrections using the inputs given in fig. 6.3 for CC DIS interactions on water for ν_μ, ν_e, $\bar{\nu}_\mu$ and $\bar{\nu}_e$. Comparisons are given in Bjorken-x. The lower panels in all the plots show the difference between reweighted MC and that generated without BY corrections.

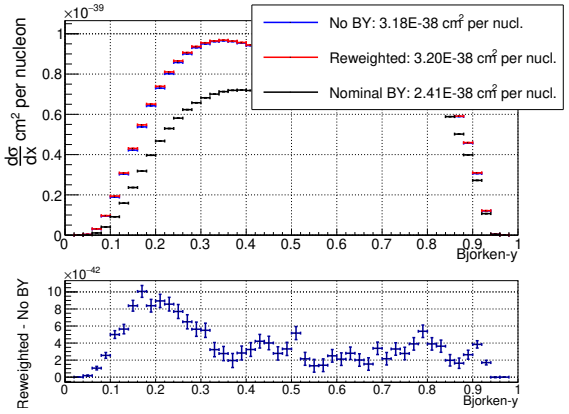

(a) ν_μ CC Multi-π BY in Bjorken-y

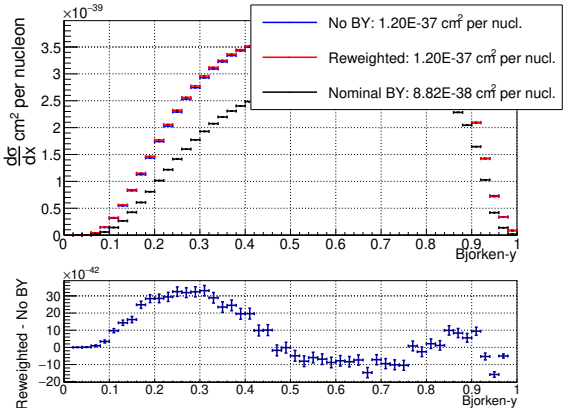

(b) ν_e CC Multi-π BY in Bjorken-y

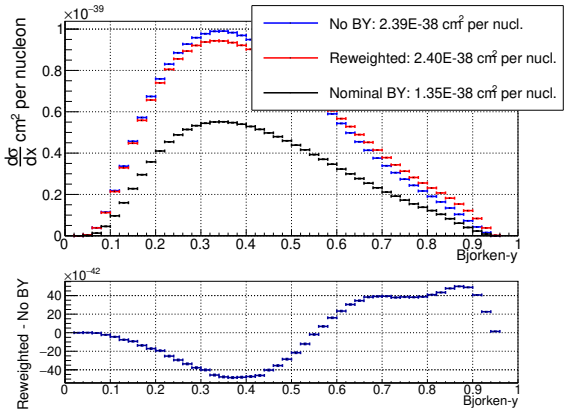

(c) $\bar{\nu}_\mu$ CC Multi-π BY in Bjorken-y

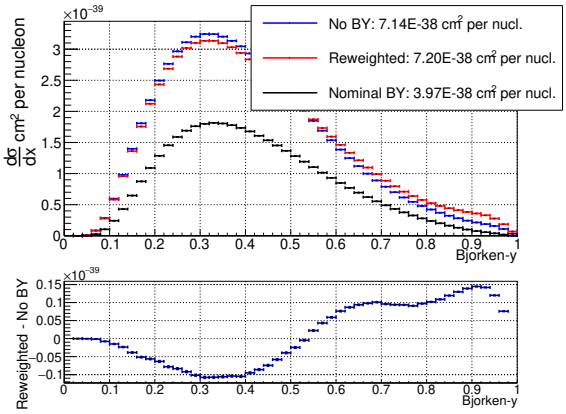

(d) $\bar{\nu}_e$ CC Multi-π BY in Bjorken-y

Figure A.9: Comparisons of MC events reweighted from using BY corrections to without BY corrections using the inputs given in fig. 6.3 for CC Multi-π interactions on water for ν_μ, ν_e, $\bar{\nu}_\mu$ and $\bar{\nu}_e$. Comparisons are given in Bjorken-y. The lower panels in all the plots show the difference between reweighted MC and that generated without BY corrections.

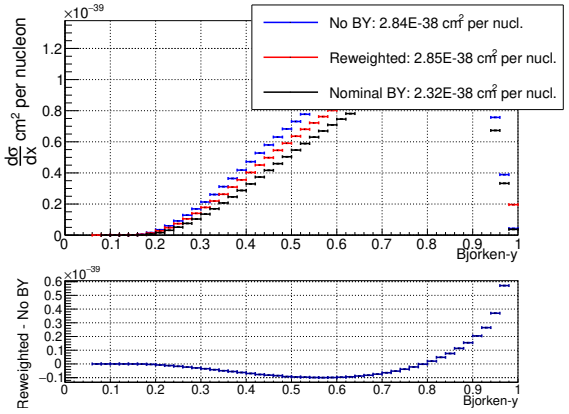

(a) ν_μ CC DIS BY in Bjorken-y

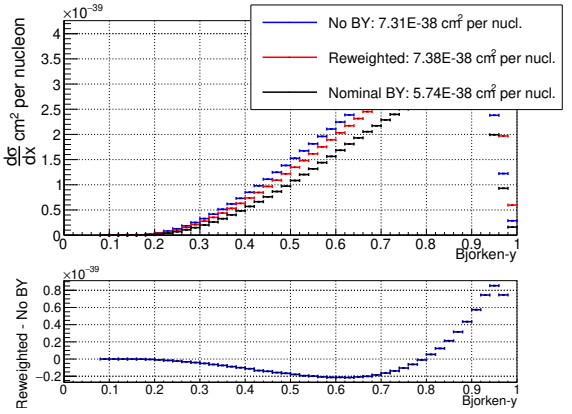

(b) ν_e CC DIS BY in Bjorken-y

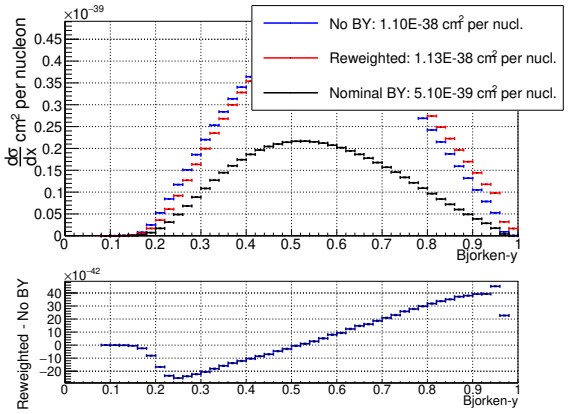

(c) $\bar{\nu}_\mu$ CC DIS BY in Bjorken-y

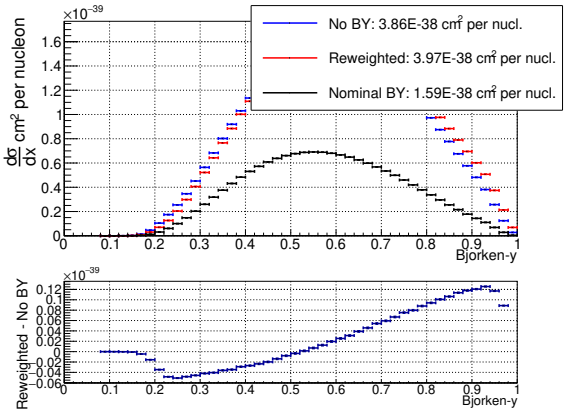

(d) $\bar{\nu}_e$ CC DIS BY in Bjorken-y

Figure A.10: Comparisons of MC events reweighted from using BY corrections to without BY corrections using the inputs given in fig. 6.3 for CC DIS interactions on water for ν_μ, ν_e, $\bar{\nu}_\mu$ and $\bar{\nu}_e$. Comparisons are given in Bjorken-y. The lower panels in all the plots show the difference between reweighted MC and that generated without BY corrections.

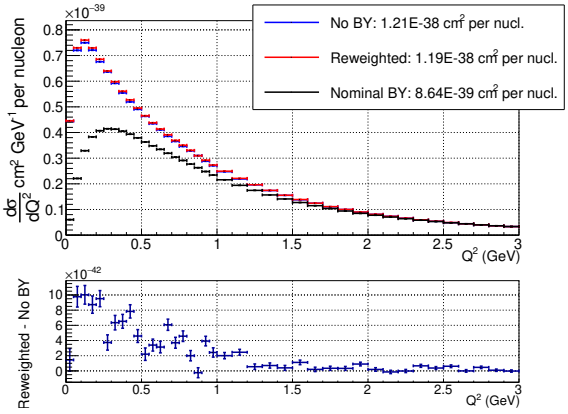

(a) ν_μ CC Multi-π BY in Q^2

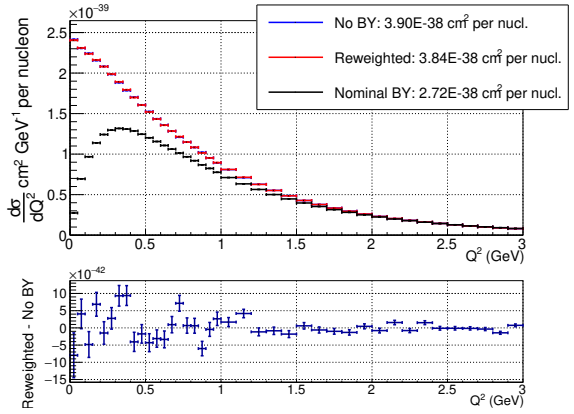

(b) ν_e CC Multi-π BY in Q^2

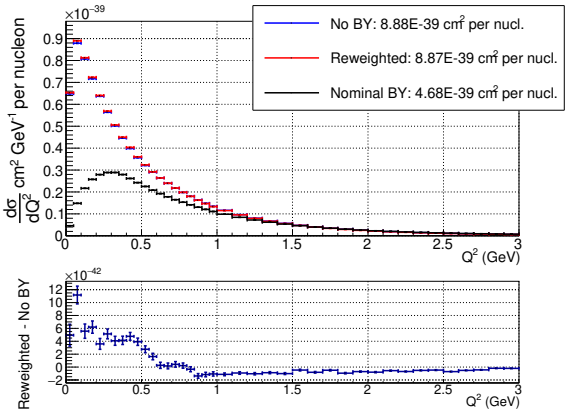

(c) $\bar{\nu}_\mu$ CC Multi-π BY in Q^2

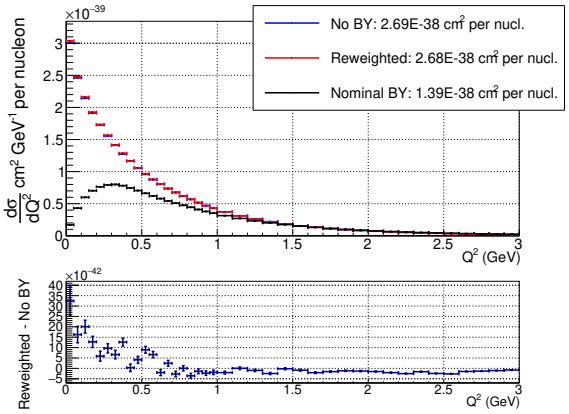

(d) $\bar{\nu}_e$ CC Multi-π BY in Q^2

Figure A.11: Comparisons of MC events reweighted from using BY corrections to without BY corrections using the inputs given in fig. 6.3 for CC Multi-π interactions on CH for ν_μ, ν_e, $\bar{\nu}_\mu$ and $\bar{\nu}_e$. Comparisons are given in Q^2. The lower panels in all the plots show the difference between reweighted MC and that generated without BY corrections.

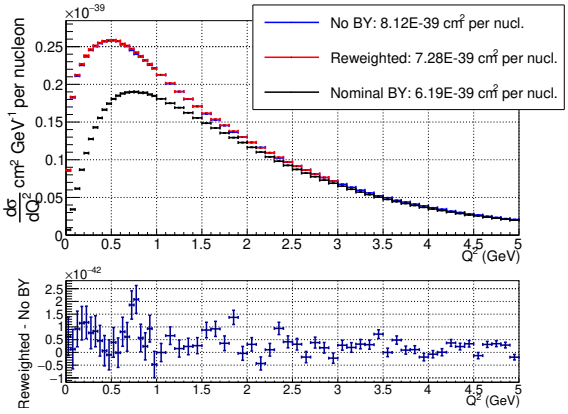

(a) ν_μ CC DIS BY in Q^2

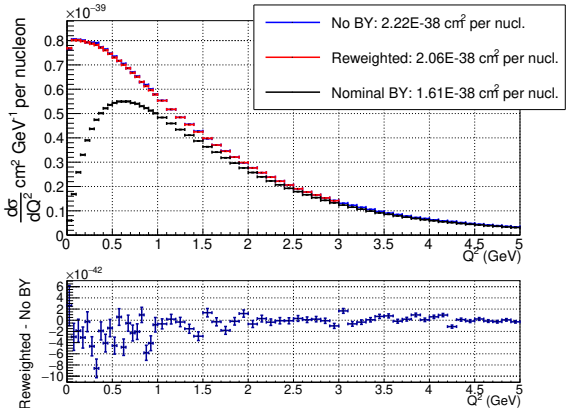

(b) ν_e CC DIS BY in Q^2

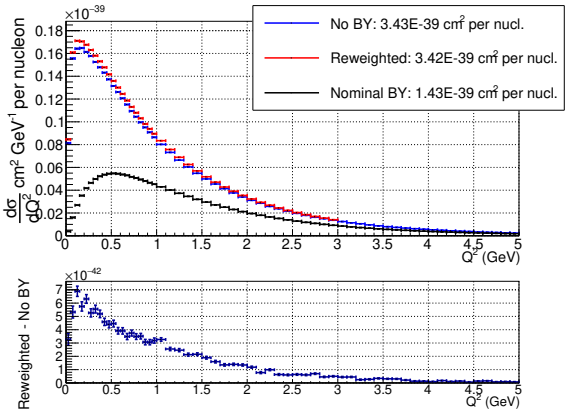

(c) $\bar{\nu}_\mu$ CC DIS BY in Q^2

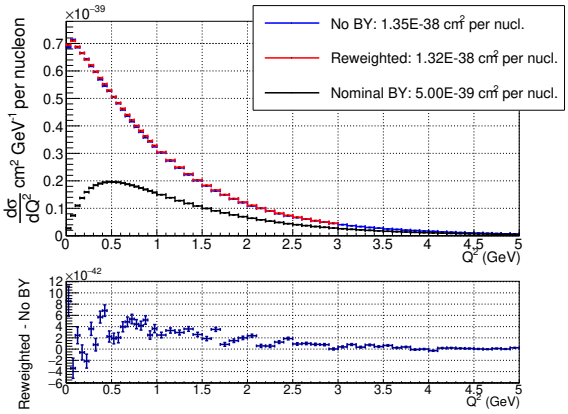

(d) $\bar{\nu}_e$ CC DIS BY in Q^2

Figure A.12: Comparisons of MC events reweighted from using BY corrections to without BY corrections using the inputs given in fig. 6.3 for CC DIS interactions on CH for ν_μ, ν_e, $\bar{\nu}_\mu$ and $\bar{\nu}_e$. Comparisons are given in Q^2. The lower panels in all the plots show the difference between reweighted MC and that generated without BY corrections.

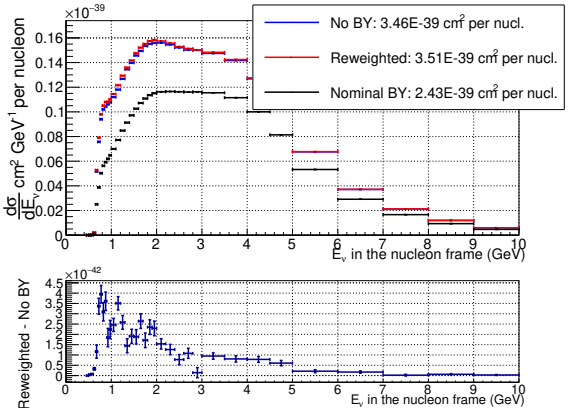

(a) ν_μ CC Multi-π BY in E_ν

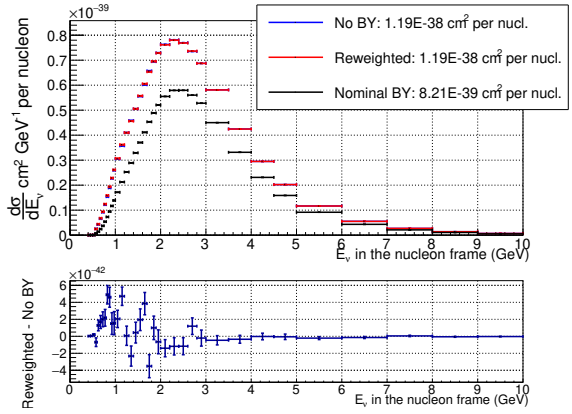

(b) ν_e CC Multi-π BY in E_ν

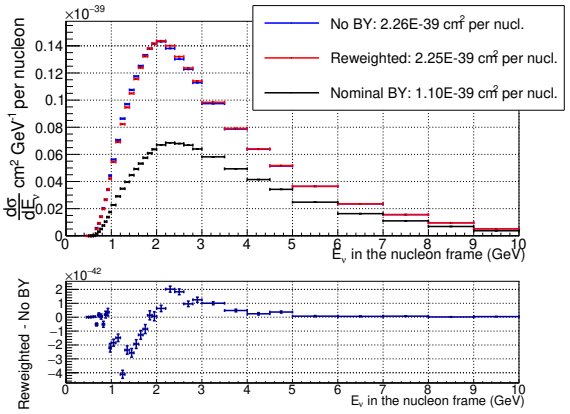

(c) $\bar{\nu}_\mu$ CC Multi-π BY in E_ν

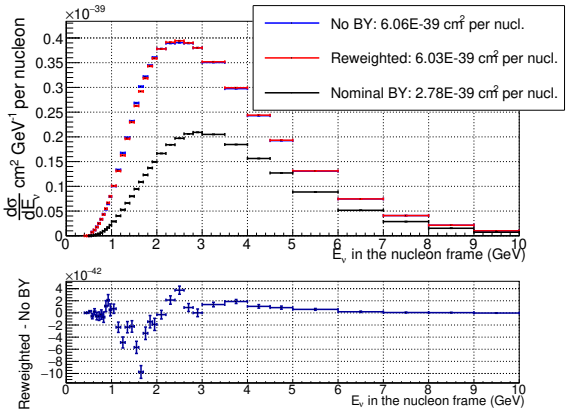

(d) $\bar{\nu}_e$ CC Multi-π BY in E_ν

Figure A.13: Comparisons of MC events reweighted from using BY corrections to without BY corrections using the inputs given in fig. 6.3 for CC Multi-π interactions on CH for ν_μ, ν_e, $\bar{\nu}_\mu$ and $\bar{\nu}_e$. Comparisons are given in E_ν. The lower panels in all the plots show the difference between reweighted MC and that generated without BY corrections.

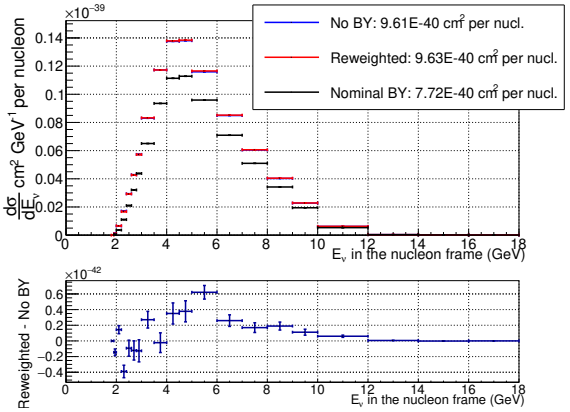

(a) ν_μ CC DIS BY in E_ν

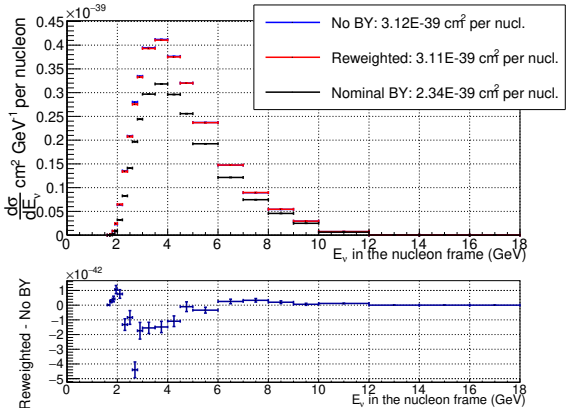

(b) ν_e CC DIS BY in E_ν

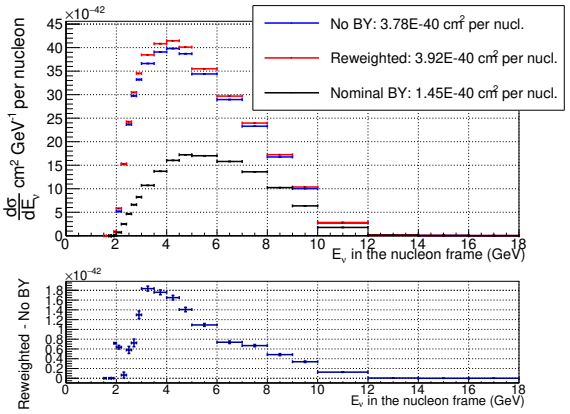

(c) $\bar{\nu}_\mu$ CC DIS BY in E_ν

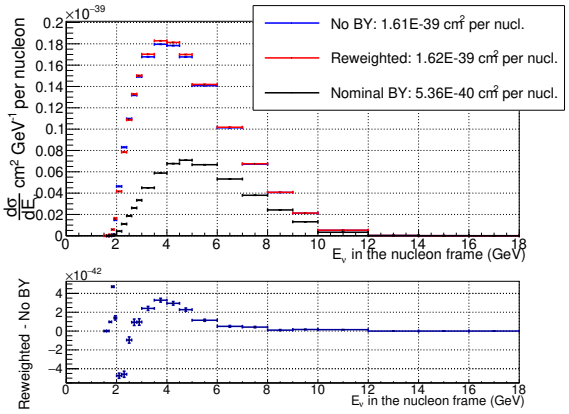

(d) $\bar{\nu}_e$ CC DIS BY in E_ν

Figure A.14: Comparisons of MC events reweighted from using BY corrections to without BY corrections using the inputs given in fig. 6.3 for CC DIS interactions on CH for ν_μ, ν_e, $\bar{\nu}_\mu$ and $\bar{\nu}_e$. Comparisons are given in E_ν. The lower panels in all the plots show the difference between reweighted MC and that generated without BY corrections.

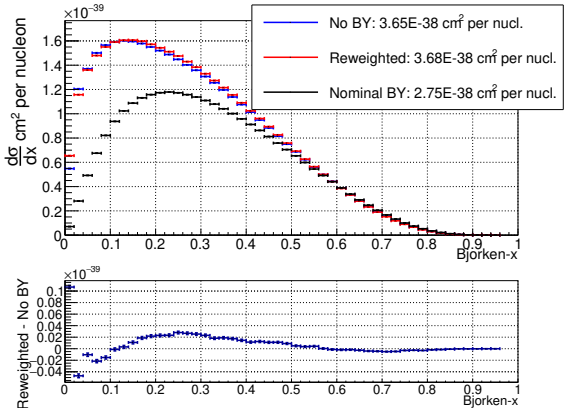

(a) ν_μ CC Multi-π BY in Bjorken-x

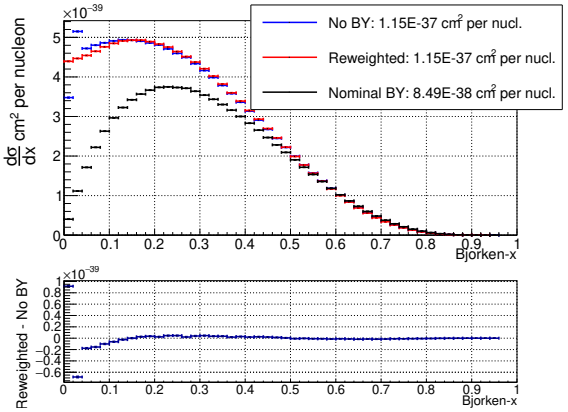

(b) ν_e CC Multi-π BY in Bjorken-x

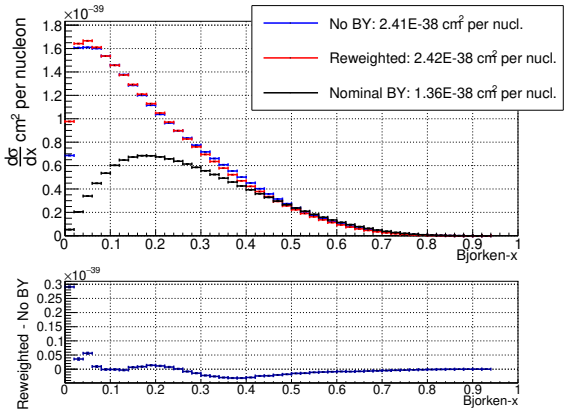

(c) $\bar{\nu}_\mu$ CC Multi-π BY in Bjorken-x

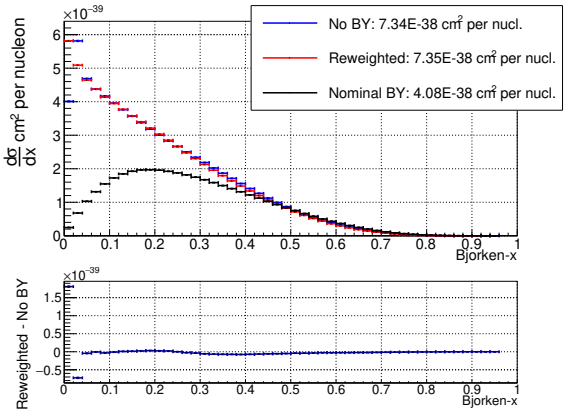

(d) $\bar{\nu}_e$ CC Multi-π BY in Bjorken-x

Figure A.15: Comparisons of MC events reweighted from using BY corrections to without BY corrections using the inputs given in fig. 6.3 for CC Multi-π interactions on CH for ν_μ, ν_e, $\bar{\nu}_\mu$ and $\bar{\nu}_e$. Comparisons are given in Bjorken-x. The lower panels in all the plots show the difference between reweighted MC and that generated without BY corrections.

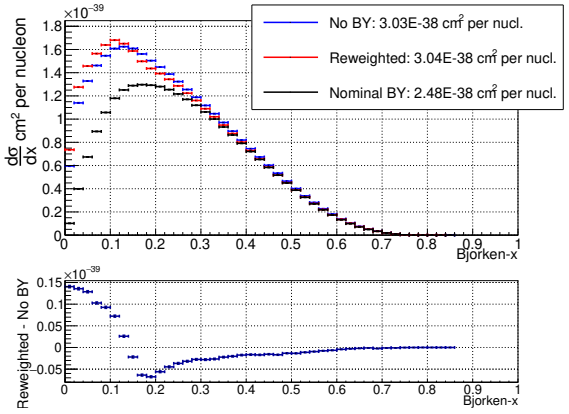

(a) ν_μ CC DIS BY in Bjorken-x

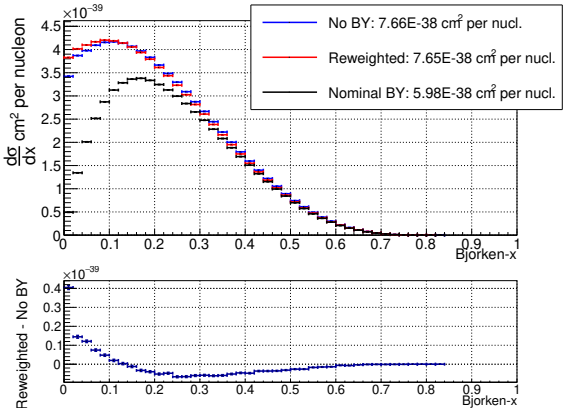

(b) ν_e CC DIS BY in Bjorken-x

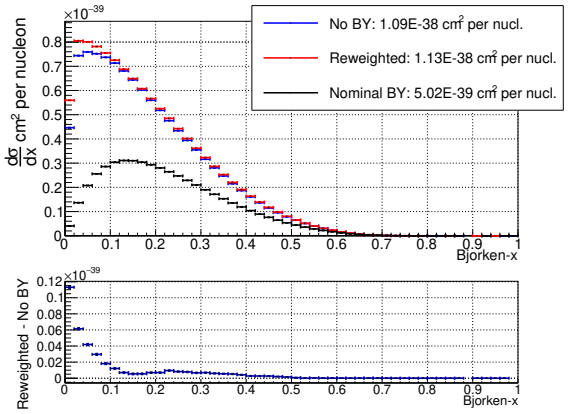

(c) $\bar{\nu}_\mu$ CC DIS BY in Bjorken-x

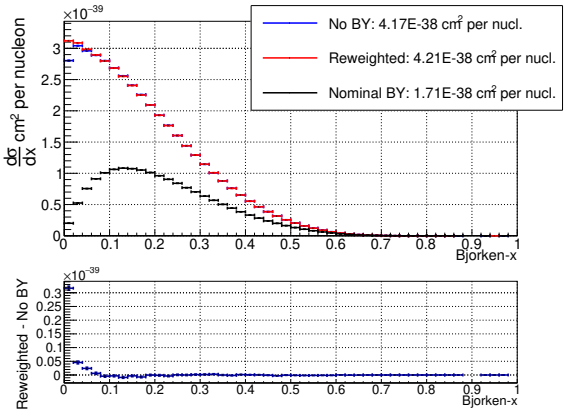

(d) $\bar{\nu}_e$ CC DIS BY in Bjorken-x

Figure A.16: Comparisons of MC events reweighted from using BY corrections to without BY corrections using the inputs given in fig. 6.3 for CC DIS interactions on CH for ν_μ, ν_e, $\bar{\nu}_\mu$ and $\bar{\nu}_e$. Comparisons are given in Bjorken-x. The lower panels in all the plots show the difference between reweighted MC and that generated without BY corrections.

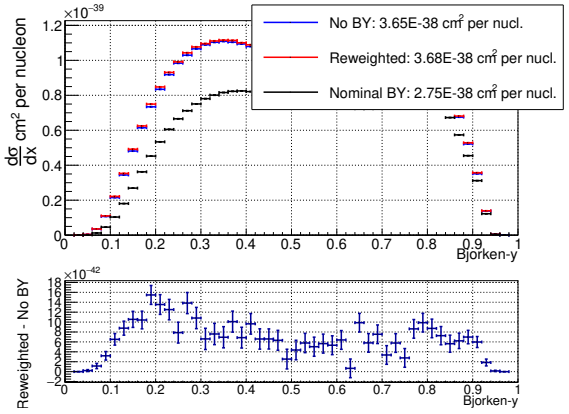

(a) ν_μ CC Multi-π BY in Bjorken-y

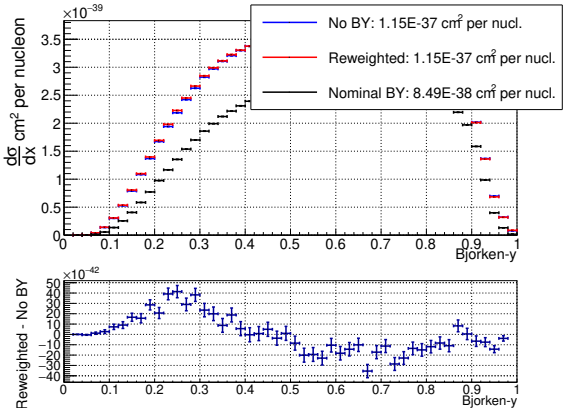

(b) ν_e CC Multi-π BY in Bjorken-y

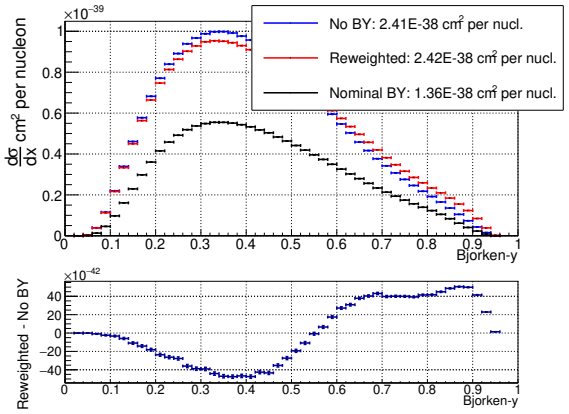

(c) $\bar{\nu}_\mu$ CC Multi-π BY in Bjorken-y

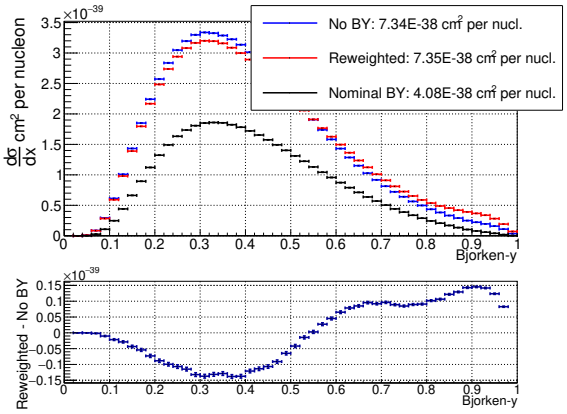

(d) $\bar{\nu}_e$ CC Multi-π BY in Bjorken-y

Figure A.17: Comparisons of MC events reweighted from using BY corrections to without BY corrections using the inputs given in fig. 6.3 for CC Multi-π interactions on CH for ν_μ, ν_e, $\bar{\nu}_\mu$ and $\bar{\nu}_e$. Comparisons are given in Bjorken-y. The lower panels in all the plots show the difference between reweighted MC and that generated without BY corrections.

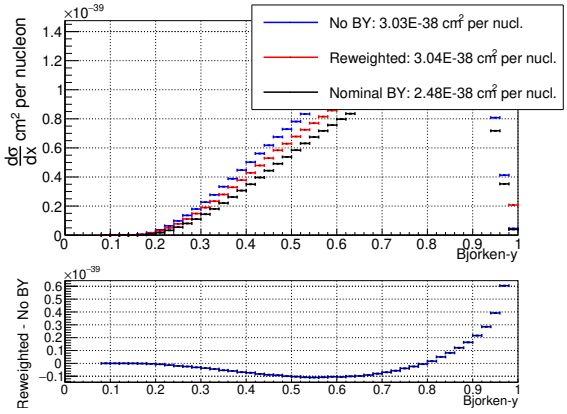

(a) ν_μ CC DIS BY in Bjorken-y

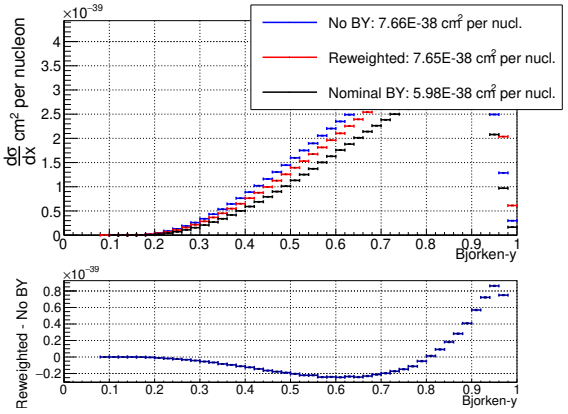

(b) ν_e CC DIS BY in Bjorken-y

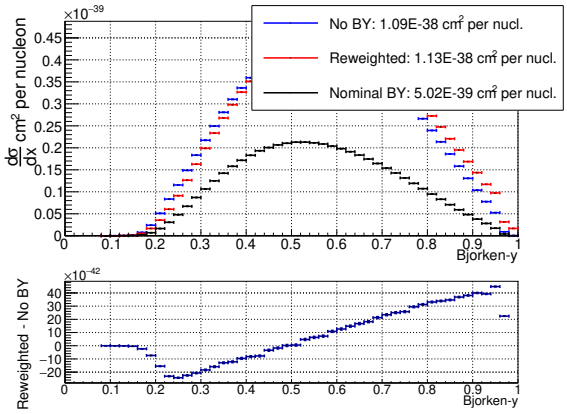

(c) $\bar{\nu}_\mu$ CC DIS BY in Bjorken-y

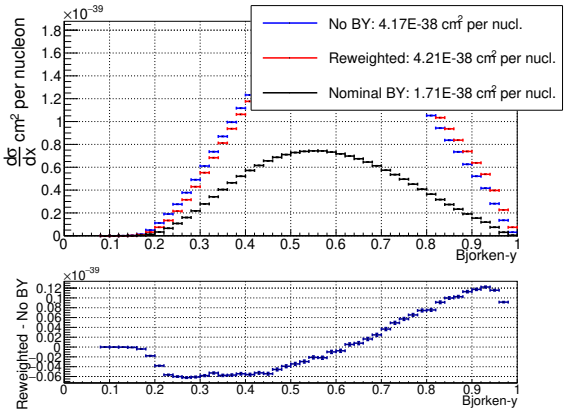

(d) $\bar{\nu}_e$ CC DIS BY in Bjorken-y

Figure A.18: Comparisons of MC events reweighted from using BY corrections to without BY corrections using the inputs given in fig. 6.3 for CC DIS interactions on CH for ν_μ, ν_e, $\bar{\nu}_\mu$ and $\bar{\nu}_e$. Comparisons are given in Bjorken-y. The lower panels in all the plots show the difference between reweighted MC and that generated without BY corrections.

Appendix B

Analysis Technique

This appendix contains the binning used for the data and MC samples at ND280 in appendix B.1 and the analysis binning used for the SK samples in appendix B.2.

B.1 ND280 sample binning

- **FHC ν_μ CC0π:**
  p (MeV/c): 0., 300., 1000., 1250., 1500., 2000., 3000., 5000., 30000.
  cos θ: -1.0, 0.6, 0.8, 0.85, 0.9, 0.92, 0.98, 0.99, 1.0

- **FHC ν_μ CC1π:**
  p (MeV/c): 0., 300., 400., 700., 800., 1000., 1500., 2000., 5000., 30000.
  cos θ: -1.0, 0.6, 0.8, 0.9, 0.92, 0.94, 0.96, 0.98, 0.99, 1.0

- **FHC ν_μ CCOther:**
  p (MeV/c): 0., 300., 400., 700., 800., 900., 1250., 2000., 3000., 5000., 30000.
  cos θ: -1.0, 0.6, 0.8, 0.85, 0.9, 0.92, 0.96, 0.98, 0.99, 1.0

- **RHC $\bar{\nu}_\mu$ CC0π:**

***p* (MeV/c):** 0., 300., 2000., 4000., 30000.

cos θ: -1., 0.6, 0.8, 0.9, 0.96, 1.

- **RHC $\bar{\nu}_\mu$ CC1π:**
  ***p* (MeV/c):** 0., 500., 30000.
  cos θ: -1, 0.7, 1.

- **RHC $\bar{\nu}_\mu$ CCOther:**
  ***p* (MeV/c):** 0., 600., 800., 30000.
  cos θ: -1., 0.7, 0.95, 0.97, 1.

- **RHC ν_μ CC0π:**
  ***p* (MeV/c):** 0., 300., 1500., 30000.
  cos θ: -1., 0.7, 1.

- **RHC ν_μ CC1π:**
  ***p* (MeV/c):** 0., 600., 800., 30000.
  cos θ: -1, 0.7, 1.

- **RHC ν_μ CCOther:**
  ***p* (MeV/c):** 0., 600., 30000.
  cos θ: -1., 0.7, 1.

B.2 SK sample binning

Below the binning used in the oscillation analysis for the samples at SK is given.

- **Muon-like binning** - the binning for the 1Rμ selection has 50MeV-width bins

from 0 to 3GeV, after which the bin edges are: 3.25, 3.5, 3.75, 4, 4.5, 5.0, 5.5, 6.0, 7.0, 8.0, 9.0, 10.0 and 30 GeV.

- **Electron-like binning** - as mentioned in section 4.1.4, electron-like samples are fitted in both reconstructed energy and the angle between the outgoing lepton and the neutrino, θ. The electron-like samples have uniform 50MeV-width bins with a reconstructed energy cut at 1.25GeV. The θ-binning has uniform binning of 10°-width bins from 0° to 140° and one bin for 140°–180°.

Appendix C

Oscillation Analysis Results

This appendix contains the pre-fit distributions for the ND280 samples used in the analysis in chapter 7 as well as the oscillated and unoscillated event rate predictions at SK.

C.1 Pre-fit ND280 predictions

Below are pre-fit MC predictions for the ND280 samples. Distributions are shown in reconstructed lepton momentum in fig. C.1 and fig. C.2 for the RHC ν_μ and $\bar{\nu}_\mu$ selections respectively. Then all ND280 samples are shown projected into cosine of the reconstructed angle between the lepton and the neutrino beam direction in fig. C.3, fig. C.4, fig. C.5 for the FHC and the RHC $\bar{\nu}_\mu$ and RHC ν_μ samples respectively. 2D distributions for the ND280 samples are then shown in fig. C.8. All figures are taken from [117].

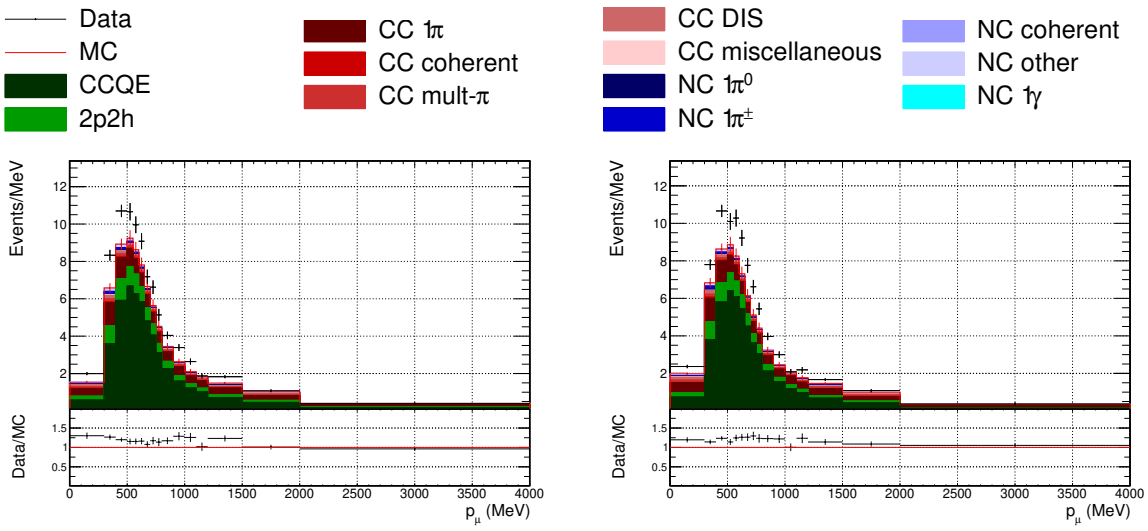

(a) FGD1 RHC $\bar{\nu}_\mu$ 0π

(b) FGD2 RHC $\bar{\nu}_\mu$ 0π

(c) FGD1 RHC $\bar{\nu}_\mu$ 1π

(d) FGD2 RHC $\bar{\nu}_\mu$ 1π

(e) FGD1 RHC $\bar{\nu}_\mu$ Other

(f) FGD2 RHC $\bar{\nu}_\mu$ Other

Figure C.1: p_μ projections of data and nominal MC broken down by interaction mode for RHC $\bar{\nu}_\mu$ selections.

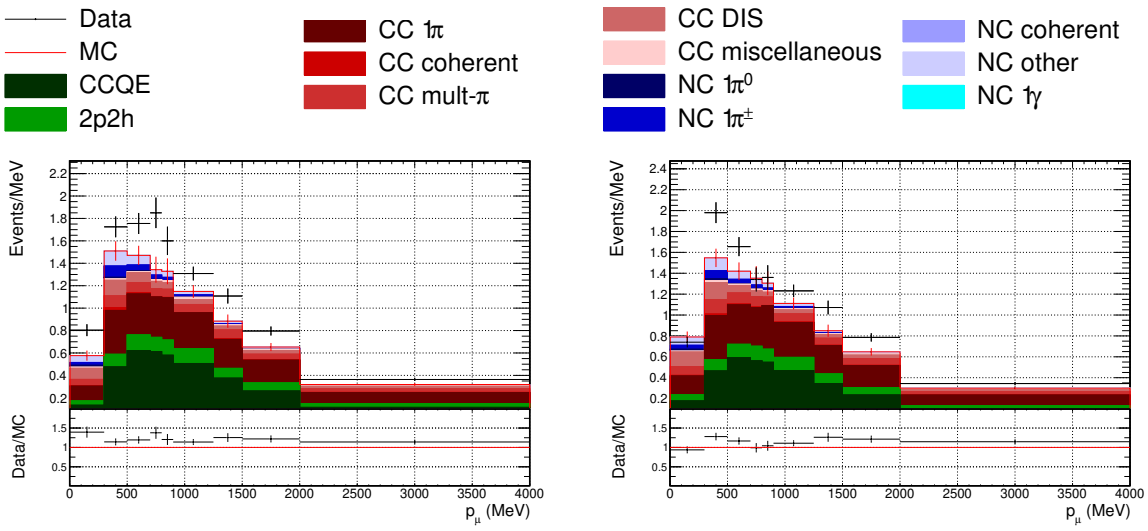

(a) FGD1 RHC ν_μ 0π

(b) FGD2 RHC ν_μ 0π

(c) FGD1 RHC ν_μ 1π

(d) FGD2 RHC ν_μ 1π

(e) FGD1 RHC ν_μ Other

(f) FGD2 RHC ν_μ Other

Figure C.2: p_μ projections of data and nominal MC broken down by interaction mode for RHC ν_μ selections.

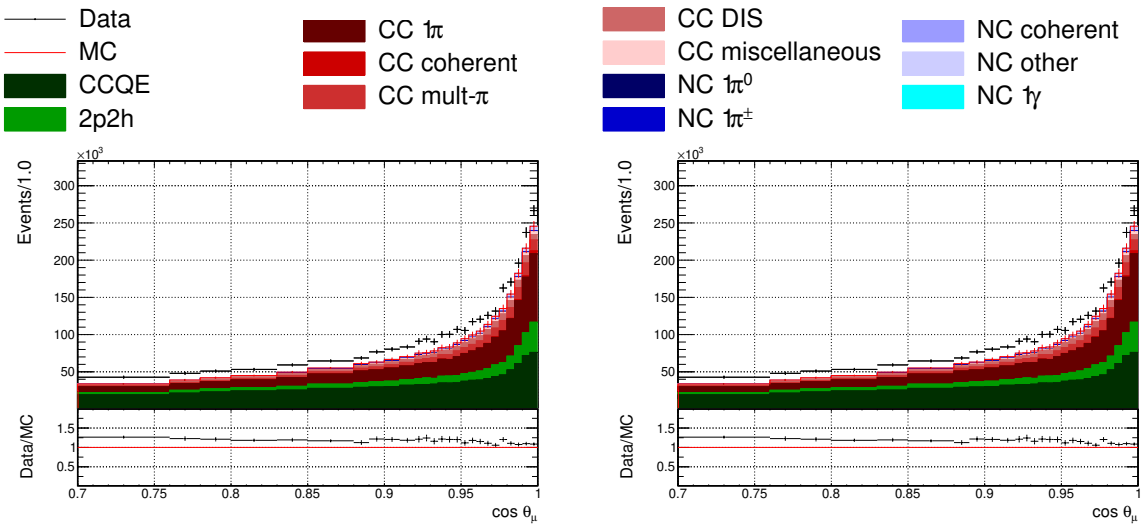

(a) FGD1 FHC ν_μ 0π

(b) FGD2 FHC ν_μ 0π

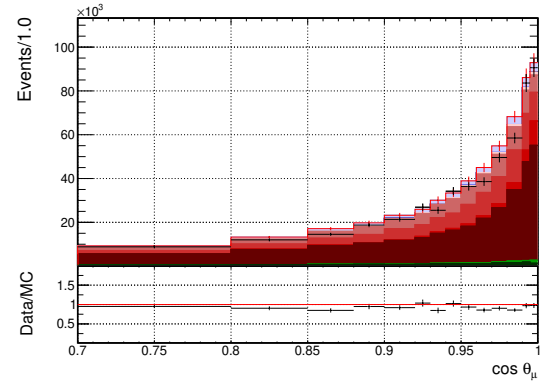

(c) FGD1 FHC ν_μ 1π

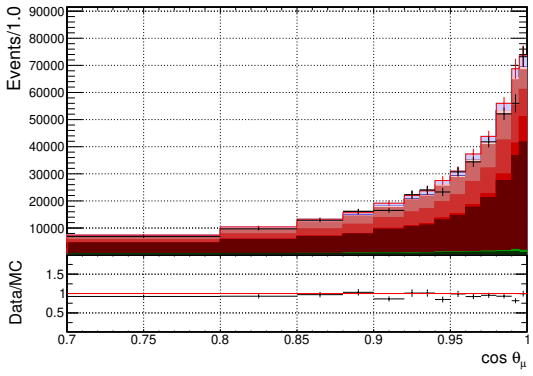

(d) FGD2 FHC ν_μ 1π

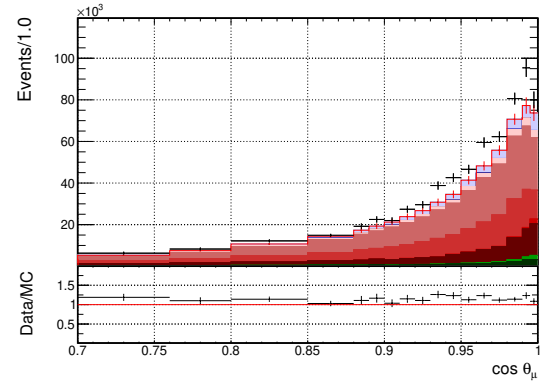

(e) FGD1 FHC ν_μ Other

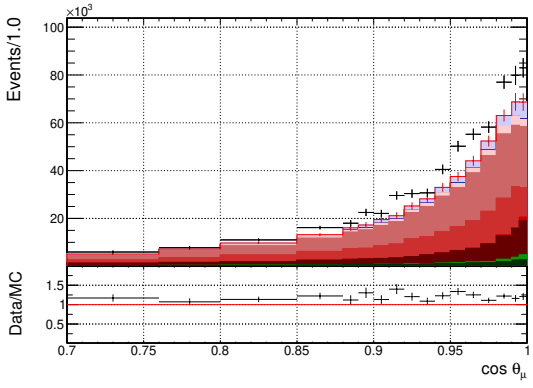

(f) FGD2 ν_μ Other

Figure C.3: $\cos\theta_\mu$ projections of data and nominal MC broken down by interaction mode for FHC selections.

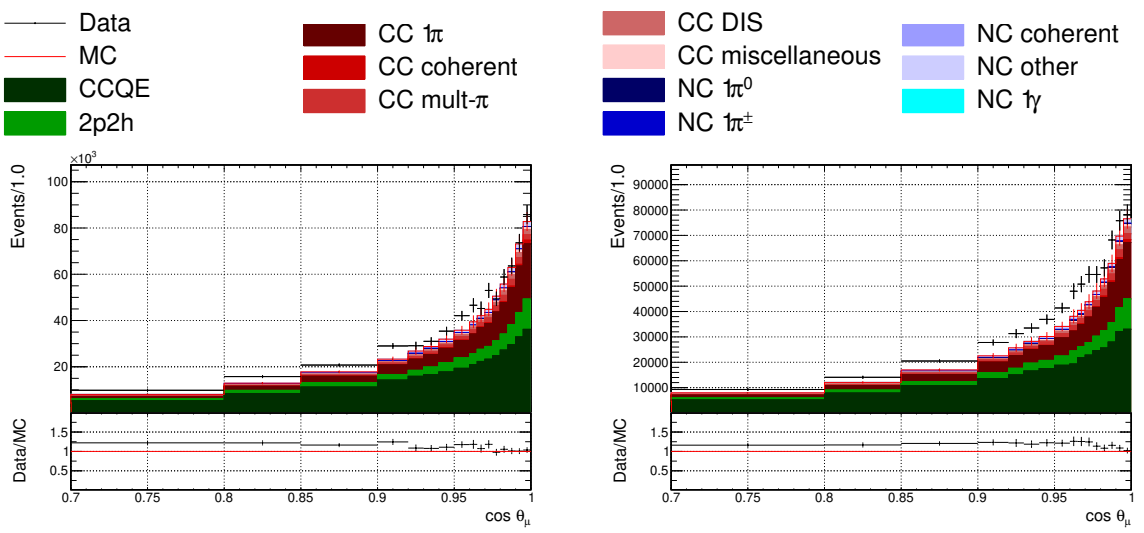

(a) FGD1 RHC $\bar{\nu}_\mu$ 0π

(b) FGD2 RHC $\bar{\nu}_\mu$ 0π

(c) FGD1 RHC $\bar{\nu}_\mu$ 1π

(d) FGD2 RHC $\bar{\nu}_\mu$ 1π

(e) FGD1 RHC $\bar{\nu}_\mu$ Other

(f) FGD2 RHC $\bar{\nu}_\mu$ Other

Figure C.4: $\cos\theta_\mu$ projections of data and nominal MC broken down by interaction mode for RHC $\bar{\nu}_\mu$ selections.

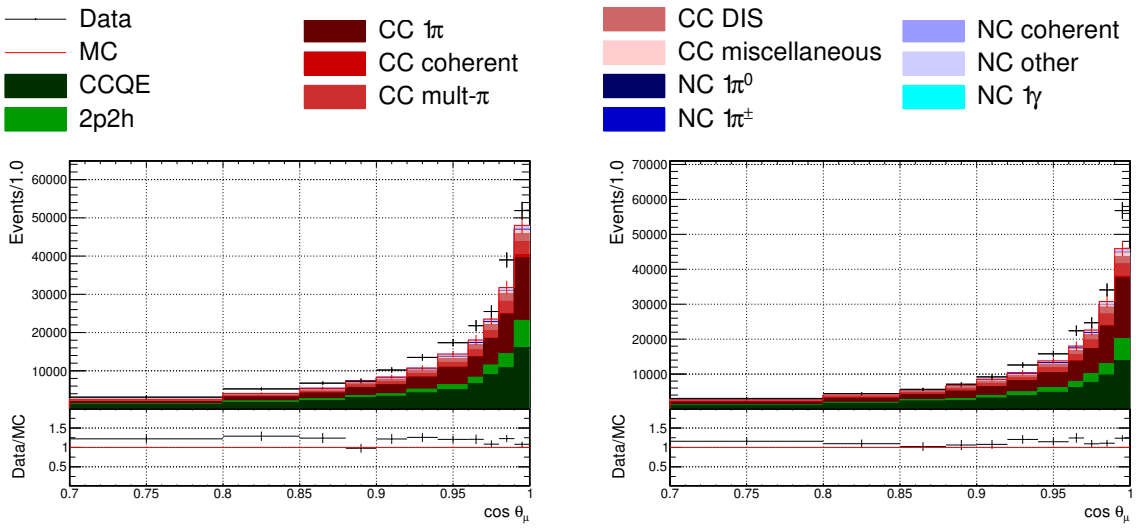

(a) FGD1 RHC ν_μ 0π

(b) FGD2 RHC ν_μ 0π

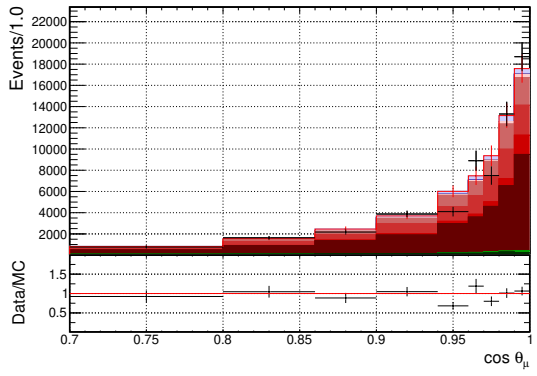

(c) FGD1 RHC ν_μ 1π

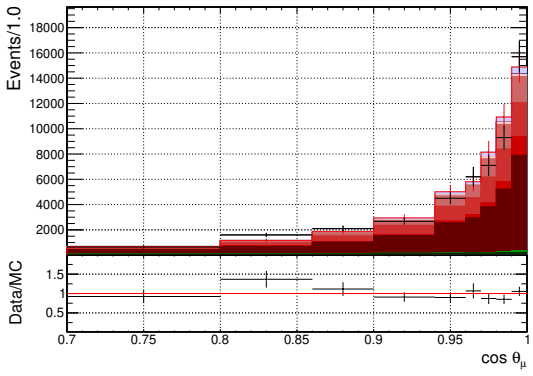

(d) FGD2 RHC ν_μ 1π

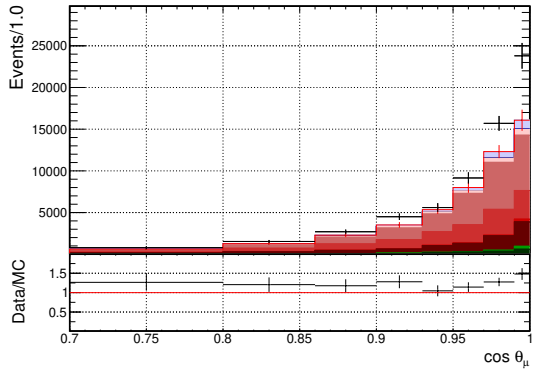

(e) FGD1 RHC ν_μ Other

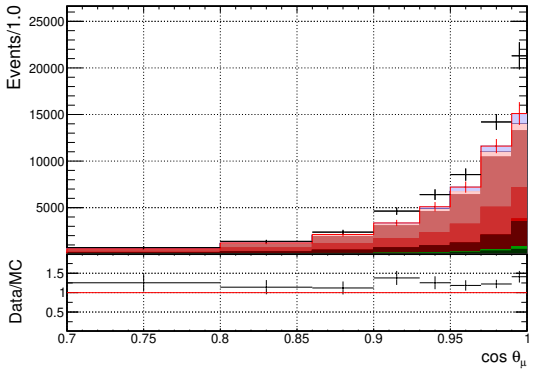

(f) FGD2 RHC ν_μ Other

Figure C.5: $\cos\theta_\mu$ projections of data and nominal MC broken down by interaction mode for RHC ν_μ selections.

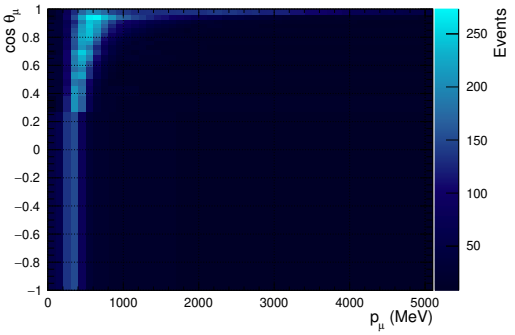

(a) FGD1 FHC ν_μ 0π

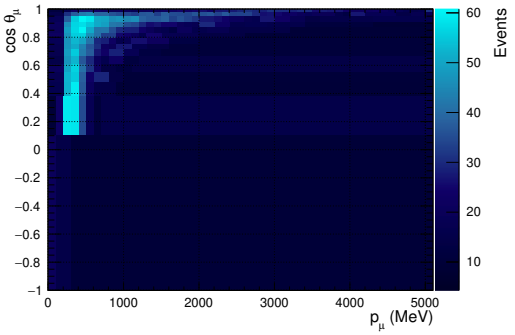

(b) FGD1 FHC ν_μ 1π

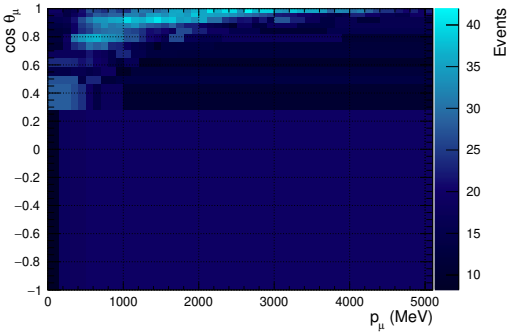

(c) FGD1 FHC ν_μ Other

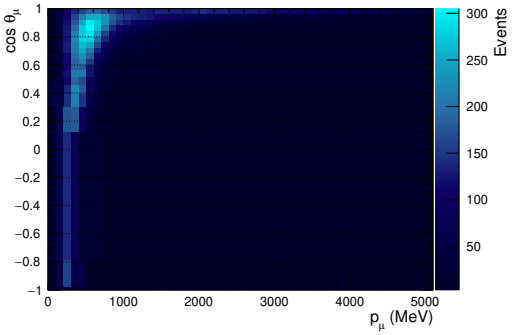

(d) FGD2 FHC ν_μ 0π

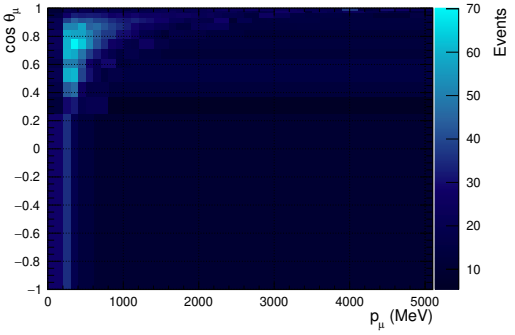

(e) FGD2 FHC ν_μ 1π

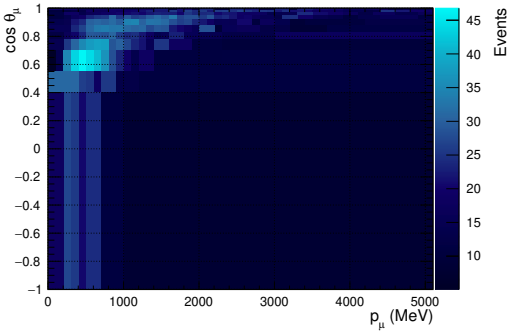

(f) FGD2 FHC ν_μ Other

Figure C.6: p_μ-cos θ_μ distributions for the nominal MC for the samples in FHC mode with the binning used in the fit to data.

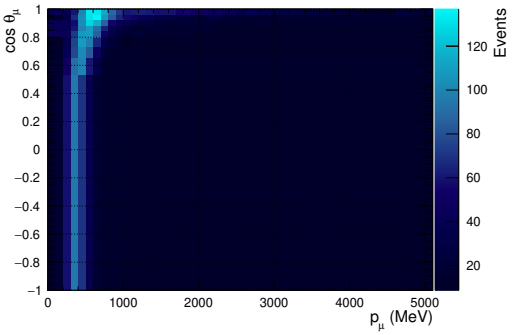

(a) FGD1 RHC $\bar{\nu_\mu}$ 0π

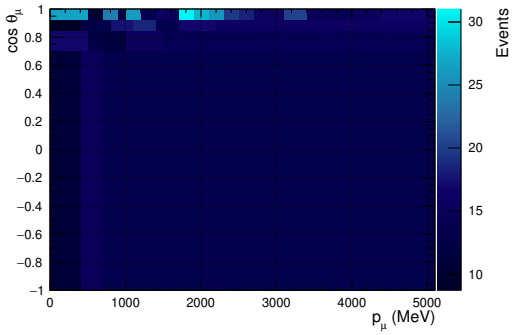

(b) FGD1 RHC $\bar{\nu_\mu}$ 1π

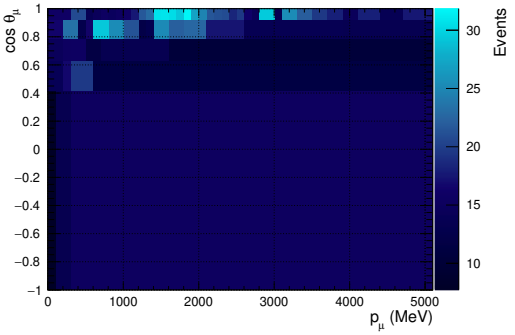

(c) FGD1 RHC $\bar{\nu_\mu}$ Other

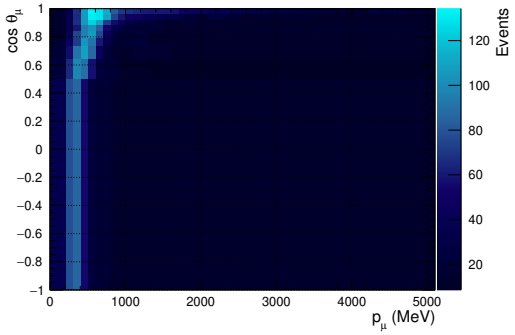

(d) FGD2 RHC $\bar{\nu_\mu}$ 0π

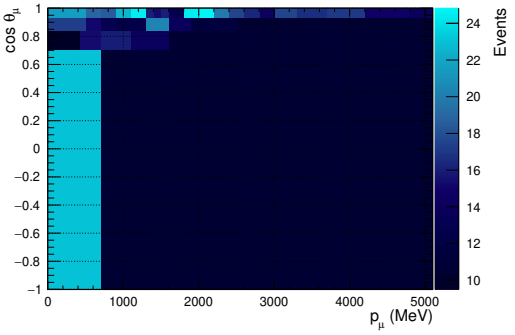

(e) FGD2 RHC $\bar{\nu_\mu}$ 1π

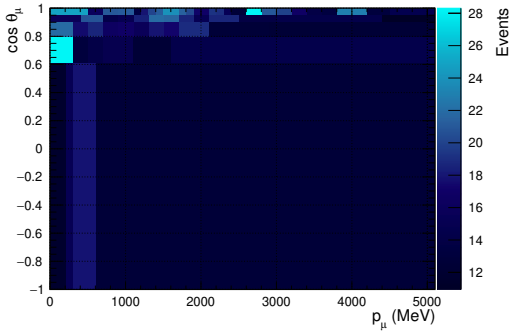

(f) FGD2 RHC $\bar{\nu_\mu}$ Other

Figure C.7: p_μ-cos θ_μ distributions for the nominal MC for the samples in RHC mode with the binning used in the fit to data.

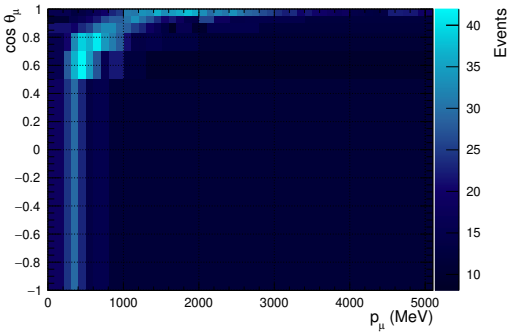

(a) FGD1 RHC ν_μ 0π

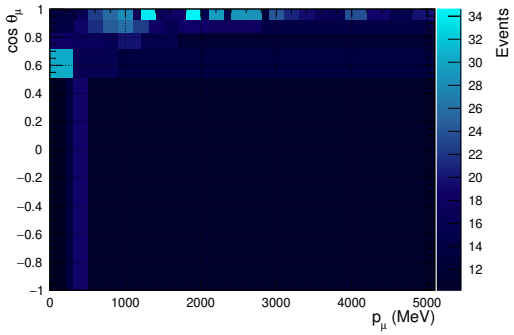

(b) FGD1 RHC ν_μ 1π

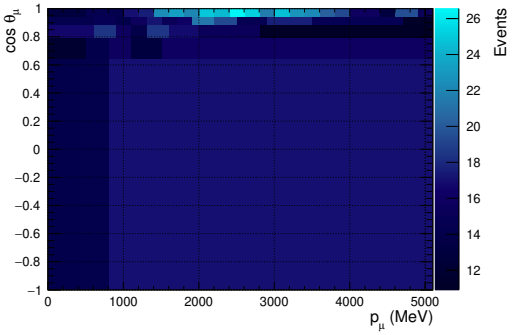

(c) FGD1 RHC ν_μ Other

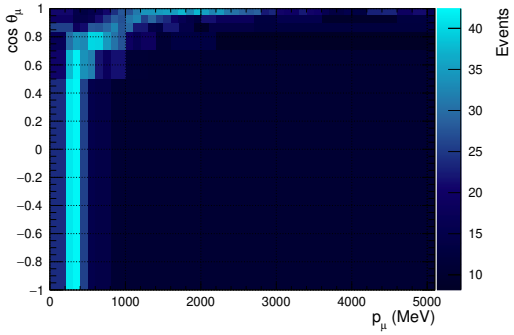

(d) FGD2 RHC ν_μ 0π

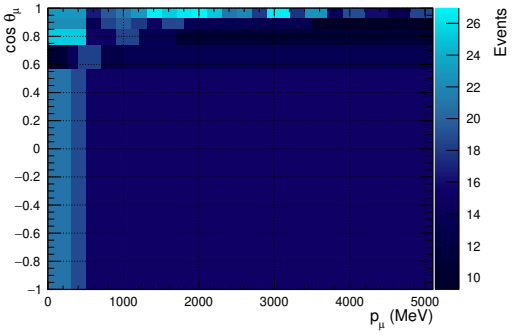

(e) FGD2 RHC ν_μ 1π

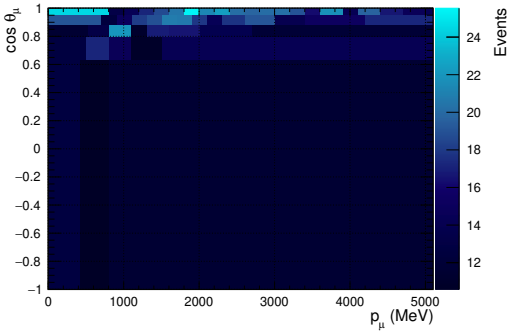

(f) FGD2 RHC ν_μ Other

Figure C.8: p_μ-cos θ_μ distributions for the nominal MC for the wrong-sign samples in RHC mode with the binning used in the fit to data.

C.2 SK Event rate predictions

Below are the event rate predictions for every sample at SK. These are presented broken down by the neutrino interaction modes used in the analysis and the true neutrino flavour. The oscillated event rate predictions use the Asimov A oscillation parameter values given in table 5.1. The predictions are shown for before a fit to the data at ND280 and afterwards showing the impact of the constraint on nuisance parameters from the ND280.

C.2.1 SK Event rate predictions with nuisance parameters at post-ND280 fit values

Table C.1: Post-ND280 fit event rate prediction for FHC 1R$_\mu$ sample: 19.664×10^{20} POT, unoscillated

	ν_μ	ν_e	$\bar{\nu}_\mu$	$\bar{\nu}_e$	ν_e signal	$\bar{\nu}_e$ signal	Total
CCQE	1220.16596	0.00613	29.19745	0.00041	0.00000	0.00000	1249.36995
CC1π	124.22964	0.00377	5.87011	0.00013	0.00000	0.00000	130.10365
CC coherent	0.78860	0.00000	0.13482	0.00003	0.00000	0.00000	0.92345
CCnπ	9.72502	0.00106	0.54632	0.00004	0.00000	0.00000	10.27244
CC DIS	0.86852	0.00000	0.04671	0.00000	0.00000	0.00000	0.91523
NCπ^0	0.51514	0.01597	0.01910	0.00152	0.00000	0.00000	0.55172
NC$\pi^{+/-}$	5.32903	0.11549	0.19730	0.01103	0.00000	0.00000	5.65285
NC coherent	0.00000	0.00049	0.00000	0.00000	0.00000	0.00000	0.00049
NC other	2.40325	0.09925	0.13430	0.01011	0.00000	0.00000	2.64691
2p-2h	161.94572	0.00198	3.95411	0.00003	0.00000	0.00000	165.90183
NC 1γ	0.00920	0.00000	0.00000	0.00000	0.00000	0.00000	0.00920
CC Other	1.52360	0.00000	0.09245	0.00000	0.00000	0.00000	1.61605
Sample totals	1527.50368	0.24413	40.19266	0.02330	0.00000	0.00000	
Total	1567.96376						

Table C.2: Post-ND280 fit event rate prediction for FHC 1R$_e$ sample: 19.664×10^{20} POT, unoscillated

	ν_μ	ν_e	$\bar{\nu}_\mu$	$\bar{\nu}_e$	ν_e signal	$\bar{\nu}_e$ signal	Total
CCQE	1.52881	8.66539	0.03234	0.31819	0.00000	0.00000	10.54474
CC1π	0.23606	1.60085	0.00730	0.09216	0.00000	0.00000	1.93638
CC coherent	0.00000	0.01042	0.00028	0.00299	0.00000	0.00000	0.01369
CCnπ	0.03394	0.19009	0.00043	0.00868	0.00000	0.00000	0.23314
CC DIS	0.00000	0.01077	0.00000	0.00193	0.00000	0.00000	0.01269
NCπ^0	1.97765	0.03923	0.07954	0.00465	0.00000	0.00000	2.10108
NC$\pi^{+/-}$	0.29557	0.00896	0.01293	0.00080	0.00000	0.00000	0.31827
NC coherent	0.31582	0.00619	0.03144	0.00187	0.00000	0.00000	0.35531
NC other	0.56707	0.01870	0.02380	0.00255	0.00000	0.00000	0.61212
2p-2h	0.21413	1.63697	0.00419	0.05710	0.00000	0.00000	1.91238
NC 1γ	1.49776	0.03374	0.06530	0.00313	0.00000	0.00000	1.59994
CC Other	0.02083	0.02890	0.00035	0.00165	0.00000	0.00000	0.05173
Sample totals	6.68763	12.25021	0.25792	0.49571	0.00000	0.00000	
Total	19.69147						

Table C.3: Post-ND280 fit event rate prediction for RHC $1R_\mu$ sample: 16.34556×10^{20} POT, unoscillated

	ν_μ	ν_e	$\bar{\nu}_\mu$	$\bar{\nu}_e$	ν_e signal	$\bar{\nu}_e$ signal	Total
CCQE	80.60139	0.00165	267.70071	0.00198	0.00000	0.00000	348.30573
CC1π	17.06663	0.00050	26.03441	0.00033	0.00000	0.00000	43.10188
CC coherent	0.10174	0.00000	0.95180	0.00000	0.00000	0.00000	1.05354
CCnπ	2.51886	0.00014	1.33900	0.00008	0.00000	0.00000	3.85809
CC DIS	0.14763	0.00000	0.11811	0.00000	0.00000	0.00000	0.26574
NCπ^0	0.07727	0.00344	0.07559	0.00147	0.00000	0.00000	0.15776
NC$\pi^{+/-}$	0.68266	0.02627	0.94557	0.02224	0.00000	0.00000	1.67673
NC coherent	0.00061	0.00000	0.00000	0.00000	0.00000	0.00000	0.00061
NC other	0.62419	0.02547	0.34814	0.01390	0.00000	0.00000	1.01170
2p-2h	15.31182	0.00044	28.43973	0.00026	0.00000	0.00000	43.75224
NC 1γ	0.00000	0.00000	0.00000	0.00000	0.00000	0.00000	0.00000
CC Other	0.44896	0.00000	0.21829	0.00013	0.00000	0.00000	0.66739
Sample totals	117.58175	0.05790	326.17136	0.04040	0.00000	0.00000	
Total	443.85141						

Table C.4: Post-ND280 fit event rate prediction for RHC $1R_e$ sample: 16.34556×10^{20} POT, unoscillated

	ν_μ	ν_e	$\bar{\nu}_\mu$	$\bar{\nu}_e$	ν_e signal	$\bar{\nu}_e$ signal	Total
CCQE	0.10146	1.11489	0.34272	1.75101	0.00000	0.00000	3.31007
CC1π	0.02714	0.26411	0.04674	0.32786	0.00000	0.00000	0.66584
CC coherent	0.00000	0.00128	0.00287	0.01404	0.00000	0.00000	0.01820
CCnπ	0.00474	0.04448	0.00392	0.01913	0.00000	0.00000	0.07228
CC DIS	0.00000	0.00047	0.00000	0.00106	0.00000	0.00000	0.00153
NCπ^0	0.24842	0.01029	0.34136	0.00838	0.00000	0.00000	0.60844
NC$\pi^{+/-}$	0.05197	0.00186	0.04267	0.00115	0.00000	0.00000	0.09765
NC coherent	0.04495	0.00156	0.15092	0.00290	0.00000	0.00000	0.20032
NC other	0.13481	0.00686	0.06324	0.00289	0.00000	0.00000	0.20779
2p-2h	0.02237	0.26331	0.03938	0.25316	0.00000	0.00000	0.57822
NC 1γ	0.17463	0.00686	0.28679	0.00534	0.00000	0.00000	0.47363
CC Other	0.00304	0.00850	0.00000	0.00450	0.00000	0.00000	0.01604
Sample totals	0.81352	1.72448	1.32060	2.39141	0.00000	0.00000	
Total	6.25001						

Table C.5: Post-ND280 fit event rate prediction for FHC CC-$1\pi^+$ sample: 19.664×10^{20} POT, unoscillated

	ν_μ	ν_e	$\bar{\nu}_\mu$	$\bar{\nu}_e$	ν_e signal	$\bar{\nu}_e$ signal	Total
CCQE	0.45534	0.04527	0.00851	0.00258	0.00000	0.00000	0.51171
CC1π	0.47162	0.99733	0.00891	0.00349	0.00000	0.00000	1.48135
CC coherent	0.00549	0.01776	0.00029	0.00017	0.00000	0.00000	0.02372
CCnπ	0.08468	0.14999	0.00084	0.00280	0.00000	0.00000	0.23832
CC DIS	0.00000	0.00345	0.00023	0.00000	0.00000	0.00000	0.00369
NCπ^0	0.02792	0.00083	0.00097	0.00000	0.00000	0.00000	0.02972
NC$\pi^{+/-}$	0.06996	0.00334	0.00287	0.00047	0.00000	0.00000	0.07665
NC coherent	0.00000	0.00000	0.00000	0.00000	0.00000	0.00000	0.00000
NC other	0.19489	0.01068	0.02023	0.00206	0.00000	0.00000	0.22786
2p-2h	0.08410	0.03031	0.00165	0.00128	0.00000	0.00000	0.11734
NC 1γ	0.00000	0.00000	0.00030	0.00017	0.00000	0.00000	0.00047
CC Other	0.15955	0.01010	0.00037	0.00019	0.00000	0.00000	0.17021
Sample totals	1.55356	1.26907	0.04518	0.01322	0.00000	0.00000	
Total	2.88103						

Table C.6: Post-ND280 fit event rate prediction for FHC 1R$_\mu$ sample: 19.664×10^{20} POT, oscillated

	ν_μ	ν_e	$\bar{\nu}_\mu$	$\bar{\nu}_e$	ν_e signal	$\bar{\nu}_e$ signal	Total
CCQE	224.30064	0.00584	13.93517	0.00039	0.04639	0.00021	238.28864
CC1π	42.52782	0.00350	3.67216	0.00013	0.04585	0.00005	46.24951
CC coherent	0.30847	0.00000	0.07060	0.00003	0.00000	0.00001	0.37912
CCnπ	7.63280	0.00104	0.44184	0.00004	0.00214	0.00000	8.07787
CC DIS	0.82632	0.00000	0.04411	0.00000	0.00000	0.00000	0.87043
NCπ^0	0.51514	0.01597	0.01910	0.00152	0.00000	0.00000	0.55172
NC$\pi^{+/-}$	5.32903	0.11549	0.19730	0.01103	0.00000	0.00000	5.65285
NC coherent	0.00000	0.00049	0.00000	0.00000	0.00000	0.00000	0.00049
NC other	2.40325	0.09925	0.13430	0.01011	0.00000	0.00000	2.64691
2p-2h	38.97606	0.00181	2.09379	0.00003	0.01310	0.00004	41.08484
NC 1γ	0.00920	0.00000	0.00000	0.00000	0.00000	0.00000	0.00920
CC Other	1.20820	0.00000	0.07410	0.00000	0.00000	0.00000	1.28230
Sample totals	324.03694	0.24339	20.68247	0.02327	0.10748	0.00031	
Total	345.09388						

Table C.7: Post-ND280 fit event rate prediction for FHC 1R$_e$ sample: 19.664×10^{20} POT, oscillated

	ν_μ	ν_e	$\bar{\nu}_\mu$	$\bar{\nu}_e$	ν_e signal	$\bar{\nu}_e$ signal	Total
CCQE	0.28155	8.04292	0.01029	0.29945	59.52396	0.34737	68.50553
CC1π	0.05199	1.49896	0.00395	0.08781	7.26942	0.07010	8.98223
CC coherent	0.00000	0.00971	0.00011	0.00283	0.04186	0.00282	0.05732
CCnπ	0.01938	0.18360	0.00030	0.00842	0.12610	0.00306	0.34086
CC DIS	0.00000	0.01064	0.00000	0.00191	0.00092	0.00002	0.01349
NCπ^0	1.97765	0.03923	0.07954	0.00465	0.00000	0.00000	2.10108
NC$\pi^{+/-}$	0.29557	0.00896	0.01293	0.00080	0.00000	0.00000	0.31827
NC coherent	0.31582	0.00619	0.03144	0.00187	0.00000	0.00000	0.35531
NC other	0.56707	0.01870	0.02380	0.00255	0.00000	0.00000	0.61212
2p-2h	0.05316	1.52789	0.00187	0.05421	9.07148	0.05101	10.75963
NC 1γ	1.49776	0.03374	0.06530	0.00313	0.00000	0.00000	1.59994
CC Other	0.00051	0.02792	0.00021	0.00160	0.02877	0.00046	0.05948
Sample totals	5.06045	11.40847	0.22975	0.46923	76.06252	0.47483	
Total	93.70526						

Table C.8: Post-ND280 fit event rate prediction for RHC $1R_\mu$ sample: 16.34556×10^{20} POT, oscillated

	ν_μ	ν_e	$\bar{\nu}_\mu$	$\bar{\nu}_e$	ν_e signal	$\bar{\nu}_e$ signal	Total
CCQE	33.93916	0.00160	59.29960	0.00188	0.00091	0.00308	93.24623
CC1π	9.98527	0.00048	10.01723	0.00032	0.00077	0.00019	20.00425
CC coherent	0.06299	0.00000	0.21543	0.00000	0.00000	0.00019	0.27861
CCnπ	1.98867	0.00014	1.04428	0.00008	0.00007	0.00017	3.03340
CC DIS	0.13813	0.00000	0.11158	0.00000	0.00000	0.00000	0.24972
NCπ^0	0.07727	0.00344	0.07559	0.00147	0.00000	0.00000	0.15776
NC$\pi^{+/-}$	0.68266	0.02627	0.94557	0.02224	0.00000	0.00000	1.67673
NC coherent	0.00061	0.00000	0.00000	0.00000	0.00000	0.00000	0.00061
NC other	0.62419	0.02547	0.34814	0.01390	0.00000	0.00000	1.01170
2p-2h	7.73840	0.00042	7.07443	0.00025	0.00069	0.00029	14.81448
NC 1γ	0.00000	0.00000	0.00000	0.00000	0.00000	0.00000	0.00000
CC Other	0.35679	0.00000	0.17156	0.00013	0.00000	0.00000	0.52848
Sample totals	55.59413	0.05781	79.30342	0.04028	0.00244	0.00391	
Total	135.00199						

Table C.9: Post-ND280 fit event rate prediction for RHC $1R_e$ sample: 16.34556×10^{20} POT, oscillated

	ν_μ	ν_e	$\bar{\nu}_\mu$	$\bar{\nu}_e$	ν_e signal	$\bar{\nu}_e$ signal	Total
CCQE	0.03551	1.03753	0.05330	1.64454	2.25983	5.74537	10.77607
CC1π	0.01229	0.24910	0.01741	0.30983	0.38817	0.74519	1.72198
CC coherent	0.00000	0.00121	0.00047	0.01320	0.00183	0.04217	0.05888
CCnπ	0.00304	0.04313	0.00226	0.01848	0.02271	0.01289	0.10250
CC DIS	0.00000	0.00047	0.00000	0.00104	0.00034	0.00000	0.00186
NCπ^0	0.24842	0.01029	0.34136	0.00838	0.00000	0.00000	0.60844
NC$\pi^{+/-}$	0.05197	0.00186	0.04267	0.00115	0.00000	0.00000	0.09765
NC coherent	0.04495	0.00156	0.15092	0.00290	0.00000	0.00000	0.20032
NC other	0.13481	0.00686	0.06324	0.00289	0.00000	0.00000	0.20779
2p-2h	0.01038	0.24726	0.00768	0.23861	0.41493	0.70257	1.62144
NC 1γ	0.17463	0.00686	0.28679	0.00534	0.00000	0.00000	0.47363
CC Other	0.00105	0.00822	0.00000	0.00436	0.00374	0.00132	0.01869
Sample totals	0.71704	1.61435	0.96609	2.25071	3.09155	7.24950	
Total	15.88925						

Table C.10: Post-ND280 fit event rate prediction for FHC CC-$1\pi^+$ sample: 19.664×10^{20} POT, oscillated

	ν_μ	ν_e	$\bar{\nu}_\mu$	$\bar{\nu}_e$	ν_e signal	$\bar{\nu}_e$ signal	Total
CCQE	0.05098	0.04192	0.00119	0.00241	0.41601	0.00355	0.51606
CC1π	0.06468	0.92460	0.00248	0.00333	6.34271	0.00307	7.34087
CC coherent	0.00039	0.01636	0.00002	0.00016	0.09292	0.00006	0.10990
CCnπ	0.04033	0.14352	0.00046	0.00270	0.14698	0.00119	0.33518
CC DIS	0.00000	0.00340	0.00019	0.00000	0.00028	0.00004	0.00391
NCπ^0	0.02792	0.00083	0.00097	0.00000	0.00000	0.00000	0.02972
NC$\pi^{+/-}$	0.06996	0.00334	0.00287	0.00047	0.00000	0.00000	0.07665
NC coherent	0.00000	0.00000	0.00000	0.00000	0.00000	0.00000	0.00000
NC other	0.19489	0.01068	0.02023	0.00206	0.00000	0.00000	0.22786
2p-2h	0.01111	0.02826	0.00040	0.00121	0.14074	0.00118	0.18289
NC 1γ	0.00000	0.00000	0.00030	0.00017	0.00000	0.00000	0.00047
CC Other	0.01154	0.00973	0.00008	0.00018	0.00452	0.00014	0.02619
Sample totals	0.47180	1.18263	0.02920	0.01271	7.14414	0.00923	
Total	8.84971						

C.2.2 SK event rates, nuisance parameter at pre-ND280 fit values

Table C.11: Pre-ND280 fit event rate prediction for FHC 1R$_\mu$ sample: 19.664×10^{20} POT, unoscillated

	ν_μ	ν_e	$\bar{\nu}_\mu$	$\bar{\nu}_e$	ν_e signal	$\bar{\nu}_e$ signal	Total
CCQE	831.09209	0.00424	21.54421	0.00030	0.00000	0.00000	852.64084
CC1π	145.64420	0.00444	6.62286	0.00014	0.00000	0.00000	152.27163
CC coherent	1.24268	0.00000	0.21194	0.00005	0.00000	0.00000	1.45467
CCnπ	8.70522	0.00098	0.54053	0.00004	0.00000	0.00000	9.24678
CC DIS	0.38365	0.00000	0.01440	0.00000	0.00000	0.00000	0.39805
NCπ^0	0.89953	0.02940	0.03489	0.00248	0.00000	0.00000	0.96631
NC$\pi^{+/-}$	7.08226	0.17327	0.27496	0.01517	0.00000	0.00000	7.54566
NC coherent	0.00000	0.00049	0.00000	0.00000	0.00000	0.00000	0.00049
NC other	2.34091	0.09768	0.12629	0.00918	0.00000	0.00000	2.57406
2p-2h	137.83427	0.00167	5.00813	0.00004	0.00000	0.00000	142.84412
NC 1γ	0.00856	0.00000	0.00000	0.00000	0.00000	0.00000	0.00856
CC Other	0.68708	0.00000	0.03939	0.00000	0.00000	0.00000	0.72647
Sample totals	1135.92046	0.31218	34.41760	0.02739	0.00000	0.00000	
Total	1170.67763						

Table C.12: Pre-ND280 fit event rate prediction for RHC $1R_\mu$ sample: 16.34556×10^{20} POT, unoscillated

	ν_μ	ν_e	$\bar{\nu}_\mu$	$\bar{\nu}_e$	ν_e signal	$\bar{\nu}_e$ signal	Total
CCQE	54.17921	0.00115	194.39377	0.00153	0.00000	0.00000	248.57566
CC1π	20.62295	0.00060	28.31589	0.00040	0.00000	0.00000	48.93983
CC coherent	0.15769	0.00000	1.46745	0.00000	0.00000	0.00000	1.62513
CCnπ	2.12531	0.00013	1.35390	0.00009	0.00000	0.00000	3.47943
CC DIS	0.07871	0.00000	0.04058	0.00000	0.00000	0.00000	0.11928
NCπ^0	0.12998	0.00599	0.13127	0.00303	0.00000	0.00000	0.27027
NC$\pi^{+/-}$	0.98528	0.03913	1.24585	0.03045	0.00000	0.00000	2.30071
NC coherent	0.00055	0.00000	0.00000	0.00000	0.00000	0.00000	0.00055
NC other	0.58584	0.02452	0.34070	0.01311	0.00000	0.00000	0.96417
2p-2h	12.92837	0.00038	35.33770	0.00034	0.00000	0.00000	48.26680
NC 1γ	0.00000	0.00000	0.00000	0.00000	0.00000	0.00000	0.00000
CC Other	0.18873	0.00000	0.09343	0.00008	0.00000	0.00000	0.28224
Sample totals	91.98262	0.07190	262.72054	0.04902	0.00000	0.00000	
Total	354.82408						

Table C.13: Pre-ND280 fit event rate prediction for FHC $1R_e$ sample: 19.664×10^{20} POT, unoscillated

	ν_μ	ν_e	$\bar{\nu}_\mu$	$\bar{\nu}_e$	ν_e signal	$\bar{\nu}_e$ signal	Total
CCQE	1.03836	5.92050	0.02359	0.24114	0.00000	0.00000	7.22359
CC1π	0.28745	1.85935	0.00863	0.10015	0.00000	0.00000	2.25558
CC coherent	0.00000	0.01623	0.00044	0.00480	0.00000	0.00000	0.02147
CCnπ	0.02774	0.15882	0.00058	0.00851	0.00000	0.00000	0.19564
CC DIS	0.00000	0.00588	0.00000	0.00029	0.00000	0.00000	0.00617
NCπ^0	2.68739	0.05847	0.11490	0.00671	0.00000	0.00000	2.86748
NC$\pi^{+/-}$	0.42214	0.01418	0.02031	0.00120	0.00000	0.00000	0.45782
NC coherent	0.29999	0.00605	0.02957	0.00174	0.00000	0.00000	0.33736
NC other	0.55988	0.01803	0.02257	0.00215	0.00000	0.00000	0.60262
2p-2h	0.18323	1.40151	0.00533	0.07387	0.00000	0.00000	1.66394
NC 1γ	1.43050	0.03347	0.06258	0.00296	0.00000	0.00000	1.52952
CC Other	0.00855	0.01095	0.00015	0.00078	0.00000	0.00000	0.02043
Sample totals	6.94524	9.50345	0.28864	0.44430	0.00000	0.00000	
Total	17.18162						

Table C.14: Pre-ND280 fit event rate prediction for RHC $1R_e$ sample: 16.34556×10^{20} POT, unoscillated

	ν_μ	ν_e	$\bar{\nu}_\mu$	$\bar{\nu}_e$	ν_e signal	$\bar{\nu}_e$ signal	Total
CCQE	0.06765	0.78631	0.24716	1.27876	0.00000	0.00000	2.37987
CC1π	0.03272	0.31297	0.04995	0.34172	0.00000	0.00000	0.73736
CC coherent	0.00000	0.00205	0.00442	0.02193	0.00000	0.00000	0.02840
CCnπ	0.00447	0.03725	0.00436	0.01844	0.00000	0.00000	0.06451
CC DIS	0.00000	0.00059	0.00000	0.00008	0.00000	0.00000	0.00068
NCπ^0	0.36704	0.01603	0.46985	0.01227	0.00000	0.00000	0.86518
NC$\pi^{+/-}$	0.08306	0.00310	0.06258	0.00169	0.00000	0.00000	0.15044
NC coherent	0.04190	0.00149	0.14077	0.00278	0.00000	0.00000	0.18693
NC other	0.12396	0.00682	0.06412	0.00288	0.00000	0.00000	0.19778
2p-2h	0.01883	0.23027	0.04847	0.31912	0.00000	0.00000	0.61669
NC 1γ	0.16483	0.00666	0.27385	0.00521	0.00000	0.00000	0.45055
CC Other	0.00113	0.00380	0.00000	0.00186	0.00000	0.00000	0.00679
Sample totals	0.90557	1.40733	1.36555	2.00674	0.00000	0.00000	
Total	5.68518						

Table C.15: Pre-ND280 fit event rate prediction for FHC CC-$1\pi^+$ sample: 19.664×10^{20} POT, unoscillated

	ν_μ	ν_e	$\bar{\nu}_\mu$	$\bar{\nu}_e$	ν_e signal	$\bar{\nu}_e$ signal	Total
CCQE	0.30569	0.03133	0.00596	0.00190	0.00000	0.00000	0.34488
CC1π	0.59222	1.26246	0.00860	0.00388	0.00000	0.00000	1.86716
CC coherent	0.00841	0.02752	0.00045	0.00027	0.00000	0.00000	0.03665
CCnπ	0.07869	0.13715	0.00088	0.00302	0.00000	0.00000	0.21975
CC DIS	0.00000	0.00290	0.00014	0.00000	0.00000	0.00000	0.00304
NCπ^0	0.05950	0.00159	0.00168	0.00000	0.00000	0.00000	0.06276
NC$\pi^{+/-}$	0.13626	0.00542	0.00493	0.00062	0.00000	0.00000	0.14723
NC coherent	0.00000	0.00000	0.00000	0.00000	0.00000	0.00000	0.00000
NC other	0.20839	0.01039	0.01981	0.00194	0.00000	0.00000	0.24053
2p-2h	0.07147	0.02653	0.00209	0.00166	0.00000	0.00000	0.10174
NC 1γ	0.00000	0.00000	0.00029	0.00016	0.00000	0.00000	0.00045
CC Other	0.06440	0.00499	0.00015	0.00009	0.00000	0.00000	0.06963
Sample totals	1.52503	1.51029	0.04499	0.01353	0.00000	0.00000	
Total	3.09384						

Table C.16: Pre-ND280 fit event rate prediction for FHC $1R_\mu$ sample: 19.664×10^{20} POT, oscillated

	ν_μ	ν_e	$\bar{\nu}_\mu$	$\bar{\nu}_e$	ν_e signal	$\bar{\nu}_e$ signal	Total
CCQE	154.32619	0.00404	10.29593	0.00029	0.03085	0.00016	164.65745
CC1π	53.50366	0.00414	4.22125	0.00013	0.04786	0.00006	57.77710
CC coherent	0.50125	0.00000	0.11115	0.00004	0.00000	0.00002	0.61246
CCnπ	6.92144	0.00097	0.43854	0.00004	0.00178	0.00000	7.36277
CC DIS	0.36572	0.00000	0.01370	0.00000	0.00000	0.00000	0.37941
NCπ^0	0.89953	0.02940	0.03489	0.00248	0.00000	0.00000	0.96631
NC$\pi^{+/-}$	7.08226	0.17327	0.27496	0.01517	0.00000	0.00000	7.54566
NC coherent	0.00000	0.00049	0.00000	0.00000	0.00000	0.00000	0.00049
NC other	2.34091	0.09768	0.12629	0.00918	0.00000	0.00000	2.57406
2p-2h	33.92794	0.00153	2.65483	0.00004	0.01101	0.00006	36.59541
NC 1γ	0.00856	0.00000	0.00000	0.00000	0.00000	0.00000	0.00856
CC Other	0.54723	0.00000	0.03158	0.00000	0.00000	0.00000	0.57882
Sample totals	260.42470	0.31154	18.20311	0.02738	0.09150	0.00029	
Total	279.05851						

Table C.17: Pre-ND280 fit event rate prediction for RHC $1R_\mu$ sample: 16.34556×10^{20} POT, oscillated

	ν_μ	ν_e	$\bar{\nu}_\mu$	$\bar{\nu}_e$	ν_e signal	$\bar{\nu}_e$ signal	Total
CCQE	22.92815	0.00112	43.84837	0.00146	0.00057	0.00199	66.78166
CC1π	12.33062	0.00058	11.59387	0.00038	0.00090	0.00028	23.92662
CC coherent	0.09834	0.00000	0.34106	0.00000	0.00000	0.00028	0.43969
CCnπ	1.69147	0.00012	1.07245	0.00008	0.00006	0.00014	2.76432
CC DIS	0.07408	0.00000	0.03872	0.00000	0.00000	0.00000	0.11280
NCπ^0	0.12998	0.00599	0.13127	0.00303	0.00000	0.00000	0.27027
NC$\pi^{+/-}$	0.98528	0.03913	1.24585	0.03045	0.00000	0.00000	2.30071
NC coherent	0.00055	0.00000	0.00000	0.00000	0.00000	0.00000	0.00055
NC other	0.58584	0.02452	0.34070	0.01311	0.00000	0.00000	0.96417
2p-2h	6.58237	0.00037	8.98513	0.00033	0.00057	0.00035	15.56912
NC 1γ	0.00000	0.00000	0.00000	0.00000	0.00000	0.00000	0.00000
CC Other	0.15083	0.00000	0.07345	0.00008	0.00000	0.00000	0.22435
Sample totals	45.55751	0.07183	67.67087	0.04891	0.00210	0.00304	
Total	113.35427						

Table C.18: Pre-ND280 fit event rate prediction for FHC $1R_e$ sample: 19.664×10^{20} POT, oscillated

	ν_μ	ν_e	$\bar{\nu}_\mu$	$\bar{\nu}_e$	ν_e signal	$\bar{\nu}_e$ signal	Total
CCQE	0.19211	5.49615	0.00756	0.22694	40.14866	0.25587	46.32728
CC1π	0.06624	1.74370	0.00467	0.09546	7.80104	0.07333	9.78444
CC coherent	0.00000	0.01513	0.00017	0.00454	0.06428	0.00441	0.08854
CCnπ	0.01592	0.15352	0.00042	0.00826	0.10106	0.00292	0.28210
CC DIS	0.00000	0.00582	0.00000	0.00028	0.00043	0.00001	0.00654
NCπ^0	2.68739	0.05847	0.11490	0.00671	0.00000	0.00000	2.86748
NC$\pi^{+/-}$	0.42214	0.01418	0.02031	0.00120	0.00000	0.00000	0.45782
NC coherent	0.29999	0.00605	0.02957	0.00174	0.00000	0.00000	0.33736
NC other	0.55988	0.01803	0.02257	0.00215	0.00000	0.00000	0.60262
2p-2h	0.04618	1.30845	0.00238	0.07015	7.63726	0.06455	9.12896
NC 1γ	1.43050	0.03347	0.06258	0.00296	0.00000	0.00000	1.52952
CC Other	0.00021	0.01058	0.00009	0.00075	0.01163	0.00018	0.02344
Sample totals	5.72056	8.86356	0.26522	0.42114	55.76436	0.40126	
Total	71.43610						

Table C.19: Pre-ND280 fit event rate prediction for RHC $1R_e$ sample: 16.34556×10^{20} POT, oscillated

	ν_μ	ν_e	$\bar{\nu}_\mu$	$\bar{\nu}_e$	ν_e signal	$\bar{\nu}_e$ signal	Total
CCQE	0.02362	0.73183	0.03833	1.20097	1.50654	4.11643	7.61772
CC1π	0.01550	0.29533	0.01930	0.32315	0.43218	0.74720	1.83265
CC coherent	0.00000	0.00193	0.00076	0.02062	0.00278	0.06440	0.09049
CCnπ	0.00289	0.03611	0.00274	0.01782	0.01781	0.01183	0.08920
CC DIS	0.00000	0.00059	0.00000	0.00008	0.00013	0.00000	0.00081
NCπ^0	0.36704	0.01603	0.46985	0.01227	0.00000	0.00000	0.86518
NC$\pi^{+/-}$	0.08306	0.00310	0.06258	0.00169	0.00000	0.00000	0.15044
NC coherent	0.04190	0.00149	0.14077	0.00278	0.00000	0.00000	0.18693
NC other	0.12396	0.00682	0.06412	0.00288	0.00000	0.00000	0.19778
2p-2h	0.00874	0.21623	0.00951	0.30082	0.34598	0.86511	1.74639
NC 1γ	0.16483	0.00666	0.27385	0.00521	0.00000	0.00000	0.45055
CC Other	0.00037	0.00367	0.00000	0.00180	0.00153	0.00057	0.00795
Sample totals	0.83189	1.31978	1.08181	1.89008	2.30696	5.80556	
Total	13.23609						

Table C.20: Pre-ND280 fit event rate prediction for FHC CC-$1\pi^+$ sample: 19.664×10^{20} POT, oscillated

	ν_μ	ν_e	$\bar{\nu}_\mu$	$\bar{\nu}_e$	ν_e signal	$\bar{\nu}_e$ signal	Total
CCQE	0.03464	0.02902	0.00081	0.00178	0.28115	0.00256	0.34997
CC1π	0.08059	1.17134	0.00247	0.00370	7.58149	0.00373	8.84332
CC coherent	0.00060	0.02535	0.00003	0.00026	0.14210	0.00009	0.16843
CCnπ	0.03858	0.13134	0.00050	0.00291	0.12747	0.00122	0.30201
CC DIS	0.00000	0.00286	0.00012	0.00000	0.00030	0.00000	0.00328
NCπ^0	0.05950	0.00159	0.00168	0.00000	0.00000	0.00000	0.06276
NC$\pi^{+/-}$	0.13626	0.00542	0.00493	0.00062	0.00000	0.00000	0.14723
NC coherent	0.00000	0.00000	0.00000	0.00000	0.00000	0.00000	0.00000
NC other	0.20839	0.01039	0.01981	0.00194	0.00000	0.00000	0.24053
2p-2h	0.00954	0.02475	0.00051	0.00156	0.11953	0.00150	0.15739
NC 1γ	0.00000	0.00000	0.00029	0.00016	0.00000	0.00000	0.00045
CC Other	0.00455	0.00481	0.00003	0.00009	0.00201	0.00006	0.01154
Sample totals	0.57265	1.40687	0.03117	0.01301	8.25406	0.00916	
Total	10.28691						

C.3 Comparison to data without reactor constraints

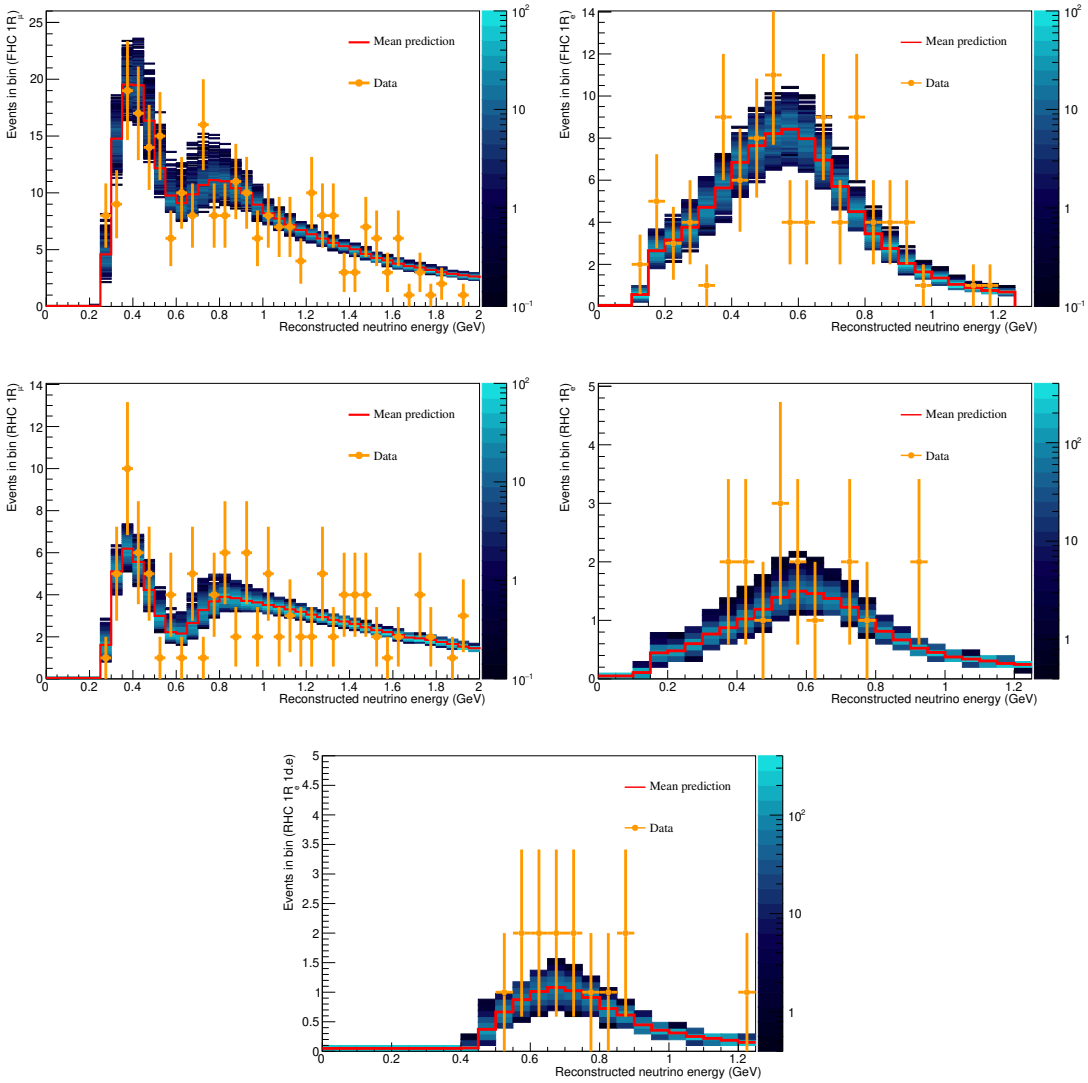

Figure C.9: Mean predictions for each SK sample from the run 1–10 data fit without reactor constraints. Data points are shown in orange. The result of 2500 randomly sampling all parameter values from the posterior is shown in the 2D histogram. The mean predictions are calculated by taking the mean of this distribution in each energy bin. A Markov chain from jointly fitting ND280 and SK data was used and all parameters are sampled.

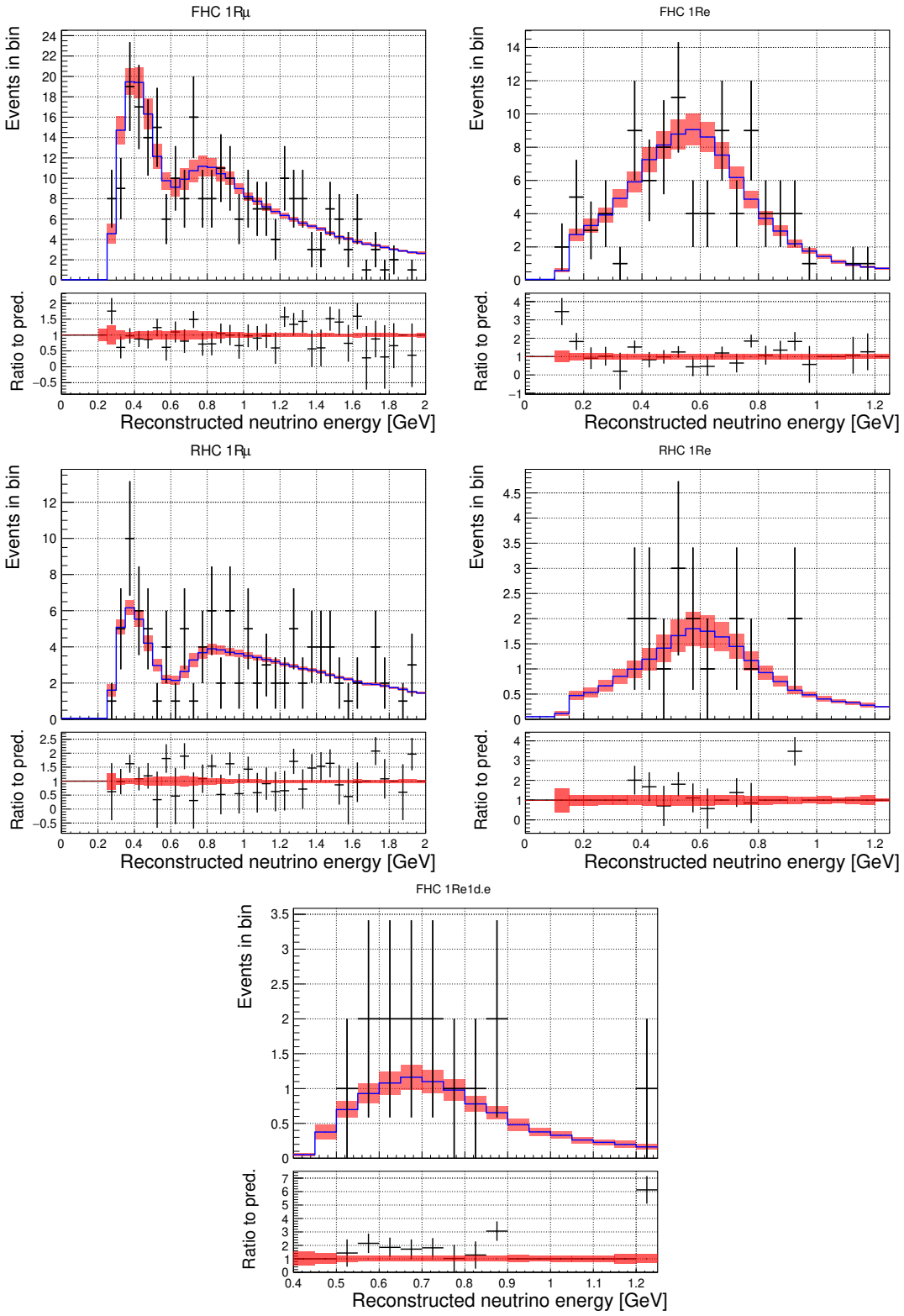

Figure C.10: Post-fit distribution (blue) and one sigma error band (red) with run 1–10 data (black) for each SK selection overlaid. Posterior predictive distributions are made using a Markov chain from a joint SK and ND fit where all parameters are sampled. The post-fit distribution is calculated by taking the mean from the posterior predictive distribution in each bin. Similarly the one sigma error band is calculated by taking the RMS of the posterior predictive distribution in each bin.

Appendix D

Oscillation Analysis including the ν_μCC1π sample at SK

D.1 Fake data at ND280

The fake data inputs used for the fake data studies in chapter 8 are shown below in fig. D.1, fig. D.2 and fig. D.3. The general features are similar to those discussed in chapter 8 in that the CC1π and CC-Other samples have the largest difference compared to the nominal MC prediction. Interactions with a lepton reconstructed in the forward direction ($\cos\theta_{lep} \sim 1$) are the most impact by the CC Multi-π and CC DIS uncertainties that are varied to create the fake data.

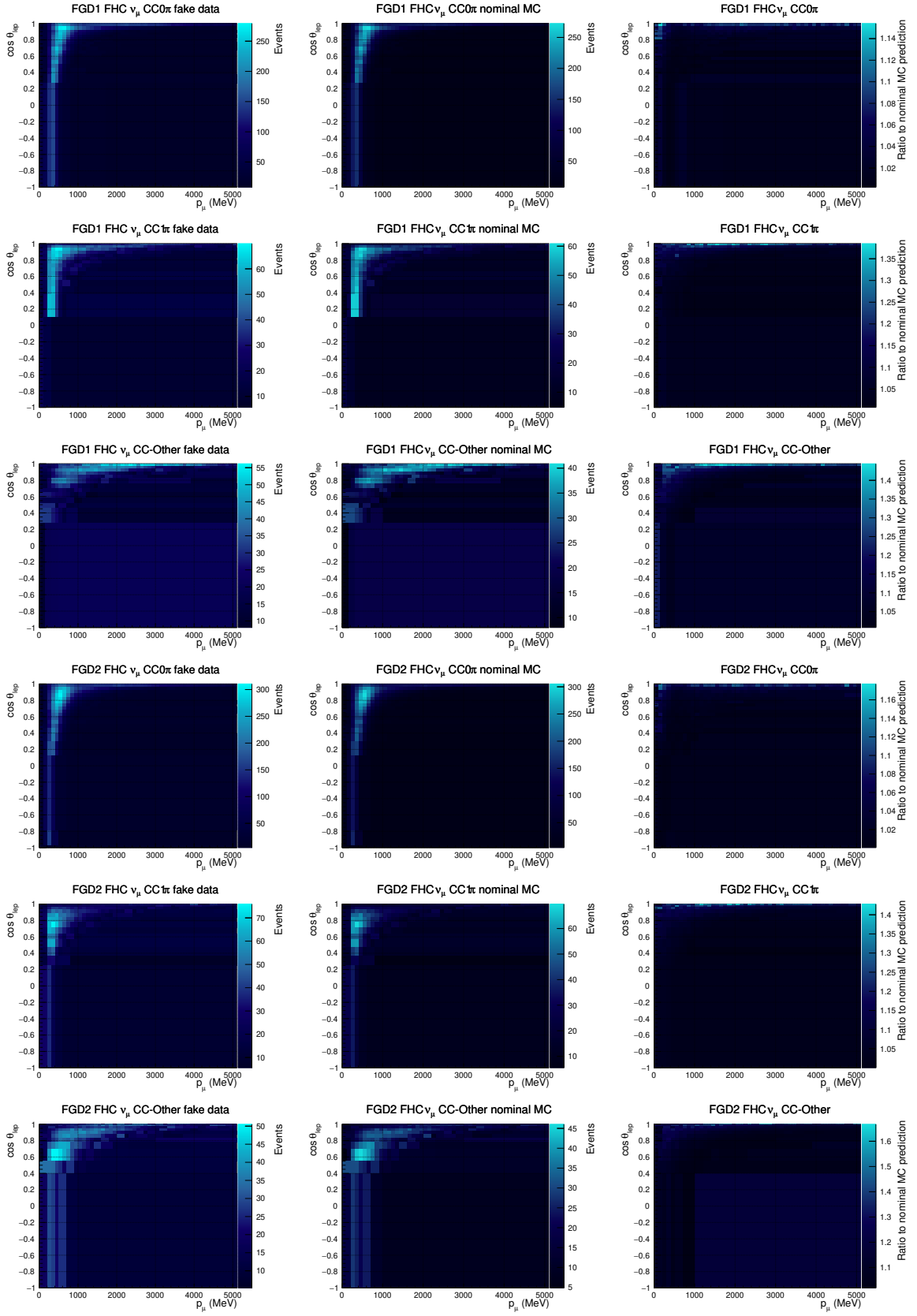

Figure D.1: The fake data (left) and nominal MC (middle) at ND280 used in the FDS as well as the ratio of the fake data to the nominal MC (right). The fake data varies from the nominal MC most in the CC1π and CC-Other samples since these samples contain the most CC Multi-π and CC DIS interactions.

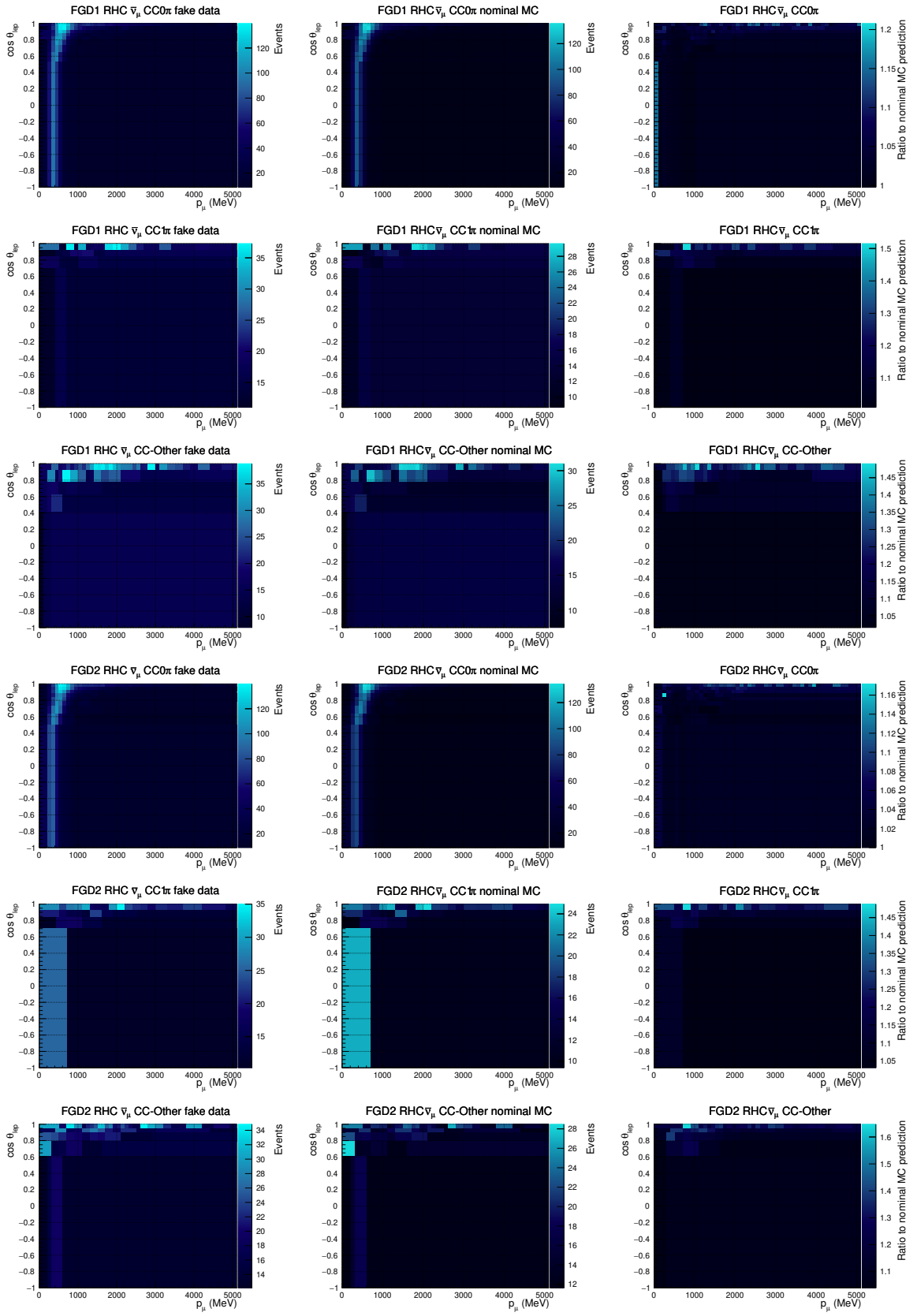

Figure D.2: The fake data (left) and nominal MC (middle) at ND280 used in the FDS as well as the ratio of the fake data to the nominal MC (right). The fake data varies from the nominal MC most in the CC1π and CC-Other samples since these samples contain the most CC Multi-π and CC DIS interactions.

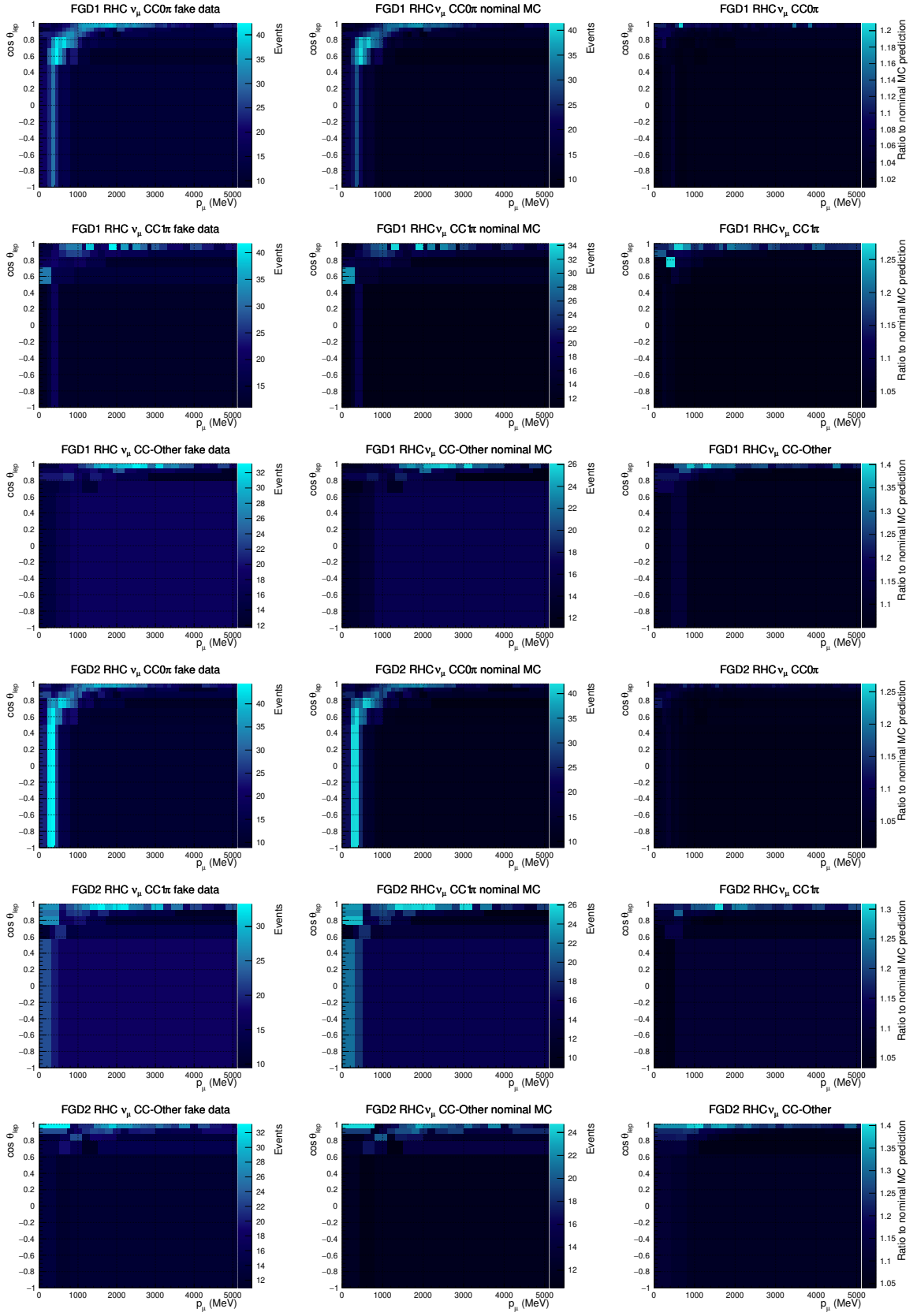

Figure D.3: The fake data (left) and nominal MC (middle) at ND280 used in the FDS as well as the ratio of the fake data to the nominal MC (right). The fake data varies from the nominal MC most in the CC1π and CC-Other samples since these samples contain the most CC Multi-π and CC DIS interactions.